

**Measurement of Neutrino Oscillation Parameters
with the Precise Neutrino Flux Prediction in the
T2K Experiment**

Akira Murakami

January, 2013

**Measurement of Neutrino Oscillation Parameters
with the Precise Neutrino Flux Prediction in the
T2K Experiment**

**A dissertation
submitted in partial fulfillment of the requirements
for the Degree of Doctor of Science
in the Graduate School of Science, Kyoto University**

Akira Murakami

January, 2013

Dissertation Committee:

Tsuyoshi Nakaya
Atsuko K. Ichikawa
Kin-ya Oda
Tomofumi Nagae
Takeshi Go Tsuru

Abstract

We present the measurement of the muon neutrino disappearance in the T2K neutrino experiment. T2K is a long baseline (295 km) neutrino oscillation experiment between Tokai and Kamioka. Muon neutrinos are produced by using the 30 GeV proton beam in J-PARC, and are observed at the near neutrino detector and the Super-Kamiokande detector (SK). The oscillation parameters are determined by comparing the event rate and energy spectrum of muon neutrinos observed at SK with the prediction including the oscillation effect. The results in this thesis are based on the data of 3.01×10^{20} protons on the target corrected taken from January 2010 to June 2012, corresponding to the 4% fraction of the T2K final statistics.

For a precise measurement of the muon neutrino disappearance, high statistics observation of neutrino events and the precise prediction for SK events are essential. The SK prediction is constructed by the predictions of the neutrino flux, the neutrino interaction models and the SK detector response. In this thesis, we established the stable beam operation and the improved predictions of the neutrino flux. The stable beam operation is realized by monitoring the beam properties with several kind of beam monitors. The achieved data taking efficiency is as high as 99.7%. The neutrino flux is predicted by using a Monte Carlo simulation, where major uncertainties raise due to the uncertainties of the hadron production models and uncertainties of beam properties used as inputs of the simulation. We improved the hadron production models by using the external hadron production data (CERN NA61/SHINE, and so on). The uncertainties of beam properties were constrained based on the measurements by the beam monitors. As a result, the uncertainty of the muon neutrino flux at SK was successfully reduced to 12% at the energy around the oscillation maximum. The uncertainty of the relation between the near detector and SK was further smaller, i.e. about 2%. Through this relation, the flux prediction for SK was refined based on the measurements at the near neutrino detector. The neutrino interaction models used in the SK prediction are also refined along with the flux prediction. Finally, we achieved the total systematic error of event rate as 14%, and that of energy spectrum at the energy around oscillation maximum as 8%. Among these, the contribution from the uncertainty from the flux and interaction model is 4% both for the event rate and energy spectrum.

We have observed 58 muon neutrino events were observed at SK, while the expectation is 57.97 at the best fit point in our measurement. From this, we determined the oscillation parameters as

$$(\sin^2 2\theta_{23}, \Delta m_{32}^2) = (1.00_{-0.04}^{+0.00}, 2.45 \pm 0.19 \times 10^{-3} [\text{eV}^2]),$$

and the 90% confidence interval:

$$\begin{aligned} 0.932 < \sin^2 2\theta_{23} \leq 1.00 & \quad (\text{at } \Delta m_{32}^2 = 2.45 \times 10^{-3} [\text{eV}^2]), \\ 2.15 \times 10^{-3} < \Delta m_{32}^2 [\text{eV}^2] < 2.75 \times 10^{-3} & \quad (\text{at } \sin^2 2\theta_{23} = 1.0). \end{aligned}$$

This is the world most precise measurement of $\sin^2 2\theta_{23}$ and the key issues to achieve this precision are the stable beam operation and the improved predictions of the neutrino flux.

Acknowledgements

My work has never achieved without any supports by a lot of people. I would like acknowledge each of them.

First of all, I am deeply grateful to Prof. Tsuyoshi Nakaya, who is my supervisor. His exciting lectures which I took in the university was my motivation to go into high energy physics. He gave me various opportunities to study the exciting parts of neutrino physics. Without his support, this thesis would not exist. I would particularly like to thank Prof. Atsuko K. Ichikawa, who is also my supervisor, for her gentle support and constant encouragement. I could learn a lot of things about not only physics and experimental technique, but also the stance of the experimentalist. I want to thank Prof. Masashi Yokoyama, who worked with me on the MUMON detector. Though I had no knowledge for the experimental technique at first, he carefully taught me them step by step on site. I am grateful to Dr. Akihiro Minamino, who worked with me on the INGRID detector and the oscillation analysis. I could not finish the oscillation analysis without his close supports.

I want to thank Dr. Kodai Matsuoka, Mr. Hajime Kubo, and Mr. Kento Suzuki, who worked together with me on the MUMON detector. Dr. Kodai Matsuoka showed me his persistence for the MUMON detector. I have taken care of the quality of my own works as like him. Mr. Hajime Kubo helped me on the software to operate the MUMON detector. I could operate the MUMON detector easily thanks to him. Mr. Kento Suzuki supported me to operate the MUMON detector on site. I was helped by his deep insight on the severe operation of the MUMON detector. I also want to thank Dr. Masashi Otani and Mr. Tatsuya Kikawa, who worked together with me on the INGRID detector. Dr. Masashi Otani help me on the analysis and operation of the INGRID detector. He answered my questions quickly and carefully. Mr. Tatsuya Kikawa also supported me on the operation of the INGRID detector. His dedicated supports realized the excellent neutrino beam generation.

I would like to express my gratitude to the current and former KEK neutrino group. Prof. Koichiro Nishikawa, Prof. Takuya Hasegawa, and Prof. Takashi Kobayashi led the T2K collaboration to achieve the great results in neutrino physics. Prof. Takeshi Nakdaira led the neutrino beamline operation, and gave me a lot of advice on the monitor operation and oscillation analysis. Prof. Soh Y. Suzuki and Dr. Ken Sakashita worked together with me on the readout electronics and online control of the neutrino beamline. Though I was outsider for the electronics and computing, they supported me kindly, and I took a great deal of interest in the readout and computing thanks to them. Prof. Takasumi Maruyama supported me on the operation of the MUMON detector on site. The quick recovery from the Tohoku earthquake was realized by his support. I also would like to appreciate the gentle supports by Y. Fujii, Y. Yamada, T. Sekiguchi, T. Tsukamoto, M. Tada, T. Ishida, T. Ishii, M. Shibata, H. Kakuno, and N.C. Hastings.

I would like to thank all collaborators of T2K and Super-Kamiokande experiments. Especially, I was helped by Dr. M. Hartz and Dr. V. Calymov on the neutrino flux simulation, and supported by Prof. Y. Hayato, Dr. P. de Perio and Dr. K. Mahn on the neutrino interaction simulation. I was supported by Prof. J. Kameda and Dr. A. Minamino and more collaborators

on the oscillation analysis. I am fortunate to work together with these collaborators.

I want to thank the J-PARC accelerator team and CERN NA61 colleagues for providing necessary particle production data and for their devoted collaboration.

I am deeply thankful to current and former members of the High Energy Group of Kyoto University: N. Sasao, M. Ishino, T. Nomura, H. Nanjo, M. Ikeda, R. P. Litchfield, C. Bronner, T. Sumida, H. Yokoyama, H. Morii, K. Shiomi, K. Hiraide, Y. Nakajima, Y. Kurimoto, K. Nitta, K. Hiraide, T. Usuki, N. Kawasaki, T. Masuda, K. Ieki, D. Naito, Y. Maeda, G. Takahashi, S. Takahashi, K. Huang, T. Hiraki, T. Yamauchi, S. Hirota, K. Goda, S. Seki, T. Tashiro, T. Nagasaki, S. Akiyama, N. Kamo, K. Tateishi and T. Hineno. I would particularly like to thank the kindness and friendship of students of the same grade: K. Ieki, D. Naito, and Y. Maeda. I wish to extend my thanks to the secretaries at Kyoto University, KEK, and J-PARC for taking care of my businesses.

Finally, I would like to express my special thanks to my parents and families for supporting my life. I feel proud to be a child of my parents.

Akira Murakami
Kyoto, Japan
January, 2013

Contents

1	Introduction	1
1.1	Physics of Neutrino Oscillation	1
1.1.1	Neutrino mixing	1
1.1.2	Neutrino oscillation probability in vacuum	3
1.1.3	Observation of Neutrino Oscillation	3
1.1.4	Current knowledge on Neutrino oscillations	4
1.1.5	Importance of the precision of the θ_{23} measurement	5
1.2	Overview of T2K Experiment	8
1.2.1	Experimental principle	9
1.3	Outline of this thesis	10
2	T2K experimental components and beam data taking summary	12
2.1	T2K overview	12
2.2	J-PARC accelerator	15
2.3	Neutrino beamline	15
2.3.1	Primary beamline	16
2.3.2	Secondary beamline	17
2.3.3	Beamline Data acquisition system	19
2.3.4	Global Time Synchronization	19
2.3.5	Alignment	24
2.4	Near Neutrino detectors	24
2.4.1	INGRID	26
2.4.2	ND280	26
2.5	Far Neutrino detector: Super-Kamiokande	27
2.6	Beam data taking history	27
2.6.1	Proton beam measurement	30
2.6.2	Horn current stability	32
2.6.3	Muon profile stability	32
3	Overview of the Oscillation analysis	35
4	Neutrino flux prediction	37
4.1	Overview of the neutrino flux simulation	37
4.2	Hadronic interaction weighting	40
4.2.1	Hadron production data used for weighting process	40
4.2.2	Hadron differential production weighting	43
4.2.3	Hadron interaction rate weighting	46
4.2.4	Summary of Hadron interaction weighting	46
4.3	T2K flux prediction	48
4.4	Flux uncertainty	48

4.4.1	Hadron production uncertainties	51
4.4.2	Summary of the hadron production uncertainties	56
4.4.3	Proton beam uncertainties	56
4.4.4	Neutrino beam direction (off-axis angle) uncertainties	60
4.4.5	Target and horn alignment uncertainties	61
4.4.6	Horn current uncertainty	61
4.4.7	Summary of flux uncertainties	62
4.4.8	Prospect	62
4.5	Extrapolation of the ND280 flux measurements to SK	62
4.5.1	Covariance matrix method	64
5	Neutrino-nucleus interaction model	69
5.1	Overview of the neutrino-nucleus interaction model	69
5.2	Model uncertainties	71
5.3	Effect of the neutrino interaction parameters	74
6	Measurements at the Near and Far detectors	76
6.1	Measurements at INGRID	76
6.1.1	Data set for INGRID measurements	76
6.1.2	Event selection	76
6.1.3	Detector simulation	78
6.1.4	Detector systematic errors	80
6.1.5	Result of the measurements	80
6.1.6	Stability of the neutrino event rate and beam direction	81
6.2	Measurements at ND280	83
6.2.1	Data set for ND280 measurements	83
6.2.2	Event selection	83
6.2.3	Detector systematic errors	86
6.2.4	Result of the measurements	87
6.3	Measurements at SK	87
6.3.1	Data set for SK measurements	91
6.3.2	Event selection	91
6.3.3	Detector systematic errors	93
6.3.4	Results of the measurement	94
7	Extrapolation of ND280 measurements to SK prediction	99
7.1	Overview of the extrapolation of ND280 measurements	99
7.2	Fit of the ND280 p - θ distribution	99
7.2.1	ND280 samples used in the fit	99
7.2.2	Parameters used in the fit	99
7.2.3	Results of the fit	100
7.3	Extrapolation to SK	100
8	Analysis of muon neutrino disappearance	106
8.1	Analysis method	106
8.1.1	Definition of the likelihood	106
8.1.2	Prediction of the event rate and energy spectrum of SK ν_μ events	107
8.2	Systematic parameters	111
8.2.1	Beam flux systematics parameters	111
8.2.2	Neutrino interaction systematics parameters	113
8.2.3	SK detection efficiency and FSI-SI systematics parameters	113

8.2.4	SK energy scale systematic parameter	113
8.2.5	Effect of systematic uncertainties	114
8.3	Sensitivity	117
8.4	Results with Run 1+2+3 data	119
8.4.1	Fit result	119
8.4.2	Allowed region	122
8.4.3	Comparison with other experimental results	126
8.4.4	Summary and prospect	126
9	Conclusion	129
	List of Tables	131
	List of Figures	133
	Bibliography	137

Chapter 1

Introduction

Neutrino is an elementary particle with spin 1/2 and no electrical charge. It interacts with matter only through the weak interaction. Neutrino was originally postulated by W. Pauli in order to explain the observed continuous electron spectrum accompanying nuclear β -decay. Now, it is known that there are three types (flavors) of neutrinos, ν_e , ν_μ and ν_τ , associating with three charged leptons; e , μ and τ . In the standard model of particle physics, neutrinos were originally considered as mass-less particles. There have been many experiments to measure the neutrino mass directly [1–3], but no finite absolute mass has been measured. However, the observation of neutrino oscillations by Super-Kamiokande [4] established the non-zero neutrino masses and neutrino mixing. This result is supported by many neutrino experiments (atmospheric, solar, accelerator, and reactor neutrino experiments [5–16]). The existence of neutrino oscillations requires the modification of the standard model and hence its study is expected to make a link to physics beyond the standard model.

1.1 Physics of Neutrino Oscillation

1.1.1 Neutrino mixing

Flavor eigenstates of neutrinos can be different from the mass eigenstates. Then the flavor eigenstate, $|\nu_\alpha\rangle$ ($\alpha = e, \mu, \tau$) can be described by superpositions of mass eigenstates, $|\nu_i\rangle$ ($i = 1, 2, 3$):

$$|\nu_\alpha\rangle = \sum_i U_{\alpha i}^* |\nu_i\rangle, \quad (1.1)$$

where $U_{\alpha i}$ is an element of the unitary matrix. Since there are three flavors, the matrix U is 3×3 with four independent parameters. Most popular way to express U is using three mixing angles (θ_{12}, θ_{23} and θ_{13}), and one CP phase (δ):

$$\begin{aligned} U_{PMNS} &= \begin{pmatrix} 1 & 0 & 0 \\ 0 & c_{23} & s_{23} \\ 0 & -s_{23} & c_{23} \end{pmatrix} \begin{pmatrix} c_{13} & 0 & s_{13}e^{-i\delta} \\ 0 & 1 & 0 \\ -s_{13}e^{i\delta} & 0 & c_{13} \end{pmatrix} \begin{pmatrix} c_{12} & s_{12} & 0 \\ -s_{12} & c_{12} & 0 \\ 0 & 0 & 1 \end{pmatrix}, \\ &= \begin{pmatrix} c_{12}c_{13} & s_{12}c_{13} & s_{13}e^{-i\delta} \\ -s_{12}c_{23} - c_{12}s_{23}s_{13}e^{i\delta} & c_{12}c_{23} - s_{12}s_{23}s_{13}e^{i\delta} & s_{23}c_{13} \\ s_{12}s_{23} - c_{12}c_{23}s_{13}e^{i\delta} & -c_{12}s_{23} - s_{12}c_{23}s_{13}e^{i\delta} & c_{23}c_{13} \end{pmatrix}, \end{aligned} \quad (1.2)$$

where $c_{ij} = \cos \theta_{ij}$ and $s_{ij} = \sin \theta_{ij}$. This matrix is called as the PMNS (Pontecorvo-Maki-Nakagawa-Sakata) matrix [17, 18] * and is analogue of the CKM (Cabibbo-Kobayashi-Maskawa) matrix in the quark sector [20, 21].

*The mixing model in two neutrinos was also discussed elsewhere [19].

A neutrino is generated and interacts as a flavor eigenstate in the charged or neutral current weak interaction, while the quantum state evolves in time according to the mass eigenstates following the Schrödinger's equation. Applying the Schrödinger's equation to the ν_i component of ν_α in the rest frame of that component, the evolution is written as:

$$|\nu_i(\tau_i)\rangle = e^{-im_i\tau_i}|\nu_i(0)\rangle, \quad (1.3)$$

where m_i is the mass of ν_i , and τ_i is the time in the ν_i rest-frame. Using the time t and position L in the laboratory frame, the Lorentz-invariant phase factor in Eq. 1.3 is written as:

$$m_i\tau_i = E_it - p_iL, \quad (1.4)$$

where E_i and p_i represent the energy and momentum of ν_i in the laboratory frame. In practice, since the neutrino is extremely relativistic due to the tiny mass, following approximation is applied to Eq. 1.4:

$$t \approx L, E_i = \sqrt{p_i^2 + m_i^2} \approx p_i + \frac{m_i^2}{2p_i}. \quad (1.5)$$

All of mass-eigenstate components in ν_α have an approximately common momentum p . The phase factor of Eq. 1.4 is then approximated as:

$$(m_i^2/2p)L. \quad (1.6)$$

From this expression and Eq. 1.3, when a neutrino is produced as ν_α and has propagated a distance L , the state of ν_α becomes

$$|\nu_\alpha(L)\rangle \approx \sum_i U_{\alpha i}^* e^{-i(m_i^2/2E)L} |\nu_i(0)\rangle, \quad (1.7)$$

where $E \sim p$ is the average energy of the various mass eigenstate components of the neutrino. Using the unitarity of U to invert Eq. 1.3, and inserting the result in Eq. 1.7:

$$|\nu_\alpha(L)\rangle \approx \sum_\beta \left[\sum_i U_{\alpha i}^* e^{-i(m_i^2/2E)L} U_{\beta i} \right] |\nu_\beta\rangle. \quad (1.8)$$

This equation represents that ν_α has turned into a superposition of all the flavors after traveling the distance L . This is the phenomenon called "neutrino oscillation". Figure 1.1 depicts the neutrino oscillation at the simply two neutrino oscillation case. If the masses of neutrinos are non-zero and are not degenerated, the neutrino flavors change according to the distance.

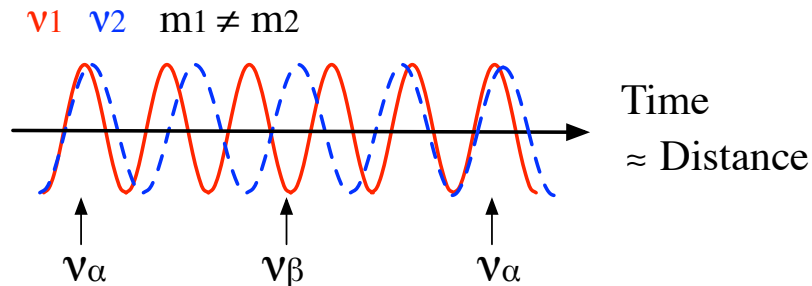


Figure 1.1: Two neutrino oscillation scenario, showing the amplitudes of ν_1 and ν_2 mass eigenstates.

1.1.2 Neutrino oscillation probability in vacuum

The neutrino oscillation probability $P(\nu_\alpha \rightarrow \nu_\beta)$ represents the probability that the flavor ν_β is observed when ν_α is generated and travels the distance L . The oscillation probability $P(\nu_\alpha \rightarrow \nu_\beta)$ between three flavors in vacuum is obtained from Eq. 1.8:

$$\begin{aligned} P(\nu_\alpha \rightarrow \nu_\beta) &= |\langle \nu_\beta | \nu_\alpha(L) \rangle|^2 \\ &= \delta_{\alpha\beta} - 4 \sum_{i>j} \text{Re}(U_{\alpha i}^* U_{\beta i} U_{\alpha j} U_{\beta j}^*) \sin^2 \left(\frac{\Delta m_{ij}^2 L}{4E} \right) \\ &\quad \pm 2 \sum_{i>j} \text{Im}(U_{\alpha i}^* U_{\beta i} U_{\alpha j} U_{\beta j}^*) \sin 2 \left(\frac{\Delta m_{ij}^2 L}{4E} \right), \end{aligned} \quad (1.9)$$

where $\Delta m_{ij}^2 = m_i^2 - m_j^2$, is mass squared difference between ν_i and ν_j . The sign of the last term in Eq. 1.9 originates from the sign of CP phase δ , and is + (−) for neutrinos (anti-neutrinos). The oscillation probability $P(\nu_\alpha \rightarrow \nu_\alpha)$ represents the survival probability of ν_α . When the omitted factors of \hbar and c are included in Eq. 1.9, and Δm_{ij}^2 , L , and E are expressed in the unit of eV^2 , km, and GeV, the oscillation phase can be written as:

$$\Phi_{ij} \equiv \frac{\Delta m_{ij}^2 L}{4E} \simeq 1.2669 \cdot \Delta m_{ij}^2 (\text{eV}^2) \cdot \frac{L(\text{km})}{E(\text{GeV})}. \quad (1.10)$$

Because $\Delta m_{12}^2 + \Delta m_{23}^2 + \Delta m_{31}^2 = 0$, there are six independent parameters in the neutrino oscillation: three mixing angles, one CP phase, and any two of three mass square differences.

From experimental data (will be described in Sec. 1.1.4), we know $|m_{32}^2| \simeq |m_{31}^2| \gg m_{21}^2$. At $E \sim (\Delta m_{32}^2 \cdot L)$, the contribution of Δm_{21}^2 term is small and the oscillation probabilities can be approximately described by two mixing angles (θ_{13}, θ_{23});

$$\begin{aligned} P(\nu_\mu \rightarrow \nu_e) &\simeq \sin^2 2\theta_{13} \cdot \sin^2 \theta_{23} \cdot \sin^2 \Phi_{32} \\ &\equiv \sin^2 2\theta_{\mu e} \cdot \sin^2 \Phi_{32}, \end{aligned} \quad (1.11)$$

$$\begin{aligned} P(\nu_\mu \rightarrow \nu_\mu) &\simeq 1 - \sin^2 2\theta_{23} \cdot \cos^4 \theta_{13} \cdot \sin^2 \Phi_{32} - P(\nu_\mu \rightarrow \nu_e) \\ &\equiv 1 - \sin^2 2\theta_{\mu\tau} \cdot \sin^2 \Phi_{32} - P(\nu_\mu \rightarrow \nu_e), \end{aligned} \quad (1.12)$$

where the following two effective mixing angles are defined: $\sin^2 2\theta_{\mu e} \equiv \sin^2 2\theta_{13} \cdot \sin^2 \theta_{23}$ and $\sin^2 2\theta_{\mu\tau} \equiv \sin^2 2\theta_{23} \cdot \cos^4 \theta_{13}$. The situation described by these equations may be called quasi-two-neutrino oscillation. The $P(\nu_\mu \rightarrow \nu_\mu)$ in Eq. 1.12 is drawn in Fig. 1.2 for several values of $\sin^2 2\theta_{23}$ and Δm_{32}^2 .

Neutrino oscillations in matter

Inside the Sun or the Earth, all flavors of neutrino have the neutral current interaction with matter ($\nu + N \rightarrow \nu + X$, where N is the nucleon, X is the hadronic final state, $\nu_e + e \rightarrow \nu_e + e$, and so on), while only ν_e has the charge current interaction ($\nu_e + N \rightarrow e + X$) in the MeV energy range. The ν_μ and ν_τ have insufficient energy to produce the associated charged leptons (μ and τ). Hence ν_e feels extra potential in matter via the neutral current interaction, and the oscillation probability in matter can be different from that in vacuum. This is known as the matter effect [22].

1.1.3 Observation of Neutrino Oscillation

Neutrino oscillations are observed in two ways: via appearance ($\nu_\alpha \rightarrow \nu_\beta$) or disappearance ($\nu_\alpha \rightarrow \nu_\alpha$). In each way, the neutrino flavors have to be identified. The flavor identification relies

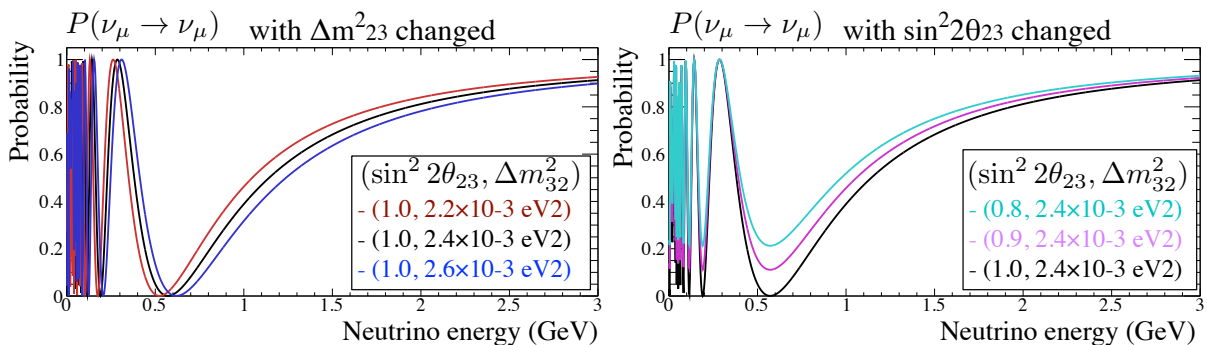


Figure 1.2: Oscillation probability for ν_μ disappearance from Eq. 1.12. Left: Δm_{23}^2 is set to be 2.2×10^{-3} , 2.4×10^{-3} , 2.6×10^{-3} eV². Right: $\sin^2 2\theta_{23}$ is set to be 0.8, 0.9, 1.0. The $\sin^2 \theta_{13}$ is fixed to 0.0251 and L to 295 km.

on the detection of the associated charged lepton produced at the charged current interaction. As mentioned, when the energy of the neutrino is less than the threshold to produce the associated charged leptons, neutrinos cannot interact in the charge current mode, and their flavors cannot be identified. Such cases are identified as disappearance.

There are several neutrino sources used to measure neutrino oscillations. The sources are summarized in Table 1.1 with the average neutrino energy (E), a typical distance between source and detector (L). The sensitivity to oscillation parameters, $\sin^2 2\theta$ and Δm^2 , depends on the value of L/E . The $\sin^2 2\theta$ determines the amplitude of the neutrino oscillation and the Δm^2 determines the scale of distance where the neutrino oscillation evolves. The maximum oscillation, (i.e. $P(\nu_\mu \rightarrow \nu_x) \simeq 1$) occurs at $\sin^2 \Phi_{32} = 1$, i.e. $\Delta m_{32}^2 L/4E = \pi/2$, and the sensitivity to $\sin^2 2\theta$ is maximum there. The precision of oscillation parameter determination depends on different experimental errors due to the statistical and systematic uncertainties. Roughly, the precision of $\sin^2 2\theta$ depends on the normalization error at the energy around the oscillation maximum, and the precision of Δm^2 the measurement accuracy of L/E , that is, the resolution of the neutrino energy (when L is fixed).

Table 1.1: Sensitivity of several neutrino oscillation experiments. \bar{E} is the average neutrino energy, L is the distance between source and detector, and corresponding $\Delta m^2 \sim \bar{E}/L$ which is a sensitive Δm^2 roughly.

Source	Flavor	\bar{E} [MeV]	L [km]	Δm^2 [eV ²]
Reactor (short or long baseline)	$\bar{\nu}_e$	~ 1	1 or 100	$\sim 10^{-3}$ or $\sim 10^{-5}$
Accelerator (short or long baseline)	$\nu_{\mu,e}, \bar{\nu}_{\mu,e}$	$\sim 10^3$	1 or 10^3	~ 1 or $\sim 10^{-3}$
Atmospheric ν	$\nu_{\mu,e}, \bar{\nu}_{\mu,e}$	$\sim 10^3$	10^4	$\sim 10^{-4}$
Sum	ν_e	~ 1	1.5×10^8	$\sim 10^{-11}$

1.1.4 Current knowledge on Neutrino oscillations

Until now, many neutrino oscillation experiments have provided the evidences for neutrino oscillations and have measured the oscillation parameters.

Measurements of θ_{23} and Δm_{23}^2 : The oscillation of atmospheric neutrinos was discovered as the muon neutrino disappearance by the Super-Kamiokande (SK) experiment [5]. This

is the first evidence of neutrino oscillations. This result has been confirmed by the long baseline accelerator neutrino experiments (K2K [6] and MINOS [7]).

Measurements of θ_{12} and Δm_{12}^2 : The disappearance of electron neutrinos from the Sun was first indicated by the experiment by R.Davis *et al.* [23] and Kamiokande [24]. Then, the oscillation of solar neutrinos was discovered by several solar neutrino experiments (SK [8], SNO [9], Brexino [10] and so on) and confirmed by a reactor neutrino experiment, KamLAND [11].

Measurements of θ_{13} : The oscillation associated with θ_{13} has been searched for a long time. The θ_{13} was found to be smaller than other mixing angle. The CHOOZ experiment determined the upper limit of $\sin^2 2\theta_{13}$: $\sin^2 2\theta_{13} < 0.15$ with 90% C.L. [25]. The accelerator experiments (T2K [12] and MINOS [13]) search for the electron neutrino appearance ($\nu_\mu \rightarrow \nu_e$) which occurs via θ_{13} . T2K first reported the indication of ν_e appearance oscillation with 2.5σ significance and measured the non-zero θ_{13} . Then non-zero θ_{13} has been confirmed by the several reactor experiments with more than 3σ significance: Double Chooz [14], Daya Bay [15], and RENO [16].

The current best knowledge of the oscillation parameters are summarized in Table 1.2. All Δm^2 s and θ_{12} are determined with few percent accuracy, while the θ_{23} and θ_{13} are determined with ~ 10 percent accuracy. The θ_{23} is consistent with the maximal mixing (45°) but the non-maximum θ_{23} is favored from the current data (from the constraint of the atmospheric neutrino data). The CP phase δ and the neutrino mass hierarchy (the sign of Δm_{32}^2) are still unknown.

Table 1.2: The best-fit values of the three-neutrino oscillation parameters, obtained from a global fit of the current neutrino oscillation data [26], including the T2K [12] and MINOS [13] (but not the Daya Bay and RENO) results. The PDG (Particle Data Group) average of the results of the three reactor experiments [14–16] is given in the last line. The 1σ accuracy is defined as the $1/6$ of the $\pm 3\sigma$ interval.

Parameter	best-fit	best-fit angle	$\pm 3\sigma$ interval	1σ accuracy
$\Delta m_{12}^2 [10^{-5} \text{eV}^2]$	$7.58_{-0.26}^{+0.22}$	–	$6.99 - 8.18$	2.5 %
$\Delta m_{32}^2 [10^{-3} \text{eV}^2]$	$2.35_{-0.09}^{+0.12}$	–	$2.06 - 2.67$	4.3 %
$\sin^2 \theta_{12}$	$0.312_{-0.015}^{+0.018}$	$34.0^\circ \pm 1.1^\circ$	$0.265 - 0.364$	5.3 %
$\sin^2 \theta_{23}$	$0.420_{-0.03}^{+0.08}$	$40.4_{-1.8}^{+4.6}^\circ$	$0.34 - 0.64$	12 %
$\sin^2 \theta_{13}$ [27]	0.0251 ± 0.0034	$9.1^\circ \pm 0.6^\circ$	$0.015 - 0.036$	14 %

1.1.5 Importance of the precision of the θ_{23} measurement

With non-zero θ_{13} , we now can approach the unsolved problems of neutrino physics:

- CP asymmetry in the lepton sector
- Neutrino mass hierarchy
- Neutrino mixing scheme

To solve these problems, it is essential to reduce the large uncertainties of θ_{23} in addition to that of θ_{13} .

CP asymmetry in the lepton sector

The CP phase δ introduces the CP asymmetry in the lepton sector and is expected to give a hint for the understanding of the origin of the matter-dominated universe. The δ is the last remaining oscillation parameter to be measured in the PMNS matrix. Now, the non-zero θ_{13} enables us to investigate the CP phase δ .

The comparison of the probabilities between $P(\nu_\mu \rightarrow \nu_e)$ and $P(\bar{\nu}_\mu \rightarrow \bar{\nu}_e)$ is one of the most promising methods to measure the δ . In the three flavor mixing including the first order of the matter effect, the probability of ν_e appearance is written as [28]:

$$\begin{aligned}
 P(\nu_\mu \rightarrow \nu_e) &= 4c_{13}^2 s_{13}^2 s_{23}^2 \cdot \sin^2 \Phi_{31} \\
 &+ 8c_{13}^2 s_{12} s_{13} s_{23} (c_{12} c_{23} \cos \delta - s_{12} s_{13} s_{23}) \cdot \cos \Phi_{32} \sin \Phi_{31} \sin \Phi_{21} \\
 &- 8c_{13}^2 c_{12} c_{23} s_{12} s_{13} s_{23} \sin \delta \cdot \sin \Phi_{32} \sin \Phi_{31} \sin \Phi_{21} \\
 &+ 4s_{12}^2 c_{13}^2 (c_{12}^2 c_{23}^2 + s_{12}^2 s_{23}^2 s_{13}^2 - 2c_{12} c_{23} s_{12} s_{13} \cos \delta) \cdot \sin^2 \Phi_{21} \\
 &- 8c_{13}^2 c_{13}^2 s_{23}^2 \cdot \frac{aL}{4E_\nu} (1 - 2s_{13}^2) \cdot \cos \Phi_{32} \sin \Phi_{31} \\
 &+ 8c_{13}^2 s_{13}^2 s_{23}^2 \frac{a}{\Delta m_{31}^2} (1 - 2s_{13}^2) \cdot \sin^2 \Phi_{31}, \tag{1.13}
 \end{aligned}$$

$$a \equiv 2\sqrt{2}G_F n_e E_\nu = 7.56 \times 10^{-5} \times \rho[\text{g/cm}^3] \times E_\nu, \tag{1.14}$$

where G_F is the Fermi weak-coupling constant, n_e is the electron density, ρ is the mass density of the Earth, and a represents the factor associated to the matter effect. $P(\bar{\nu}_\mu \rightarrow \bar{\nu}_e)$ is derived by replacing $\delta \rightarrow -\delta$ and $a \rightarrow -a$. The first term is the probability of the ν_e appearance in the quasi-two-neutrino oscillation (called the leading term). The third term is the CP asymmetry term which flips its sign between ν and $\bar{\nu}$ (called the CP violation term). The amplitude of the CP asymmetry depends on the all mixing angles and δ . The last two terms represent the correction from the matter effect, and produce a non CP-related asymmetry between ν and $\bar{\nu}$. Figure 1.3 shows $P(\nu_\mu \rightarrow \nu_e)$ and $P(\bar{\nu}_\mu \rightarrow \bar{\nu}_e)$ with $\delta = \pi/2$ (the normal mass hierarchy is assumed). The leading term is a dominant contribution in the ν_e appearance probability. The CP violation term is second dominant as large as 27% of the leading term and flips for ν and $\bar{\nu}$ as shown in this figure.

From the current knowledge of mixing angles, the effect of the uncertainty of each mixing angle is calculated on the amplitude of $P(\nu_\mu \rightarrow \nu_e)$. Here, the effects on the amplitude of the leading and CP violation terms are calculated. Table 1.3 summarizes the fractional change of the amplitudes under the change to each mixing angle by $\pm 1 \sigma$ accuracy shown in Table 1.2. The uncertainty of the CP violation term comes from the uncertainty of $\sin^2 \theta_{13}$ dominantly. The uncertainty of the leading term, however, comes from not only the uncertainty of $\sin^2 \theta_{13}$, but also that of $\sin^2 \theta_{23}$. To observe the CP asymmetry, both the large uncertainties of $\sin^2 \theta_{13}$ and $\sin^2 \theta_{23}$ need to be improved.

Table 1.3: Summary of the fractional change of the amplitude for the leading and CP violation terms in the ν_e appearance probability (shown in Eq. 1.13). The fractional change is calculated under the change of each mixing angle by $\pm 1 \sigma$ accuracy shown in Table 1.2.

	$\delta(\sin^2 \theta_{12})$	$\delta(\sin^2 \theta_{23})$	$\delta(\sin^2 \theta_{13})$
Leading term	-	$\pm 11.9 \%$	$+14.3/-13.5 \%$
CP violation term	$\pm 1.5 \%$	$+1.0/-2.2 \%$	$+5.8/-6.5 \%$

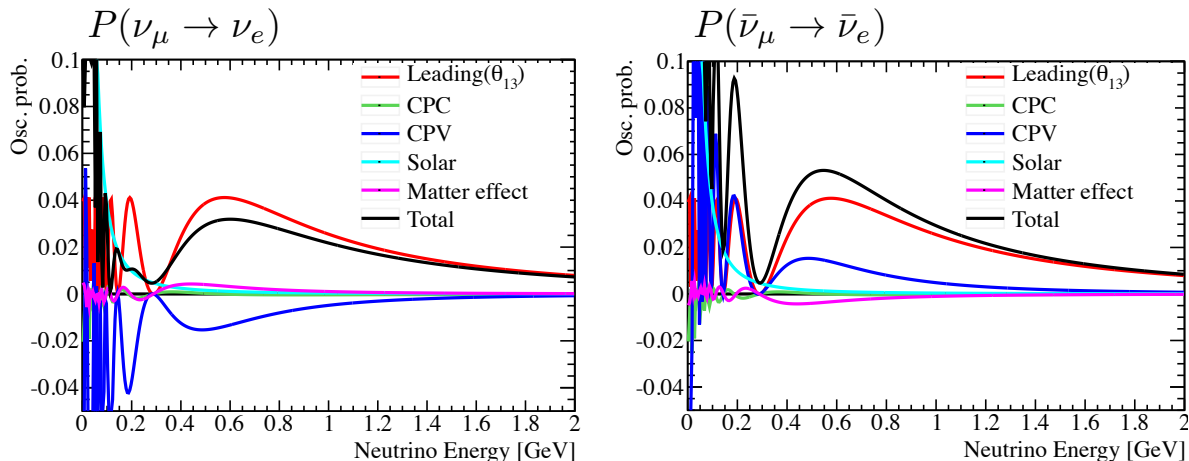


Figure 1.3: ν_e appearance probabilities of $\nu_\mu \rightarrow \nu_e$ (left) and $\bar{\nu}_\mu \rightarrow \bar{\nu}_e$ (right) as a function of the neutrino energy with a baseline of 295 km. The CP phase δ is set to $\pi/2$ and the other oscillation parameters is set to the best fit values shown in Table 1.2. The density ρ is 2.6 g/cm^3 . The normal hierarchy is assumed. Contribution from each term of Eq. 1.13 is shown separately: "Leading(θ_{13})" is the first term, "CPC" is the second, "CPV" is the third, "Solar" is the fourth, and "Matter effect" is the last two terms.

Neutrino mass hierarchy

From the current neutrino oscillation data, the sign of Δm_{32}^2 (and Δm_{31}^2) is not yet determined. There are two possible hierarchy for the neutrino masses as shown Fig. 1.4: the normal hierarchy with ($\Delta m_{32}^2 > 0$, $\Delta m_{31}^2 > 0$) and the inverted hierarchy with ($\Delta m_{32}^2 < 0$, $\Delta m_{31}^2 < 0$). The experimental determination of the mass hierarchy is important to understand the origin of the neutrino masses. In the atmospheric neutrino experiment, the mass hierarchy can be determined by measuring the matter effect of the atmospheric ν_e appearance because the contribution of the matter effect is affected by the sign of Δm_{32}^2 as shown in Eq. 1.13. The sensitivity to determination depends on not only θ_{13} , but also θ_{23} (See, for example, [29]). This is because the ν_e appearance component depends on θ_{13} and θ_{23} as shown in Eq. 1.11. The precision of θ_{23} is critical to solve the mass hierarchy.

Neutrino mixing scheme

From the best fit values of mixing angles shown in Table 1.2, the PMNS matrix is calculated:

$$U_{PMNS} = \begin{pmatrix} 0.82 \pm 0.01 & 0.55^{+0.02}_{-0.01} & 0.16 \pm 0.01 \\ -0.51^{+0.01}_{-0} & 0.57^{+0.03}_{-0.06} & 0.64^{+0.06}_{-0.02} \\ 0.26^{+0.05}_{-0.02} & -0.61^{+0.02}_{-0.04} & 0.75^{+0.02}_{-0.06} \end{pmatrix}, \quad (1.15)$$

where δ is set to zero. The mixing in the leptonic sector is very different from that in the quark sector [27]:

$$U_{CKM} = \begin{pmatrix} 0.97427 \pm 0.00015 & 0.22534 \pm 0.00065 & 0.00351^{+0.00015}_{-0.00014} \\ 0.22520 \pm 0.00065 & 0.97344 \pm 0.00016 & 0.0412^{+0.0011}_{-0.0005} \\ 0.00867^{+0.0029}_{-0.0031} & 0.0404^{+0.0011}_{-0.0005} & 0.999146^{+0.00021}_{-0.00046} \end{pmatrix}, \quad (1.16)$$

Considering this mixing difference and the contrast between the tiny neutrino masses and the large quark masses, it is suggested that physics underlying neutrino masses and mixing may be very different from the physics behind quark masses and mixing. To find a hint for this mystery,

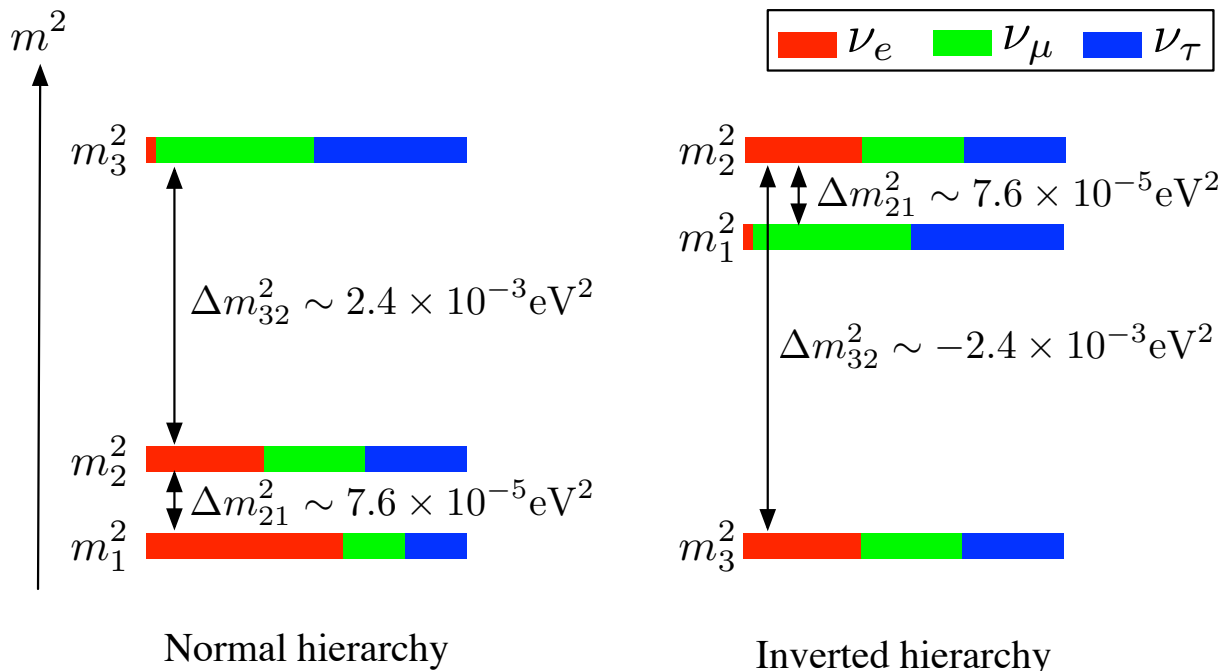


Figure 1.4: Two possible hierarchy cases for the neutrino masses. The normal mass hierarchy is the case where $\Delta m_{32}^2 > 0$, and the inverted mass hierarchy where $\Delta m_{32}^2 < 0$.

more precise measurements of the mixing angles are necessary. The θ_{23} causes the large mixing in the lepton sector and its uncertainty needs to be reduced. Also, if the θ_{23} is not maximal exactly ($\neq 45^\circ$) as $\sin^2 2\theta_{23} < 0.99$, the $\sin^2 \theta_{23}$ can be two values: $\sin^2 \theta_{23} < 0.5$ or $\sin^2 \theta_{23} > 0.5$ (e.g. if $\sin^2 2\theta_{23} = 0.96$, $\sin^2 \theta_{23} = 0.4$ or 0.6). As mentioned, the size of $\sin^2 \theta_{23}$ is essential for the measurement of the CP asymmetry and the neutrino mass hierarchy. It is important to conclude how the θ_{23} is close to 45° based on the precise measurement with 1% accuracy (the same accuracy as Cabibo angle in the quark mixing).

1.2 Overview of T2K Experiment

The T2K (Tokai-to-Kamioka) neutrino experiment is a long-baseline accelerator neutrino oscillation experiment between Tokai and Kamioka [30, 31]. The baseline is 295 km as shown in Fig. 1.5. An intense muon neutrino beam (the energy ~ 0.6 GeV) is produced at Japan Proton Accelerator Research Complex (J-PARC) in Tokai. The neutrinos are measured at the near neutrino detectors in the J-PARC before oscillation, and are measured at the Super-Kamiokande water Cherenkov detector after oscillation. T2K measures the mixing angle θ_{13} via the ν_e appearance [12], and the mixing angle θ_{23} and mass difference Δm_{32}^2 via the ν_μ disappearance [32]. The original goals of T2K are:

- Measurement of the non-zero $\sin^2 2\theta_{13}$ (with sensitivity down to 0.006) via the ν_e appearance.
- Measurement of $\sin^2 2\theta_{23}$ and Δm_{32}^2 with the precision of $\delta(\Delta m_{32}^2) \sim 10^{-4}$ eV² and $\delta(\sin^2 2\theta_{23}) \sim 0.01$ via the ν_μ disappearance.
- Search for sterile components in ν_μ disappearance by detecting the neutral current events.

In this thesis, we focus on the measurement of $\sin^2 2\theta_{23}$ and Δm_{32}^2 via the ν_μ disappearance.



Figure 1.5: Bird's eye view of T2K layout

1.2.1 Experimental principle

The ν_μ disappearance has two features: the distortion of the ν_μ energy spectrum and the deficit of the number of SK ν_μ events. Most of the ν_μ oscillate into ν_τ . The ν_τ cannot be detected because the neutrino energy in T2K is below the τ production threshold. Therefore, the ν_μ energy spectrum at SK shows deficit depending on the neutrino energy as shown in Fig. 1.6. To measure $\sin^2 2\theta_{23}$ and Δm_{32}^2 :

- The number of SK ν_μ events is measured as a function of neutrino energy, $N_{SK}^{obs}(E_\nu)$.
- The number of SK ν_μ events is predicted as a function of neutrino energy, $N_{SK}^{exp}(E_\nu)$. This prediction takes into account the neutrino oscillation.
- The $N_{SK}^{obs}(E_\nu)$ and $N_{SK}^{exp}(E_\nu)$ are compared to determine the $\sin^2 2\theta_{23}$ and Δm_{32}^2 .

where the E_ν represents the neutrino energy.

$N_{SK}^{obs}(E_\nu)$ is obtained by selecting the ν_μ charged current quasi-elastic interaction ($\nu_\mu + n \rightarrow \mu^- + p$), called CCQE. The CCQE interaction is a dominant interaction mode in the T2K neutrino energy region, and its fraction is expected to be $\sim 54\%$ ($\sim 75\%$) in neutrino events selected at SK with (without) oscillation. The neutrino energy E_ν is reconstructed as E_ν^{rec} based on the muon momentum and angle in the CCQE interactions. In the charge current interactions other than CCQE (CC nonQE), the neutrino energy is mis-reconstructed to the lower energy.

The expectation as a function of reconstructed neutrino energy, $N_{SK}^{exp}(E_\nu^{rec})$ is described:

$$N_{SK}^{exp}(E_\nu^{rec}; \theta_{23}, \Delta m_{32}^2) = \int dE_\nu \Phi_{SK}(E_\nu) \cdot P(E_\nu; \theta_{23}, \Delta m_{32}^2) \cdot \sigma(E_\nu) \cdot \epsilon_{SK}(E_\nu) \cdot R_{SK}(E_\nu^{rec}, E_\nu) \times M_{SK} \times \text{POT}, \quad (1.17)$$

where Φ_{SK} is the neutrino flux at SK, P is the oscillation probability, σ is the cross-section of the neutrino-nucleus interaction, ϵ_{SK} is the SK detection efficiency, R_{SK} is the SK detector response function representing the probability to observe E_ν as E_ν^{rec} , M_{SK} is the target mass of SK, and the POT represents the number of protons on the target. The Φ_{SK} is predicted by using the neutrino flux simulation. The σ is calculated based on the neutrino-nucleus interaction models. The ϵ_{SK} and R_{SK} is estimated with the SK detector simulation.

The precision of $\sin^2 2\theta_{23}$ and Δm_{32}^2 depends on the following uncertainties:

- The statistical uncertainties of $N_{SK}^{obs}(E_\nu)$

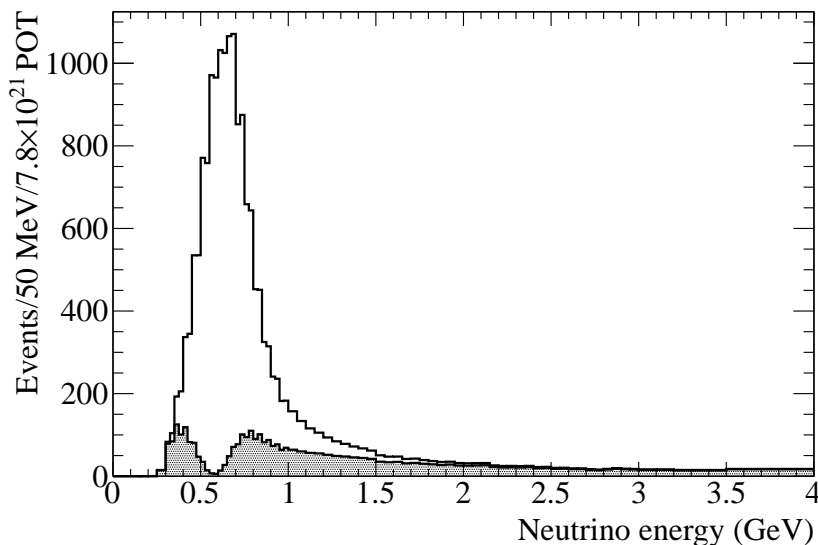


Figure 1.6: Expected neutrino energy spectrum for the null oscillation case (solid line) and the oscillation case ($\sin^2 2\theta_{23} = 1.0$ and $\Delta m_{32}^2 = 2.4 \times 10^{-3} \text{ eV}^2$) (hatched region) at 7.8×10^{21} POT (protons on the target) which corresponds to the T2K final goal.

- The systematical uncertainties of $\Phi_{SK}(E_\nu)$, $\sigma(E_\nu)$ and $\epsilon_{SK}(E_\nu)$. Especially, $\Phi_{SK}(E_\nu)$ and $\sigma(E_\nu)$ have large uncertainties.

For the precise measurement of $\sin^2 2\theta_{23}$ and Δm_{32}^2 , T2K utilizes following approach:

- To reduce statistical uncertainties, high intensity neutrino beam and low background condition are achieved.
- To reduce systematic uncertainties of $\Phi_{SK}(E_\nu)$ and $\sigma(E_\nu)$, the neutrino flux simulation and neutrino interaction models are tuned in situ measurements. The measurements not covered by T2K rely on external data.

1.3 Outline of this thesis

In this thesis, we describe the measurement of the oscillation parameters, $\sin^2 2\theta_{23}$ and Δm_{32}^2 , via ν_μ disappearance. We have archived the most precise measurements for $\sin^2 2\theta_{23}$ so far. The key issues for the precise measurements are the statistical increase of neutrino events based on the high power and stable beam operation, and the improved predictions of neutrino flux based on measurements.

Improved predictions of neutrino flux

The neutrino flux and energy spectrum at T2K neutrino detectors are predicted by using a Monte Carlo simulation based on the experimental data. The simulation first starts with the hadronic interaction of 30 GeV protons in the target where pions are mainly generated. The generated pions are focused forward in the horn magnetic fields, then decay to generate neutrinos in flight. So far, the flux prediction had $\sim 20\%$ uncertainty. The dominant error source is the hadron production models used in the simulation since the models have large uncertainties due to lack of data for 30 GeV protons. To achieve the T2K's physics requirement, it is essential to improve the precision of the simulation. This is achieved by the following procedures:

- Improvement of the hadron production model in the simulation. We improved the model based on the measurements of the hadron production, especially by the CERN NA61/SHINE experiment [33,34]. The CERN NA61/SHINE measurements have been performed for T2K to measure the properties of hadron productions with 30 GeV proton energies. Other external measurements are also used for the model tuning.
- Measurements of the beam properties (proton and neutrino beam parameters) used as inputs in the simulation. They were measured at the several kinds of beam monitors. The measured horn currents which affects the pion focusing were also used in the simulation.
- Refining the predicted Φ_{SK} based on the measurements at the near neutrino detector. Similar to the SK prediction, the prediction for the near detector is constructed by using the flux prediction for the near detector (Φ_{ND}) and also neutrino interaction cross-section (σ). The Φ_{ND} and σ are refined based on the measurements at the near neutrino detector. The refined Φ_{ND} is reflected to the prediction of Φ_{SK} through the correlation between fluxes at the near detector and SK. This correlation was also estimated with the flux simulation. The refined Φ_{SK} and σ realize the further precise measurements of $\sin^2 2\theta_{23}$ and Δm_{32}^2 .

The outline of this thesis is as follows. Chapter 2 describes the T2K experimental components and the beam data taking history. Chapter 3 describes the overview of the oscillation analysis. Detail of the flux prediction is explained in Chapter 4. The neutrino-nucleus interaction models are briefed in Chapter 5. Chapter 6 describes the neutrino measurements at near detectors and SK. Chapter 7 describes the extrapolation from the ND280 measurements to the SK prediction. The oscillation analysis is described in Chapter 8. Finally, the conclusion is summarized in Chapter 9.

Chapter 2

T2K experimental components and beam data taking summary

2.1 T2K overview

Figure 2.1 shows the schematic view of the T2K components. Pions and kaons are produced at the interaction of the 30 GeV proton beam from the J-PARC Main Ring (MR) with a graphite target. Pions are focused by three magnetic horns [35,36] to increase the neutrino beam intensity. A muon neutrino beam is produced from decay products of pions and kaons. The yield and direction of the neutrino beam are monitored by two beam monitors (the muon beam monitor and the neutrino beam monitor). The properties of the neutrinos are measured at near detectors placed 280 m from the target and at the far detector, SK, which is located 295 km away.

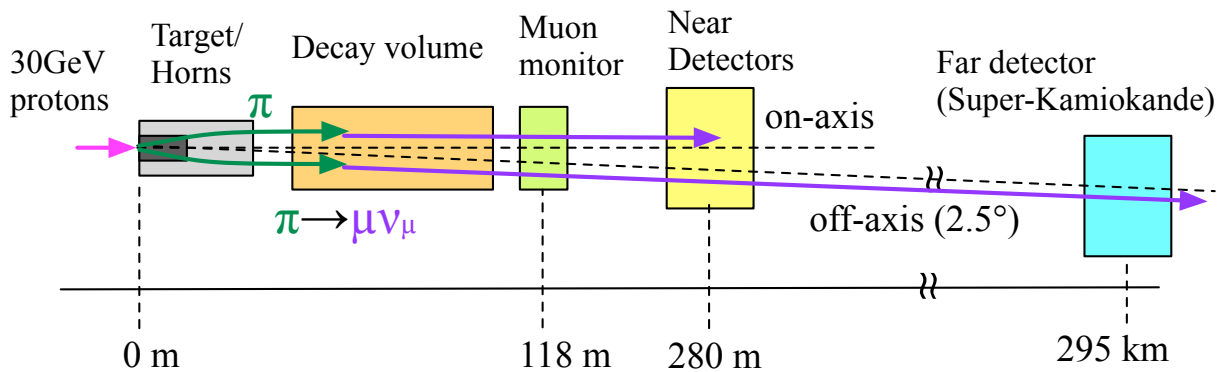


Figure 2.1: Schematic view of T2K components.

J-PARC accelerator

The 30 GeV protons are provided from the J-PARC MR (Sec. 2.2) which is designed to be the most powerful beam (design intensity of 750 kW) in the world. The high intensity proton beam can realize the more neutrinos than ever before.

Off-axis beam

The off-axis beam method [37] is used to generate a narrow-band neutrino beam. The beam axis is slightly shifted away from the direction of SK. In the pion two-body decay ($\pi \rightarrow \mu \nu_\mu$),

the neutrino energy E_ν in the laboratory system is describe as:

$$E_\nu = \frac{m_\pi^2 - m_\mu^2}{2(E_\pi - p_\pi \cos \theta_\nu)}, \quad (2.1)$$

where m_π and m_μ are the pion and muon mass, and E_π is the pion energy, p_π is the pion momentum and θ_ν is the angle between the pion and neutrino directions. Figure 2.2 shows the relation between p_π and E_ν in the two body decay. By using the off-axis beam method, the energy of a neutrino from the two-body decay weakly depends on the p_π and has a narrow spread.

In T2K, the pion two-body decay is the main source for the neutrino production. The pions are focused in parallel to the beam axis. The narrow energy range of the neutrino beam can be varied by changing the off-axis angle as illustrated in the lower plot of Fig. 2.3. In T2K, the off-axis angle is set at 2.5° so that the neutrino beam at SK has a peak energy at about 0.6 GeV which is close to the expected oscillation maximum (Fig. 2.3). The off-axis beam maximizes the effect of the neutrino oscillations. This also increases the fraction of CCQE events (in $E_\nu < 1$ GeV) to other CCQE events (in higher energy region) ratio For the event selection and energy reconstruction at SK, the CCQE events are signal while other CCQE events are background. Since the energy spectrum changes according to the off-axis angle, a shift of neutrino beam direction causes a shift of the energy spectrum, resulting in the uncertainty of Φ_{SK} . The neutrino beam direction is required to be tuned within 1 mrad.

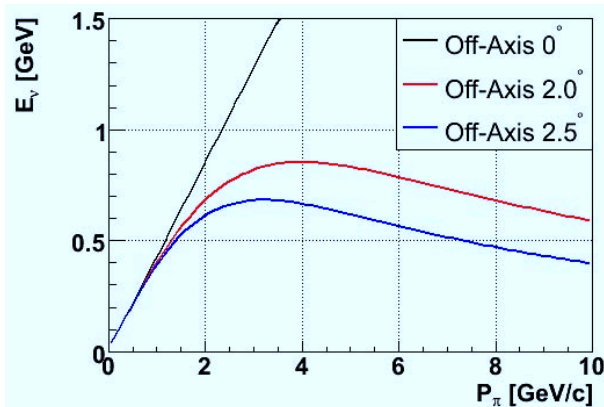


Figure 2.2: The relation between neutrino energy (E_ν) and pion momentum (p_π) in the pion two body decay.

Beam monitors

The stable beam operation is one of the most important issues both for the quick accumulation of data and the protection of the beam equipment from the high intensity proton beam. For the stable beam operation, the several beamline conditions are monitored and controlled: the proton beam parameters (intensity, position, and profile), neutrino beam direction and the horn currents. The proton beam parameters and neutrino beam direction change off-axis angle effectively, hence they affect the energy spectrum which depends on the off-axis angle. The proton beam parameters are measured by several proton beam monitors (CTs, ESMs, SSEMs, described in Sec. 2.3.1). The yield and direction of the neutrino beam are monitored two beam monitors: the muon beam monitor, MUMON, and the neutrino beam monitor, INGRID. MUMON is placed at 118 m from the target. MUMON measures the yield and direction of the neutrino beam indirectly by measuring those of the muon beam because a muon is produced

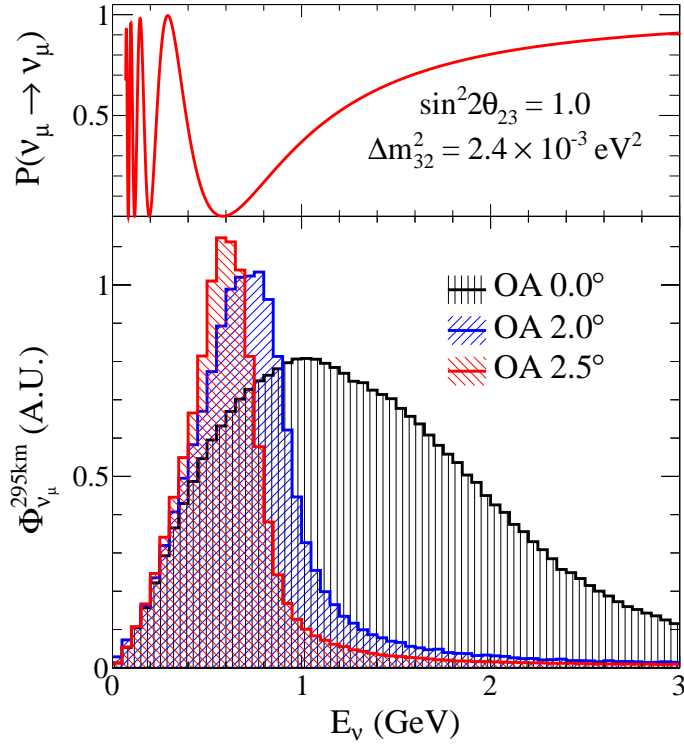


Figure 2.3: The ν_μ survival probability at 295 km (top) and expected neutrino fluxes for different off-axis angles (bottom).

along with a neutrino from pion two-body decay. MUMON is used to monitor and control the neutrino beam every beam pulse. INGRID is installed at 280 m from the target on the beam-axis. INGRID measures the yield and direction of the neutrino beam directly. Since one month data is needed for the precise beam measurement, INGRID is used to determine the systematic error of the off-axis angle from the neutrino measurement.

In addition, the primary proton beam and the horn current are also monitored because these affect the yield and direction of the neutrino beam.

Off-axis Near detector: ND280

The near detector on the off-axis, ND280 observes the neutrinos in the same direction to SK. ND280 measures the event rate and energy spectrum of neutrinos before oscillation. At ND280, the CC inclusive events (including all CC interaction modes) are selected by tracking the outgoing charged particles from the neutrino interactions. The ND280 measurements is used to tune the neutrino flux prediction and neutrino-nucleus interaction models for more precise prediction of $N_{SK}^{exp}(E_\nu)$.

Far detector: Super-Kamiokande

SK is employed as the far detector of T2K. SK measures the event rate and energy spectrum of neutrinos after oscillation. SK has sufficient mass of 50 kton to accumulate neutrino events and the good energy resolution ($\sim 2\%$) for the sub-GeV neutrino, which is interest of T2K. SK can select CCQE neutrino events by identification with the Cherenkov ring produced by outgoing charged particles from the neutrino interaction and reconstruct the neutrino energy.

Timing synchronization

Timing synchronization between J-PARC and SK is performed by using the Global Positioning System (GPS). By selecting the events synchronized with a beam pulse, not beam-related events (e.g. cosmic-ray) becomes negligible.

2.2 J-PARC accelerator

The J-PARC is designed to provide the most powerful beam (~ 750 kW) in the world. The J-PARC Main Ring (MR) accelerates a proton beam to 30 GeV every 2 to 3 seconds. For each acceleration cycle, the beam is fast-extracted to the T2K neutrino beamline as a "spill". One spill contains eight bunches in $4.1 \mu\text{s}$ (shown in Fig. 2.4). The design machine parameters of J-PARC MR for the fast extraction is summarized in Table 2.1.

Table 2.1: Design machine parameters of J-PARC MR for the fast extraction.

Parameter	Design value
Circumference	1567 m
Beam power	~ 750 kW
Beam kinetic energy	30 GeV
Beam intensity	$\sim 3 \times 10^{14}$ p/spill
Spill cycle	~ 0.3 Hz
Number of bunches	8 bunches/spill
Bunch interval	581 ns
Bunch width	58 ns
Spill width	$4.1 \mu\text{sec}$

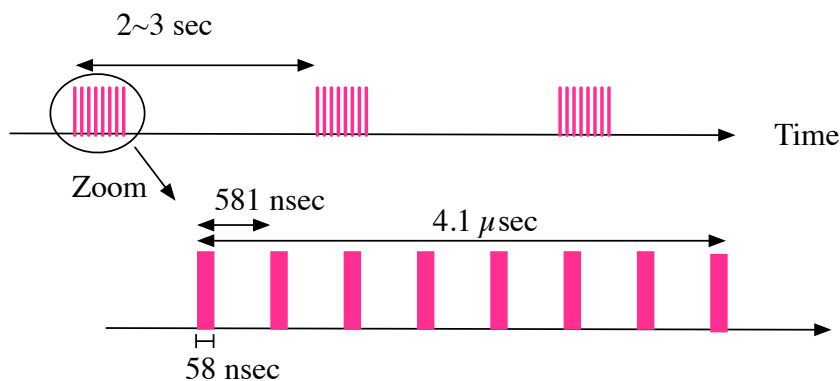


Figure 2.4: Schematic view of the beam spill.

2.3 Neutrino beamline

The neutrino beamline is composed of two sections: the primary and secondary beamlines. An overview of the neutrino beamline is shown in Fig. 2.5.

In the primary beamline, the extracted proton beam is transported to the point in the direction of the secondary beamline, and focused to have the desired profile at the target. In

the secondary beamline, the proton beam impinges on a target to produce secondary pions and other hadrons, which are focused by magnetic horns and decay into neutrinos. The details of the beamline and its components are described in [31].

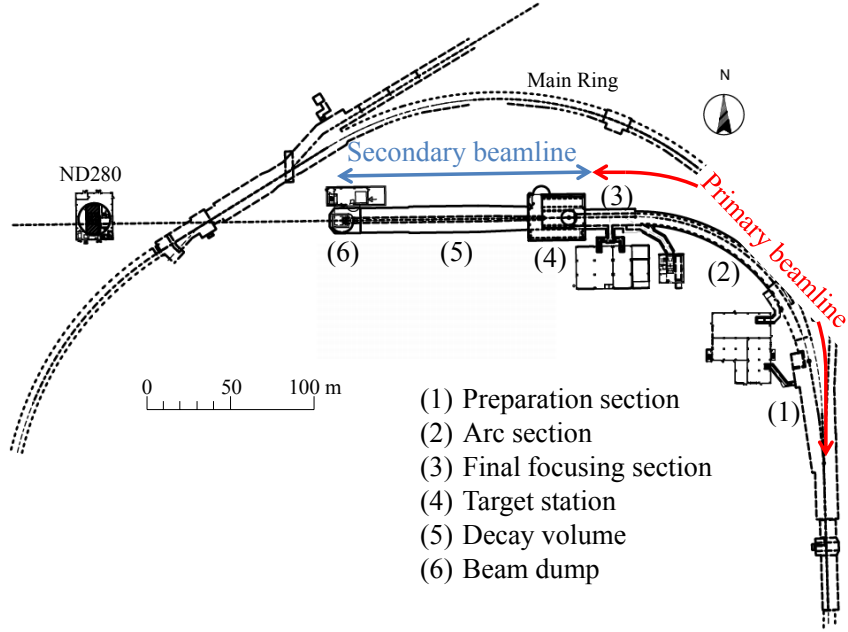


Figure 2.5: An overview of the T2K neutrino beamline.

2.3.1 Primary beamline

The primary beamline consists of the preparation section (54 m long), arc section (147 m) and final focusing section (37 m). In the final focusing (FF) section, ten normal conducting magnets (four steering, two dipole and four quadrupole magnets) guide and focus the beam onto the target, while directing the beam downward by 3.64° with respect to the horizontal.

The intensity, position and profile of the proton beam in the primary sections are precisely monitored by five current transformers (CTs), 21 electrostatic monitors (ESMs), 19 segmented secondary emission monitors (SSEMs), respectively. The monitor locations in the FF section are shown in Fig. 2.6.

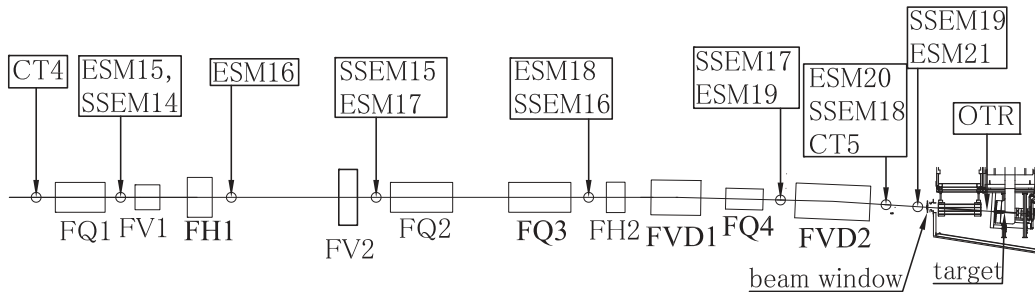


Figure 2.6: Location of the primary beamline monitors in the final focusing section. This location is the place (3) in Fig. 2.5. The left side in this figure is upstream.

Proton beam monitors

The beam intensity is measured with five CTs. Each CT is a 50-turn toroidal coil around a cylindrical ferromagnetic core. The uncertainty on the beam intensity is 2%, which originates from the calibration accuracy (1.7%), the effect of secondary electrons produced at the SSEM foils (<0.7%), the long term stability of the individual CT monitors relative to each other and the CT monitor measurement from the J-PARC MR (0.5%). For the normalization of the flux, the proton beam intensity measured by CT5, located most downstream, is used.

The ESMs have four segmented cylindrical electrodes surrounding the proton beam orbit. By measuring the top-bottom and left-right asymmetry of the beam-induced current on the electrodes, they monitor the proton beam center position nondestructively (without directly interacting with the beam). The measurement precision of the beam position is better than 450 μm .

The SSEMs have two 5 μm thick sets of titanium foil strips oriented horizontally and vertically in the plane perpendicular to the beam axis, and a high voltage anode foil between them. They measure the horizontal and vertical projections of the proton beam profile. The systematic uncertainty of the beam width measurement is 200 μm . The uncertainty of the beam center position measurement is dominated by the monitor alignment uncertainty discussed in Section 2.3.5. Since each SSEM causes a beam loss (0.005% loss), they are inserted into the beam orbit only during the beam tuning, and removed from the beam orbit during the continuous beam operation except for the most downstream SSEM (SSEM19).

An optical transition radiation monitor (OTR) is positioned 30 cm upstream of the target. OTR measures the two dimensional profiles of the beam by imaging transition radiation produced when the beam crosses a 50 μm thick titanium alloy foil. The details of OTR have been described elsewhere [38].

Using the ESMs, SSEMs and OTR measurements, the beam position at the upstream side of the baffle (shown in Fig. 2.7) is reconstructed.

2.3.2 Secondary beamline

Pions and kaons are produced by the interaction of protons with a graphite target. They decay in flight inside a single volume of $\sim 1500 \text{ m}^3$ filled with helium gas. The helium vessel is connected with the primary beamline using a titanium-alloy beam window that separates the vacuum in primary beamline and helium gas volume in the secondary beamline.

The secondary beamline consists of three sections: the target station, decay volume and beam dump (Fig. 2.7). The helium vessel in the target station is 15 m long, 4 m wide and 11 m high. The decay volume is a 96 m long steel tunnel. The cross section is 1.4 m wide and 1.7 m high at the upstream end, and 3.0 m wide and 5.0 m high at the downstream end. The beam dump sits at the end of the decay volume. The distance between the center of the target and the upstream surface of beam dump is 109 m.

The target station contains a baffle, the OTR monitor, the target and three magnetic horns. The baffle is a collimator to protect the horns. The 250 kA current pulses magnetize the three horns to focus the produced pions. The focused pions then decay in the decay volume mainly into muons and muon neutrinos. All the remnants of the decayed pions and other hadrons are stopped by the beam dump, while the neutrinos pass through the beam dump. The muons above 5 GeV that also pass through the beam dump are detected by a muon monitor (MUMON) that measures the beam direction and intensity spill-by-spill.

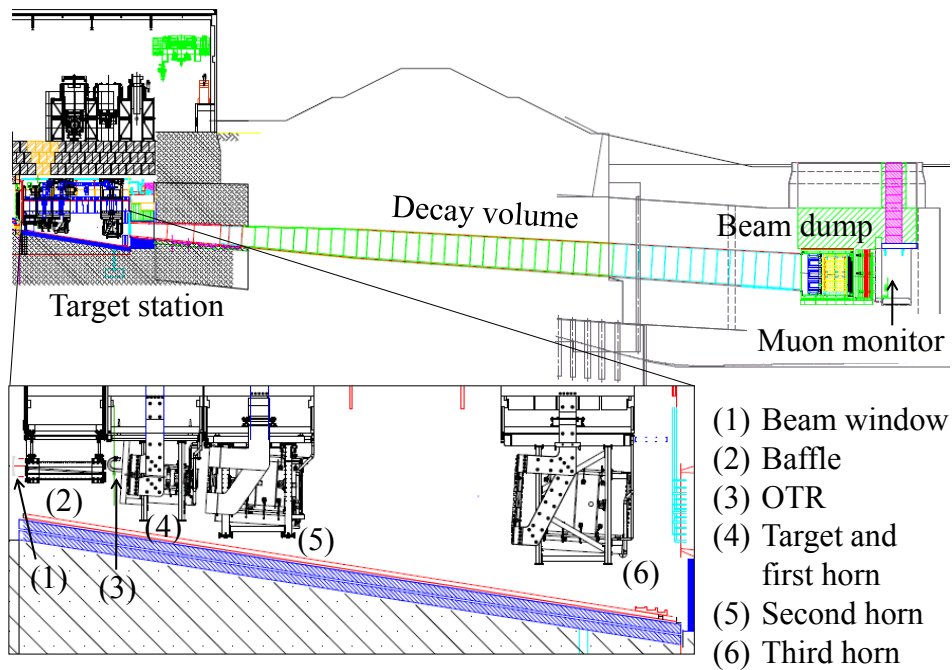


Figure 2.7: Side view of the secondary beamline.

Target and Horns

The target core is a 1.9 interaction length (91.4 cm long), 2.6 cm diameter graphite rod with a density of 1.8 g/cm^3 . The core and a surrounding 2 mm thick graphite tube are sealed inside a 0.3 mm thick titanium case. The target assembly is cantilevered inside the bore of the first horn inner conductor.

In T2K, three magnetic horns are used. Each horn consists of two coaxial (inner and outer) conductors which encompass a closed volume [35, 36]. A toroidal magnetic field is generated in that volume. The field varies as $1/r$, where r is the distance from the horn axis. The first horn (Horn 1) collects the pions that are produced at the target installed in its inner conductor. The second (Horn 2) and third (Horn 3) horns focus the pions. A schematic view of the horns is shown in Fig. 2.8. The horn conductor is made of an aluminum alloy. The thickness of the inner conductors is 3 mm. They are optimized to maximize the neutrino flux; the inside diameter is as small as possible to achieve the maximum magnetic field, and the conductor is as thin as possible to minimize pion absorption while still being tolerant of the Lorentz force from the 250 kA current and the thermal shock from the beam [39].

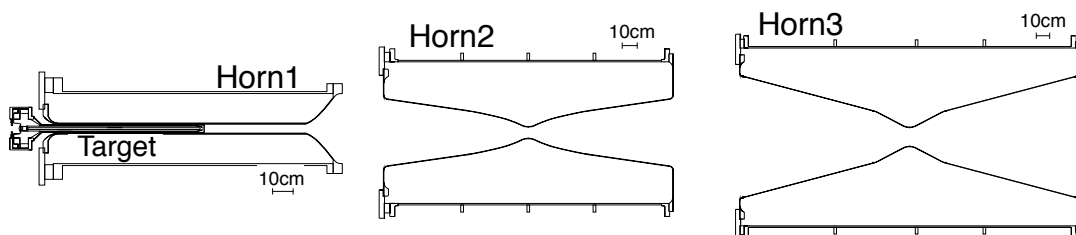


Figure 2.8: Cross sectional view of horns.

Muon beam monitor (MUMON)

The neutrino beam intensity and direction can be monitored on bunch-by-bunch basis by measuring the profile of muons which are produced along with neutrinos from the pion two-body decay. The neutrino beam direction can be measured indirectly as the direction from the target to the center of the muon profile. The muon monitor (MUMON) is located behind the beam dump at a distance of 118 m from the target, as shown in Fig. 2.7. The schematic view and photograph of the muon monitor is shown in Fig. 2.9. It consists of two kinds of detector arrays: ionization chambers and silicon PIN photodiodes. Each array consists of 49 sensors at 25 cm intervals and covers a $150 \times 150 \text{ cm}^2$ area. The center of the muon profile can be measured with 2.95 cm accuracy, which corresponds to 0.25 mrad precision on the beam direction. More details of this monitor are described in [40].

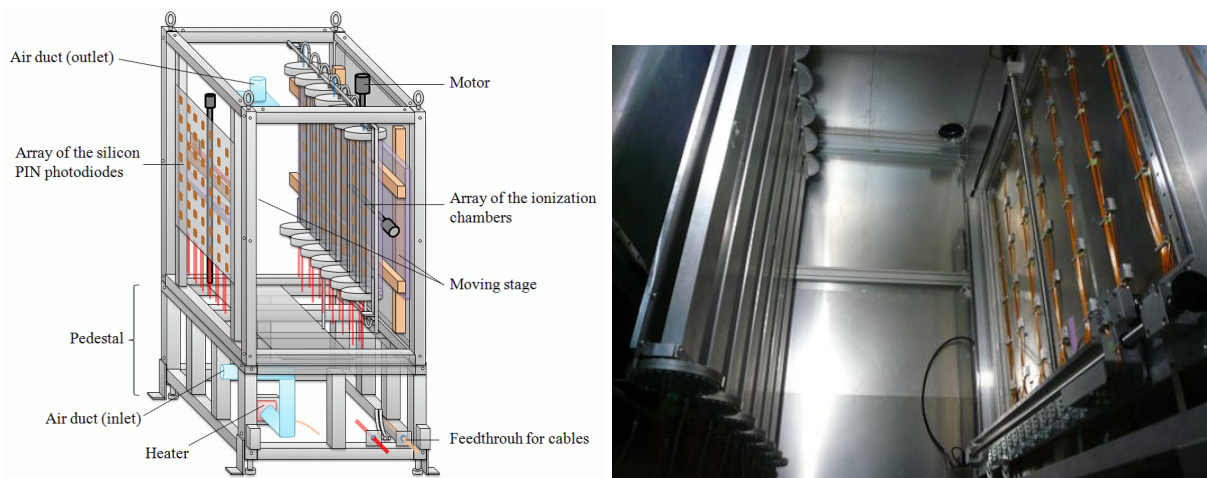


Figure 2.9: Muon beam monitor. Right: the schematic view of the muon monitor (the beam enters from the left side). Left: the photograph of the silicon PIN photodiodes (right) and the ionization chambers (left) in the support enclosure (the beam enters from the right side).

2.3.3 Beamline Data acquisition system

For the stable and safe the beam operation, the beamline data acquisition (DAQ) system collects information on the beamline monitors spill-by-spill. The DAQ also provides the spill information to SK for the time synchronization based on the GPS time stamp.

The signals of SSEM, BLM, and horn current are digitized by the 65 MHz Flash ADC (FADC) in the COPPER system [41]. The signals of CT and ESM are digitized by the 160 MHz VME FADC [42]. The GPS time synchronization and the OTR use the custom-made readout electronics. All of these readout systems are managed by the MIDAS framework [43], and the event builder records the concatenated data of all monitors every spill, before the next spill comes.

2.3.4 Global Time Synchronization

The T2K GPS time synchronization system builds on experience from K2K [44], which is a predecessor of T2K. The system provides the time synchronization between the neutrino event trigger time at SK, and the beam spill time at J-PARC.

At SK, all hits of photomultiplier tubes (PMTs) are recorded without the dead time. Among recorded PMT hits, hits within $\pm 500 \mu\text{sec}$ around the expected neutrino beam timing at SK are

used for the T2K analysis (corresponding to T2K window in Fig. 2.10). The expected neutrino timing at SK is calculated from the beam spill timing measured at CT5, the time of flight (TOF) of the neutrino (~ 1 msec), and the delay by electronics at both J-PARC and SK. To estimate the expected neutrino timing at SK correctly, the precise time synchronization between J-PARC and SK is required (if the time clock at J-PARC and SK was different 600 nsec, the bunch timing would be different by one bunch).

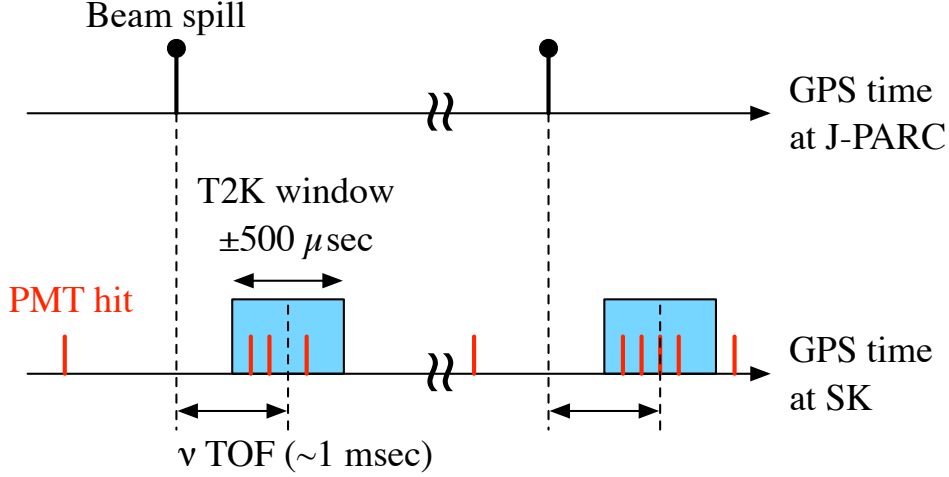


Figure 2.10: Overview of SK event timing.

The Global Positioning System (GPS) is a space-based satellite navigation system which provides location and time information. This was created and controlled by the U.S. Department of Defense (DoD). The GPS satellites have an atomic clock, which refer to the same master clock. Receiving the information from four or more satellites at the same time, a GPS receiver can calculate its precise position and time. More satellites the GPS receiver view make the precision better. The identical GPS systems to log the time stamp were installed at both J-PARC and SK and are used as the common clock. The time stamp of the beam timing is logged at J-PARC spill-by-spill based on the GPS time information, and the neutrino timing at SK is calculated based on the time stamp of the beam timing and the GPS time information.

The commercial GPS receiver provides Coordinated Universal Time (UTC) stamps every 1 sec and 1 Hz pulses (1 pulse per sec, 1PPS) at same time. The sub-second time stamp cannot be obtained by only the 1PPS time information, hence, the 100 MHz 32 bit local time clock (LTC) is combined to measure the sub-second time stamp at J-PARC, while 80 MHz LTC is used at SK. The time synchronization system is composed of the GPS receiver and LTC module. The overview of this system is shown in Fig. 2.11). The time stamp from the GPS receiver is recorded in every 1 sec. The 1PPS provided along with UTC stamp is fed to the LTC counter and its count number is recorded. The beam timing (first extraction timing) from the J-PARC MR is fed to the LTC clock and its count number is recorded. The time calculation is shown in Fig. 2.12. From the UTC stamp, the LTC counts at the 1PPS and the LTC counts of the beam timing, the time of the beam timing (for spill number is N), T_N^{Beam} is calculated:

$$T_N^{Beam} = T_N^{1PPS} + \frac{C_N^{Beam} - C_N^{1PPS}}{1 \times 10^6}, \quad (2.2)$$

where T_N^{1PPS} represents the UTC of 1PPS just before the beam spill $\#N$, C_N^{Beam} and C_N^{1PPS} represent the LTC counts at the beam spill timing and 1PPS timing. Actually, the T_N^{Beam} has the time offset from the signal propagation between the GPS satellite and receiver, the delay in the electronics, and so on. In T2K, two GPS receivers and one atomic clock are used:

- Primary GPS receiver (GPS1): Symmetricom/TrueTime XL-DC,
- Secondary GPS receiver (GPS2): M12M Timing Oncore Receiver,
- Atomic clock (Rub): FS725 Benchtop rubidium frequency standard.

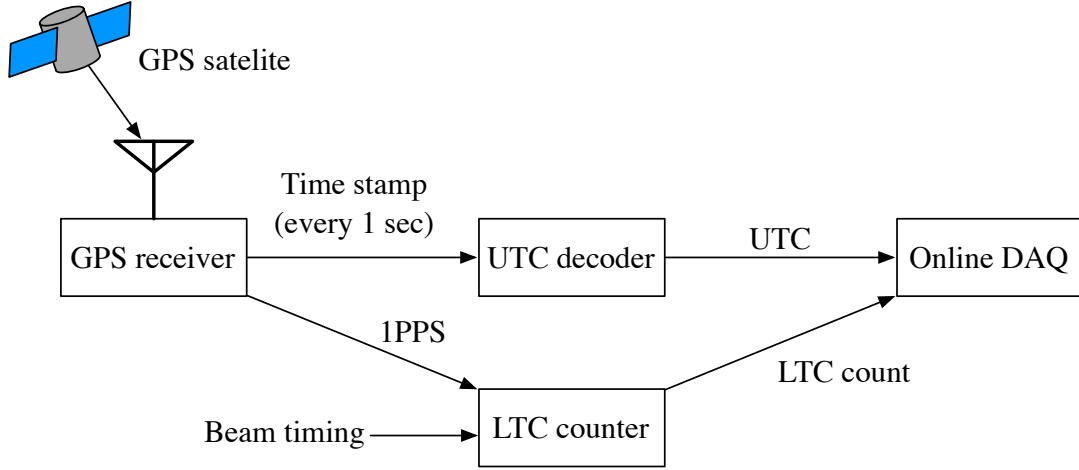


Figure 2.11: Overview of the T2K event timing synchronization system.

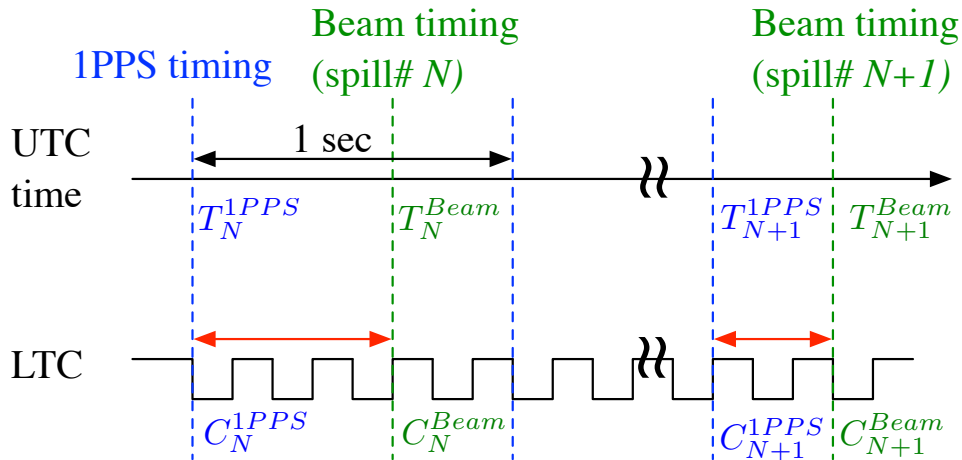


Figure 2.12: Overview of time stamp calculation.

Stability of the time synchronization system

The stability of the time synchronization system is evaluated from the difference of the time stamps by two GPS systems. Figure 2.13 shows the history of the time difference between GPS 1 and GPS 2 during all run periods (described in Sec. 2.6). The time difference can be deviated from zero due to the different delay by the electronics, but there was some significant discrete jump (~ 100 nsec). The reason of this discrete fluctuation is considered that the intrinsic offset in the GPS system may change at power cycle. To keep the intrinsic offset constant, the power of the time synchronization system should not be turned off. The reason of the offset

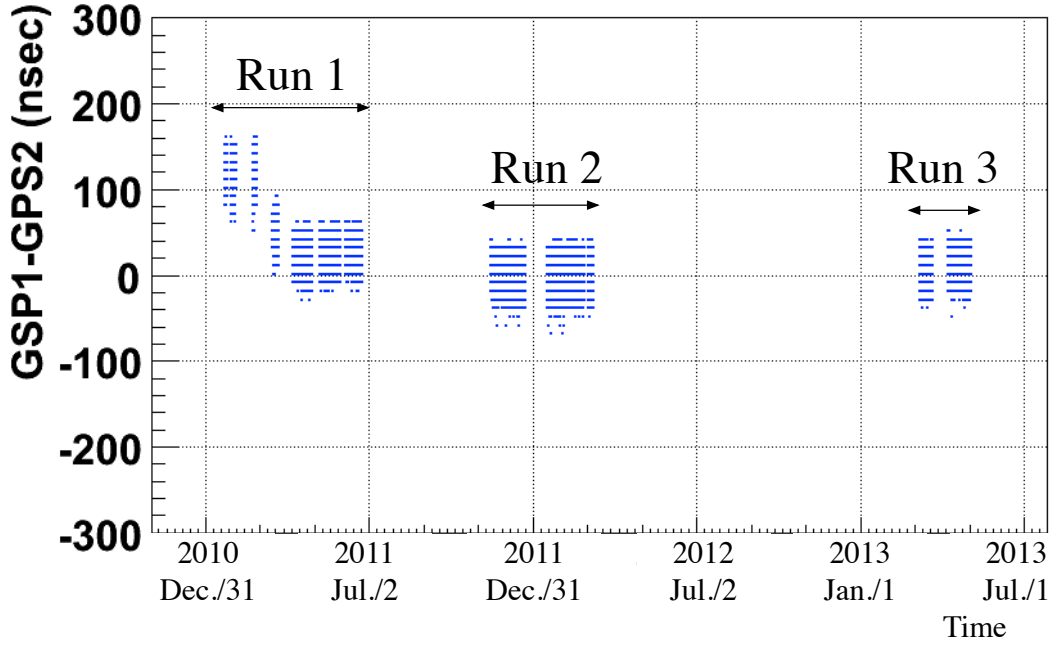


Figure 2.13: History of the time difference between GPS 1 and GPS 2.

change was not understood at Run 1. After that, the power-on/off is repeated until the offset becomes zero.

From Fig. 2.13 and the history of the hardware operation, there was no significant jump during Run 3. Figure 2.14 shows the distributions of the time differences during Run 3 (~ 51 day's data with 2.5 sec). The fluctuations of time difference are represented as $\sigma_{GPS2-GPS1}$, $\sigma_{Rub-GPS1}$, $\sigma_{Rub-GPS2}$. The r.m.s. of the time difference distribution is evaluated as its fluctuation:

$$\sigma_{GPS2-GPS1} = 10.82 \text{ nsec} \quad (2.3)$$

$$\sigma_{Rub-GPS1} = 7.57 \text{ nsec}, \quad (2.4)$$

$$\sigma_{Rub-GPS2} = 11.03 \text{ nsec}. \quad (2.5)$$

The fluctuations of the time stamp logged by GPS1, GPS2, and Rub are represented as σ_{GPS1} , σ_{GPS2} , and σ_{Rub} . The σ_{GPS1} , σ_{GPS2} , and σ_{Rub} are evaluated as:

$$\sigma_{GPS1} = \sqrt{\frac{\sigma_{GPS1-GPS2}^2 + \sigma_{Rub-GPS1}^2 - \sigma_{Rub-GPS2}^2}{2}} \sim 5.1 \text{ (nsec)}, \quad (2.6)$$

$$\sigma_{GPS2} = \sqrt{\frac{\sigma_{GPS1-GPS2}^2 - \sigma_{Rub-GPS1}^2 + \sigma_{Rub-GPS2}^2}{2}} \sim 9.5 \text{ (nsec)}, \quad (2.7)$$

$$\sigma_{Rub} = \sqrt{\frac{-\sigma_{GPS1-GPS2}^2 + \sigma_{Rub-GPS1}^2 + \sigma_{Rub-GPS2}^2}{2}} \sim 5.6 \text{ (nsec)}. \quad (2.8)$$

The GPS time fluctuation in T2K are much better than in that K2K (~ 100 nsec [44]). The possible reasons of this improvement are the upgrade of the system components and improvement of the GPS measurements.

Good GPS status

Following conditions are applied to select the spills with "Good GPS status":

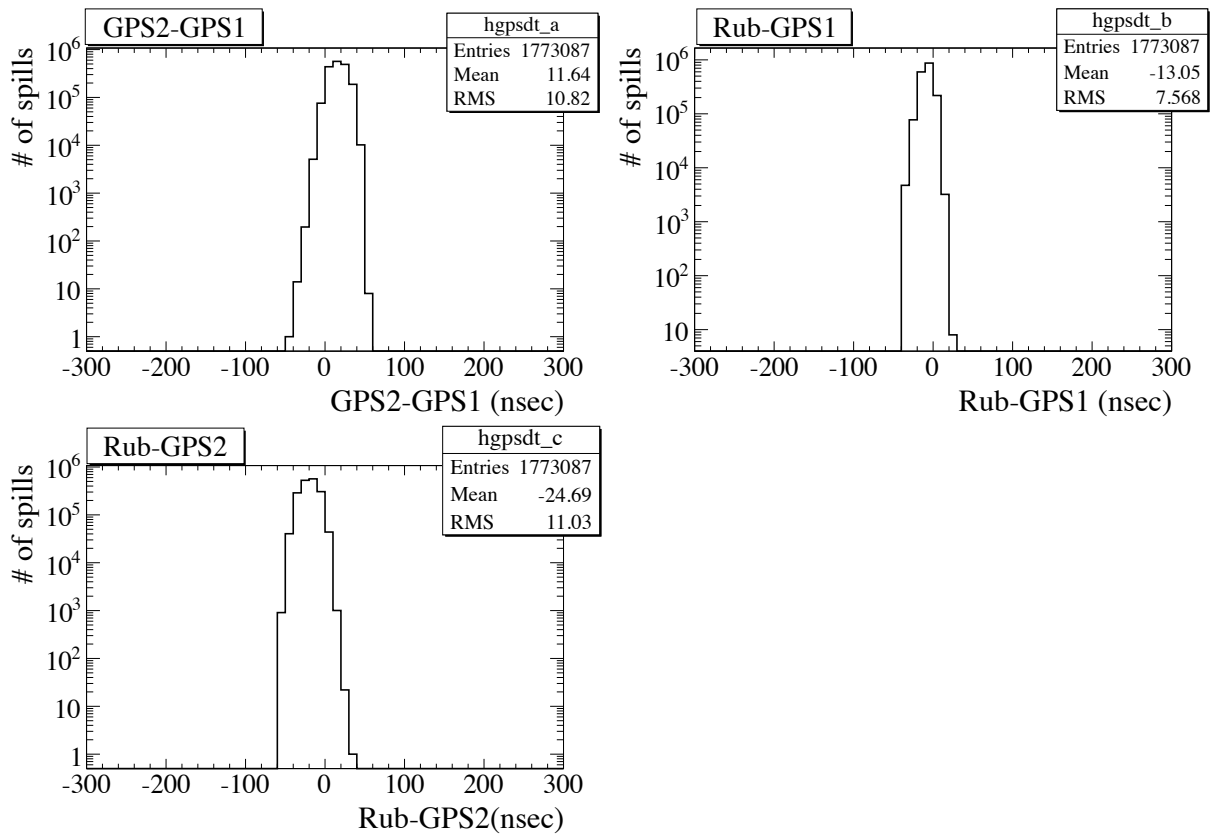


Figure 2.14: Distribution of the time differences in GPS1, GPS2 and Rub during Run 3.

1. The absolute time difference between GPS1 and GPS2 is less than 200 nsec. If this condition is not satisfied, the next condition is applied.
2. The time difference between GPS1 and Rub is less than 200 nsec. If this condition is not satisfied, the next condition is applied.
3. The time difference between GPS2 and Rub is less than 200 nsec. If this condition is not satisfied, the next condition is applied.

There is no spills with the bad GPS status during all run periods and all spills satisfy the condition 1 so far.

2.3.5 Alignment

The GPS survey is performed to obtain the neutrino beam direction with respect to SK (off-axis angle) and the distance between the target and SK. The distance between the target and the center position of SK is $295,335.9 \pm 0.7$ m. The off-axis angle is measured to be $2.504 \pm 0.004^\circ$. The directional accuracy of a long-baseline GPS survey is about 3×10^{-6} rad. Based on the GPS surveys, the primary beamline components, target, and horns were aligned in order to send the neutrino beam in the right direction. The MUMON and the neutrino near detectors were also aligned in order to monitor the neutrino beam direction. The systematic errors associated with the horn and target alignment is summarized in Table 2.2.

Table 2.2: Summary of the horn and target alignment uncertainties. x , y , and z represent the horizontal, vertical position and the parallel position to the proton beam axis. The θ_H and θ_V represent the rotation in the horizontal and vertical plane.

	Target	Horn 1	Horn 2	Horn 3
δx (mm)	–	0.3	0.3	0.3
δy (mm)	–	1.0	1.0	1.0
δz (mm)	–	1.0	1.0	1.0
$\delta\theta_H$ (mrad)	1.3	0.2	0.2	0.2
$\delta\theta_V$ (mrad)	0.1	0.2	0.2	0.2

After the 2011 Tohoku earthquake, movements was observed for the GPS survey points, the primary beamline tunnel and the beamline components. The baseline to SK was increased by 0.9 m, while the beam angle was rotated by 3×10^{-5} rad. Both of these shifts have a small effect on the physics performance of the experiment. The beamline components were re-aligned to the same alignment accuracy with the fixed point of reference at the most downstream end of the primary beamline. The horns were also re-aligned using the survey markers on the support modules, and found to be at the expected position, within the 1 mm accuracy of the survey method. The MUMON was surveyed after the earthquake and its position relative to the target station shifted by less than 1 mm.

2.4 Near Neutrino detectors

The schematic view of the T2K near neutrino detectors in Fig 2.15. The T2K near neutrino detectors are composed of the neutrino beam monitor (INGRID) and the neutrino spectrometer (ND280). These detectors are set in a pit inside the ND280 hall. The pit has a diameter of 17.5 m and a depth of 37 m.



Figure 2.15: T2K near neutrino detectors. The ND280 detector and the magnet are located at the upper level, and the vertical and horizontal INGRID modules are located at the middle and bottom levels. The magnet is opened in this figure, though it is operated with its close position.

2.4.1 INGRID

The neutrino beam intensity and direction are monitored directly by measuring the profile of neutrinos at the INGRID detector [45], located 280 m away from the target. The schematic view of INGRID is shown in Fig. 2.16. It consists of 16 identical neutrino detectors arranged in horizontal and vertical arrays around the beam center. The daily event rate and monthly beam direction of neutrinos are monitored. The neutrino event rate can be measured with 4% precision and the neutrino beam direction with an accuracy of better than 0.4 mrad.

The schematic view of the INGRID module is shown in Fig. 2.17. The INGRID module consists of a sandwich structure of nine iron plates and eleven tracking scintillator planes. The dimension of the iron plate is 124 cm \times 124 cm in the horizontal and vertical direction and 6.5 cm along the beam direction. The total iron mass serving as a neutrino target is 7.1 tons per module. Each of the 11 tracking planes consists of 24 scintillator bars in the horizontal direction glued to 24 perpendicular bars in the vertical direction, for a total number of 8,448. The dimensions of the scintillator bars used for the tracking planes are 1.0 cm \times 5.0 cm \times 120.3 cm. The INGRID module is surrounded by veto scintillator planes to reject interactions outside the module. Each veto plane consists of 22 scintillator bars segmented in the beam direction. The light yields in the scintillators are read out with the wave length shifting fiber and the photo-sensors: Multi-Pixel Photon Counter (MPPC). The total channels for INGRID is 9,592. The details of the INGRID detector are given in [45, 46].

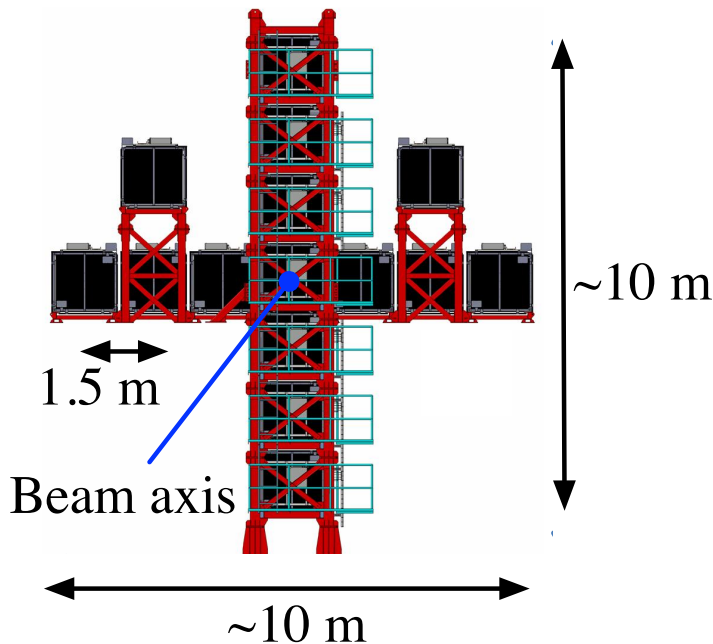


Figure 2.16: Schematic view of INGRID. The center of INGRID is set at the beam axis.

2.4.2 ND280

The ND280 detector measures the off-axis neutrino flux and energy spectrum at a baseline of 280 m. ND280 effectively sees a line source of neutrinos rather than a point source. Therefore it covers a range of off-axis angles. The off-axis angle to ND280 from the target position is 2.04° . This angle was chosen to make the neutrino spectrum at ND280 as similar as possible to the spectrum at SK. The ND280 detector is a complex of many components: the electromagnetic

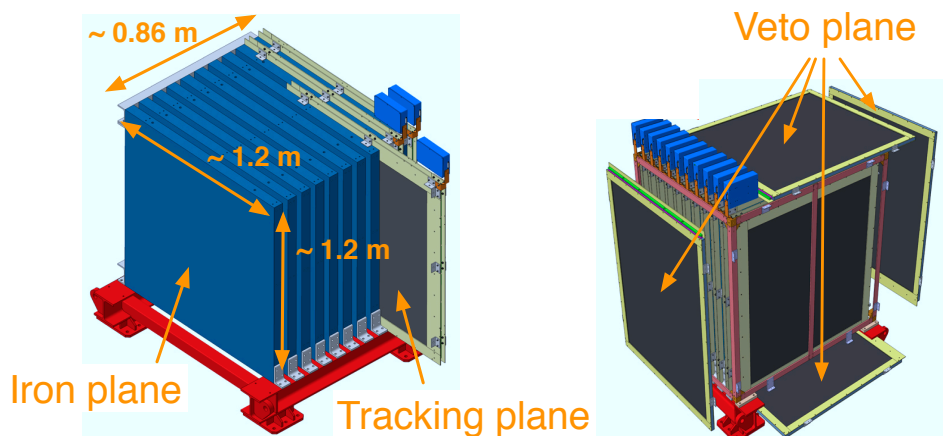


Figure 2.17: Schematic view of INGRID module.

calorimeters (Ecal), π^0 detectors (P0D), scintillating trackers (FGD), and time projection chambers (TPC). The ND280 detector is set in a magnetic field to identify produced charge particles (UA1 magnet). In this thesis, FGDs and TPCs are used. FGDs serve as a neutrino target and track charged particles with the tracking scintillator planes. FGDs have outer dimensions of 2.3 m \times 2.4 m \times 3.65 m (width height depth in beam direction), and contains 1.1 tons of target material. TPCs measure the momentum of charged particles because TPCs operate in a magnetic field. They also measure the amount of ionization left by each particle so that they can identify the types of charged particles with combination of the measured momentum. The details of the ND280 components are given in [31, 47, 48].

2.5 Far Neutrino detector: Super-Kamiokande

Super-Kamiokande (SK) is a water Cherenkov detector and measures the event rate and energy spectrum in the off-axis direction at a baseline of 295 km. The water tank of SK is a cylindrical cavern whose geometry is 39 m in diameter and 41 m in height (shown in Fig. 2.19), filled with 50 kton of pure water. The SK tank consists of the inner detectors (ID) and outer detectors (OD). The geometry of ID is 36.2 m in height and 33.8 m in diameter, having 32 kton of water (shown in Fig. 2.20). ID (OD) has 11129 (1885) inward-facing (outward-facing) 20-inch (8-inch) diameter PMTs on its cylindrical wall. The fiducial volume of SK is defined as a virtual cylindrical cavern whose geometry is 33.8 m in diameter and 36.2 m in height, filled with 22.5 kton of pure water (shown in Fig. 2.20). Neutrinos are detected with the PMTs by measuring the Cherenkov lights emitted by charged particles from the neutrino interactions in the water. The particle's vertex, energies, directions are reconstructed from the timing and position of the Cherenkov lights. The particle identification (muon/electron separation) is performed based on the edge of the Cherenkov lights: the Cherenkov lights by muon have a sharp outer ring edge, while the Cherenkov lights by electrons have characteristic fuzzy edges due to electromagnetic showers. More details of SK are described in [31, 49].

2.6 Beam data taking history

T2K physics data taking started from January 2010. The data taking period for this thesis is divided into three periods: Run 1 (January – June 2010), Run 2 (November 2010 – March 2011), Run 3 (March – June 2012). The Run 3 period is further divided into three sub periods: Run

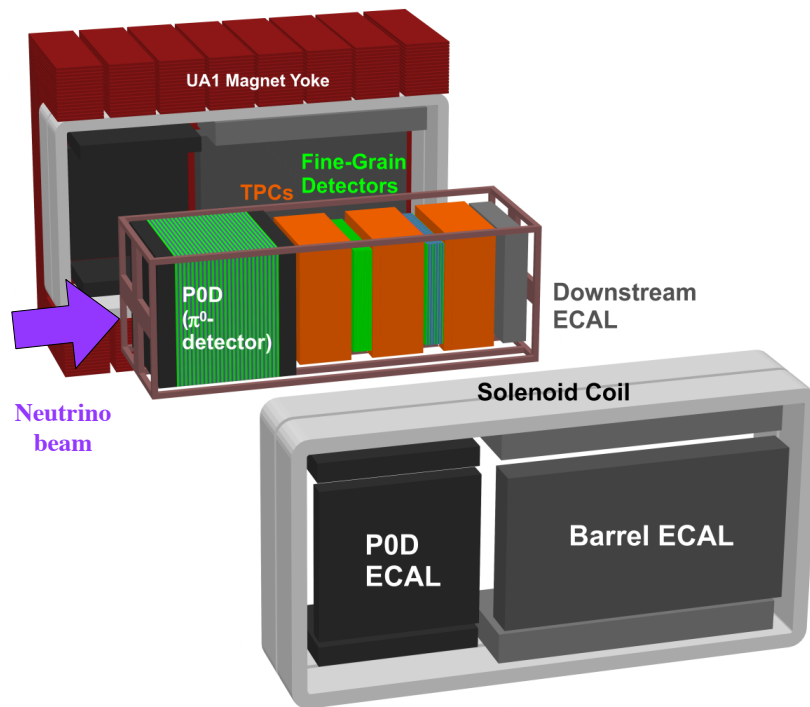


Figure 2.18: Schematic view of ND280. The neutrino beam enters from the left side. The magnet is shown in its open position, though it is operated with its close position.

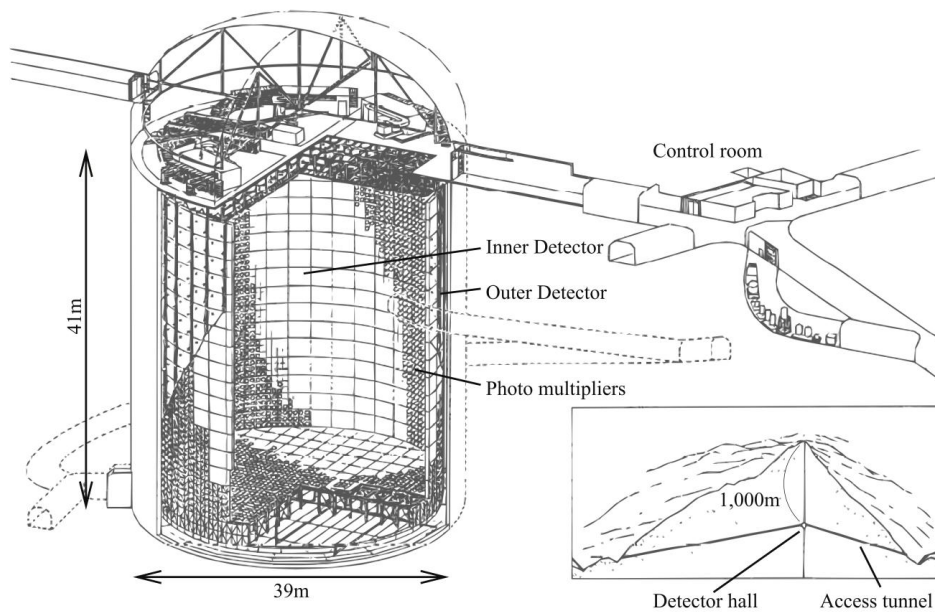


Figure 2.19: Schematic overview of SK. This figure comes from [50]

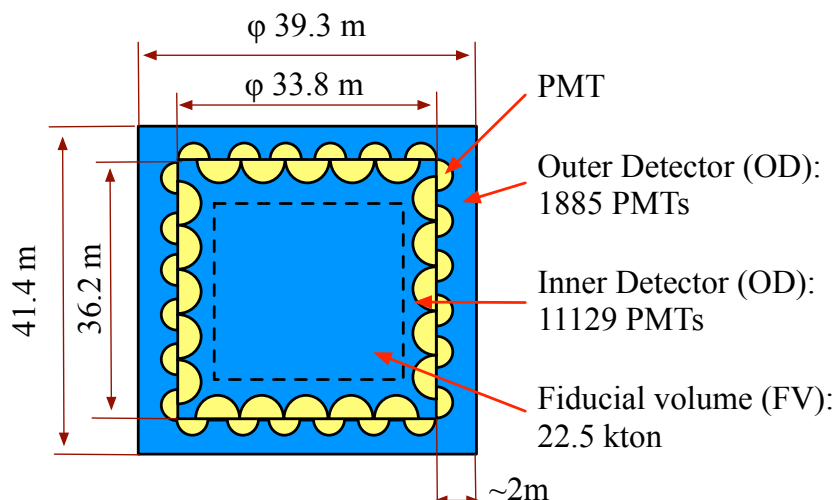


Figure 2.20: Cross section view of the SK water tank.

3a (December 2011 and January 2012), Run 3b (March 2012) and Run 3c (April – June 2012), according to the horn current settings (0 kA setting in Run 3a, 205 kA setting in Run 3b instead of the nominal 250 kA). The Run 3a data is not used in this thesis because the data in this period is small (0.3% of the total) and the horn current was 0 kA.

During the data taking, the proton beam position and angle on the target, horn currents, and muon beam position are monitored to progress data taking safely (for example, if the proton beam drastically deviated from the beam-axis, it can damage hardware components). Furthermore, in order to select good quality data for the oscillation analysis, the following selection criteria are applied for data spill-by-spill:

- The GPS status is good (described in Sec. 2.3.4).
- Each hardware component (beam monitors, focusing magnets, etc) works normally
- The deviation of all horns currents from the nominal value is within ± 5 kA.
- The deviation of the beam angle measured by MUMON from the nominal value is within 1 mrad.
- The deviation of the total muon yield measured by MUMON from the nominal value is within ± 5 %.

The total good beam spills are summarized in Table 2.3.

Table 2.3: Number of spills and POT after each good quality data selection.

Selection	Number of spills	Efficiency
Beam spills in Physics run	4280612	100%
Hardwares selection	4266831	99.9%
Horn current selection	4266056	99.7%
MUMON selection	4265638	99.7%

The accumulated POT and protons per pulse are shown in Fig 2.21 for good spills. The protons per pulse corresponds the the instantaneous beam power. The total accumulated POT

in all run periods is 3.04×10^{20} POT, corresponding to 4% of T2K's exposure goal. The maximum beam power reached so far is about 200 kW. The data taking history with total accumulated POT is summarized in Table 2.4.

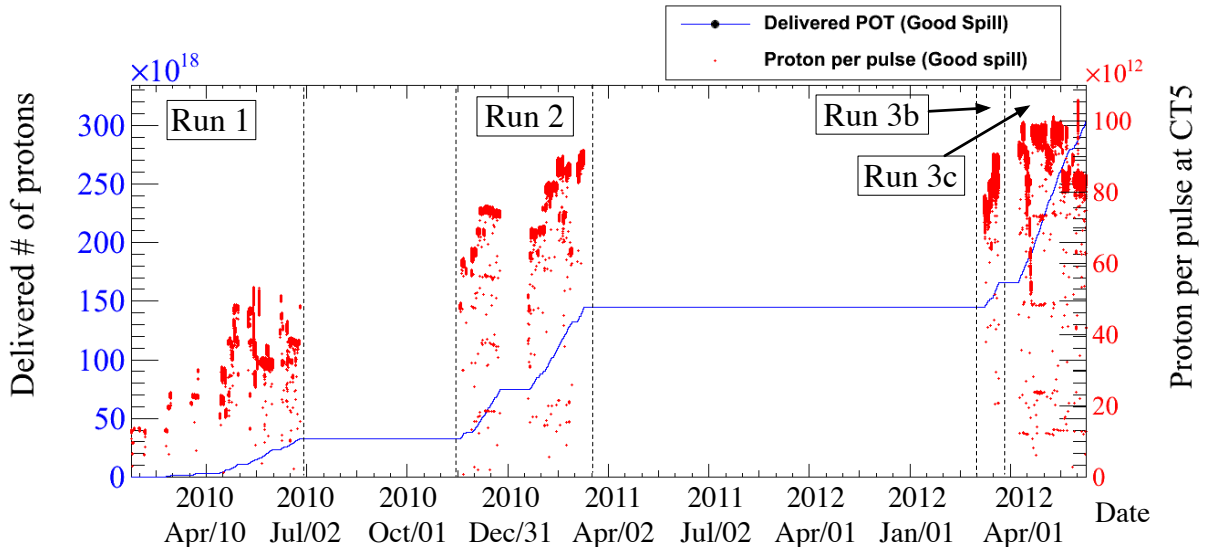


Figure 2.21: History of total accumulated protons and protons per pulse for the good quality beam data. The solid line shows the accumulated POT. The dot points show the number of protons per pulse.

Table 2.4: Summary of the data taking, horn current setting, good beam spills and accumulated POT for the oscillation analysis

Run#	Period	Horn current [kA]	Good beam spills	POT ($\times 10^{20}$)
RUN1	January – June 2010	250	1006982	0.326
RUN2	November 2010 – March 2011	250	1492031	1.12
RUN3b	March 2012	205	265230	0.219
RUN3c	April – June 2012	250	1507828	1.37

As already mentioned, the measured proton beam parameters, horn currents, and neutrino beam direction are used in the neutrino flux prediction. The details of the flux prediction are described in Sec. 4. The measurement of the neutrino beam direction is described in the other section (Sec. 6.1).

2.6.1 Proton beam measurement

The center position and angle of the proton beam are reconstructed at the upstream surface of the baffle for each spill. The used monitors are the beam profile and position monitors on just upstream the baffle: ESM20, SSEM19 and OTR for the vertical, and ESM19, ESM20, SSEM19 and OTR for the horizontal direction (shown in Fig. 2.6).

Each time the beam conditions change, all of the SSEMs are inserted into the beamline and beam profiles are measured for 100 spills. The beam width and divergence at the baffle are calculated from the profile measurements. After 100 spills, all SSEMs except for SSEM19 are

extracted from the beam orbit and the beam width and divergence are then obtained by scaling ones from the change of the profile measured at SSEM19 and OTR for each spill.

The averaged beam parameters in each run period is used in the flux prediction. The measured parameters are summarized in Table 2.5 and 2.6. The emittance and Twiss parameter are the optics parameters related to the proton beam divergence. To evaluate the flux uncertainties from proton beam errors, the systematic errors of proton beam measurements (position, angle, width and divergence) need to be estimated. In this analysis, only errors of the beam Y center and Θ_Y angle are used in the estimation of flux uncertainties. This reason is described in Sec. 4.4.3. The following error sources of the proton beam position and angle measurement are

Table 2.5: Summary of measured proton beam parameters in the horizontal direction at the baffle for each run period : center position (X) and angle (Θ_X), Gaussian width (σ), emittance (ϵ), and Twiss (α) parameter.

Period	X (mm)	Θ_X (mrad)	σ (mm)	ϵ (π mm mrad)	α
Run1	0.37	-0.044	4.27	2.12	0.60
Run2	0.149	-0.080	4.04	5.27	0.16
Run3b	0.087	0.020	4.13	6.50	0.16
Run3c	-0.001	0.032	4.03	4.94	0.33

Table 2.6: Summary of measured proton beam parameters in the vertical direction at the baffle for each run period : center position (Y) and angle (Θ_Y), Gaussian width (σ), emittance (ϵ), and Twiss (α).

Period	Y (mm)	Θ_Y (mrad)	σ (mm)	ϵ (π mm mrad)	α
Run1	0.84	0.004	4.17	2.29	-0.09
Run2	-0.052	-0.007	4.08	5.17	0.14
Run3b	-0.024	0.043	3.97	5.30	0.25
Run3c	-0.366	0.068	4.22	6.02	0.34

considered:

- Alignment uncertainty of the proton beam monitors.
- Alignment uncertainty between the primary beamline and secondary beamline.
- Systematic errors in the proton beam position measurements.

These errors are included in the proton beam orbit reconstruction. The systematic errors and their correlations are summarized in Table 2.7 for the proton beam position and angle. On the other hand, the following sources are the error sources of the proton beam width and divergence:

- Systematic error in the profile measurements by the proton beam monitors.
- Effects of the momentum dispersion $\Delta p/p$, where a conservative estimate of 0.3% is assumed.
- Uncertainties in the quadrupole magnet (FQ2, 3, and 4) field model

Table 2.7: Systematic errors and correlations for the position and angle of the beam center at the baffle front surface. The $X(Y)$ and $\Theta_X(\Theta_Y)$ stand for horizontal (vertical) position and angle of the beam center, respectively.

Period	X (mm)	Y (mm)	Θ_X (mrad)	Θ_Y (mrad)	$\text{corr}(X, \theta_X)$	$\text{corr}(Y, \theta_Y)$
Run1	0.38	0.58	0.056	0.29	0.517	0.392
Run2	0.27	0.62	0.064	0.32	0.752	0.398
Run3b	0.28	0.58	0.064	0.29	0.614	0.386
Run3c	0.35	0.58	0.072	0.28	0.697	0.417

2.6.2 Horn current stability

The history of the horns current are shown in Fig 2.22. Horns were usually operated at 250 kA except for Run 3b (205 kA). During the data taking periods, the monitored values of the horn current drifted within 2% (5 kA). This drift is most likely due to the temperature dependence in the operation of the monitoring hardware, but variations of the actual horn current have not been definitively ruled out.

2.6.3 Muon profile stability

The history of the muon profile center is shown in Fig 2.23. In all data taking period, the profile center is stable within 12 cm, which corresponds to 1 mrad from the designed beam axis. During Run 3b, both of horizontal and vertical direction at MUMON were deviated from the beam-axis more than in other period. The possible reason of this difference is mis-alignments in the horns. The beam might be focused in the deviated direction if there are mis-alignments in the horns. This focusing strength at 205 kA can be smaller from at 250 kA, therefore the deviation is also different. Now, the reason is still under investigation, but this deviation is much smaller than the 1 mrad requirement. The beam operation was controlled as required during all periods.

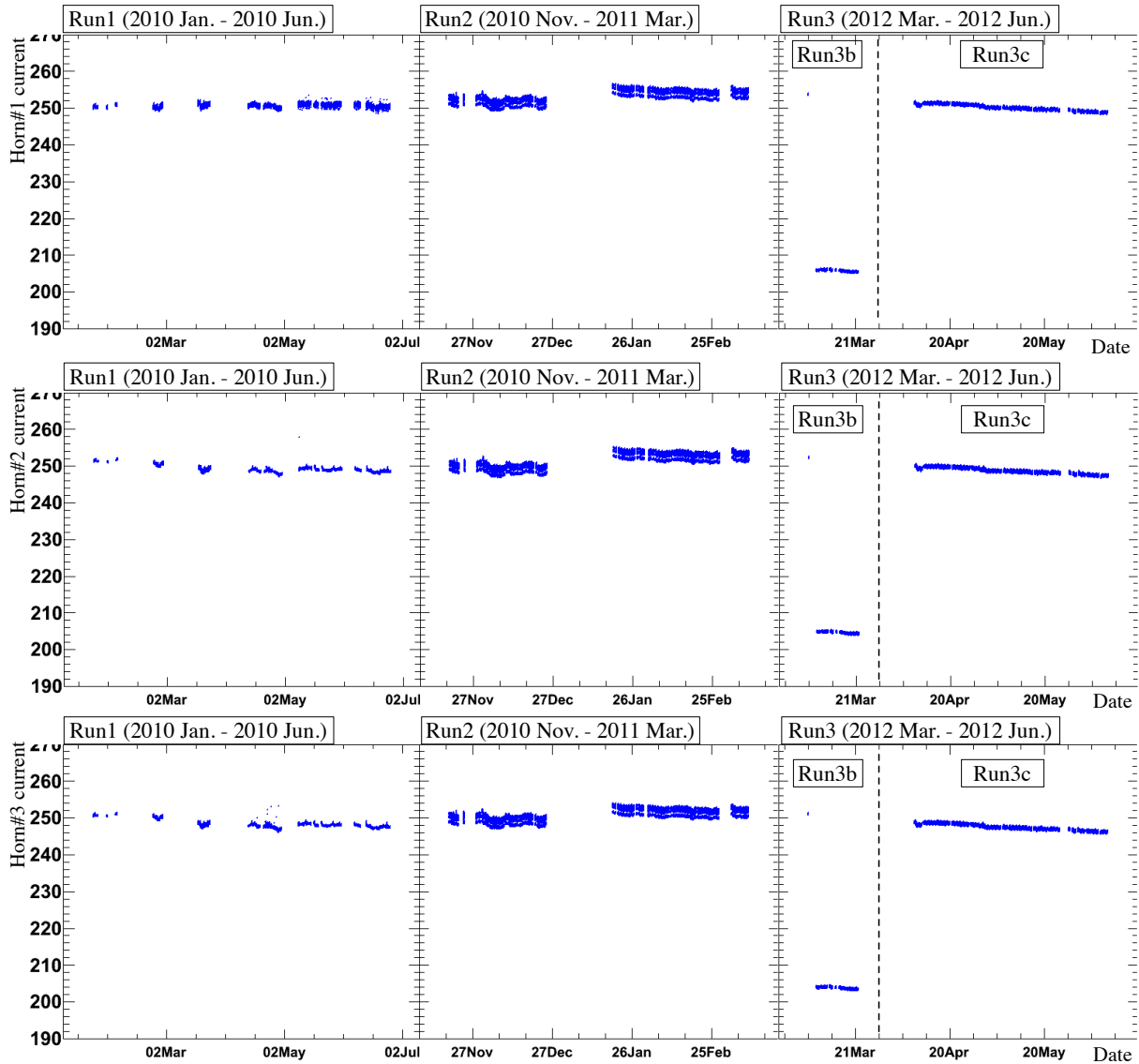


Figure 2.22: History of the measured horn current during all data taking period. Top: Horn 1, Middle: Horn 2, Bottom: Horn 3. The current is stable within 5kA from mean values of each data taking period.

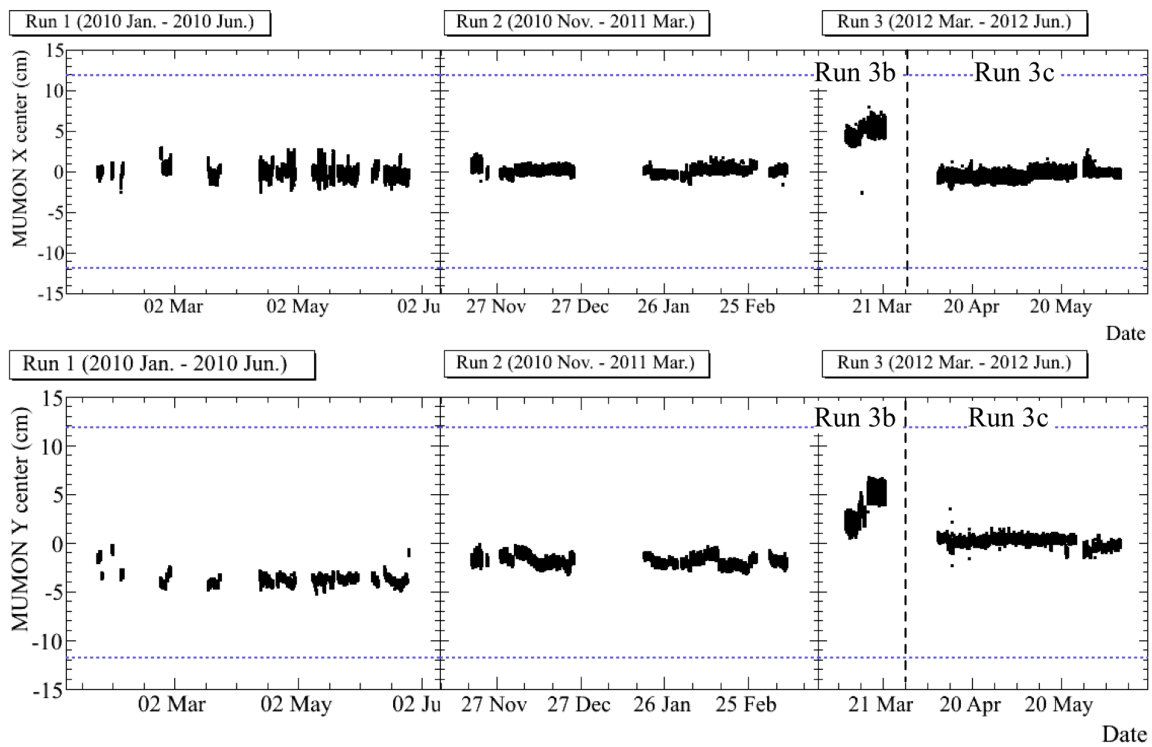


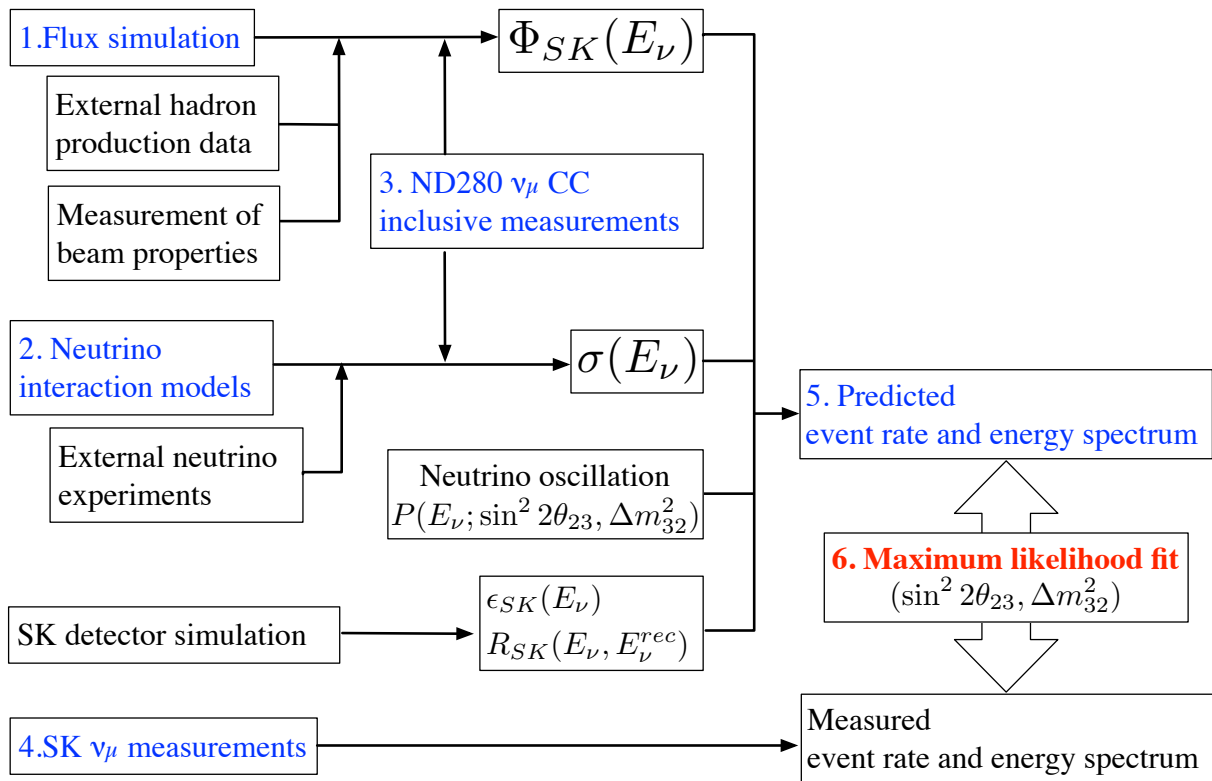
Figure 2.23: History of the measured muon profile center at MUMON in all run periods. A top and bottom figure shows the profile center in the horizontal(X) and the vertical(Y), respectively. A dashed line corresponds to 1 mrad at MUMON.

Chapter 3

Overview of the Oscillation analysis

We measure the oscillation parameters, $\sin^2 \theta_{23}$ and Δm_{32}^2 by comparing the measured rate and energy spectrum of the ν_μ events at SK with the predictions. In the oscillation analysis, we use the event rate which is the number of events divided by POT, instead of the number of events because the event rate is convenient to normalize the data among different detectors (ND280 and SK). The prediction are derived in Eq. 1.17. The overview of the oscillation analysis is shown in Fig. 3.1. The oscillation analysis is performed as follows:

1. The neutrino fluxes at ND280 and SK ($\Phi_{ND280}(E_\nu)$, $\Phi_{SK}(E_\nu)$) are estimated with the neutrino flux simulation. This simulation is improved by external hadron production data (CERN NA61/SHINE [33, 34], and so on) and the measurements of beam properties (proton beam parameters, horn currents, the neutrino beam direction). The flux prediction is described in Chapter 4.
2. The cross-section of the neutrino interaction ($\sigma(E_\nu)$) is evaluated with the neutrino-nucleus interaction models. Based on the interaction models and flux prediction, a neutrino-nucleus interaction generator, NEUT [51] simulates events at ND280 and SK. Then, the expected rate and energy spectrum are estimated by integrated these events. The interaction models are tuned with external data. Details are described in Chapter 5.
3. The Φ_{ND280} and σ are refined by the measurements of ND280. The ND280 ν_μ inclusive charged current (CC) samples are analyzed. The ND280 measurement is described at Section 6.2. The Φ_{SK} is further refined based on the refined Φ_{ND280} via the correlation between Φ_{ND280} and Φ_{SK} . This correlation is estimated with the flux simulation (described at Section 4.5). The refining of the flux and neutrino interaction models is described in Sec. 7.
4. The rate and energy spectrum of the ν_μ events are measured at SK. The SK events with a single muon-like Cherenkov ring are selected. This event selection enhances the ν_μ charged current quasi-elastic interactions (CCQE). For these events, the neutrino energy is properly reconstructed from the measured momentum and angle of the muon (described in Eq. 6.1). The SK efficiency ϵ_{SK} and response function R_{SK} are estimated with the SK detector simulation.
5. The rate and energy spectrum of SK ν_μ events are predicted based on the refined Φ_{SK} , σ , ϵ_{SK} , R_{SK} and the neutrino oscillation probability. This prediction is described in Chapter 8.
6. The oscillation parameters are determined by comparing the measured rate and energy spectrum of the SK ν_μ events with the prediction. The oscillation parameter fit is based on the unbinned maximum likelihood method. These are described in Chapter 8.

Figure 3.1: Overview of the ν_μ disappearance analysis flow.

Chapter 4

Neutrino flux prediction

As already described, the precise flux prediction is one of the most important issues to improve the sensitivity of the oscillation analysis.

The neutrino fluxes and spectra at INGRID, ND280, and SK are predicted with the flux simulation improved based on the experimental data. The hadron production models in the simulation are improved to reproduce the measurement of the hadron production experiments. The beam properties (the proton beam parameters, the neutrino beam direction and so on) are reflected in the simulation. The uncertainties on the flux prediction originate from the uncertainties of the hadronic productions and the uncertainties of the beam properties.

The flux correlation is estimated as the covariance matrix between bins in neutrino energies, neutrino flavors, and neutrino detectors (ND280 and SK) by considering the sources of uncertainties. This matrix can be used to refine the SK flux prediction based on the ND280 flux measurements. The refined SK flux prediction results in the more precise measurement of the oscillation parameters.

4.1 Overview of the neutrino flux simulation

The neutrino fluxes and spectra at INGRID, ND280, and SK is predicted with a flux simulation shown in Fig. 4.1 and 4.2. The flux simulation first produces the primary proton beam upstream of the baffle and predicts the decay of hadrons or muons that produce neutrinos. The simulation and its associated uncertainties are driven by measured proton beam parameters, measurements of the horns' magnetic fields, and hadron production data, including NA61/SHINE measurements [33, 34].

For the hadronic interactions inside the target, FLUKA2008 [52] is used. FLUKA2008 is found to have the best agreement with external hadron production data. In this part, the primary proton beam first interacts in the target and produces the majority of the secondary pions. Kinematic information for particles emitted from the target is saved and transferred to the JNUBEAM simulation.

JNUBEAM is a custom-made simulation based on GEANT3 [53] Monte Carlo simulation. JNUBEAM reproduces the baffle, target, horn magnets, helium vessel, decay volume, beam dump, and muon monitor. The geometry of these components is based on the final mechanical drawings of the constructed beamline. JNUBEAM also includes the INGRID, ND280, and SK detectors. These detectors are positioned in the simulation according to the latest survey results. In JNUBEAM, particles outgoing from the target are propagated through the horn magnetic field, and may interact with the horn material. After that, particles are propagated through the decay volume until they interact or decay. Neutrinos are produced from decay of the particles. Hadronic interactions are modeled by the GCALE model [54] in JNUBEAM.

The flux samples are first generated with the nominal hadron interaction models (the hadron production multiplicity and interaction rate). Then, the generated flux samples can be tuned based on the external hadron interaction data (described in Sec. 4.2.1). Since each flux sample has the full hadron interaction history producing the neutrino, the normalization of each flux sample is changed based on the difference of the hadron interaction model and data. This procedure is called "hadron production weighting" in Fig. 4.2. The weighting method can reproduce the flux samples based on the hadron interaction data without regeneration. The detail of the hadron production weighting is described in Sec. 4.2. In addition to the hadron interaction history, each sample has the kinematic information of the used initial proton. From this proton information, the flux samples can be reproduced based on different initial proton condition.

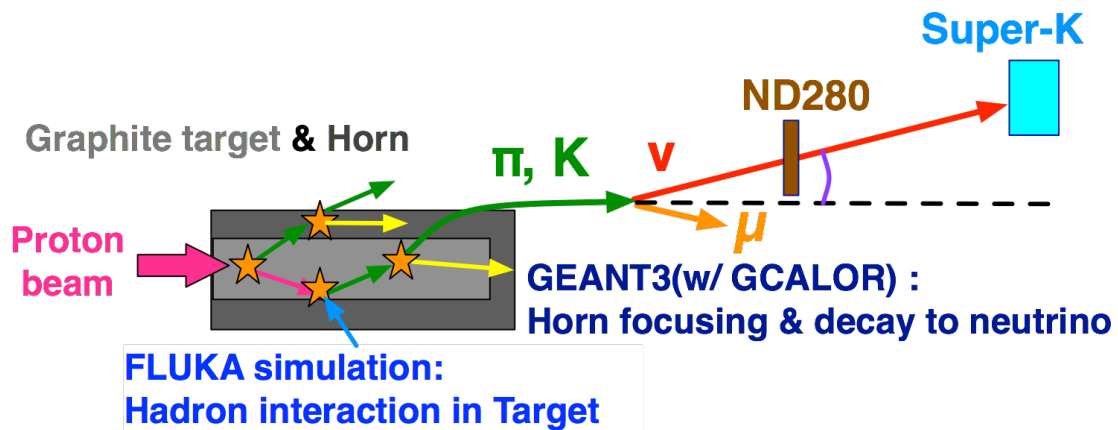


Figure 4.1: Overview of the neutrino flux simulation

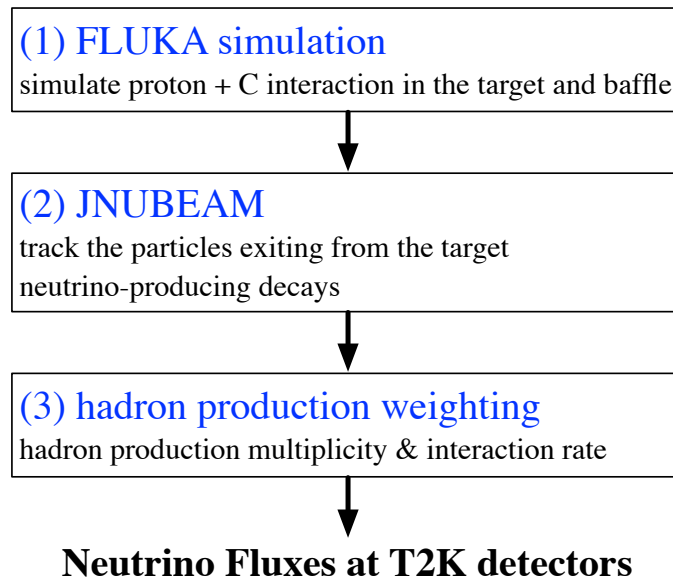


Figure 4.2: Flow diagram of the flux prediction.

Hadronic interaction in the target

The interactions of the primary beam protons with the graphite of the baffle and the target is simulated by using FLUKA2008. Incident protons are generated according to the measured proton beam spatial distribution and divergence. Its kinetic energy is set to 30 GeV. The geometry in FLUKA2008 is shown in Fig. 4.3. The baffle is depicted as a graphite block with the dimensions $29 \times 40 \times 171.145 \text{ cm}^3$ and a 3.0 cm diameter cylindrical hole through the center. The target is modeled as a graphite cylinder 90 cm long and 2.6 cm in diameter. The volume inside the baffle hole and between the baffle and the target is filled with He gas. The generated particles are traced until they emerge from the model geometry, then information such as kinematic variables and hadron interaction history is recorded at that point.

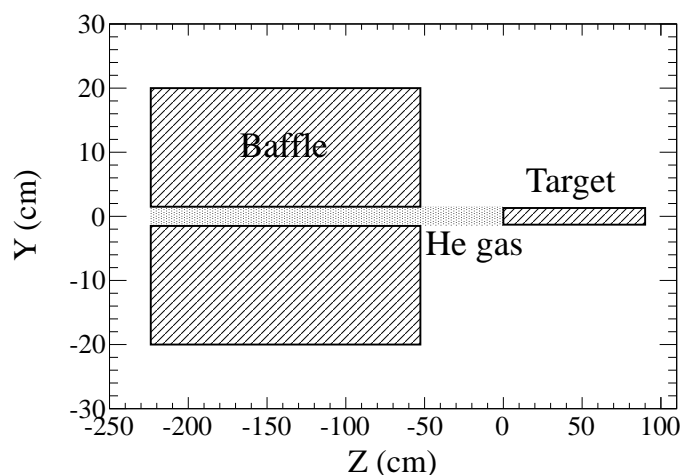


Figure 4.3: A two-dimensional projected view of the geometrical set-up in the FLUKA simulation of the baffle and the target.

Tracking inside horns and helium vessel.

Particles are generated in JNUBEAM according to the recorded information in FLUKA2008, and then are tracked through the horns and helium vessel. The graphite tube and titanium case surrounding the target are modeled in JNUBEAM. The thickness of graphite tube and titanium case is 2 mm and 0.3 mm. The interaction of particles with the materials is modeled by GCALOR in JNUBEAM.

Magnetic field of the horn inside inner conductors

The horn conductor is made of aluminum, and the thickness of the inner conductor is 3 mm. Since the low frequency pulsed current (3.6 msec full width) is loaded into the horn, the skin effect is small (the estimated skin depth is approximately 5 mm). Therefore, it is assumed that the current flows in the conductor uniformly. On this assumption, the magnetic field at radius r in the inner conductor is calculated with the Ampère's law as:

$$B(r) = \frac{\mu_0 I}{2\pi r} \frac{r^2 - a^2}{b^2 - a^2}, \quad (4.1)$$

where μ_0 is the magnetic permeability, I is the current and a and b are, respectively, the inner and outer radii of the inner conductor.

Neutrino production

Particles travel in the horn, the helium vessel, the decay volume, and the surrounding concrete shield including the beam dump, then decay into neutrinos, or stop when their kinetic energy drops below 10 MeV. Thus, neutrino are generated. In JNUBEAM, decays of π^\pm , K^\pm , K_L^0 and μ^\pm are considered as neutrino sources. The current best knowledge [55] on the branching ratios and $K_{\ell 3}^\pm$ decay ($K^+ \rightarrow \pi^0 l^+ \nu_l / K^- \rightarrow \pi^0 l^- \bar{\nu}_l$, $l = e, \mu$) form factors is used. When a muon is generated from the decay of pion or kaon, its polarization information is stored. This polarization is taken into account at the muon decay.

When a particle decays into neutrino(s), the neutrino(s) are forced to point in the direction of SK or a randomly chosen point in the near detector planes in order to save computing time. The neutrino energy in the center of mass frame is assigned based on the decay kinematics. The neutrino is then boosted into the laboratory frame under the assumption that it points towards the desired detector, and the probability of production in the selected direction is stored. The neutrino flux spectrum is obtained by scaling each event with the stored probability.

For neutrinos produced with energy less than 4 GeV, the storage of events is pre-scaled (and event scaling are adjusted accordingly) to allow for sufficient statistics in the high energy tail of the flux prediction without producing prohibitively large file sets.

4.2 Hadronic interaction weighting

Particles traversing in the target encounter a significant amount of material and can undergo multiple interactions. In addition particles can also interact with the material outside the target. The hadronic interaction weighting is therefore applied to the each hadronic interaction of the interaction history in each event. Each weighting factor is estimated so that the hadron interaction model (FLUKA2008 or GCALOR) reproduces the hadron interaction data. The hadron interaction data used are thin target data and described in Sec. 4.2.1. The data include measurements of inelastic cross sections and differential hadron production. The hadron interaction weighting is composed of the following processes:

1. weighting for the π^\pm differential production cross-section.
2. weighting for the K^\pm and K_L^0 differential production cross-section.
3. weighting for the hadronic interaction rate (production cross-section).

where, the produced hadrons are labeled as secondary (tertiary) hadrons if they are produced in interactions of the original protons (hadrons other than original protons) as shown in Fig. 4.4. The hadron differential productions are composed of the three types; the secondary and tertiary hadron production in the target (C), the tertiary hadron production in the horn (A1),

The breakdown of the predicted flux for each flavor is described in Table 4.1 according to the final parent hadron in the interaction history. The ν_e and $\bar{\nu}_e$ are from the decay of muon decays originating from secondary or tertiary pions. A significant fraction of the fluxes come from tertiary pions and kaons, so it is important to investigate hadron interaction data for both the T2K beam momentum and lower momentum.

4.2.1 Hadron production data used for weighting process

The used hadron differential production data are summarized in Table 4.2 and the used hadronic interaction rate data are summarized in Table 4.3.

To predict the neutrino flux precisely, T2K relies primarily on the measurements of pion [33] and kaon [34] yields by the NA61/SHINE experiment at the CERN SPS. These measurements

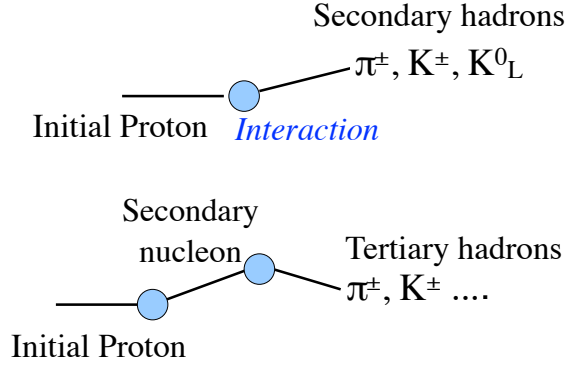


Figure 4.4: Labels of hadrons produced in each hadronic interaction.

Table 4.1: The fraction of the neutrino flux by the final hadron in the interaction history.

Parent	Flux Percentage of Each(All) Flavors			
	ν_μ	$\bar{\nu}_\mu$	ν_e	$\bar{\nu}_e$
Secondary				
π^\pm	60.0(55.6)%	41.8(2.5)%	31.9(0.4)%	2.8(0.0)%
K^\pm	4.0(3.7)%	4.3(0.3)%	26.9(0.3)%	11.3(0.0)%
K_L^0	0.1(0.1)%	0.9(0.1)%	7.6(0.1)%	49.0(0.1)%
Tertiary				
π^\pm	34.4(31.9)%	50.0(3.0)%	20.4(0.2)%	6.6(0.0)%
K^\pm	1.4(1.3)%	2.6(0.2)%	10.0(0.1)%	8.8(0.0)%
K_L^0	0.0(0.0)%	0.4(0.1)%	3.2(0.0)%	21.3(0.0)%

Table 4.2: Differential hadron production data used for the T2K neutrino flux predictions.

Experiment	Beam Mom. (GeV/c)	Target	Particles
NA61/SHINE [33] [34]	31	C	π^\pm, K^+
Eichten <i>et al.</i> [56]	24	Be, Al, ...	p, π^\pm, K^\pm
Allaby <i>et al.</i> [57]	19.2	Be, Al, ...	p, π^\pm, K^\pm
BNL-E910 [58]	6.4 – 17.5	Be	π^\pm

Table 4.3: Inelastic and production cross-section data used for the T2K neutrino flux predictions.

Data	Beam	Target	Beam Momentum (GeV/c)	Measurement
Abrams <i>et al.</i> [59]	K^\pm	C, Cu	1 – 3.3	σ_{inel}
Allaby <i>et al.</i> [60]	π^-, K^-	C, Al, ...	20 – 65	σ_{inel}
Allardyce <i>et al.</i> [61]	π^\pm	C, Al, ...	0.71 – 2	σ_{inel}
Bellettini <i>et al.</i> [62]	p	C, Al, ...	19.3, 21.5	σ_{inel}
Bobchenko <i>et al.</i> [63]	π^-, p	C, Al, ...	1.75 – 9	σ_{inel}
Carroll <i>et al.</i> [64]	π^\pm, K^\pm, p	C, Al, ...	60 – 280	σ_{prod}
Cronin <i>et al.</i> [65]	π^-	C, Al	0.73 – 1.33	σ_{inel}
Chen <i>et al.</i> [66]	p	C, Al, ...	1.53	σ_{inel}
Denisov <i>et al.</i> [67]	π^\pm, K^\pm, p	C, Al, ...	6 – 60	σ_{inel}
Longo <i>et al.</i> [68]	π^+, p	C, Al	3	σ_{inel}
NA61/SHINE [33]	p	C	31	σ_{prod}
Vlasov <i>et al.</i> [69]	π^-	C, Al	2 – 6.7	σ_{inel}

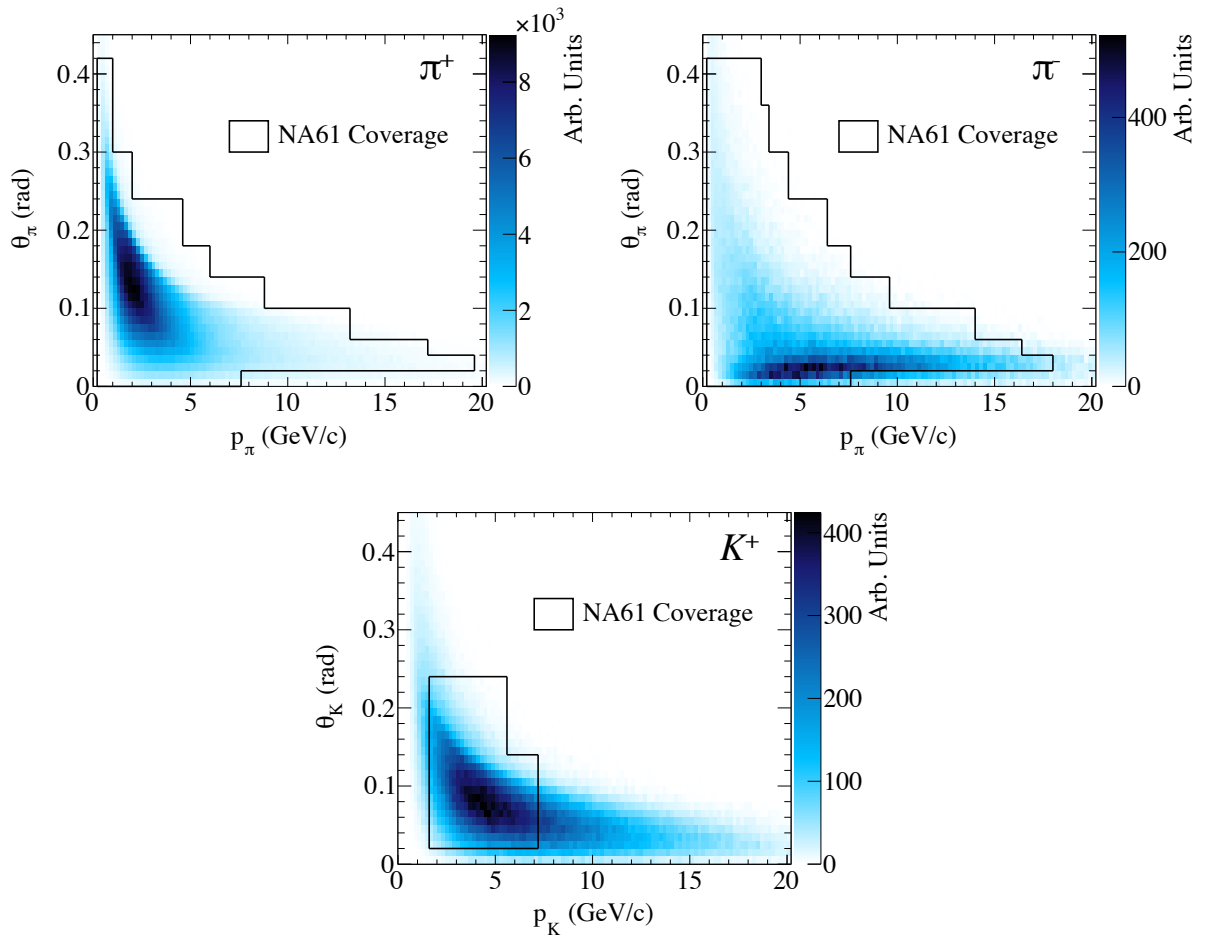


Figure 4.5: The phase space of π^\pm and K^+ contributing to the predicted neutrino flux at SK, and the regions covered by NA61/SHINE measurements.

were taken with a thin (2 cm) graphite target and the same proton beam energy as that of T2K. The differential production measurements are based on the data collected in 2007 during a first, limited statistics, run with about 6.7×10^5 registered events. An additional data set, taken with the target removed, was used to account for the contamination by particles produced in interactions of the proton beam occurring outside the target. The NA61/SHINE data covers most of the relevant hadron production phase space for the T2K flux, as illustrated in Fig. 4.5, which shows the predicted momentum and production angle of pions and kaons that are generated in primary proton interactions and decay to contribute to the neutrino flux at SK. More than 90% of the pion phase space is covered, and the K^+ data covers 60% of the kaon phase space. The measurements of the differential kaon production by Eichten *et al.* [56] and Allaby *et al.* [57] cover the forward production of high energy kaons, which has not been measured yet by the NA61/SHINE experiment. These data are used to re-weight the model predictions in these regions. In addition, the differential proton production measurements in these experiments are used to evaluate systematic uncertainties in secondary nucleon production. Also, the pion production data from the BNL-E910 experiment [58] is used to evaluate systematic uncertainties associated with tertiary pion production.

The particle interaction rates and absorption are weighted based on the measurements of the inelastic cross section for proton, pion, and kaon beams with carbon and aluminum targets. These data is summarized in Table 4.3. These results are typically the inelastic cross section σ_{inel} which is defined as the total cross section minus the elastic cross section. Some experiments measure the production cross section, σ_{prod} , which is defined as:

$$\sigma_{prod} \equiv \sigma_{inel} - \sigma_{qe}, \quad (4.2)$$

where σ_{qe} is the quasi-elastic scattering off of individual nuclei. The production cross section represents the rate of interactions where hadrons are produced in the final state.

4.2.2 Hadron differential production weighting

The hadron differential production cross-section is weighted by using the differential multiplicity in the momentum, p , of the produced particle and its angle, θ , relative to the incident particle:

$$\frac{dn}{dp}(\theta, p_{in}, A) = \frac{1}{\sigma_{prod}(p_{in}, A)} \frac{d\sigma}{dp}(\theta, p_{in}, A). \quad (4.3)$$

The cross section $\sigma_{prod}(p_{in}, A)$ depends on the incident particle momentum, p_{in} , and target nucleus, A . The following weight is applied to a given simulated interaction that produces hadrons:

$$w(p_{in}, A) = \frac{[\frac{dn}{dp}(\theta, p_{in}, A)]_{data}}{[\frac{dn}{dp}(\theta, p_{in}, A)]_{MC}}. \quad (4.4)$$

For weighting the hadron productions based on data with several incident nucleon momenta or inside the several materials, the following scalings are applied to the hadron differential production:

- The momentum scaling is carried out assuming Feynman scaling [70] for the hadron productions with different incident nucleon momenta from the T2K primary proton momentum (31 GeV/c) (for example, the incident momenta of tertiary pion productions are lower than ones of secondary pion productions). The Feynman variable, x_F , is defined as:

$$x_F = \frac{p_L}{p_{L(max)}} \quad (4.5)$$

where p_L is the longitudinal momentum of the produced particle in the center of mass frame and $p_{L(max)}$ is the maximum allowed longitudinal momentum of the produced particle. The differential production weights converted to an x_F - p_T dependence are approximated to be independent of the center of mass energy (p_T represents the transverse momentum of the produced particles). The differential production weights are converted to an x_F - p_T dependence and applied to the hadron productions with the different incident nucleon momenta based on x_F and p_T of those productions. This scaling method assumes perfect scaling, and the systematic effect is evaluated using data with lower incident particle momenta (at Sec. 4.4).

- The nucleon-number-dependent (A -dependent) scaling is carried out for the hadron productions with different target materials from the T2K graphite target (for example, the hadron productions inside the horns whose materials are aluminum). The A -dependent scaling assumes a parametrization proposed by Bonesini *et al.* [71] based on works by Barton *et al.* [72] and Skubic *et al.* [73]:

$$E \frac{d^3\sigma(A_1)}{dp^3} = \left[\frac{A_1}{A_0} \right]^{\alpha(x_F, p_T)} E \frac{d^3\sigma(A_0)}{dp^3} \quad (4.6)$$

where:

$$\alpha(x_F, p_T) = (a + bx_F + cx_F^2)(d + ep_T^2), \quad (4.7)$$

A_0 or A_1 represents the target nucleon number of each experiment. The parameters a through e are determined by fitting the A -dependence in the data from Eichten *et al.* [56] and Allaby *et al.* [57]. The uncertainty of the scaling for the individual data points is evaluated as the uncertainty of the flux prediction (at Sec. 4.4).

Pion production weighting

The procedure of pion production weighting contains the following ways:

- Secondary pions which are produced in the target (C) are weighted by the weights of NA61/SHINE data / FLUKA2008. The weights are shown in Fig. 4.6.
- Tertiary pions which are produced in the target (C) are weighted by the scaled weights of NA61/SHINE / FLUKA2008. The scaled weights are estimated by the Feynman scaling.
- Tertiary pions which are produced in the horn (Al) are weighted by the scaled weights of the scaled data / GCALOR. The scaled weights is estimated by the Feynman scaling. The scaled data is estimated by A -dependent scaling based on the NA61/SHINE. The ratio of scaled NA61/SHINE data / GCALOR provides the weight for tertiary pion production inside the horn. The weights applied to the production in GCALOR are shown in Fig. 4.7
- In addition, for pion produced from neutrons, isospin invariance is used to make weights : $\sigma(n + A \rightarrow \pi^\pm) = \sigma(p + A \rightarrow \pi^\mp)$.

The σ_{prod} of 225.0 mb is used for the differential multiplicity measured by NA61/SHINE, otherwise σ_{prod} of 231.3 mb is used in FLUKA2008.

Kaon production weighting

The weighting procedure for the kaon production is similar to the procedures for pion production, but the coverage of NA61/SHINE data is different. As already described, Eichten *et al.* [56] and Allaby *et al.* [57] data are used for this weighting in addition to NA61/SHINE data. The usage of data is according to the following rules:

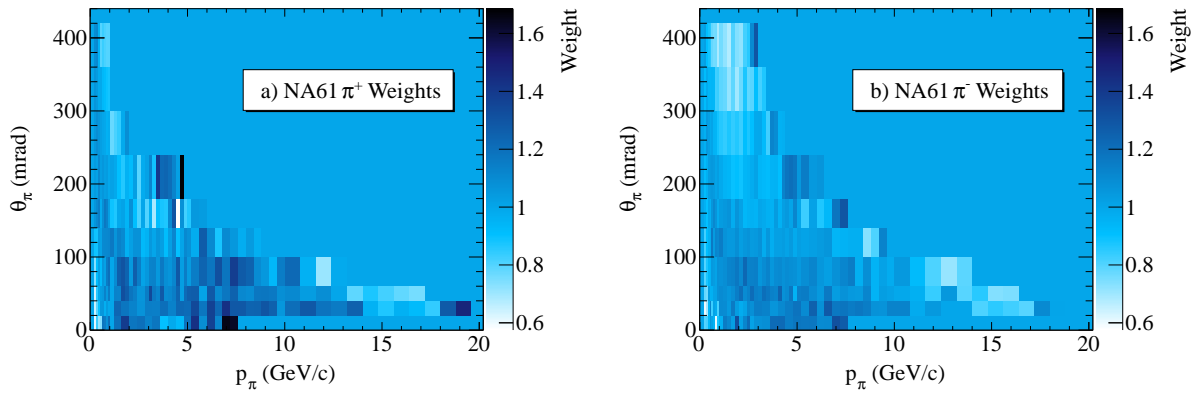


Figure 4.6: The differential production weights from NA61/SHINE data for π^\pm

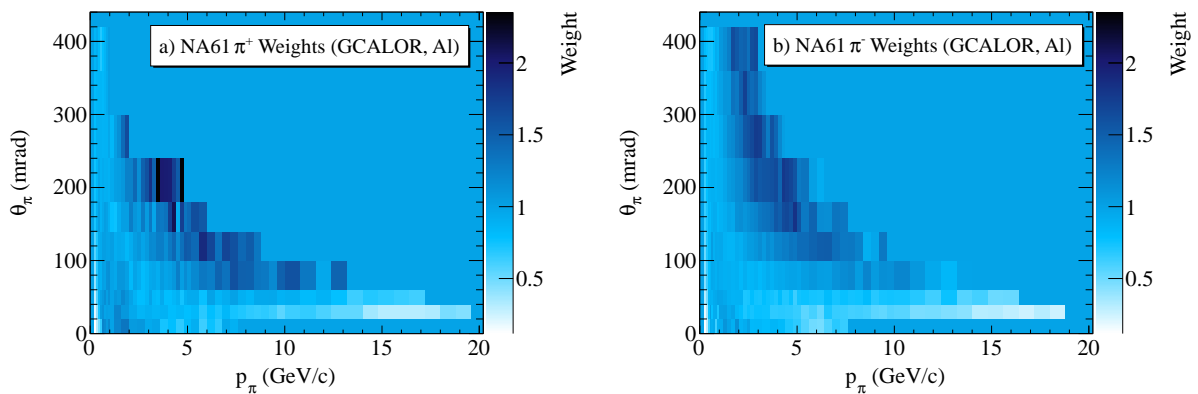


Figure 4.7: The differential production weights for GCALOR (Al) from *A*-scaled NA61/SHINE data for π^\pm

- K^+ whose momentum and angle are in the NA61/SHINE phase space is weighted based on NA61 data.
- K^+ outside of the NA61/SHINE phase space or K^-/K_L^0 are weighted base on scaled Eichten or Allaby data. The scaled data is estimated by Feynman scaling or A -dependent scaling based on each data point.

The σ_{prod} of 195 mb is used for the differential multiplicity of Eichten *et al.* and Allaby *et al.*, otherwise σ_{prod} of 195.6 mb is evaluated for FLUKA2008. The weighting procedures for charged kaons are same as ones for pions. The K_L^0 multiplicity is calculated from the Eichten and Allaby data using a simple quark parton model (QPM) [74, 75]. Assuming the following conditions on the number densities of sea and valence quarks:

$$u_s = \bar{u}_s = d_s = \bar{d}_s, s_s = \bar{s}_s \quad (4.8a)$$

$$n \equiv u_v/d_v = 2, \quad (4.8b)$$

a relation between the number of produced K_L^0 (K_S^0), K^+ , and K^- can be established:

$$N(K_L^0) = N(K_S^0) = \frac{N(K^+) + 3N(K^-)}{4}. \quad (4.9)$$

After calculating the K_L^0 production according to Eq. 4.9, the K_L^0 multiplicity is weighted in the same manner as in the case of K^\pm . Although Eq 4.9 is only strictly valid for proton-proton collisions ($n = 2$), the effect of proton-neutron ($n = 1$) interactions leads to only small changes in the flux predictions that are $< 1\%$. It is, therefore, not considered at this time.

4.2.3 Hadron interaction rate weighting

The production cross-section defined in Eq. 4.2 is weighted to modify the hadron interaction rate. The diagonal of a particle traveling is shown in Fig. 4.8. A particle interacts with momentum p_1 after traveling a distance x_1 in a material to produce a particle with p_2 that travels x_2 before leaving the material. When the production cross section changes, $\sigma_{prod} \rightarrow \sigma'_{prod}$, the weight applied to the model is the ratio of the probabilities:

$$W(\sigma', \sigma; p_1, x_1, p_2, x_2) = \frac{\sigma'(p_1)}{\sigma(p_1)} e^{-x_1[\sigma'(p_1) - \sigma(p_1)]\rho} e^{-x_2[\sigma'(p_2) - \sigma(p_2)]\rho}. \quad (4.10)$$

The cross sections calculated by FLUKA2008 is in good agreement with the data, while GEANT3 (GCALOR) has significant disagreement at low incident particle momenta. Therefore, no weights are applied to the FLUKA2008 simulation for interactions in the target, but the GEANT3 (GCALOR) production cross sections are weighted to the FLUKA2008 value.

4.2.4 Summary of Hadron interaction weighting

The ratio of the flux with and without the weighting applied are shown in Fig. 4.9 as a function of neutrino energy every the effect of the weighting. The weighting for the pion differential production has the largest effect at the energy around oscillation maximum, while the weighting for the kaon differential production is dominant at high energies.

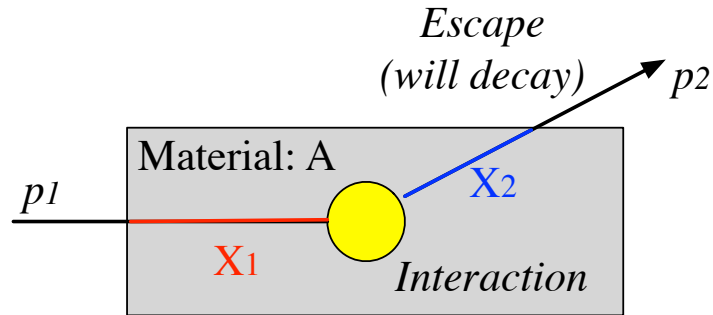


Figure 4.8: Diagram of a particle with momentum p_1 interacting a material A to produce a particle with momentum p_2

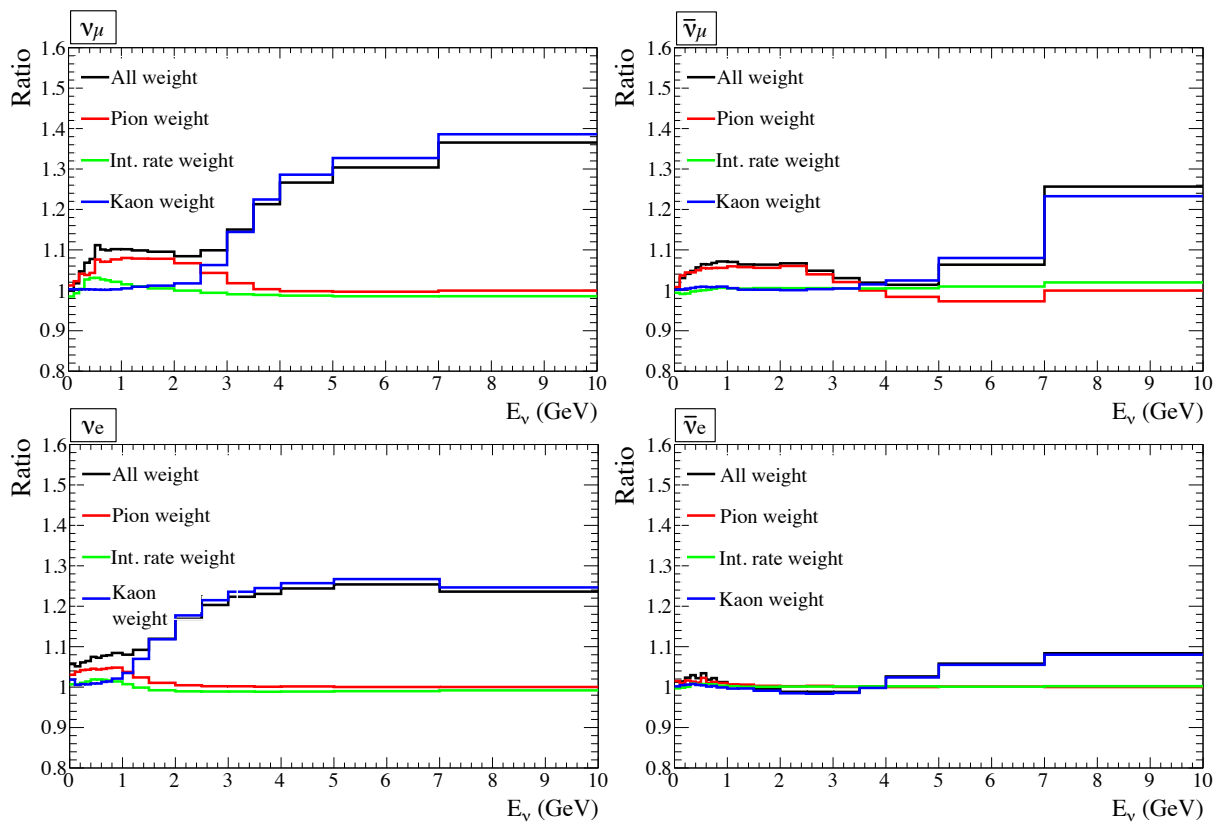


Figure 4.9: Ratio of the hadron interaction weighted flux over the not weighted flux for ν_μ (upper left), $\bar{\nu}_\mu$ (upper right), ν_e (lower left), $\bar{\nu}_e$ (lower right). These ratio is calculated based on the 250kA horn current simulation.

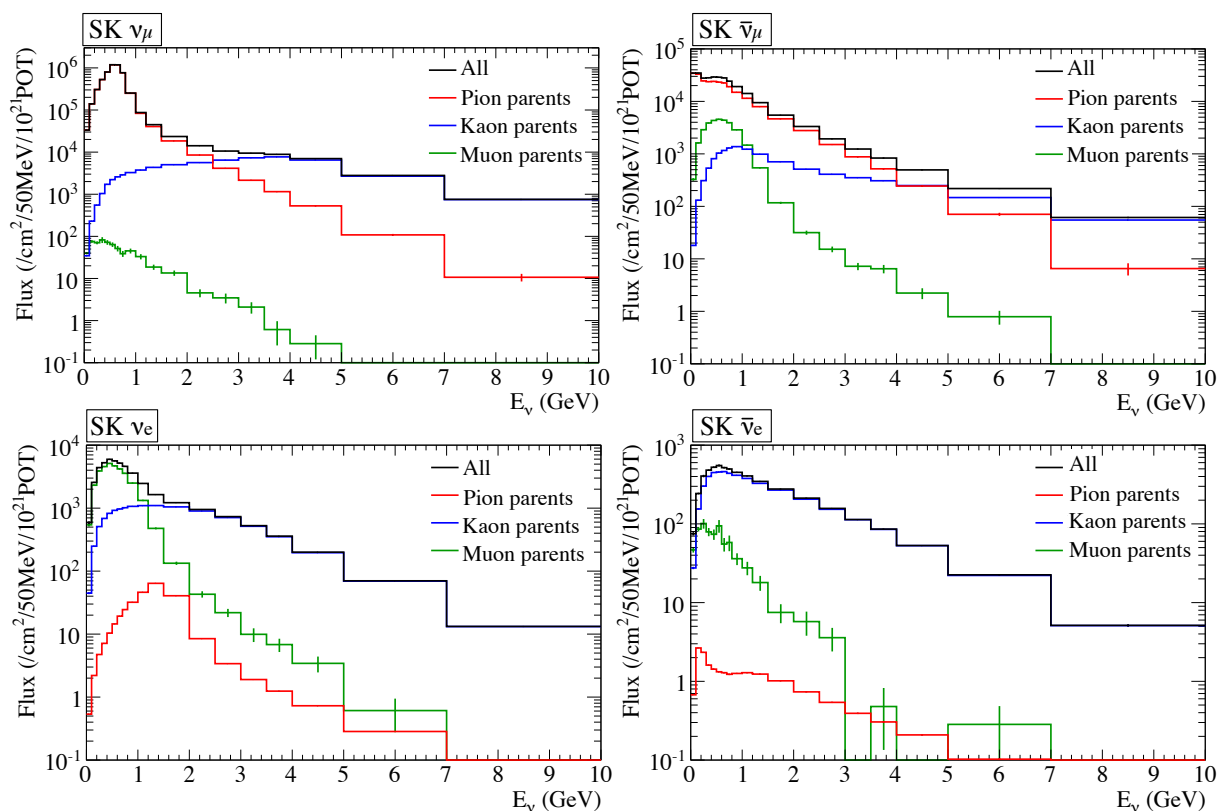


Figure 4.10: The flux predictions for the SK far detector broken down by the neutrino parent particle type. The ν_μ (upper left), $\bar{\nu}_\mu$ (upper right), ν_e (bottom left), and $\bar{\nu}_e$ (bottom right) fluxes are shown. The error bars, which is too small to be seen in most of the region, are MC statistical error.

4.3 T2K flux prediction

The T2K flux is predicted with the flux simulation including the weighting for the hadron interaction models. The flux is predicted for each neutrino flavor at the far and near detectors. The predicted fluxes at SK and ND280 are shown in Fig 4.11. The fluxes are broken down by the parent particle that decays to the neutrinos. The relative fractions of each flavor in the SK flux is shown in Table 4.4. These fractions are estimated for $0\sim 1.5$, $1.5\sim 3.0$ and >3.0 GeV energy ranges. The ν_μ flux is dominant in the flux below 1.5 GeV, and the $\bar{\nu}_\mu$ contamination is $\sim 5\%$. In the intermediate ($1.5\sim 3.0$ GeV) energy region, the relative fraction of $\bar{\nu}_\mu$ increases as the flux becomes more dominated by forward going pions that are not focused, which include π^- that decay to $\bar{\nu}_\mu$. The ν_e fraction also increases as the contribution from kaon decays becomes dominant.

4.4 Flux uncertainty

Here, the uncertainties associated to the neutrino flux prediction are evaluated for the oscillation analysis. The flux uncertainties arise from the following sources along with the error size of the SK ν_μ flux at the oscillation maximum energy:

- Hadron interaction uncertainties (Sec. 4.4.1).
 - Pion and kaon production uncertainties: 6% and $<1\%$

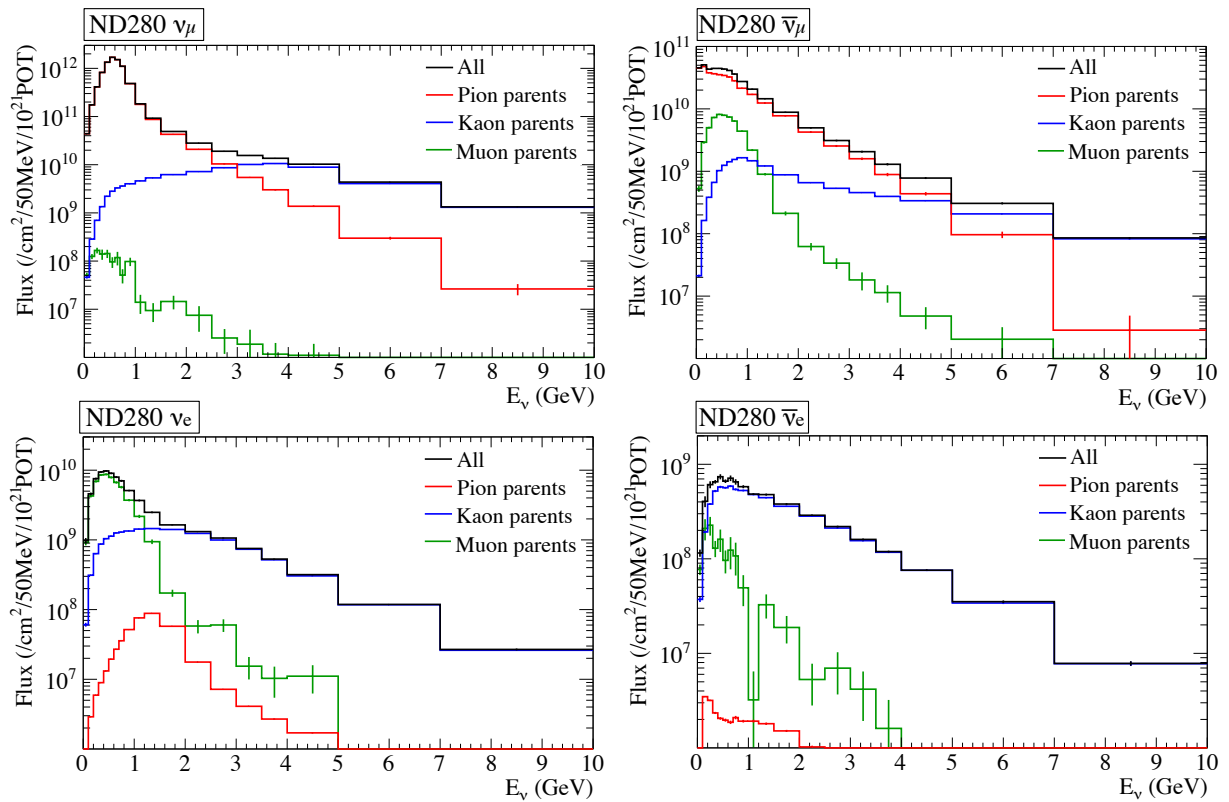


Figure 4.11: The flux predictions for the ND280 near detector broken down by the neutrino parent particle type. The ν_μ (upper left), $\bar{\nu}_\mu$ (upper right), ν_e (bottom left), and $\bar{\nu}_e$ (bottom right) fluxes are shown. The error bars, which is too small to be seen in most of the region, are MC statistical error.

Table 4.4: The fraction of the total SK flux by flavor in bins of the neutrino energy. The fractions in parentheses are relative to the total flux over all neutrino energies.

Flavor	Energy Range (GeV)		
	0 – 1.5	1.5 – 3.0	> 3.0
ν_μ	0.9363(0.8570)	0.7719(0.0391)	0.8821(0.0372)
$\bar{\nu}_\mu$	0.0542(0.0496)	0.1729(0.0087)	0.0795(0.0034)
ν_e	0.0085(0.0078)	0.0451(0.0023)	0.0304(0.0013)
$\bar{\nu}_e$	0.0010(0.0009)	0.0100(0.0005)	0.0080(0.0003)

- Secondary nucleon production uncertainties: 7%
- Hadronic interaction rate uncertainties: 7%
- Primary beam optics uncertainty (Sec. 4.4.3): 1%.
- Off-axis angle uncertainty (Sec. 4.4.4): 1%.
- Target and horn alignment error (Sec. 4.4.5): <1%.
- Horn current and magnetic field uncertainty (Sec. 4.4.6): 1%.

The flux uncertainties are estimated by changing underlying parameters associated to the flux prediction (the hadron production model, the proton beam profile, the horn currents, etc) and evaluating the deviation of the nominal flux. Here, the "nominal" flux means the predicted flux after hadron interaction tuning. The flux correlation among bins (neutrino flavors, energies, and detectors) are needed along with the size of flux uncertainties. The flux uncertainties and correlation are evaluated as a form of the covariance matrix. The element of the covariance matrix is defined as:

$$cov(i, j) = \langle (\phi_{nom}^i - \phi^i)(\phi_{nom}^j - \phi^j) \rangle = \sigma_{\phi_i} \sigma_{\phi_j} \cdot corr(i, j), \quad (4.11)$$

where the ϕ_{nom}^i are the nominal flux, and i specifies the bin number. The ϕ^i are the varied fluxes by changing underlying parameters. The σ_{ϕ_i} represents the uncertainty of ϕ^i and $corr(i, j)$ is the flux correlation factor between ϕ^i and ϕ^j . The flux uncertainty is derived from the the square root of the diagonal term of the covariance matrix ($=\sqrt{\sigma_{\phi_i} \sigma_{\phi_i} \cdot corr(i, i)} = \sigma_{\phi_i}$). The flux measured at ND280 can refine the SK flux prediction through the covariance matrix (described at Sec 4.5). The covariance matrixes are calculated for each error source. The combined uncertainty of all sources is simply represented by the sum of the covariances from each independent source. According to the kinds of underlying parameters, there are two methods to estimate flux covariances.

The first method is used at the case that an error source contains many correlated underlying parameters. The underlying parameters are changed according to their covariance. The flux prediction is re-weighted based on each of N sets (500 or more) of the changed parameters. A covariance matrix from the N sets of the re-weighted flux:

$$V_{ij} = \frac{1}{N} \sum_{k=1}^{k=N} (\phi_{nom}^i - \phi_k^i)(\phi_{nom}^j - \phi_k^j), \quad (4.12)$$

where the ϕ_k^i are the corresponding bins of the k^{th} set of the re-weighted flux. This method are used for the hadron interaction uncertainties and the proton beam profile uncertainties.

The second method is used for uncertainties represented by variations of the flux under the changes in single underlying parameter. For these uncertainties the flux is typically re-generated for variations of the parameter at $\pm 1\sigma$ (the σ represents the error size). A covariance matrix is calculated:

$$V_{ij} = \frac{1}{2}[(\phi_{nom}^i - \phi_+^i)(\phi_{nom}^j - \phi_+^j) + (\phi_{nom}^i - \phi_-^i)(\phi_{nom}^j - \phi_-^j)], \quad (4.13)$$

where the ϕ_+^i and ϕ_-^i are the re-generated flux for $+1\sigma$ and -1σ variations of the underlying parameter.

4.4.1 Hadron production uncertainties

Pion and kaon production uncertainties

The flux uncertainties associated with pion and kaon differential production models arise from the following sources.

- Experimental systematic errors. The total errors of NA61/SHINE pion measurements are shown in Fig. 4.12 for each of the NA61/SHINE p - θ bins. These errors include statistical errors. The total errors are typically 5 to 10% in the most important regions of the phase space. The total errors of NA61/SHINE K^+ measurements are shown in Fig. 4.13. The experimental errors in the kaon production data are summarized in Table 4.5. To estimate flux covariance, the correlations between p - θ bins from experimental systematic errors are taken into account.
- Systematic uncertainties associated with the Feynman momentum scaling. This flux uncertainty is evaluated as the difference of flux prediction by using an alternative scaling method from that by using Feynman scaling. The alternative method is called the radial scaling. The radial scaling variable x_R is defined as:

$$x_R = \frac{E^{cm}}{E_{max}^{cm}}, \quad (4.14)$$

where E^{cm} is the energy of the produced particle in the center of mass frame, and E_{max}^{cm} is the maximum energy that particle can have. Taylor *et al.* [76] found that the invariant cross-section when parametrized in x_R and p_T (the transverse momentum) does not depend on the total center of mass energy \sqrt{s} for $\sqrt{s} \gtrsim 10$ GeV.

To estimate the uncertainty associated with the momentum scaling of NA61/SHINE pion data, the radial scaling is applied to the combined data with NA61/SHINE and BNL-E910 [58] (beam momenta is 12.3 GeV and 17.5 GeV). BNL-E910 data is used to increase the reliability of the radial scaling for the low incident momentum region.

For the uncertainty associated with the momentum scaling of kaon data, the radial scaling is applied to the combined data with Eichten *et al.* and Allaby *et al.*

- Systematic uncertainties associated with A -dependent scaling. Parameters of A -dependent scaling in Eq. 4.6 are determined from Eichten *et al.* and Allaby *et al.* data. The uncertainties of A -dependent scaling are estimated from the discrepancy between their measurements with the Al targets and the expectations derived by scaling their measurements from Be to Al. These uncertainties of the A -dependent scaling are added to the experimental errors. (for example, NA61/SHINE pion data (C) is applied to the pion production inside horns (Al)).

- The uncertainties from the phase space not covered by any data. This flux uncertainties are evaluated as the change of the flux when the hadron productions in the uncovered region are re-weighted based on the extrapolated data by using the empirical parametrization developed by Bonesini *et al.* [71] (BMPT).

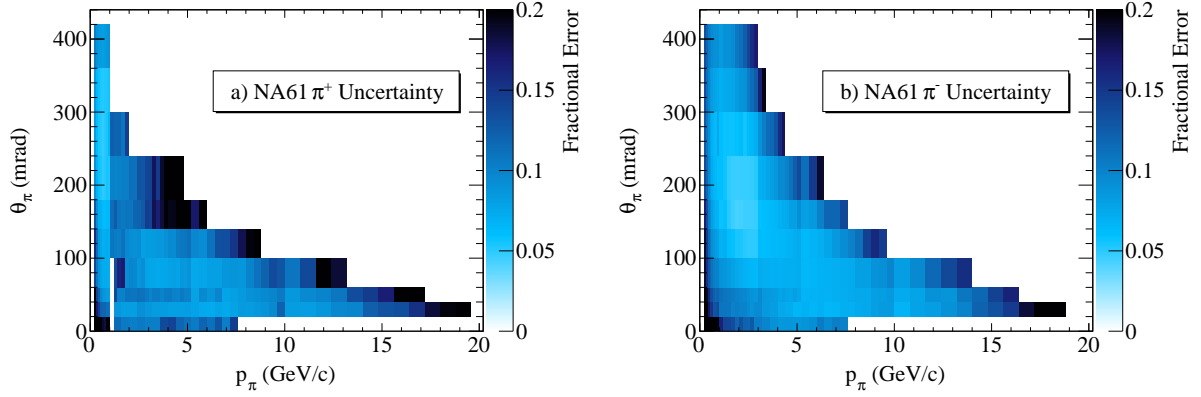


Figure 4.12: The fractional error on the NA61/SHINE measurements in each of the p - θ bins. The gap at π^+ momentum of 1.0-1.2 GeV/ c is a region with no NA61/SHINE data points.

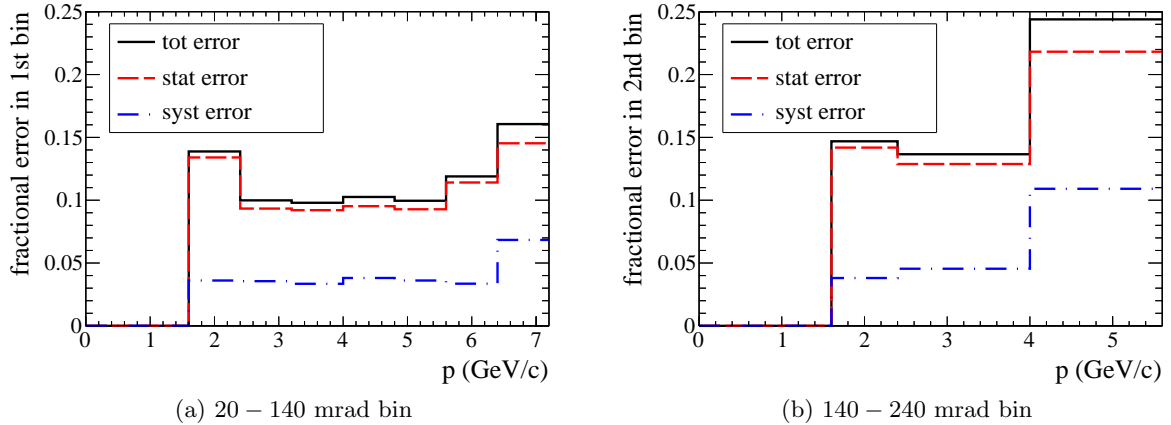


Figure 4.13: The fractional error on the NA61/SHINE K^+ measurements for two covered regions (bins) of reconstructed angle (20 – 140 mrad and 140 – 240 mrad).

Summary of pion production uncertainties

The flux uncertainties from the pion production uncertainties are shown in Fig. 4.14. The error sources are categorized as follows:

NA61 Error The uncertainty on the NA61/SHINE pion data.

Tertiary Tuning Error The uncertainty on the Feynman momentum scaling

Outside NA61 Error The uncertainty from phase space not covered by the NA61/SHINE data.

The dominant error source for the ν_μ and ν_e flux predictions around the flux peak is the errors of the NA61/SHINE pion measurements.

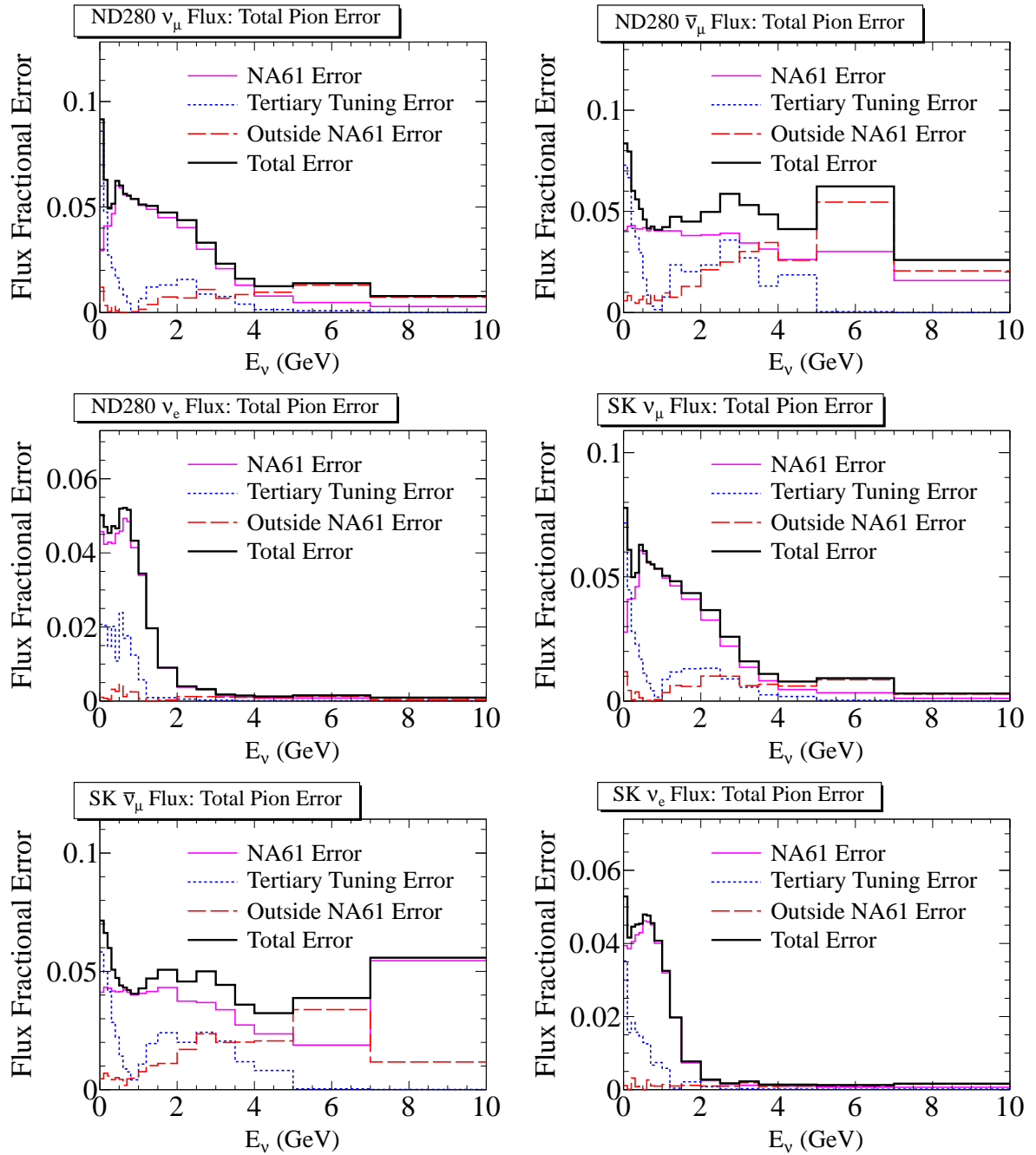


Figure 4.14: Fractional flux uncertainties from pion production uncertainties as a function of neutrino energy, for each flavor and at the near and far detectors. The breakdowns of the flux uncertainties are defined as follows: "NA61 Error" represents the uncertainty on the NA61/SHINE data. "Tertiary Tuning Error" represents the uncertainties on the Feynman momentum scaling. "Outside NA61 Error" represents the uncertainty from phase space not covered by the NA61/SHINE data.

Table 4.5: Summary of the fractional errors in the kaon production data. The error in the overall normalization is σ_N . The error for a given data bin is $\sigma_{\Delta p \Delta \theta}$. The error in the normalization for a given angular bin is $\sigma_{\Delta \theta}$.

	σ_N	$\sigma_{\Delta p \Delta \theta}$	$\sigma_{\Delta \theta}$
NA61/SHINE	2.3%	11 ~ 24%	—
Eichten <i>et al.</i>	15%	4%	5%
Allaby <i>et al.</i>	10%	2 ~ 5%	10%

Summary of kaon production uncertainties

The flux uncertainties from the kaon production uncertainties are shown in Fig. 4.15. The error sources are categorized as follows:

NA61 Error The uncertainty on the NA61/SHINE kaon data.

Other Data Error The uncertainties on the Eichten *et al.* and Allaby *et al.* data.

Tertiary Tuning Error The uncertainties on the Feynman momentum scaling.

No Data Error The uncertainty from phase space not covered by the NA61/SHINE data.

Out-of-target Error The uncertainty on the kaon production model inside horns (A1). This uncertainty is evaluated based on the difference between Eichten *et al.* data (A1) and GCALOR prediction.

The dominant error sources are the measurement errors of NA61/SHINE, Eichten *et al.* and Allaby *et al.* at high energy region.

Secondary nucleon production uncertainties

Interactions of the secondary protons (neutrons) inside the target contribute $\sim 16\%$ (5%) to the neutrino flux. The contribution of the secondary nucleon production uncertainties are not negligible. The flux uncertainties from these sources are evaluated based on the discrepancy between FLUKA2008 model and the proton production data of Eichten *et al.* and Allaby *et al.* The flux uncertainties are calculated by re-weighting the FLUKA2008 secondary proton and neutron production with the ratio of data to the FLUKA2008 model. The flux uncertainties are shown in Fig 4.17 and 4.18 as "secondary nucleon production".

Hadronic interaction rate uncertainties

The uncertainties of the hadronic interaction rate are conservatively assigned based on the magnitude of the quasi-elastic correction, σ_{qe} . This is because there is a discrepancy between the cross-section measurements for protons of Denisov *et al.* [67] and those of Bellettini *et al.* [62], Carroll *et al.* [64], and NA61/SHINE [33]. The size of the discrepancy is same as σ_{qe} . In the experiment by Denisov *et al.*, it is not clear if they measured the inelastic or production cross sections. These data are plotted in Fig. 4.16. For the Bellettini *et al.* data, the quasi-elastic contribution of 30.4 mb [33] has been subtracted from the measured value of 254 mb. In addition, the measurements by Denisov *et al.* are also shown after an estimated quasi-elastic contribution has been subtracted from the measured values. After this subtraction, the agreement between all of the four data is better. A conservative approach is therefore taken by using σ_{qe} as the uncertainty of the hadronic interaction rate.

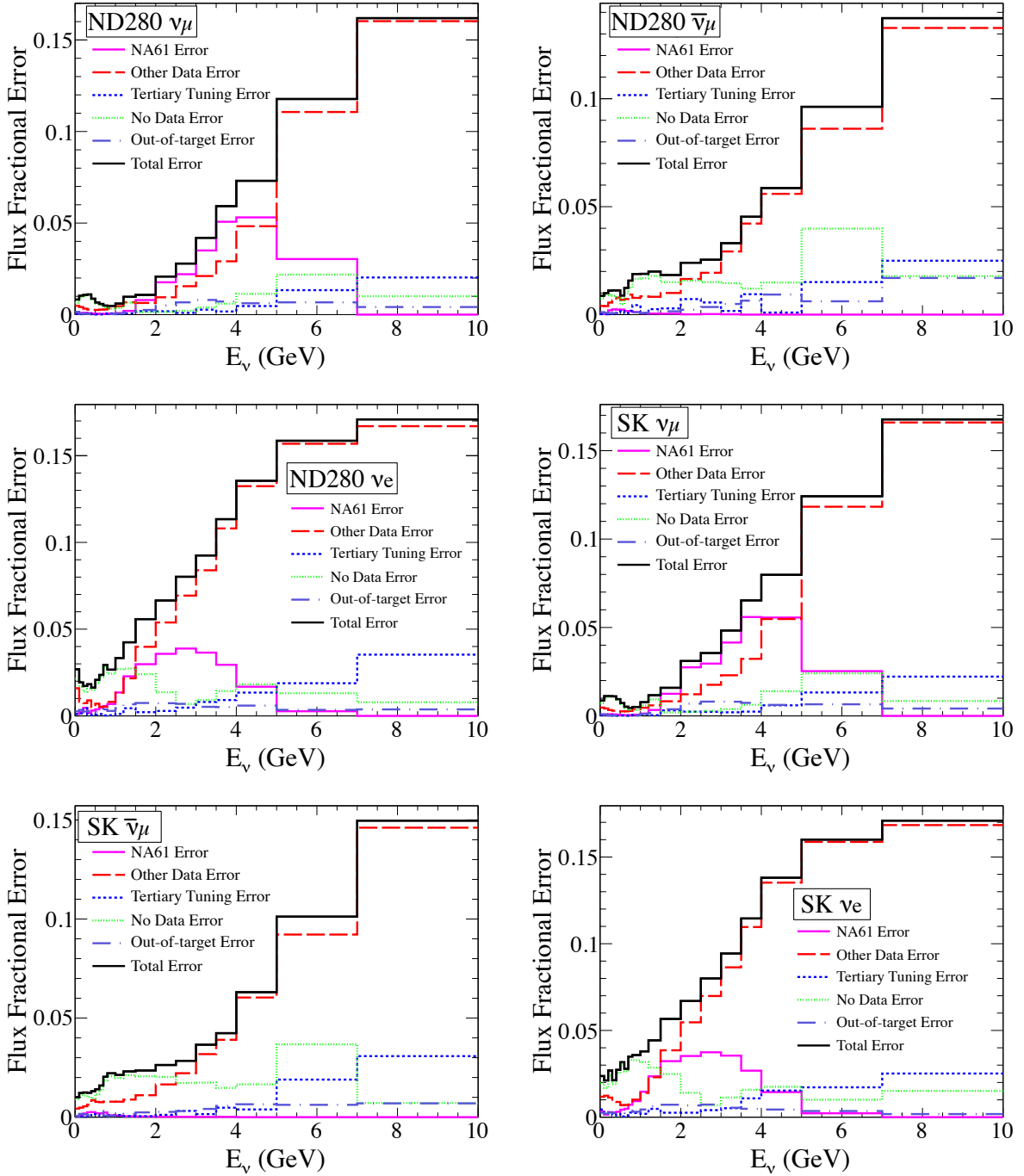


Figure 4.15: Fractional flux uncertainties from kaon production uncertainties as a function of neutrino energy, for each flavor and at ND280 and SK. The breakdowns of the kaon flux uncertainties are defined as follows: "NA61 Error" represents the uncertainty on the NA61/SHINE data, "Other Data Error" represents the uncertainty on the Eichten *et al.* and Allaby *et al.* data. "Tertiary Tuning Error" represents the uncertainties on the Feynman momentum scaling. "No Data Error" represents the uncertainty from phase space not covered by any data. "Out-of-target Error" represents the uncertainty on the kaon production outside the target.

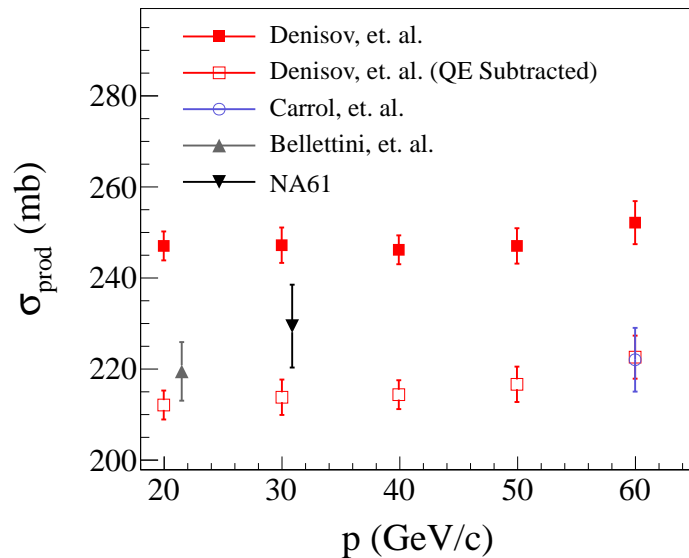


Figure 4.16: Production cross-section measurements for protons on graphite targets for momenta 20–60 GeV/c. The data from Denisov *et al.* are shown with and without the quasi-elastic subtraction since the measured quantity is ambiguous.

4.4.2 Summary of the hadron production uncertainties

Figure 4.17 and 4.18 shows the fractional uncertainties on the SK and ND280 fluxes due to hadronic interaction uncertainties. These figures include the flux uncertainties from pion and kaon production uncertainties shown in Fig 4.14 and 4.15. At low energy, the largest sources of uncertainty in the ν_μ flux are from the secondary nucleon production and hadronic interaction rate. The uncertainties of pion production is constrained well by the NA61/SHINE measurements. At high energy, the flux uncertainty is instead dominated by the uncertainties of kaon production.

4.4.3 Proton beam uncertainties

The proton beam uncertainties affect the neutrino flux prediction by the following reason. Neutrinos are generated from the decay of pions and kaons. An overview of a track of a secondary hadron is shown in Fig. 4.19. When the secondary hadron is generated from the entering proton whose position and angle is different from the center, the hadron has a different path length inside the target and feels different 1st horn magnetic field. The neutrino flux can be changed because the yield and direction of parent hadrons are different from the nominal ones.

To estimate the effect of the proton beam errors on the flux prediction, proton beam parameters were changed randomly within their errors described in Table 2.7. The correlation among parameters was considered. It was found that the errors for the vertical center position (Y) and center angle (Θ_Y) have a sizable effect. This is because Y and Θ_Y effectively change the off-axis angle at SK, which is displaced from the beam axis predominantly in the vertical direction. Therefore, only Y and θ_Y errors are considered in the evaluation of the flux uncertainty. Fig. 4.20 shows the flux change when (Y, θ_Y) are changed by their error sizes.

To construct the covariance matrix, a large number of flux samples were prepared with many (Y, Θ_Y) sets randomized according to the correlated uncertainties listed in Table 2.7. In order to avoid re-generate JNUBEAM flux samples, a special sample was generated with a large position-angle phase space and then re-weighted to reproduce each randomized pair of (Y, Θ_Y) . Figure 4.21 shows the phase space distribution for this widened beam and the actual measured

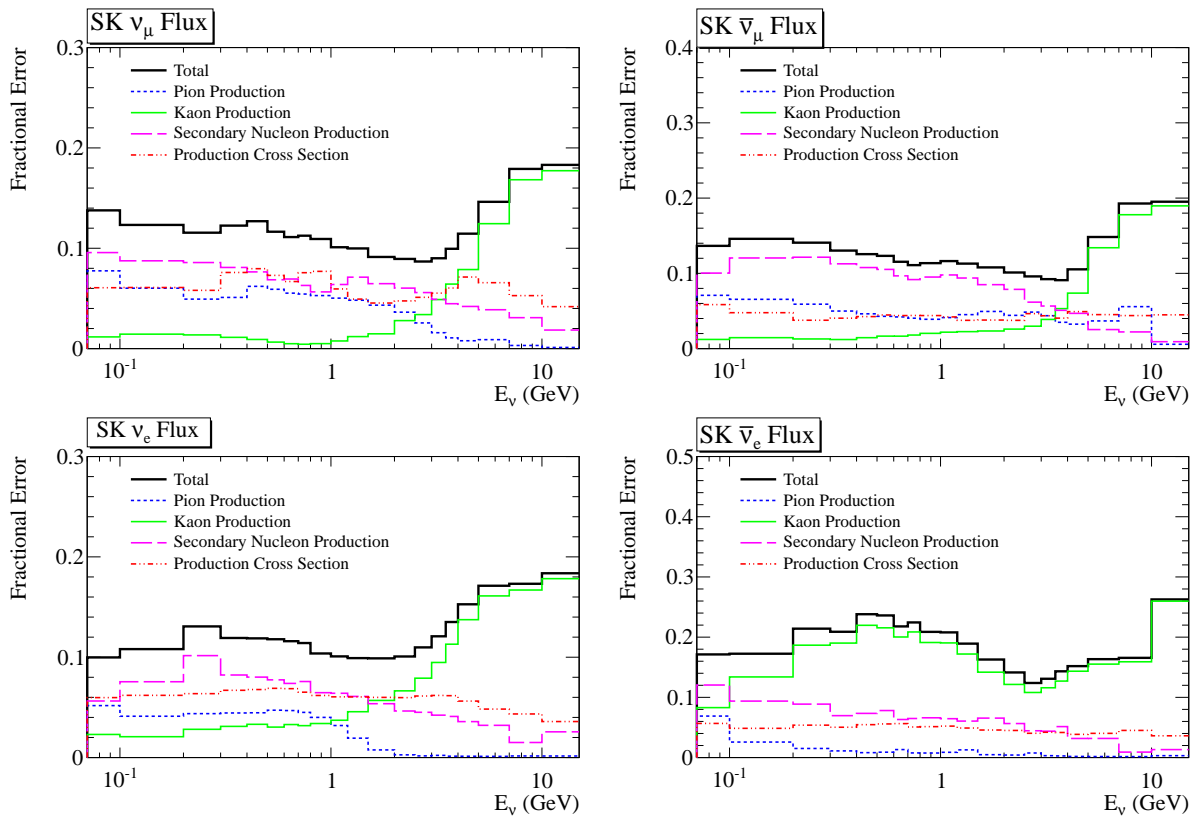


Figure 4.17: Fractional SK flux uncertainties from hadron production uncertainties.

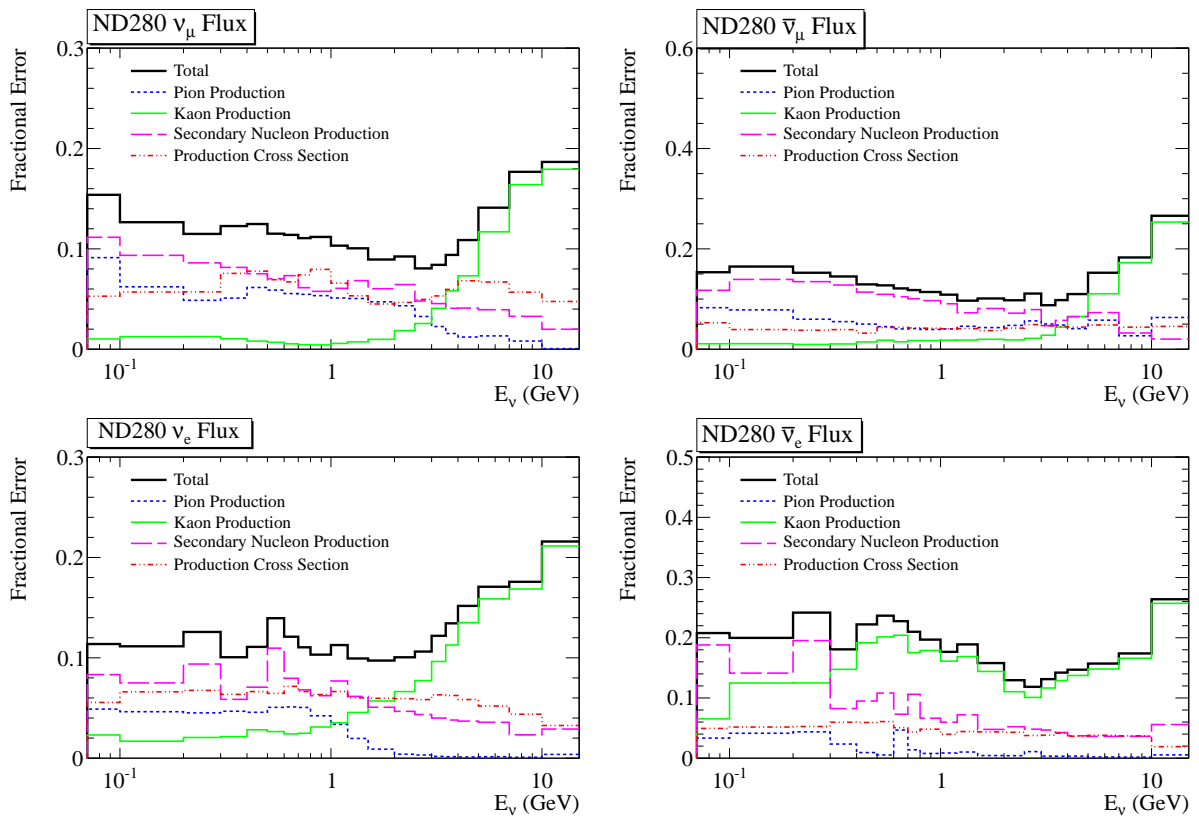


Figure 4.18: Fractional ND280 flux uncertainties from hadron production uncertainties.

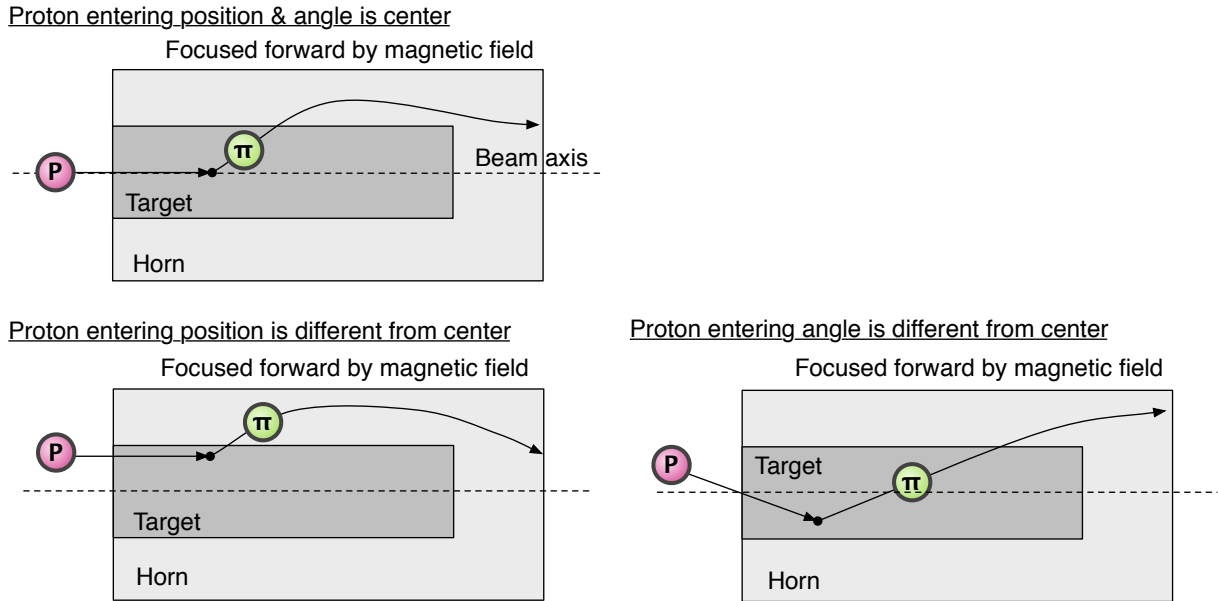


Figure 4.19: Overview of the generated pion tracking for nominal case (top right), different position (bottom right) and angle (bottom left) of inject proton beam.

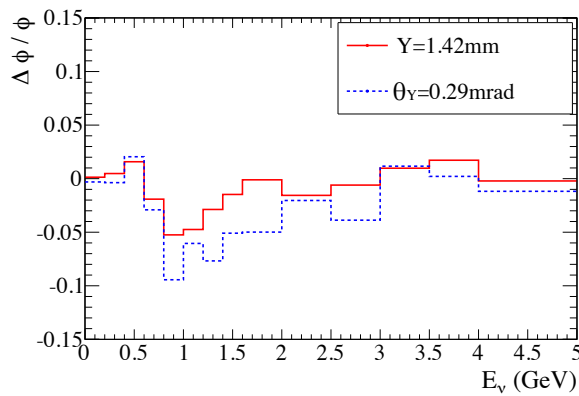
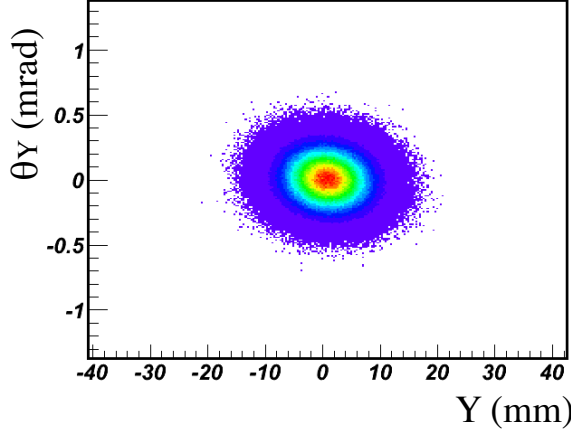


Figure 4.20: The fractional change of SK ν_μ flux when the beam center position (Y) and center angle (θ_Y) are changed by 1σ (σ means the error size) from the measured values in Run 1, i.e. set to 1.42 mm and 0.29 mrad, respectively.

beam profile for the neutrino flux simulation.

Actual beam profile



Wide beam profile

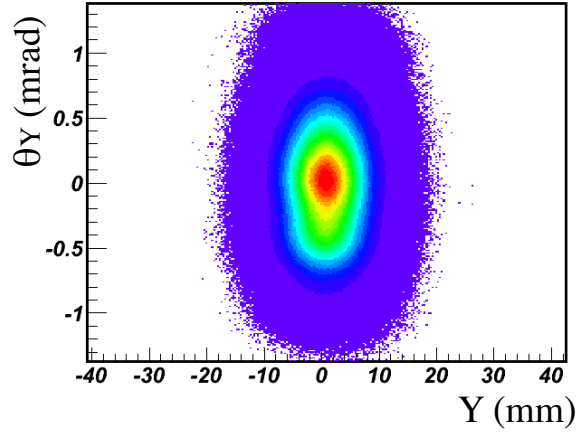


Figure 4.21: Beam profile in the position-angle phase space: left plot shows actual beam profile for the neutrino flux simulation (at Run1 case), right plot shows wide beam used to simulate the sample for re-weighting

For the re-weighting based on (Y, Θ_Y) sets, the re-weighting factor is the ratio of the probability density function (PDF) on the phase space:

$$PDF(y, \theta_y; Y, \Theta_Y, \sigma_Y, \sigma_{\Theta_Y}, \rho) = \frac{1}{2\pi\sigma_Y\sigma_{\Theta_Y}\sqrt{1-\rho^2}} \times \exp\left(-\frac{1}{2(1-\rho^2)}\left[\frac{\Delta_y^2}{\sigma_y^2} + \frac{\Delta_{\theta_y}^2}{\sigma_{\theta_y}^2} - \frac{2\rho\Delta_y\Delta_{\theta_y}}{\sigma_y\sigma_{\theta_y}}\right]\right) \quad (4.15)$$

where:

- $\Delta_y = y - Y$: y is the proton beam position of each event
- $\Delta_{\theta_y} = \theta_y - \Theta_Y$: θ_y is the proton beam angle of each event
- σ_Y and σ_{Θ_Y} are the width of the beam position and angle with the correlation ρ in the phase space

(Y^i, Θ_Y^i) is i th set of many (Y, Θ_Y) sets. The re-weighting factor for the j th event of the flux sample based on (Y^i, Θ_Y^i) is calculated from the following equation:

$$w^{(j)}_{(Y^i, \Theta_Y^i)} = \frac{PDF(y^j, \theta_y^j; Y^i, \Theta_Y^i, \sigma_Y^{data}, \sigma_{\Theta_Y}^{data}, \rho^{data})}{PDF(y^j, \theta_y^j; Y^{wide}, \Theta_Y^{wide}, \sigma_Y^{wide}, \sigma_{\Theta_Y}^{wide}, \rho^{wide})} \quad (4.16)$$

where:

- y^j, θ_y^j : the proton beam position and angle of j th event.
- $(variable)^{data}$: average measured variable in each run period.
- $(variable)^{wide}$: variable of the special flux sample with a large position-angle phase space.

The re-weighted flux samples are calculated from the factor in 4.16 for all (Y, Θ_Y) sets and then the covariance matrix is calculated from Eq. 4.12. The fractional ν_μ flux uncertainties for ND280 and SK is shown in Fig. 4.22 based on Run1 proton beam errors. The flux covariance matrixes are estimated for each run period separately. Also, the combined covariance matrix is calculated as a sum of all covariance matrixes weighted according to the corresponding POT (called POT-weighted). The combined covariance matrix is used in the oscillation analysis.

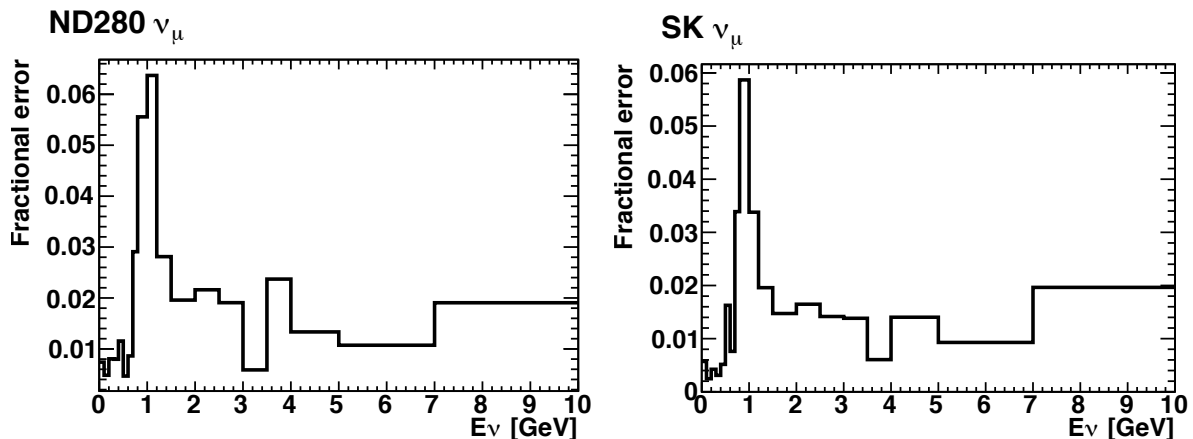


Figure 4.22: Fractional ND280/SK ν_μ flux uncertainties from proton beam errors for Run1 measurements

In addition to the measured proton beam uncertainties, the absolute flux normalization uncertainty arises from the uncertainties on the proton beam intensity measured by CT5, i.e. 2% as described in Sec. 2.3.1.

4.4.4 Neutrino beam direction (off-axis angle) uncertainties

The uncertainties on the neutrino beam direction results in the wrong off-axis angle and change the neutrino flux. Following sources are considered in the beam direction uncertainties:

- The deviation of the neutrino beam direction from the beam axis
- Statistical and systematic errors of INGRID measurements
- The alignment errors of INGRID modules
- Survey errors of ND280 and SK (0.0024 mrad both in horizontal (x) and vertical (y) for SK, and 0.026 mrad in x and 0.038 mrad in y for ND280)

The neutrino beam direction measurements at INGRID are described in Sec. 6.1 and the error in each Run period is summarized in Table 6.4. These values are used to estimate the flux uncertainties from the off-axis angle errors. The errors in the x and y direction are converted to the error in the off-axis angle based on the relation the beam axis and SK direction. The converted errors are summarized in Table 4.6. Here, the error size of off-axis angle is described as σ_{OA} .

The effect of the off-axis angle uncertainty on the neutrino flux is estimated by checking at a variation of the neutrino flux when the SK and ND280 detectors are moved by $1\sigma_{OA}$. To save computational time, the nominal flux samples are re-weighted to generate the flux samples for

Table 4.6: Summary of the off-axis angle error (σ_{OA}) in each period

	RUN1	RUN2	RUN3b	RUN3c
σ_{OA} [mrad]	0.465	0.366	0.488	0.428

the shifted SK and ND280 by $\pm 1\sigma_{OA}$. Figure 4.23 shows the variation of the SK and ND280 ν_μ flux for the $\pm 1\sigma$ off-axis angle shift for Run 1 measurement ($\sigma_{OA}=0.465$). The flux covariance matrix is calculated for each run period separately and the combined one is also calculated (similarly to the proton beam uncertainties).

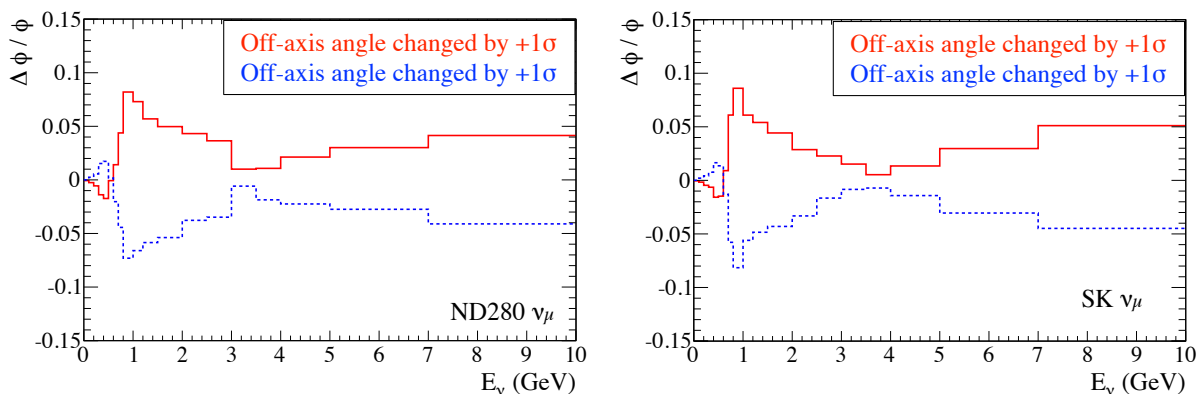


Figure 4.23: Fractional change of the ν_μ flux at ND280 (left) and SK (right) for the $\pm 1\sigma_{OA}$ off-axis angle shift for the Run 1 measurement ($\sigma_{OA}=0.465$).

4.4.5 Target and horn alignment uncertainties

The systematic uncertainties associated with the target and horn alignments, discussed in Section 2.3.5, are summarized in Table 2.2. The effects of the systematic uncertainties in the target and horn alignments on the predicted ν_μ fluxes at ND280 and SK are estimated by shifting and rotating the target at the horn geometry in JNUBEAM according to Table 2.2. For neutrinos with energies below 7 GeV, the fractional uncertainties due to these sources are smaller than 3%. This flux uncertainties are shown in Fig. 4.24.

4.4.6 Horn current uncertainty

As discussed in Sec. 2.3.2, the total uncertainty of the horn current measurement is 1.3% and the measured magnetic field strength is consistent with the expected one within 2%. Therefore, 2% (5 kA) is assigned as the total uncertainty on the absolute field strength. This results in 2% uncertainty at most in the neutrino flux.

An anomalous on-axis magnetic field was found at the magnetic field measurements along the horn's axis inside the inner conductor. This field has a direction perpendicular to the beam axis, and reaches a maximum magnitude of 0.065 T near the center of the horn. The reason of this anomalous on-axis field is not yet known. Therefore, the effect of this field was estimated and accounted for the flux uncertainty. This anomalous field is also simulated by JNUBEAM. The effect on neutrino flux is less than 1% for energies up to 1 GeV, and less than 4% for energies greater than 1 GeV shown in Fig 4.24.

4.4.7 Summary of flux uncertainties

Figure 4.24 shows the flux uncertainties as a function of neutrino energy. For the proton beam and off-axis angle uncertainties, the combined errors are shown in the figures. The main flux uncertainty originates from the hadron interaction uncertainties. Also, a significant contribution to the uncertainty around the flux peak arises from the off-axis angle and proton beam uncertainties. These effects tend to just shift the peak energy position of the flux.

4.4.8 Prospect

The main flux uncertainty originates from the hadron interaction uncertainties. The hadron interaction uncertainty comes from the experimental errors. The NA61/SHINE errors can be improved by using new high statistical data. The contributions from the off-axis angle and proton beam uncertainties are also significant. The current flux uncertainty from the off-axis angle is estimated conservatively and this part will be improved. The prospects to improve flux uncertainties are summarized as follows:

- Incorporation of the new NA61/SHINE data.

The results of the next set of data from NA61/SHINE will reduce the overall uncertainty on the neutrino flux prediction. Higher statistics thin target data have been collected with an upgraded detector configuration that increases the small angle acceptance. These data will reduce uncertainties on the primary interaction.

The ultimate precision on the flux prediction will be achieved through the measurements of hadron emission from the same (replica) target as the one used by T2K. With precise replica target measurements, it will be possible to reduce the uncertainties related to the hadron production via re-interactions inside the target.

- Prospect of flux uncertainties from the off-axis angle errors.

The INGRID detector systematic error is dominant in the off-axis angle error. In the INGRID detector systematic error, errors associated with tracking are dominant (described in Table 6.2). A new INGRID analysis method has been developed and reduces the off-axis angle error. By using the new INGRID analysis method (in Sec. 6.1.4), the off-axis angle error is reduced by $\sim 40\%$ and the associated flux uncertainty is expected to be reduced by $\sim 40\%$ and becomes approximately same as that due to the proton beam uncertainties. In this thesis, however, the new INGRID analysis is not used because its systematic errors are not yet finalized.

The measured deviation of the neutrino beam center from the beam axis is not used in the flux prediction, but considered as one of flux error sources. The flux is always predicted based on the ideal off-axis angle. However, the measured deviation can be reflected into the flux prediction to reduce the flux uncertainty.

The current off-axis angle errors includes the effect of the proton beam errors. If the off-axis angle error can be estimated independently from the proton beam errors, it is expected to reduce the flux uncertainties from off-axis angle errors.

4.5 Extrapolation of the ND280 flux measurements to SK

In the oscillation analysis, the SK flux prediction is refined more precisely based on the ND280 measurements (called extrapolation). The extrapolation is based on the correlation between fluxes at ND280 and SK. The ratio of the predicted flux at SK and ND280 is one method to extrapolate the flux measurement at ND280 to the flux prediction at SK; the SK flux can be

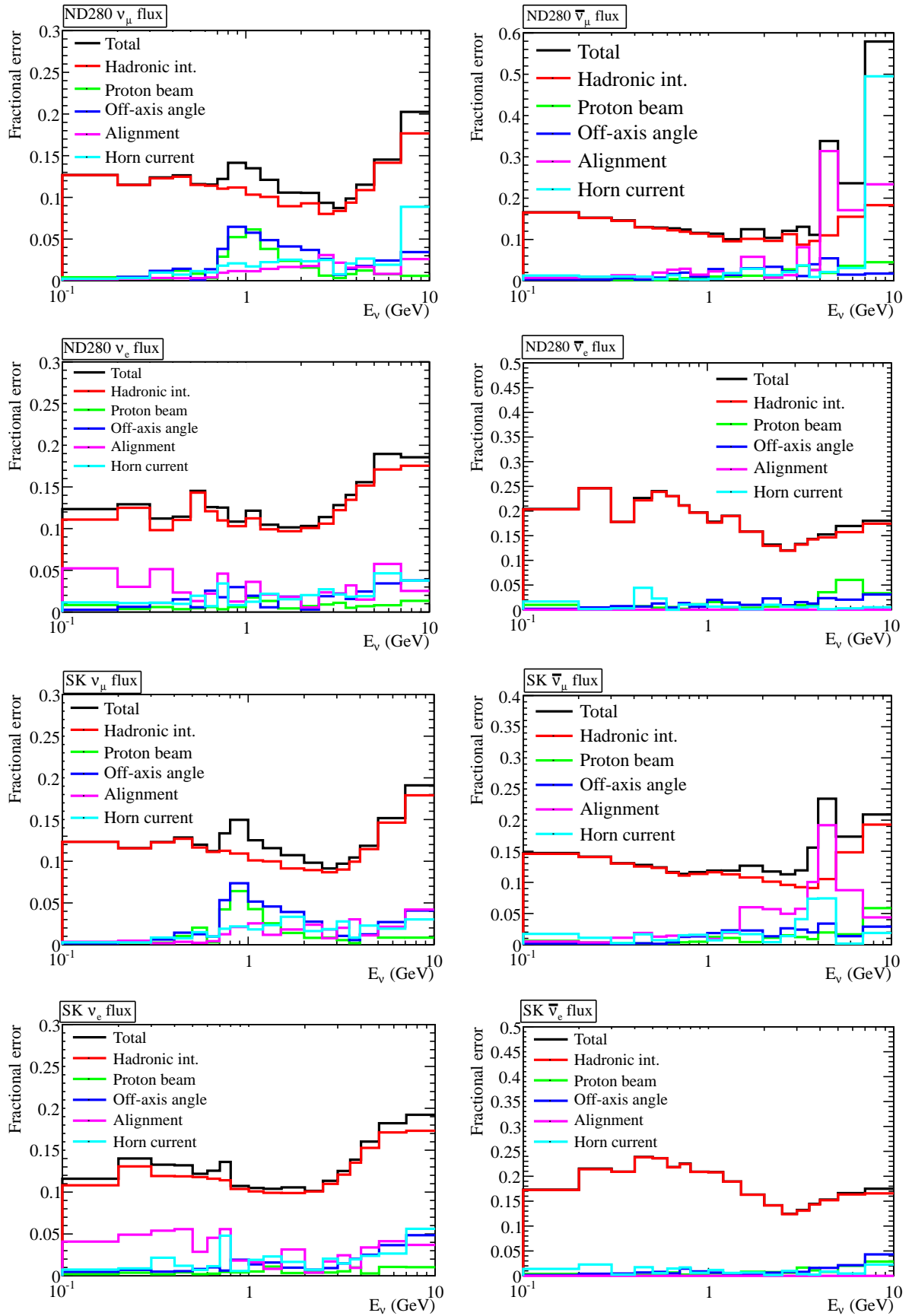


Figure 4.24: Fractional flux uncertainties for all sources of uncertainties.

estimated by multiplying the measured flux at ND280 by the flux ratio (Φ_{SK}/Φ_{ND280}). This is called the far/near ratio method. The benefit of this method is to cancel the flux uncertainties correlated between ND280 and SK. The uncertainty on the far/near is a measure of how the uncertainty is reduced when the flux is extrapolated from ND280 measurements. As shown in Fig. 4.25, the uncertainty on the far/near ratio for the ν_μ flux prediction is less than 2% near the flux peak and less than 6% for all energies. The non-uniform shape of the far/near ratio is due to the fact that ND280 sees a line-like source of neutrinos and hence a range of off-axis angles, while SK see a point-like source. In the K2K experiment, the far/near ratio method was used to extrapolate the ν_μ flux measured at the near detector to the ν_μ flux prediction at SK. In T2K, as mentioned in Sec. 4.4, the flux covariance matrix is used to extrapolate among different flavors (for example, ν_μ at ND280 to ν_e at SK). This method is called the covariance matrix method.

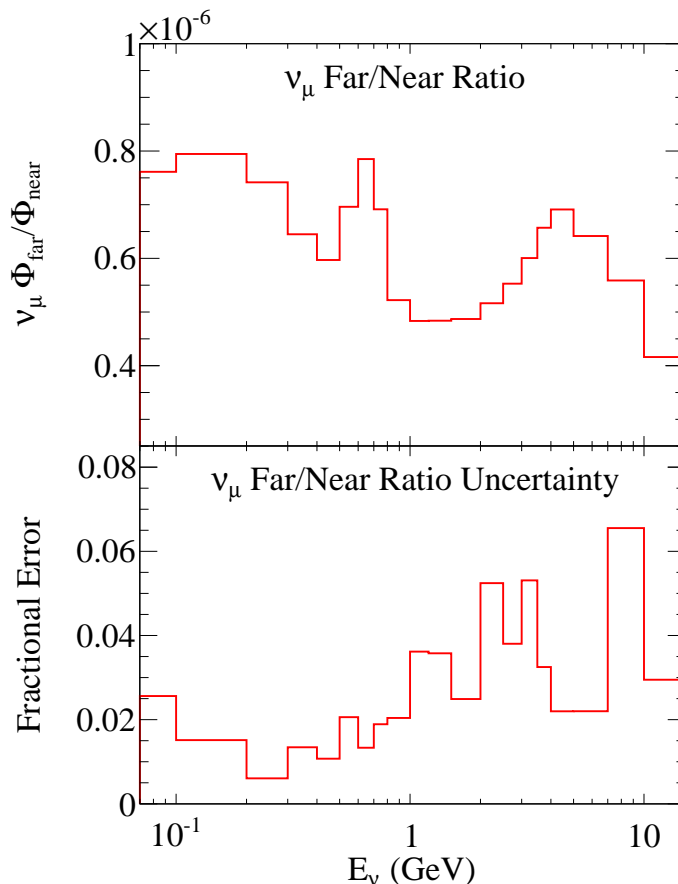


Figure 4.25: The far/near ratio for the ν_μ flux prediction (top) and the uncertainty on the ratio (bottom).

4.5.1 Covariance matrix method

The flux covariance matrix contains the flux uncertainties and the correlation between fluxes at SK and ND280. By using this correlation, the uncertainties of the SK and ND280 flux are constrained simultaneously by the ND280 measurements. In particular, the joint probability distribution function (PDF) for fluxes at SK and NT280 is constructed from the flux covariance matrix. Suppose that the ϕ_{ND280} (ϕ_{SK}) represents the ND280 (SK) flux normalizations according to flavors and neutrino energy bins. The joint PDF is defined as a multivariate normal

distribution including the ND280 and SK flux normalizations $(\phi_{ND280}, \phi_{SK})$ as:

$$PDF(\phi_{ND280}, \phi_{SK}) = \frac{1}{\sqrt{(2\pi)^n |V_\phi|}} \exp\left(-\frac{1}{2} \Delta\phi^T V^{-1} \Delta\phi\right), \quad (4.17)$$

where $\Delta\phi = \phi - \phi_{nom}$, $\phi^T = (\phi_{ND280}, \phi_{SK})^T$, the ϕ_{nom} is the nominal flux normalization, n is the number of normalization parameters in ϕ , and V is the flux covariance matrix. As an example, think about the two parameters case; the overall normalizations for the SK and ND280 fluxes are considered ($\phi^T = (\Phi_{ND280}, \Phi_{SK}$, two dimension). The covariance matrix and the PDF in this case are:

$$V = \begin{pmatrix} \sigma_{\Phi_{ND280}}^2 & \rho\sigma_{ND280}\sigma_{SK} \\ \rho\sigma_{ND280}\sigma_{SK} & \sigma_{SK}^2 \end{pmatrix} \quad (4.18)$$

$$PDF(\Phi_{ND280}, \Phi_{SK}) = \frac{1}{2\pi\sigma_{ND280}\sigma_{SK}\sqrt{1-\rho^2}} \times \exp\left[-\frac{1}{2(1-\rho^2)} \left(\frac{\Delta\Phi_{ND280}^2}{\sigma_{ND280}^2} + \frac{\Delta\Phi_{SK}^2}{\sigma_{SK}^2} - \frac{2\rho\Delta\Phi_{ND280}\Delta\Phi_{SK}}{\sigma_{ND280}\sigma_{SK}} \right)\right] \quad (4.19)$$

where σ_{ND280} (σ_{SK}) are the uncertainties of Φ_{ND280} (Φ_{SK}) estimated with the flux simulation. The ρ represents the correlation coefficient between Φ_{ND280} and Φ_{SK} . Figure 4.26 shows the scheme of the flux extrapolation with the covariance matrix. The allowed regions for Φ_{ND280} and Φ_{SK} are derived from Eq 4.18 as shown in Fig. 4.26. The allowed region for Φ_{ND280} is constrained by the ND280 measurement (as shown in the right plot of Fig. 4.26). The constrained allowed region for Φ_{ND280} is extrapolated to that for Φ_{SK} through ρ , resulting in the reduction of σ_{SK} (to σ'_{SK} in Fig. 4.26).

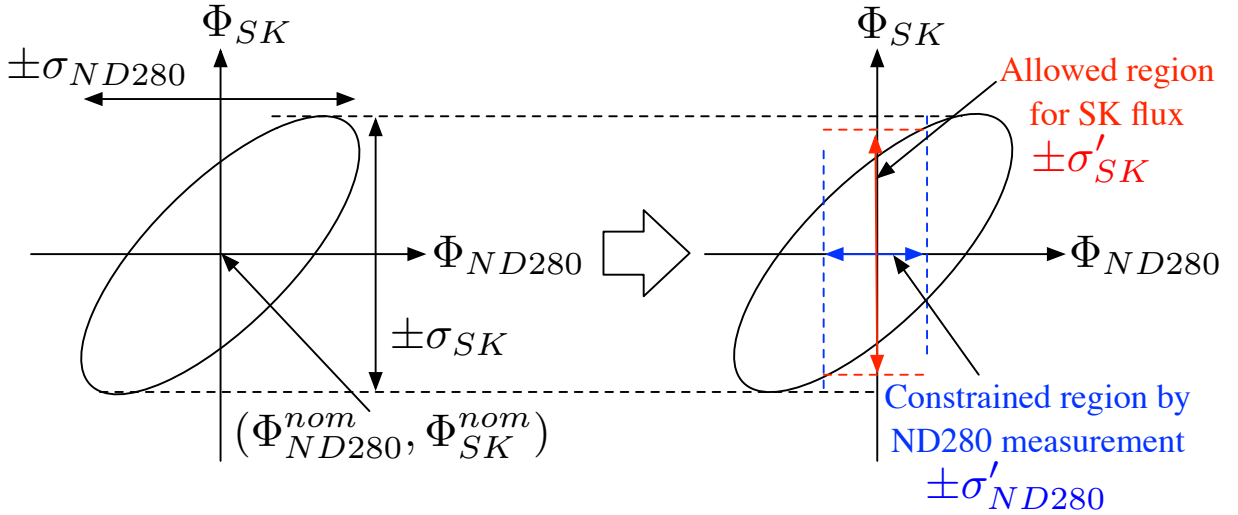


Figure 4.26: Conceptual scheme of the flux extrapolation. These two ellipses represent the PDF contours for flux normalizations at ND280 and SK $(\Phi_{ND280}, \Phi_{SK})$ represented by Eq. 4.18. The left plot shows the uncertainty of Φ_{ND280} and Φ_{SK} before constrained by the ND280 measurements. The center of the ellipses are the nominal flux normalization for ND280 and SK. The right plot shows the uncertainty of Φ_{ND280} and Φ_{SK} constrained by the ND280 measurements. The blue region represents the constrained region for Φ_{ND280} and the red one represents the region for Φ_{SK} (σ'_{SK}) after the ND280 constraint. The σ'_{SK} is smaller than σ_{SK} .

The total covariance matrix is calculated as a sum of covariance matrixes of all error sources (shown in Fig 4.27). Figure 4.28 shows zoom up of the part of the matrix corresponding to the

covariance between the ND280 ν_μ and SK ν_μ fluxes, or the ND280 ν_μ and SK ν_e fluxes. The neutrino energy binning for each flavor and detector is defined as follows:

Bin Edge (GeV) 0.0, 0.1, 0.2, 0.3, 0.4, 0.5, 0.6, 0.7, 0.8, 1.0, 1.2, 1.5, 2.0, 2.5, 3.0, 3.5, 4.0, 5.0, 7.0, 10.0.

To show the correlation, the correlation matrix is calculated from the covariance matrix and is shown in Fig 4.29. Figure 4.28 shows zoom up of the part of the matrix corresponding to the correlation between the ND280 ν_μ and SK ν_μ fluxes, or the ND280 ν_μ and SK ν_e fluxes. One can see that there are strong correlation between ν_μ fluxes at ND280 and SK. There are also significant correlation between the ND280 ν_μ flux and SK ν_e flux. The reason of this correlation between different flavors is that some portion of ν_e flux originates from the decay of muons which are produced from the pions decay (for example of π^+ decay: $\pi^+ \rightarrow \mu^+ \nu_\mu$, $\mu^+ \rightarrow e^+ \bar{\nu}_\mu \nu_e$). Thus, the ND280 measurements can refine both the SK ν_μ and ν_e fluxes.

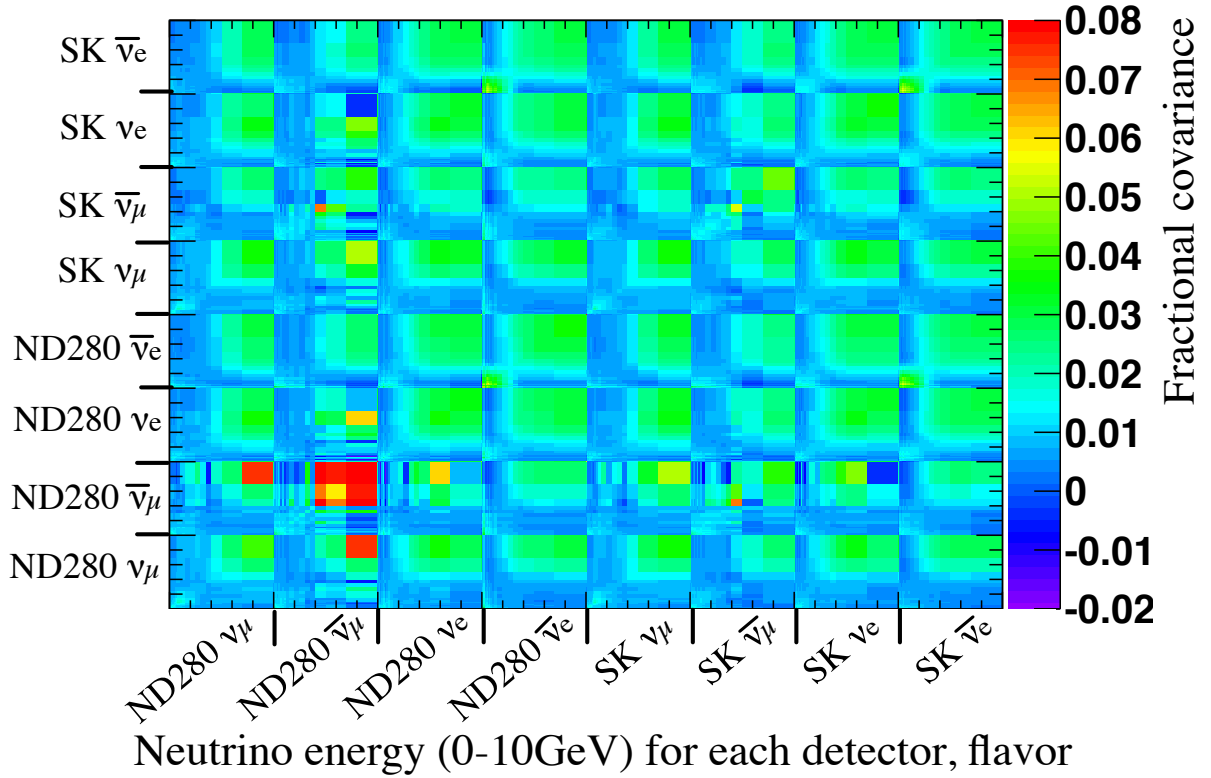


Figure 4.27: Fractional covariance matrix of the neutrino flux for each flavor, energy and detector.

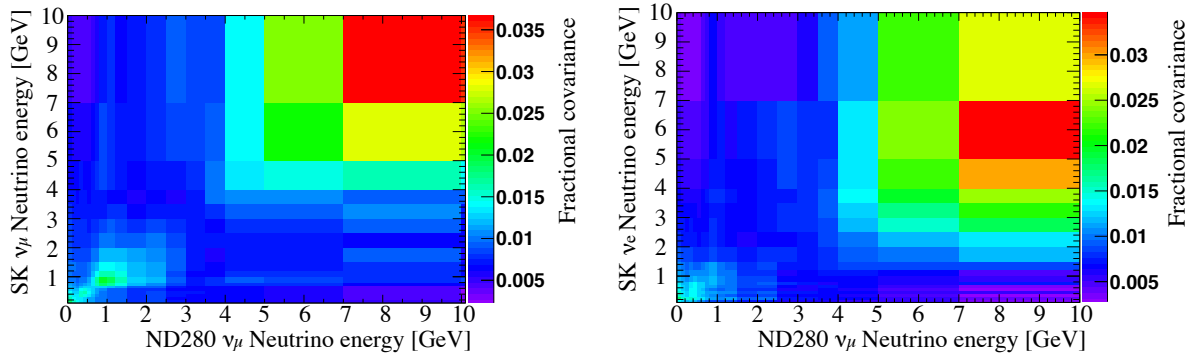


Figure 4.28: Fractional covariance matrix of the neutrino flux for ND280 ν_μ v.s. SK ν_μ (left) or SK ν_e (right)

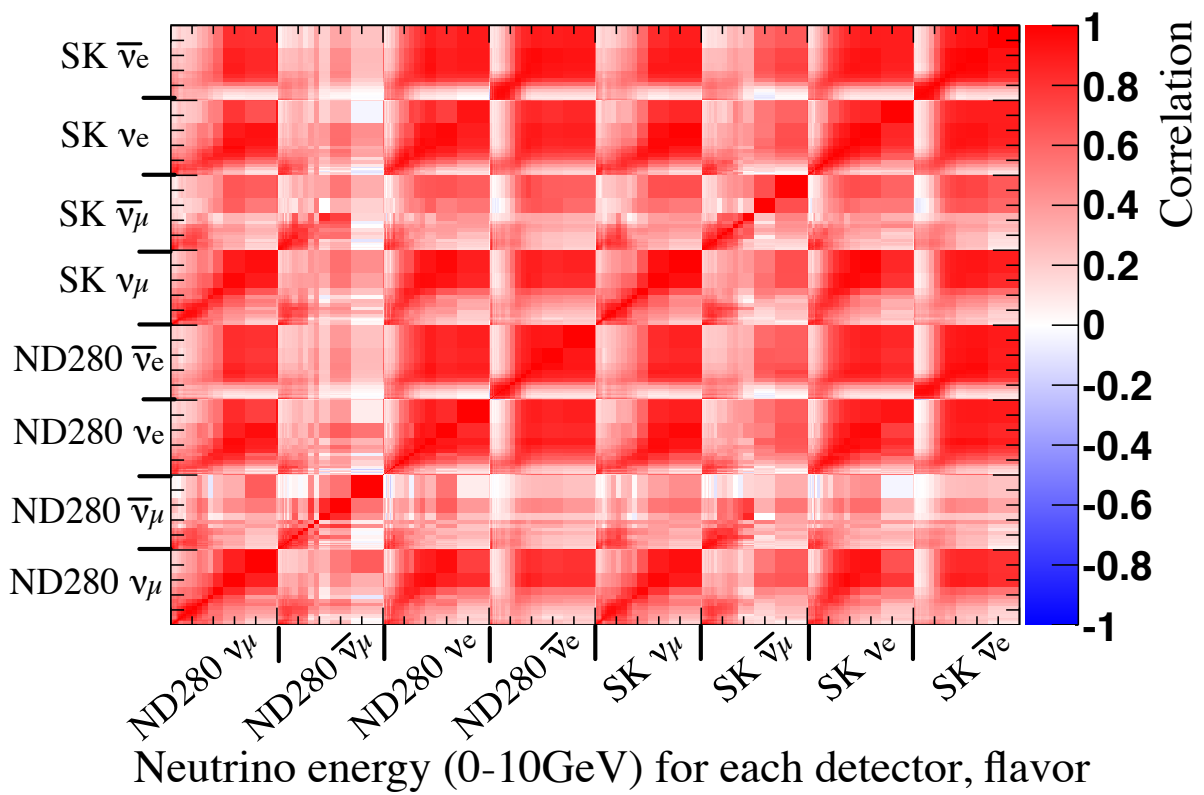


Figure 4.29: Correlations of the neutrino flux for each flavor, energy and detector.

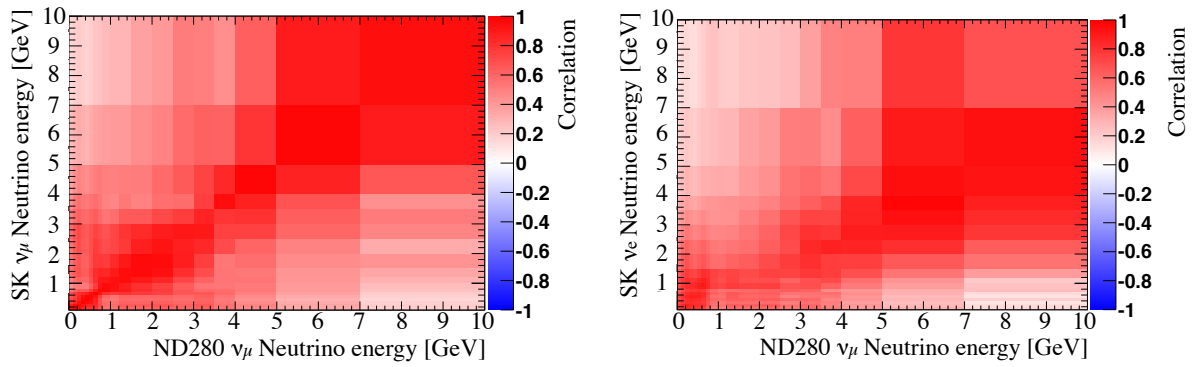


Figure 4.30: Correlation of the neutrino flux for ND280 ν_μ v.s. SK ν_μ or SK ν_e

Chapter 5

Neutrino-nucleus interaction model

The cross-sections of the neutrino-nucleus interactions are used to predict the event rate and energy spectrum of the SK ν_μ candidates for the oscillation analysis. The cross-sections are predicted with the interaction physics models. The uncertainties on the cross-sections are estimated from the uncertainties on the parameters describing the interaction physics models.

5.1 Overview of the neutrino-nucleus interaction model

The neutrino-nucleus interactions are predicted with interaction physics models. The properties of outgoing particles from the interaction are predicted by the interaction simulation. Based on the flux prediction and interaction model, a neutrino-nucleus interaction generator NEUT [51] generates simulated interactions. Nuclear targets handled in NEUT are hydrogen, oxygen, carbon, and iron, covering all materials of T2K neutrino detectors. The energy of neutrinos handled in NEUT covers the energy region interested of T2K. The following neutrino interaction modes in both the charged current (CC) ($\nu_l + N \rightarrow l + X$) and neutral current (NC) ($\nu_l + N \rightarrow \nu_l + X$) are considered in NEUT:

- Quasi-elastic scattering (QE): $\nu_l + N \rightarrow l(\nu_l) + N'$
- Resonant single (π, γ, K, η) production: $\nu_l + N \rightarrow l(\nu_l) + N' + (\pi, \gamma, K, \eta)$
- Coherent π production: $\nu_l + {}^{16}\text{O} \rightarrow l(\nu_l) + X + \pi$
- Deep inelastic scattering (DIS): $\nu_l + N \rightarrow l(\nu_l) + N' + \text{hadrons}$

where N and N' represent nucleons and l represents a charged lepton. The neutrino-nucleus cross-sections predicted with the interaction models are shown in Fig. 5.1. Among these interactions, the CCQE interaction is dominant at the energy around the oscillation maximum.

For convenience, the interaction modes in NEUT are classified into the following categories in oscillation analysis:

”**CCQE**” Charge current quasi-elastic scattering

”**CC1 π** ” Single π production from resonance

”**CCCoh**” Charge current coherent π production

”**CCOth**” Other charge current interaction mode

”**NC1 π C**” Single charged π production from resonance

”**NCOth**” Other neutral current interaction mode

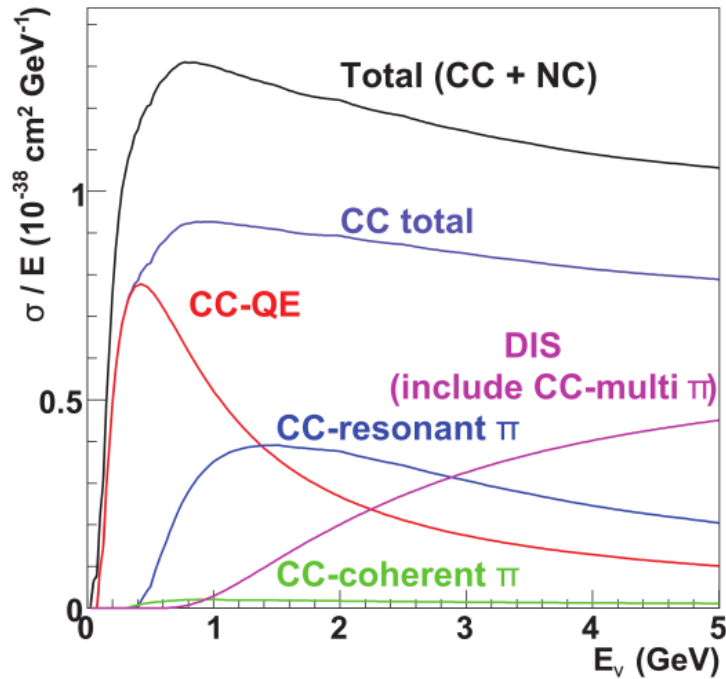


Figure 5.1: Neutrino-nucleus cross-sections per nucleon as a function of neutrino energy in NEUT

Quasi-elastic scattering (QE)

The CCQE interaction is implemented with the Smith and Moniz model [77]. In this model, the nucleons are treated as quasi-free particles. The relativistic Fermi gas formalism is used to describe the nuclear potential.

Resonant single (π, γ, K, η) production

The resonant single π , K , and η production is described by the Rein-Sehgal's (RS) model [78,79]. The RS model assumes an intermediate baryon resonance, N^* , in the reaction of $\nu N \rightarrow lN^*$, and their decay: $N^* \rightarrow N'm$ (m represents meson). All intermediate baryon resonances with invariant mass less than $2 \text{ GeV}/c^2$ are considered. Baryon resonances with invariant mass greater than $2 \text{ GeV}/c^2$ are simulated as deep inelastic scattering (described later). The RS model does not simulate the multi-pion production. The multi-pion production is also simulated as the deep inelastic scatterings.

Coherent π production

The coherent π production is implemented with the model developed by Rein and Sehgal [80,81]. This model is based on Adler's PCAC theorem [82,83]

Deep inelastic scattering (DIS)

The deep inelastic scattering (DIS) is treated as the neutrino-quark scattering. The nucleon structure functions is based on the GRV98 parton distribution functions [84]. Additionally, the corrections in the small Q^2 region developed by Bodek and Yang [85] are taken into account.

The "W" represents the invariant mass of hadronic system (pion+nucleon, photon+nucleon). The DIS is considered for $W > 1.3 \text{ GeV}/c^2$. The pion multiplicity is additionally restricted to be greater than one (multi-pion production) for $W < 2 \text{ GeV}/c^2$ to avoid double-counting the

contribution of the single pion production. The multi-hadron final states are simulated with two models according to the invariant masses: a custom-made program [86] for $1.3 \text{ GeV}/c^2 < W < 2 \text{ GeV}/c^2$, PYTHIA/JETSET [87] for $W > 2 \text{ GeV}/c^2$.

Final state interaction (FSI)

In addition to neutrino interactions described above, the generated meson, mainly pions, can interact with the nucleus inside the nucleus before they escape. This re-interaction process is called as the final state interaction (FSI). The pion FSI process is important for the SK event selection. In the SK event selection, the CCQE-like events are selected and the neutrino energy in each event is reconstructed assuming the CCQE interaction (Eq. 6.1). If the charged pion generated at the CC resonant neutrino interaction cannot escape from the nucleus, this event is mis-identified as a CCQE-like event where only single muon is observed. The neutrino energy is mis-reconstructed to the lower energy than true one.

In the FSI processes, the quasi-elastic (QE) scattering, charge exchange, and absorption of pions in nuclei are mainly considered at the energy region of interest of T2K. For the QE scattering and charge exchange interactions, the direction and momentum of pions are affected. In the scattering amplitude, the Pauli blocking is also taken into account.

5.2 Model uncertainties

There are considerable uncertainties on the following parameters describing the neutrino-nucleus interaction models:

- Model parameters in the group-A:
 - Axial mass: M_A^{QE}, M_A^{RES}
 - Fermi Gas model parameters: E_b, p_F
 - Spectral function parameter
 - CC other shape parameter
 - W shape parameter
 - Pion-less Δ decay parameter
- Model parameters in the group-B:
 - Absolute cross-section normalization
 - Cross-section difference among flavors
- Model parameters in the group-C: Final state interaction (FSI) and Secondary interaction at (SI) parameters

The model parameters in the group-A change the absolute normalization and energy dependence of the interaction cross-section simultaneously. The absolute cross-section normalization parameters are additional weights to change the normalization of each interaction category from the nominal prediction. In addition, the cross-section normalization differences among flavors are also considered. The FSI and SI parameters represent the rate of re-interaction processes inside nucleus (SI is explained later). The uncertainties of the interaction parameters affect the rate and energy spectra of the ND280 and SK neutrino events.

Axial mass: M_A^{QE}, M_A^{RES}

M_A^{QE} is the axial mass in the CCQE cross-section calculation, which appears in the axial vector form factor. M_A^{RES} is the axial mass in the CC and NC single resonance meson production. The axial appears in a dipole form, i.e., $\sim \frac{1}{(1+Q^2/M_A^2)}$ and has a non-linear response to the interaction cross-section.

Fermi Gas (FG) Parameters: p_F, E_B

In the CCQE interaction mode, the nuclear potential is characterized by two parameters: Fermi momentum of the nucleus, p_F and the nuclear potential (binding energy), E_B . The center value and uncertainties on p_F and E_B are determined from the electron scattering data [88].

Spectral function parameter

A more sophisticated and realistic model of the nuclear potential than Fermi Gas (FG) is built based on electron scattering data [88]. This model is called by the spectral function (SF) [89] model. The FG formalism nucleons are assumed to have a uniform distribution of nucleon inside the Fermi sphere and a constant value of the binding energy. The SF model defines the probability distribution of nucleon momenta and removal energies within the nucleus.

Since NEUT does not adopt SF models, another neutrino interaction simulation (NuWro [90]) is used to evaluate the effect of SF. The SF parameter describes the difference between the SF and default FG models.

CC other shape parameter

The CC other shape parameter provides an additional freedom to change the energy dependency of the cross-section normalization of CCOth. From external data [91], the uncertainty on the cross-section normalization of CCOth is estimated to be $O(10\%)$ at 4 GeV. Using this as a reference point, the normalization of CCOth events is multiplied by the following weight: $1 + x/E_\nu(\text{GeV})$, where x is CC other shape parameter and E_ν is the neutrino energy (>0.6 GeV).

W shape parameter

The "W shape" parameter is introduced to vary the shape of the pion momentum distributions in resonance interactions, which shows poor agreement with data. In practice, the approach of this parameter is to re-weight events with a pion or photon and nucleon before FSI (ignoring pion-less Δ decay events which is explained later) by varying the hadronic invariant mass W , since this is an invariant quantity correlated with pion momentum.

Pion-less Δ decay

Pion-less Δ decay is known as Δ re-absorption ($\Delta N \rightarrow NN$) in the nucleus without a decay into a pion. This process is currently implemented in NEUT as energy and target independent, and the Δ simply does not decay into any products, resulting in a CCQE-like event. The pion-less Δ decay happens $\sim 20\%$ of the time [92]. The parameter of the pion-less Δ decay changes the event probability of this phenomena.

However, the same authors [92] tested their FSI model against π photo-production without the effect of the pion-less Δ decay and see good agreement with the data. This suggests that it may be redundant to consider both effects of pion-less and FSI in NEUT.

Absolute cross-section normalization

For the CCQE (CC1 π) interaction categories, the absolute cross-section normalizations are defined as the following neutrino energy E_ν regions: : $E_\nu < 1.5$ GeV, $E_\nu = 1.5 \sim 3.5$ GeV and $E_\nu > 3.5$ GeV ($E_\nu < 2.5$ GeV, $E_\nu > 2.5$ GeV). The cross-section normalization of other categories are defined as an overall one.

The cross-section differences are considered between ν_e - ν_μ ($\sigma_{\nu_e}/\sigma_{\nu_\mu}$), or $\bar{\nu}$ - ν ($\sigma_{\bar{\nu}}/\sigma_{\nu_\mu}$). The cross-section differences are defined as an overall difference.

Summary of neutrino interaction parameter values

Table 5.1 summarizes the central values and uncertainties of neutrino interaction parameters. These values and uncertainties were evaluated based on the results of external neutrino experiments. The parameters p_F , E_B and spectral function depend on the target nuclei, hence, the values for ND280 (^{12}C) and SK (^{16}O) are listed up separately.

Table 5.1: Summary of nominal values and errors of neutrino interaction parameters. The nominal values and errors are constrained by external data. E_ν represents the neutrino energy (GeV).

Parameter	Group	Nominal value	Error
M_A^{QE}	A	1.21 GeV/c ²	0.45 GeV/c ²
M_A^{RES}	A	1.41 GeV/c ^{2*}	0.22 GeV/c ²
p_F (^{12}C)	A	217 MeV/c	30 MeV/c
E_B (^{12}C)	A	25 MeV/c	9 MeV/c
p_F (^{16}O)	A	225 MeV/c	30 MeV/c
E_B (^{16}O)	A	27 MeV/c	9 MeV/c
Spectral function ($^{12}\text{C}\&^{16}\text{O}$)	A	0 (OFF)	1 (ON)
CC other shape	A	0	0.4
W shape	A	87.7 MeV/c ²	45.3 MeV/c ²
Pion-less delta decay	A	0.2	0.2
CCQE norm. $E_\nu < 1.5$	B	1	0.11
CCQE norm. $E_\nu = 1.5 \sim 3.5$	B	1	0.3
CCQE norm. $E_\nu > 3.5$	B	1	0.3
CC1 π norm. $E_\nu < 2.5$	B	1.15*	0.32
CC1 π norm. $E_\nu > 2.5$	B	1	0.40
CCCoh norm.	B	1	1
NC1 π C norm.	B	1	0.3
NCOth norm.	B	1	0.3
$\sigma_{\nu_e}/\sigma_{\nu_\mu}$	B	1	0.06
$\sigma_{\bar{\nu}_\mu}/\sigma_{\nu_\mu}$	B	1	0.4

FSI uncertainties

The rates of the FSI processes are constrained by the external pion-nuclei scattering data. These rates are simultaneously varied within their uncertainties with correlation among them. The

*The default value of M_A^{RES} and CC1 π norm. ($E_\nu < 2.5$) in NEUT is 1.21 GeV and 1.0, but these values shown Table 5.1 are tuned by the MiniBooNE measurements [93]

contribution of the FSI uncertainties for the ND280 and SK measurements are evaluated as the changes of the observables in MC by varying the FSI probabilities. In practice, since the MC samples have the information of final state interactions inside a nucleus, they are re-weighted according to sets of varied FSI parameters, and then the covariance matrix of the normalization parameters for reconstructed energies can be built. The correlation of FSI uncertainties between ND280 and SK measurements are not considered because the difference of nucleus targets causes the difference effect.

SI uncertainties

The outgoing pion from a nucleus may interact with the other nucleus in the water of SK. This hadronic interaction is called the secondary interaction, SI and is handled in the SK detector simulation. The NEUT FSI model can be used in the SI model of the SK detector simulation. The contributions of the SI uncertainties are estimated similarly to the FSI uncertainties. The SI contributions are combined with the FSI uncertainties as the common uncertainties (FSI-SI uncertainties).

5.3 Effect of the neutrino interaction parameters

The effect of neutrino interaction parameters are different for the prediction of the interaction cross-section according to their groups. Here, the effects of the model parameters in the group-A are described. These effect are estimated with response functions. The response function provide a weighting factor for each simulated event and is defined according to the neutrino energy and reconstructed energy. A following weight to the i th event in simulation samples is calculated under a change of a parameter ($x \rightarrow x'$, x represents a model parameter in the group-A):

$$w_{x'}(i) = \frac{\sigma_{x'}(i)}{\sigma_x(i)}. \quad (5.1)$$

This ratio depends on a neutrino flavor, interaction category, neutrino energy and reconstructed energy. The following response factor R in a given event type (a given flavor (f), interaction mode (m), neutrino energy (t) and reconstructed energy (r)) is calculated:

$$R_{x'}(f, m, t, r) = \frac{\sum_i w_{x'}(i)}{T_x(f, m, t, r)}, \quad (5.2)$$

where $w_{x'}(i)$ is the weight in Eq. 5.1 for the i th simulated event in a given event type and $T_x(f, m, t, r)$ is the sum of events in the un-weighted simulation samples. The response functions are estimated for all model parameters in the group-A shown in Fig 5.1.

Figure 5.2 shows the response function of M_A^{QE} for one energy bin (neutrino energy is in 0.6~0.7 GeV and reconstructed energy is in 0.65~0.7 GeV). Figures 5.3 shows the fractional change of the reconstructed energy distribution at SK under the change of M_A^{QE} . The number of SK events and energy spectrum change simultaneously under the change of M_A^{QE} . The uncertainties from model parameters in the group-A are estimated with the response functions and considered in the oscillation analysis.

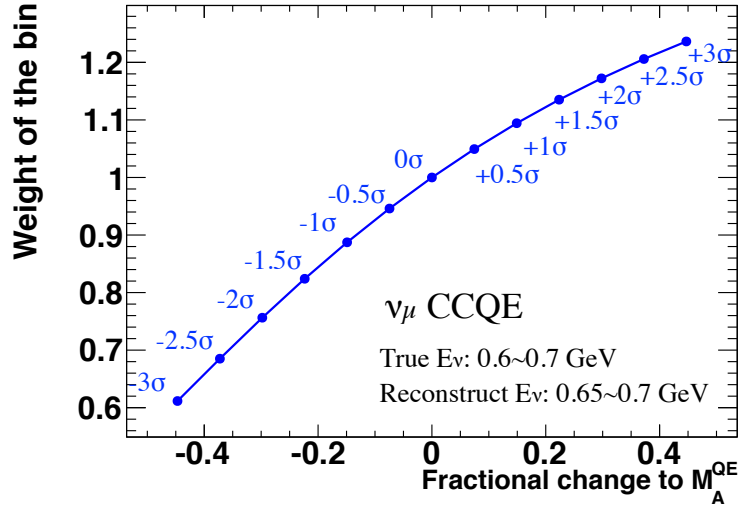


Figure 5.2: The M_A^{QE} response function for one energy bin of ν_μ CCQE event. The " σ " represents a error size of M_A^{QE} .

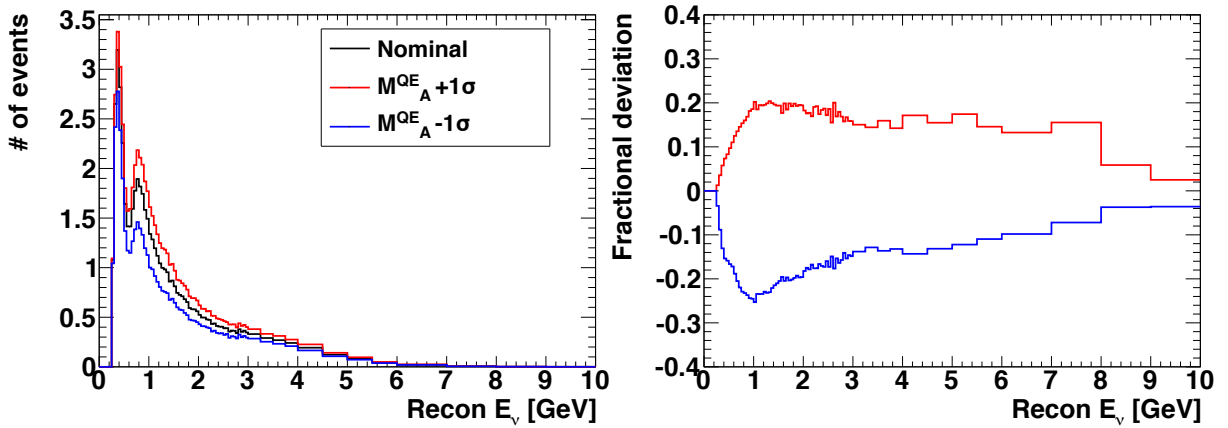


Figure 5.3: The change of the reconstructed energy distribution of SK ν_μ candidate events under the change of M_A^{QE} by $\pm 1\sigma$. The " σ " represents a error size of M_A^{QE} . The oscillation effect is included. Left plot shows the the energy distribution at each case and right plot shows the fractional deviation from the center.

Chapter 6

Measurements at the Near and Far detectors

In T2K, three neutrino detectors are installed: INGRID, ND280, and SK. INGRID measures the neutrino beam direction and event rate. The neutrino beam direction measurement is used to predict the SK flux precisely. The neutrino event rate is kept as much as possible to increase the statistics of neutrino events. ND280 (SK) measures the event rate and energy spectrum of neutrinos in the off-axis direction before (after) oscillation. The ND280 measurements are used to refine the flux prediction and neutrino-nucleus interaction models. The SK measurements are compared with the SK prediction to measure the oscillation parameters.

6.1 Measurements at INGRID

Since the neutrino energy spectrum at SK varies by the change of the off-axis angle, the neutrino beam direction should be controlled and monitored. To monitor the neutrino beam direction, the neutrino beam profile is reconstructed at INGRID. The center of the neutrino beam profile corresponds to the neutrino beam direction. The neutrino event rate at INGRID is used to confirm the stability of the neutrino beam intensity. From the stability of the neutrino event rate and beam direction, the neutrino beam production is confirmed to be stable during all periods. From the stable neutrino production, the measurements at ND280 and SK in all run periods can be combined without additional uncertainties even if the alive period of ND280 is different from one of SK.

6.1.1 Data set for INGRID measurements

INGRID data taking continue from the first of Run 1 to Run 3. The INGRID data taking is summarized in Table 6.1. The good INGRID spills are calculated by applying the INGRID data quality cut to the good beam spills (described at Sec 2.6). The inefficiency of INGRID data taking was $\sim 0.3\%$ during all run periods. There were some missed spills mainly due to the troubles of the INGRID data acquisition system. These INGRID good spills were used in the neutrino events selection.

6.1.2 Event selection

The inclusive charged current (CC) neutrino events inside an INGRID module are selected. Since a single muon is produced at the CC interaction, the inclusive CC events remain by selecting events with a long track of the charged particle (muon-like) starting inside the module. The neutrinos interact inside the wall of the near detector hall. This beam related interaction is

Table 6.1: Summary of data taking of INGRID

Run period	Good spill ratio (INGRID/Beam)	POT
Run 1	0.999	0.325×10^{20}
Run 2	0.996	1.11×10^{20}
Run 3b	0.995	0.219×10^{20}
Run 3c	0.997	1.37×10^{20}
Total	0.997	3.02×10^{20}

called "sand interaction". Especially, the muon generated at the sand interaction is called "sand muon". It is required to reject the incoming particles from outside modules (cosmic-ray or sand muon). A typical neutrino event at INGRID is shown in Fig. 6.1.

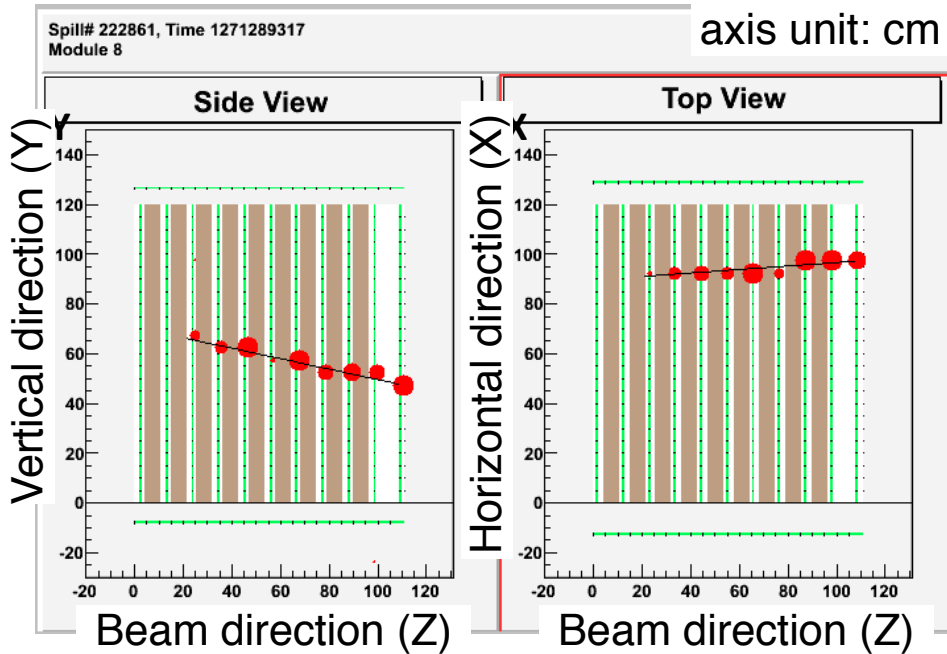


Figure 6.1: A typical neutrino event detected at INGRID. The neutrino entered from the left and interacted in the module, then produced the charged particle. Each of the green cells in this figure is a scintillator and the red circles represent the MPPC hits. The size of the red circles indicates the size of the observed energy deposit. The black line connecting the hits represents the reconstructed track.

The selection criteria are described as follows:

- 1. Coincident hits with light yield selection** This selection is composed of three sub-steps mainly to reject MPPC noise events:
 1. The hit threshold is set to 2.5 photo-electrons (PEs). A hit cluster is defined as four or more MPPC hits clustering within ± 50 nsec. The event with one or more hit clusters is selected to remove the random MPPC noise hits.
 2. An active plane is defined as a tracking plane with one or more hits in both the horizontal and vertical layers. These hits are called coincident hits in both layers.

Events whose number of active planes is three or more are selected.

3. The light yields averaged over horizontal or vertical layers of the active planes are required to be larger than 6.5 PEs for both the horizontal and vertical layers.
2. **2D-Tracking** Tracks are reconstructed in a projected plane of the horizontal and beam direction, or the vertical and beam direction separately. The hits on the active planes are used in the track reconstruction, and the track length and angle are obtained by fitting these hits with a linear function. The vertex of the track is determined as the most upstream point of hits associated the track. If there are two or more candidate tracks, the longest one is selected.
3. **3D-Track matching** The difference of the vertex of tracks in both projections is required within ± 1 plane width.
4. **Timing selection** The expected timing of the neutrino beam arrival is estimated spill-by-spill based on the primary proton beam timing at CT5, the time of flight of neutrinos, and the delay in the electronics. The hit timing at the vertex is required within ± 100 nsec around the expected timing. Cosmic-ray events are rejected by this selection.
5. **VETO and fiducial volume selections** These selection leaves neutrino events inside modules and rejects incoming particles from outside the modules. When there is no coincident hits in the VETO planes or the first tracking plane at the upstream position extrapolated from the track direction, the event are selected (VETO selection). The fiducial volume (FV) of the module is defined as a volume composed of the 3rd to 22nd of the 24 scintillators. After the VETO selection, the event with the vertex inside FV is selected (FV selection).

6.1.3 Detector simulation

The efficiency and systematic error were evaluated by a Monte Carlo (MC) simulation based on Geant4, in which events are generated according to the neutrino flux prediction (JUNBEAM) and the neutrino-nucleus interaction model (NEUT). This overview is shown in Fig. 6.2.

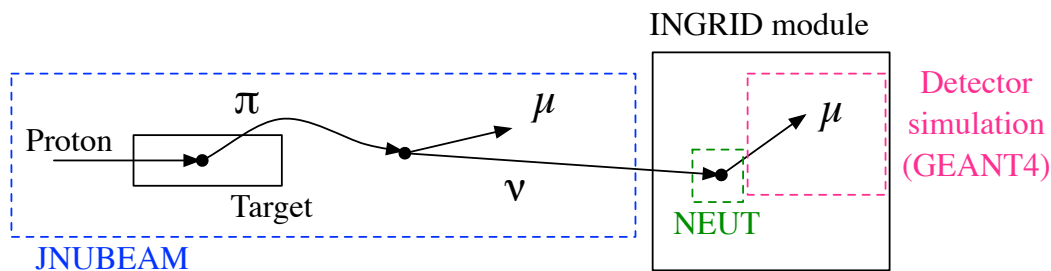


Figure 6.2: The overview of the simulation for the INGRID neutrino event.

The simulation contains following steps:

1. The neutrino flux at INGRID is predicted with JNUBEAM. As described in Sec 4, JNUBEAM generates neutrinos at the specified area. The flavor and energy of each neutrino are recorded. Position and angle are also recorded in case of the near detectors. For the INGRID simulation, fluxes are separately generated for the horizontal module area ($10.22 \text{ m (horizontal)} \times 1.44 \text{ m (vertical)}$) and the vertical area ($1.44 \text{ m (horizontal)} \times 10.22 \text{ m (vertical)}$). The neutrinos into the INGRID modules are generated on the plane whose horizontal and vertical region covers the horizontal or vertical seven modules ($1.44 \times 10.22 \text{ m}^2$)

and position in the beam direction is the center of the module. The fluxes for horizontal and vertical seven modules are generate separately and neutrino events in the horizontal or vertical modules are simulated separately.

2. The neutrino interactions inside modules are generated with NEUT. The cross-section of each interaction mode is calculated according to the flavor and energy of each neutrino. Based on each cross-section, the interaction mode is determined randomly for each neutrino. The kind and kinetic variables of generated particles are used in the detector simulation.

The MC normalization is determined from the flux normalization and the neutrino interaction probability. The neutrino interaction probability is calculated from the cross-section of each neutrino interaction and the number of target nucleus of Fe and CH. The mass ratio of scintillator planes to iron planes is 0.038. The cross-section of each interaction is calculated based on the neutrino-Fe interaction model. The vertex in the beam direction is uniformly generated in both the iron plates and the scintillator trackers. The vertex in the horizontal and vertical is given from the neutrino information.

3. The particles generated from the neutrino interaction are tracked with the INGRID detector simulation. The detector simulation models the real detector structures (geometries, materials). The particles' motion and physics interactions with the materials are simulated, and the energy deposit of each particle inside the scintillator is stored.
4. The energy deposit is converted into the number of PEs. The quenching effect of the scintillation is taken into account. The attenuation of PEs propagating in the optical fiber is taken into account. The non-linearity of the MPPC response is also taken into account because the detectable PEs are limited by the number of the MPPC pixels. The number of PEs is smeared according to the statistical fluctuation.

The conversion factor to PEs and the shape of the scintillator bar are optimized based on the measurements. The conversion factor is optimized by adjusting the peak of the PE distribution in MC to the one in the sand muon data (failed by the FV selection). The PE distribution in MC is based on muons generated outside modules. Figure 6.3 shows the typical PE distribution of the sand muon data and the MC prediction (after optimization). The MC prediction is adjusted data well. The real cross-section of the scintillator bar is like to octagon and has the thin edge (shown at Fig. 6.4). This thickness of the edge causes the tracking inefficiency. The cross-section of the scintillator bar is changed to reproduce the tracking inefficiency in cosmic-ray data (shown in Fig. 6.5).

The particles produced from the sand interaction are considered as the background source. In the background MC simulation, the neutrino flux at the upstream plane from INGRID is generated and the neutrino interaction is uniformly generated in the upstream wall region shown in Fig. 6.6. The dimensions of the plane are 20 m×20 m and covers the whole of INGRID. The plane is located at 10 m upstream from INGRID. The neutrino interaction is simulated with CH as the target nucleus. The normalization of the background is determined based on data so that the number of sand muon events is equal to that of data which is calculated from the number of events failed with the FV selection.

The detection efficiency is defined as the fraction of events remaining after all selections to the neutrino interactions inside FV. The CC purity is defined as the fraction of the inclusive CC events among selected events. The detection efficiency and CC purity are estimated with the detector simulation as shown in Fig 6.7. The detection efficiency is estimated for the inclusive CC, neutral current (NC) and CC+NC interactions. The flux-integrated efficiency for all interaction is $\sim 54\%$ (70%) for all (CC) interaction and the CC purity is $\sim 90\%$. The inclusive CC events are selected efficiently by the INGRID event selection.

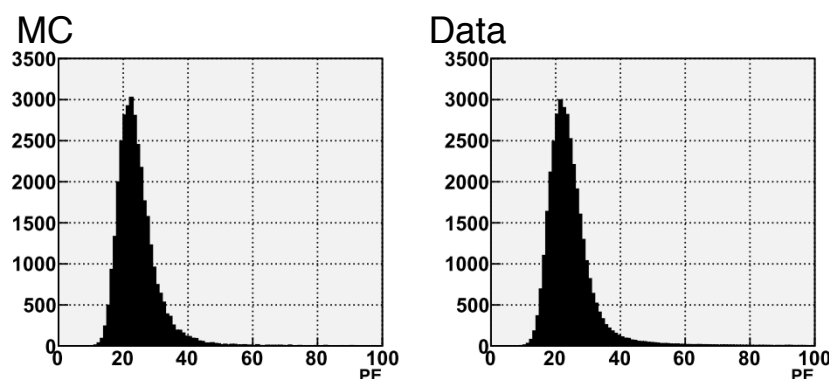


Figure 6.3: PE distribution of beam related sand muon. Left plot shows the distribution of the MC samples and right plot shows one in data.

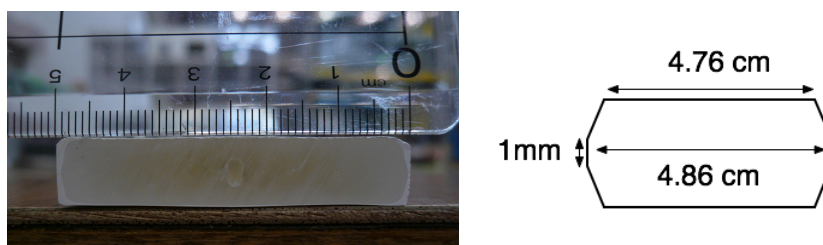


Figure 6.4: Photo of the cross-section of the scintillator bar (left) and the cross-section in the MC simulation (right) after changed.

6.1.4 Detector systematic errors

The systematic errors of the INGRID detection efficiency is summarized in Table 6.2. The dominant error source is from the 3D track matching selection. Total detector systematic error is 3.7%, which is evaluated as a quadratic sum of all error sources. The correlation of detector systematic errors between modules are not considered. More detail of the error evaluation is described elsewhere [45].

New INGRID analysis has been developed to increase the detection efficiency and improve its systematic errors. The main improvement is that the new tracking algorithm is less affected by the MPCC noise than current one. The total detector systematic error is found to be reduced approximately by half. In this thesis, the new analysis is not used because the systematic errors are still investigated.

6.1.5 Result of the measurements

The neutrino beam profile is reconstructed from the number of neutrino events measured at each INGRID module. The neutrino beam profile for the horizontal (vertical) direction is based on the measurements at seven horizontal (vertical) modules. The center of neutrino beam profile is obtained by fitting the beam profile with the Gaussian function. Figure 6.8 shows the predicted and measured horizontal neutrino beam profile for Run 1. One month data is needed to determine the neutrino beam direction with the better than 1 mrad accuracy. Table 6.3 shows the comparison of the predicted and measured beam center and event rate during Run 1. In this period, the proton beam was aimed slightly off center of the target in the vertical direction due to the mis-alignment of the MUMON. The measurements are consistent with the expected neutrino interaction rate and profile center within errors.

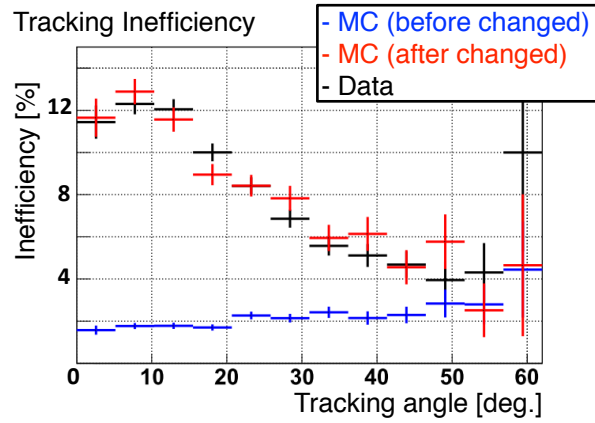


Figure 6.5: Tracking inefficiency as a function of the reconstructed track angle with respect to the beam direction. The cosmic-ray data is used.

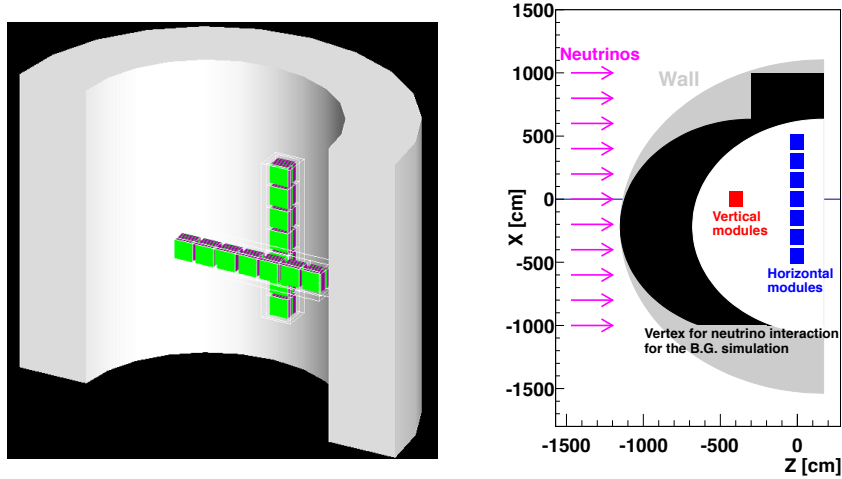


Figure 6.6: Left: The wall of the ND280 hall reproduced in the GEANT4 simulation (downstream view). The INGRID 14 modules (green and purple boxes) and the wall of the ND280 hall (gray wall) are shown. Right: Black shows the vertex of the neutrino interaction in the background MC simulation (top view)

6.1.6 Stability of the neutrino event rate and beam direction

Figure 6.9 shows the stability of the measured neutrino event rate. A decrease of event rate by 2% was observed from the first of Run 1 to the end of Run 3. There are several sources to cause the decrease; the reduction of the neutrino production, or the beam intensity dependence in the INGRID analysis (the detector efficiency can be reduce because of the pile-up events). At any rate, the neutrino event rate is confirmed to be stable within 2%.

Figure 6.10 shows the horizontal and vertical beam center approximately every month. The neutrino beam center averaged for each run period are summarized in Table 6.4. The systematic errors shown in this table is from only detector systematic errors. The neutrino beam direction was confirmed within 1 mrad from the beam axis during all run periods.

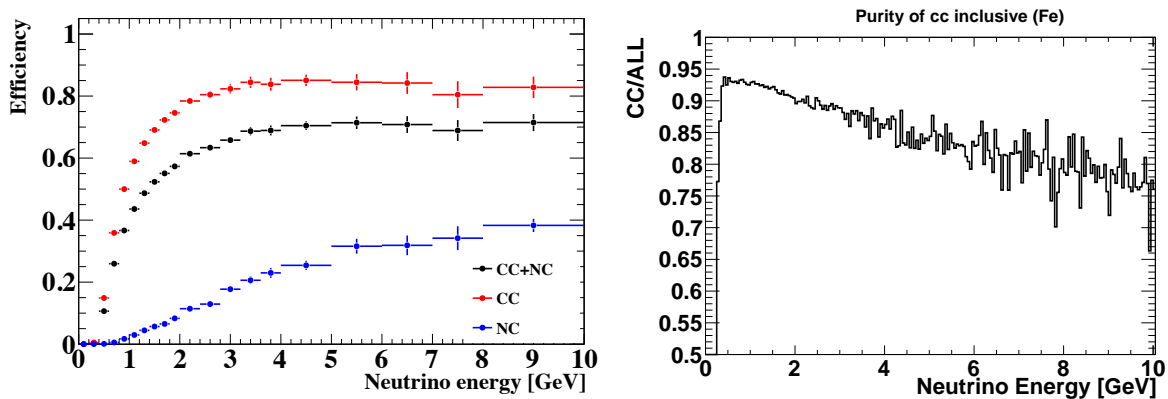


Figure 6.7: Efficiency (right) and CC purity (left) as a function of energy for the INGRID event selection. The error bars in the efficiency represent the MC statistic errors.

Table 6.2: Summary of INGRID detector systematic errors.

Error source	Error [%]
3D track matching	2.7
Channel hit efficiency	1.8
Tracking efficiency	1.4
Accidental MPPC noise	0.7
Beam-related background	0.2
Iron mass	0.1
Average light yield	<0.1
Out-of-beam events	<0.1
Beam timing	<0.1
Total	3.7

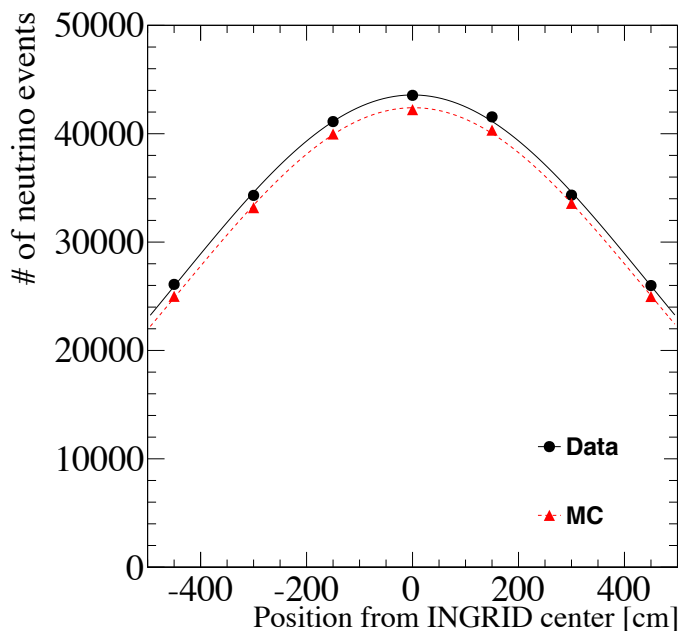


Figure 6.8: The horizontal neutrino beam profile reconstructed by INGRID for Run 1. The profile is fitted with a Gaussian function (lines in this plot). The statistical errors are smaller than the marks. Systematic errors are not shown.

Table 6.3: Summary of the predicted and measured INGRID beam center and event rate for Run 1. The systematic error is only from the uncertainty of the detection efficiency and does not include uncertainties of the flux and neutrino interaction cross-section.

	Data	Prediction
Rate [events/POT]	1.59×10^{-14}	1.53×10^{-14}
Horizontal center [mrad]	$0.009 \pm 0.052(\text{stat.}) \pm 0.336(\text{syst.})$	0.064
Vertical center [mrad]	$-0.314 \pm 0.055(\text{stat.}) \pm 0.373(\text{syst.})$	-0.477

6.2 Measurements at ND280

The event rate and energy spectrum of neutrinos are measured at ND280. The inclusive CC ν_μ events are selected, and then subdivided into "CCQE-like" and "CC nonQE-like" samples ("CC nonQE" means the CC interactions except for CCQE).

6.2.1 Data set for ND280 measurements

The ND280 data taking is summarized in Table 6.5. The good ND280 spills are obtained by applying the ND280 data quality cuts to the good beam spills. The inefficiency of ND280 is about 15%. The main causes to of the inefficiency is the problems of the TPC hardware components in Run 2.

6.2.2 Event selection

A negative charged muon-like long track starting from the FGD1 is selected to detect the inclusive CC ν_μ interaction. FGD1 works a neutrino interaction target and a detector. TPCs identify

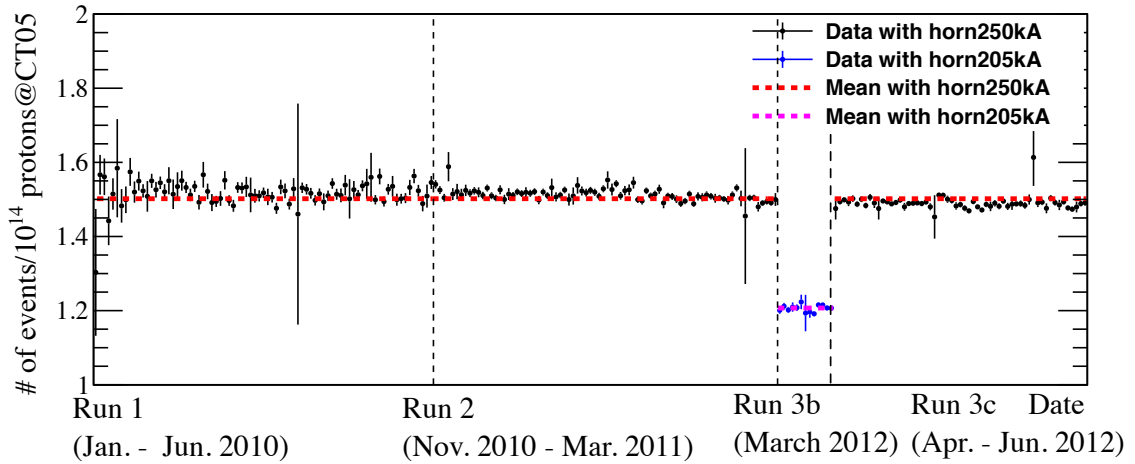


Figure 6.9: Neutrino event rate measured by INGRID (points) overlaid with mean value (dashed lines). The error bar represents the statistical error of INGRID measurement.

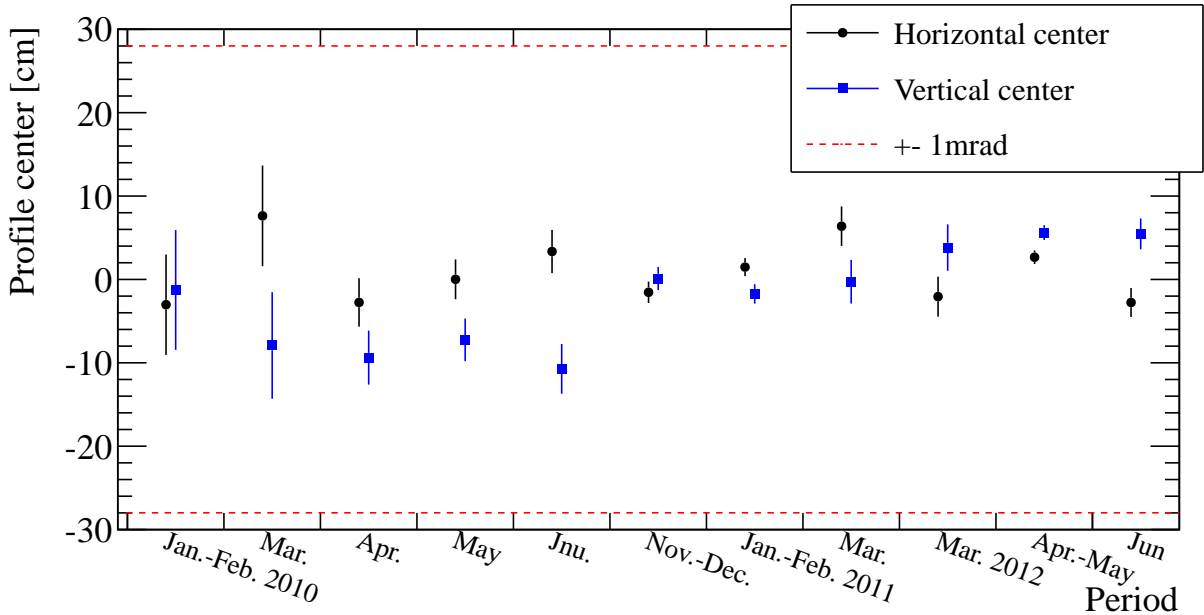


Figure 6.10: Neutrino beam center measured at INGRID at each month. The error bar represents the statistical error. The dashed line corresponds to the 1 mrad from the designed beam axis.

Table 6.4: Neutrino beam direction measured by INGRID in each run period. The first error is statistical error, and the second error is detector systematic error.

Period	X center [mrad]	Y center [mrad]
RUN1	$0.009 \pm 0.052 \pm 0.336$	$-0.314 \pm 0.055 \pm 0.373$
RUN2	$-0.028 \pm 0.027 \pm 0.333$	$0.050 \pm 0.030 \pm 0.374$
RUN3b	$-0.110 \pm 0.085 \pm 0.385$	$0.152 \pm 0.100 \pm 0.472$
RUN3c	$-0.001 \pm 0.026 \pm 0.331$	$0.232 \pm 0.029 \pm 0.378$

Table 6.5: Summary of data taking at ND280

Run period	Good spill ratio (ND280/Beam)	POT
Run 1	0.859	0.308×10^{20}
Run 2	0.686	0.786×10^{20}
Run 3b	0.977	0.211×10^{20}
Run 3c	0.978	1.353×10^{20}
Total	0.848	2.657×10^{20}

a muon by measuring the momentum and ionization loss of the charged particle. A typical neutrino event at ND280 is shown in Fig. 6.11. The selection criteria of the inclusive CC ν_μ interaction event are described as follows:

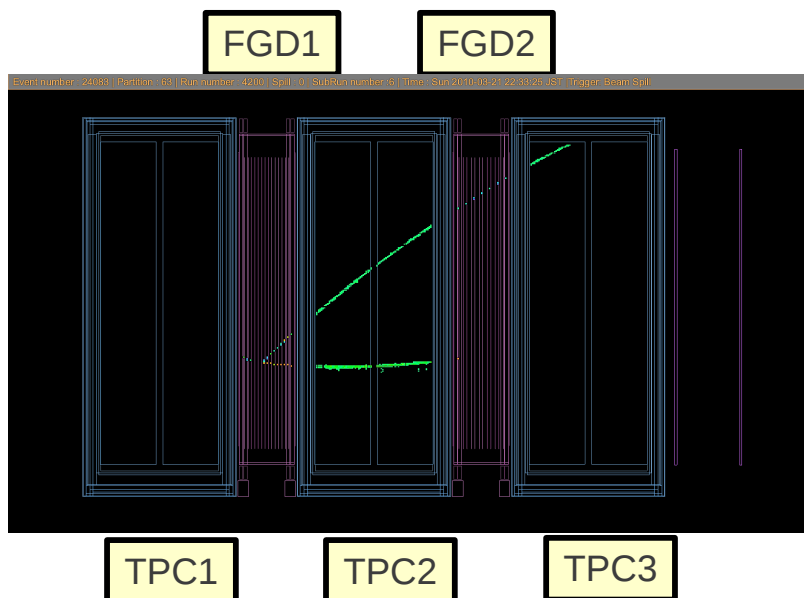


Figure 6.11: A typical neutrino signal event at ND280. The neutrino entered from the left and interacted in FGD1, producing charged particles whose tracks are found as the green list points. A proton or pion in the neutrino interaction is also observed unlike to INGRID.

- 1. Timing:** The event timing is required to be within ± 60 nsec from the expected timing of the neutrino beam arrival.
- 2. Negative track in FGD1's fiducial volume:** One or more negative tracks are required in both FGD and TPC are required. The FGD1 fiducial volume (FV) is defined as a volume which has the central 182 scintillator bars in the horizontal and vertical layers and the 2nd to 14th of the horizontal and vertical layers. The track is required to start in the FGD1 FV. The TPC track is required to have significant clusters for a reliable reconstruction. If there are more than one negative tracks passing this selection, the highest momentum one is selected as the muon track.
- 3. Backwards-going tracks and TPC1 VETO:** If the negative track starting inside the FGD1 FV is backward-going (end position upstream of start position), the event is re-

jected. This event is considered as a mis-reconstructed event where charged particles enter the FGD1 FV from the upstream.

- 4. TPC particle identification (PID):** The PID selection is performed based on the relation of the energy loss and momentum measured by TPCs. This relation is shown in Fig 6.12. A muon-like track is selected.

The remaining CC inclusive events after these selections are categorized into the CCQE-like or CC nonQE-like events. The CCQE-like event is required to satisfy the following two selections:

Track multiplicity selection: Only one matched TPC-FGD track to select μ in the CCQE interaction. A proton in the CCQE interaction tends to stop in FGD1 and not to reach TPCs. Many pions from the CC nonQE events tend to have a TPC track.

Michel electron selection: No Michel-like electron activity in FGD1. The Michel electron is identified by a delayed FGD1 hit cluster.

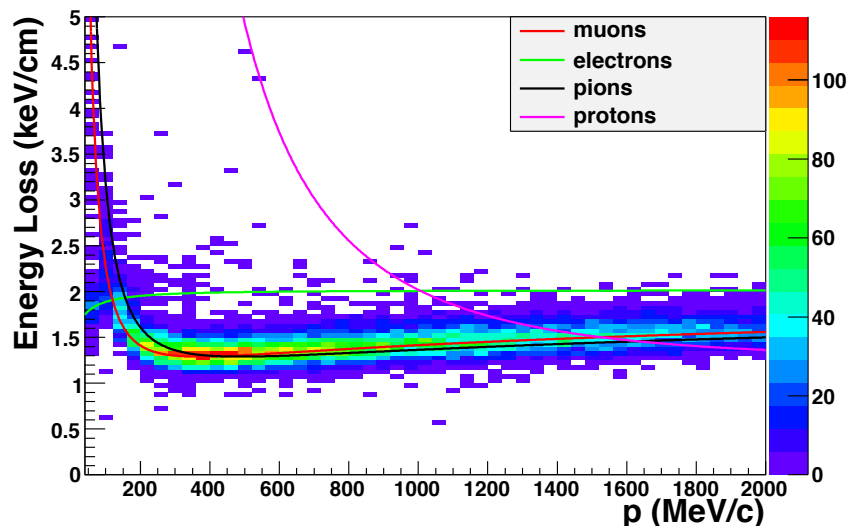


Figure 6.12: Energy loss distribution as a function of the reconstructed momentum for negative particles measured by TPC.

6.2.3 Detector systematic errors

All ND280 detection systematic errors are shown in Table 6.6 . There are seven major systematic errors and other minor systematic errors are classified into "Others". In the major systematic errors, the errors associated with the track reconstruction are as follows: the TPC magnetic field, momentum resolution, and TPC-FGD matching. The pion absorption inside nucleus makes the CC nonQE event mis-reconstructed to the CCQE event. There are two main background in the ND280 events. One is the sand interaction which is described in Sec 6.1.2. Another is the "Out-of-FV background" which is the neutrino interaction outside the FGD1 FV (but inside FGD1). The event migration from CCQE-like events to CC nonQE-like events raises from the event pile up of CCQE and background events.

Table 6.6: Summary of all ND280 detector systematic errors.

Error source	Error size [%]
Pion absorption	1~5
TPC magnetic field distortion	1~7
TPC momentum resolution	2
TPC-FGD matching	<1
Sand interaction	1.5
Out-of-FV background	1~9
Pileup: CCQE to CCnonQE	1.5
Others	1.3

6.2.4 Result of the measurements

Figure 6.13 and 6.14 show the distributions of the reconstructed muon momentum and angle after the selections. The two dimensional distribution of the momentum and angle is shown in Fig 6.15. The distributions predicted by MC including background are also shown. The shown background is composed the following: "Anti-numu", "out FGD FV", "out of FGD", "Sand". "Anti-numu" is the $\bar{\nu}_\mu$ interaction. "out FDG FV" is the neutrino interaction outside FGD1 FV but in FGD1. "out of FGD" is the neutrino interaction in ND280 components around FGD1. "Sand" is the sand interaction. The number of events after the selections is summarized in Table 6.7 along with the MC expectation. The measurements is consistent with the predictions. The CCQE-like event selection increases the fraction of the CCQE events.

These ND280 measurements are used to refine the flux and neutrino interaction models for ND280. The ND280 constraint is extrapolated to SK so that the uncertainties of the flux and interaction models for SK are constrained to increase the sensitivity of the oscillation analysis. The detail of the ND280 constraints is described in Sec. 7.

Table 6.7: Summary of the ND280 measurement in Run1+2+3. Here, the error represents the only statistic error.

	Data	MC
inclusive CC selection	11055±105	11499.2±107.2
CCQE-like	5841±76	6343.8±79.6
CCnonQE-like	5214±72	5255.4±72.5

6.3 Measurements at SK

The rate and energy spectrum of the neutrino events are measured at SK after oscillation. A single muon produced in the ν_μ CCQE interaction is selected to reconstruct the neutrino energy efficiently. The neutrino energy E_ν is reconstructed as E_ν^{rec} based on the muon momentum and angle in the CCQE interactions:

$$E_\nu^{rec} = \frac{(M_n - V) \cdot E_\mu - m_\mu^2/2 + M_n \cdot E_b - V^2/2 + (M_p^2 - M_n^2)/2}{M_n - E_b - E_\mu + P_\mu \cos \theta_\nu}, \quad (6.1)$$

where:

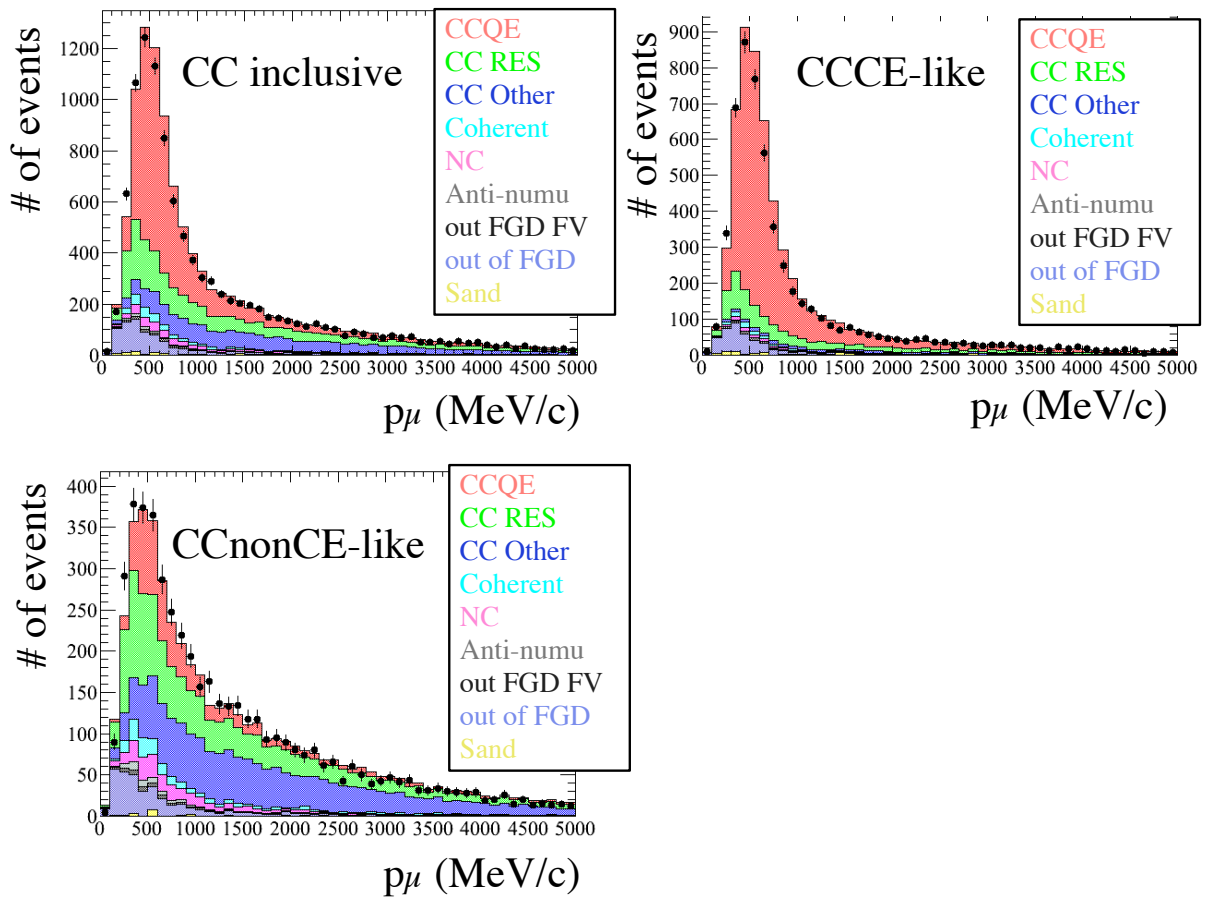


Figure 6.13: Reconstructed muon momentum distribution of the inclusive CC, CCQE-like, and CC nonQE-like events in Run1+2+3. Black points show the data and colored histograms show the MC expectation.

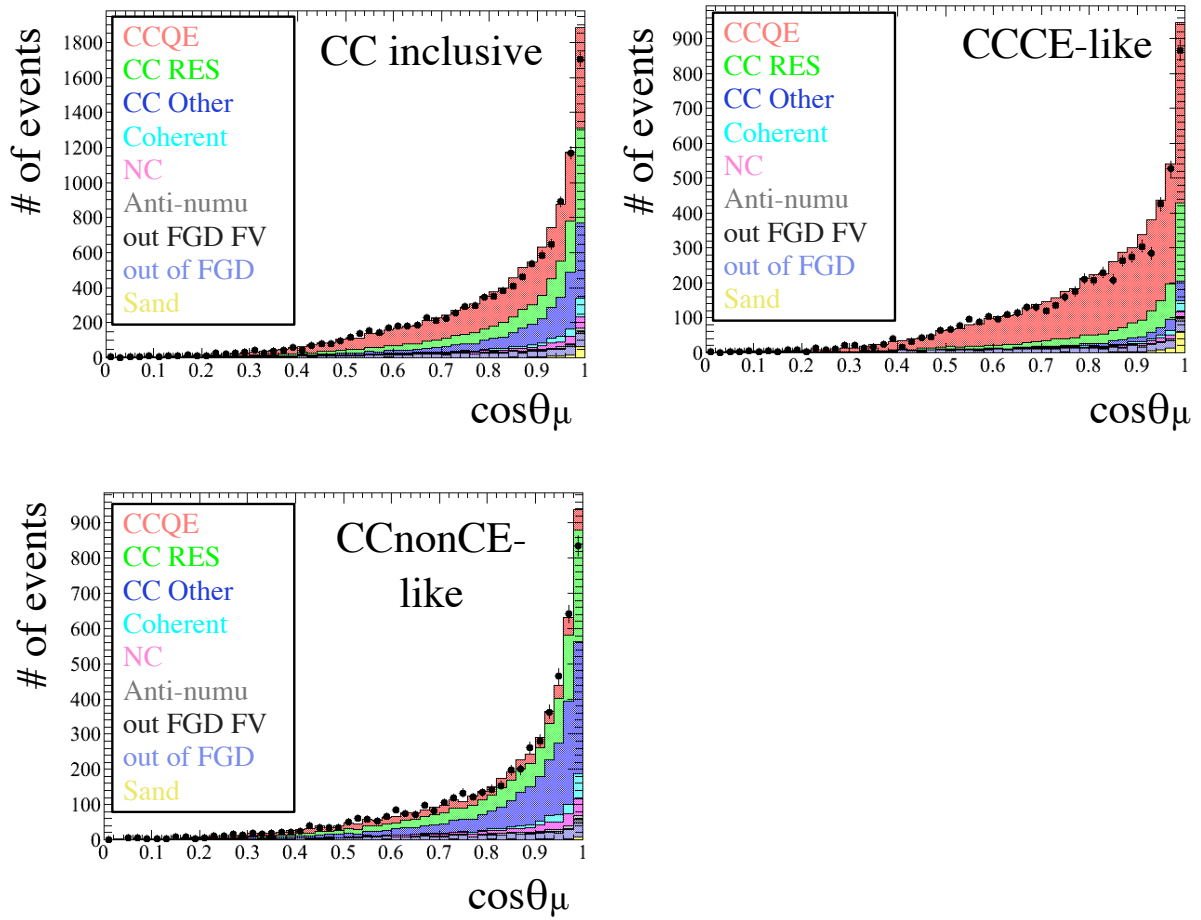


Figure 6.14: Reconstructed muon angle distribution of the inclusive CC, CCQE-like, and CC nonQE-like events in Run1+2+3. Black points show the data and colored histograms show the MC expectation.

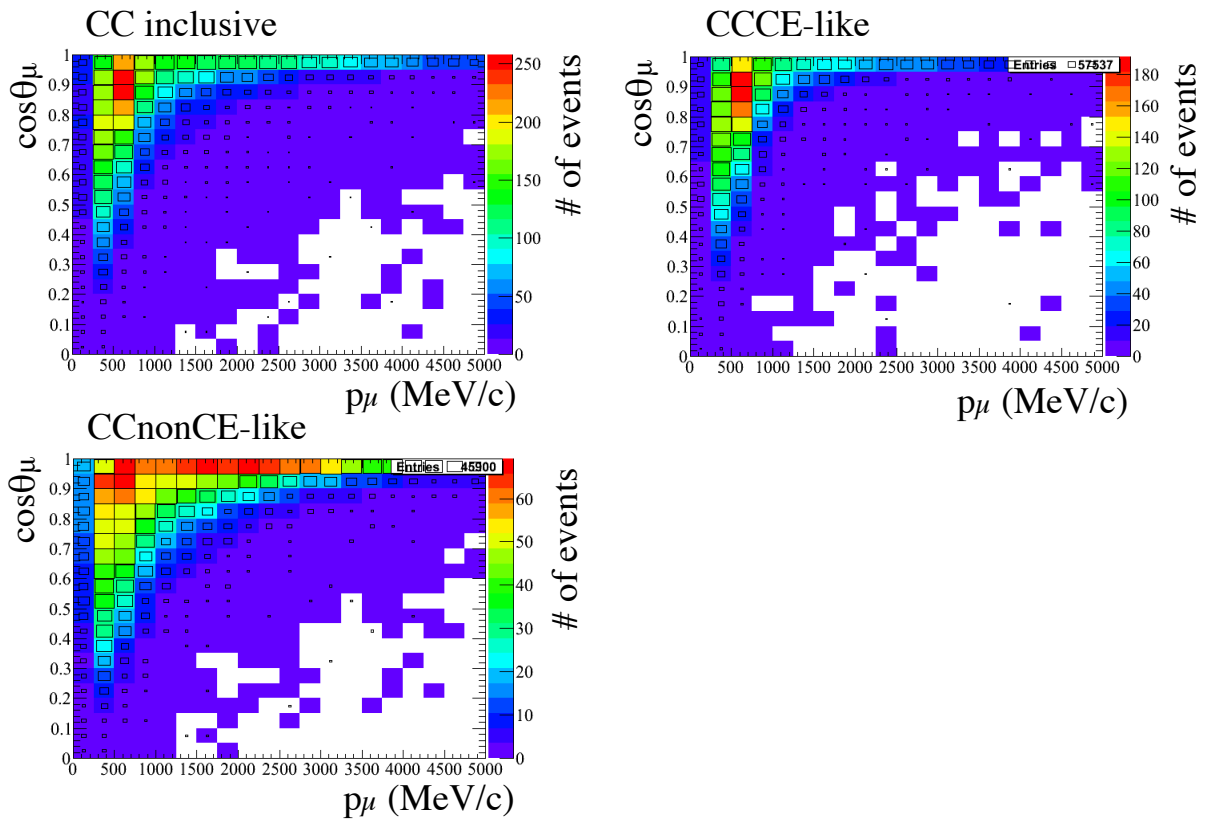


Figure 6.15: Two dimensional distribution of the reconstructed muon momentum and angle of the inclusive CC, CCQE-like, and CC nonQE-like events in Run1+2+3. The black line boxes show the data and colored boxes show the MC expectation.

M_n, M_p : the neutron, proton mass

V : the nuclear potential energy (taken to be 27 MeV for ^{16}O)

m_μ : the mass of the muon

P_μ, E_μ : the reconstructed momentum of the muon and its total energy

θ_ν : the angle between the neutrino beam and the outgoing muon

In this reconstruction, the Fermi momentum of the bound neutron is neglected. The Fermi momentum smears the reconstructed neutrino energy. As already mentioned, in the charge current interactions except for CCQE (CC nonQE), the neutrino energy is mis-reconstructed to the lower energy.

6.3.1 Data set for SK measurements

The SK data taking is summarized in Table 6.8. The good SK spills are calculated by applying the SK data quality cuts to the good beam spills. The inefficiency of SK is $\sim 1\%$. The accumulated POT for the oscillation analysis is 3.01×10^{20} . This POT corresponds to about 4% of the T2K final statistics.

Table 6.8: Summary of data taking at SK

Run period	Good spill ratio (SK/Beam)	POT
Run 1	0.992	0.324×10^{20}
Run 2	0.989	1.109×10^{20}
Run 3	0.990	1.579×10^{20}
Total	0.990	3.010×10^{20}

6.3.2 Event selection

An example of a single-ring μ -like event measured at SK is shown in Fig. 6.16. The selection criteria are described as follows:

1. Fully-contained fiducial volume (FCFV) selection
2. Single-ring μ -like selection
3. Reconstructed momentum is greater than 200 MeV/c
4. Number of decay electrons is equal to or less than one

FCFV selection

”Fully contained” (FC) events are required to have particles remaining inside the inner detector volume (ID) with no energy deposit in the outer veto detector (OD). The fiducial volume (FV) is defined in Sec. 2.5. An event is considered as the FV if the distance between the closest ID wall and the reconstructed event vertex is greater than 200 cm. Finally, the FCFV event is defined as that the visible energy from reconstructed Cherenkov rings, E_{vis} , is larger than 30.0 MeV.

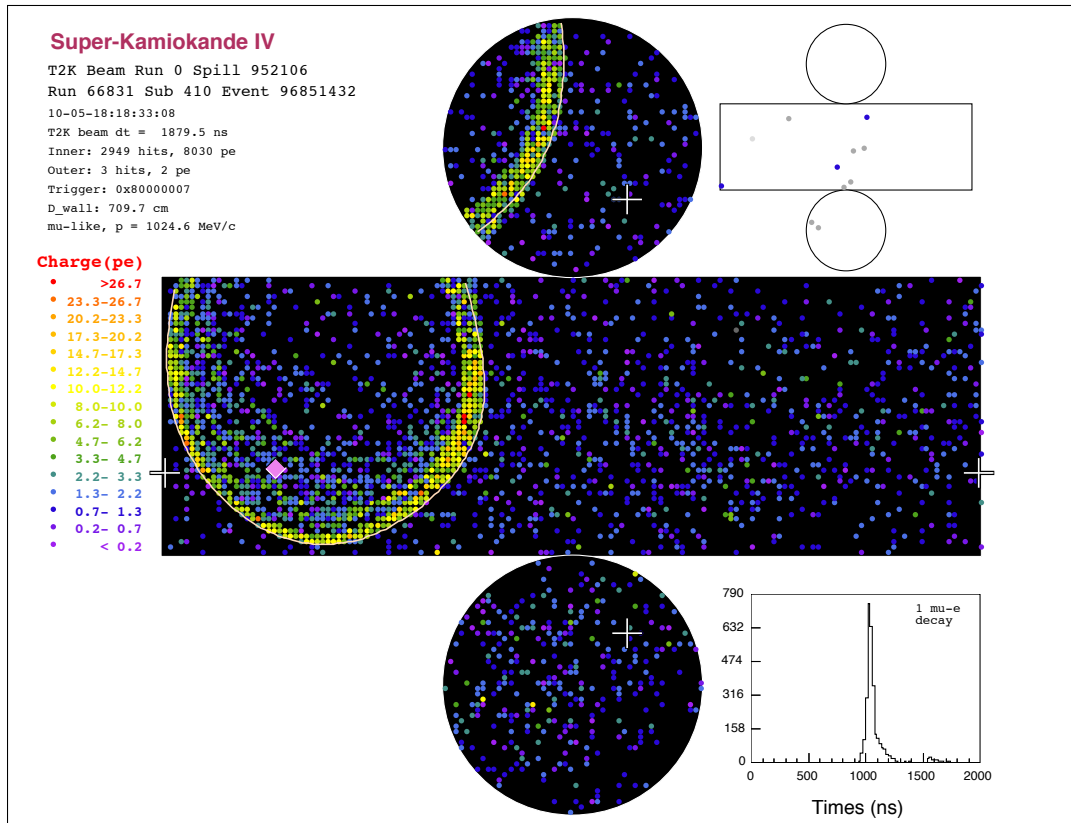


Figure 6.16: Example of a single-ring μ -like event detected at SK. Developed figure of the SK tank is shown. The middle square box represents the side area of the SK tank. The top (bottom) circle represents the top (bottom) edge of the SK tank. The white circle indicates the fitted Cherenkov ring. Four white crosses indicate the reconstructed vertex position. A pink diamond is placed on the wall in the beam direction starting from the reconstructed vertex. The bottom right figure is the hit timing distribution with information on the number of the tagged μ -decay electrons.

This condition is to reject low energy events such as the NC background because charged pions with low energy may be produced and cannot produce the Cherenkov rings.

The PMTs emit light from the internal corona discharges. This is called "flashing". The flasher event is the event occurred from the sudden flashing PMTs. The flasher event is the dominant source of the systematic uncertainty in the FC event selection. This event is removed based on the PMT hit timing distribution and its periodic event cycle.

Single-ring μ -like selection

In the CC nonQE interaction, for example the CC1 π interaction, a pion are produced in addition to a muon, then more than one reconstructed rings is observed if a Cherenkov ring by a pion is observed. The number of rings is required to be one to reject the CC nonQE events. The efficiency of the single ring identification for CCQE events is evaluated as $\sim 96\%$ in the simulation. The particle identification (PID), i.e. the separation of e-like and μ -like rings can be performed from the edge of the Cherenkov ring as described in Sec. 2.5. Events with one μ -like ring are selected as the single-ring μ -like events.

Reconstructed momentum is greater than 200 MeV/c

The momentum of the μ -like particle is estimated by measuring the total number of photoelectrons associated with the Cherenkov ring. The reconstructed momentum is required to be more than 200 MeV to keep the good performance of the μ/e separation.

Number of decay electrons is equal or less than one

In order to reject the event with charged pions not reconstructed, the number of decay electrons is required to be 0 or 1. Decay electrons are tagged by looking for hit activities after the primary event. The tagging efficiency is estimated $\sim 90\%$ from the measurement of the cosmic-ray stopped muon in the tank.

6.3.3 Detector systematic errors

The SK detector systematic errors consist of the systematic errors of the detection efficiency and the energy scale. The SK detector systematic error are summarized in Table 6.9.

Table 6.9: Summary of the SK detector systematic errors. E^{rec} represents the reconstructed neutrino energy.

Error	Error size
$\nu_\mu, \bar{\nu}_\mu$ CCQE efficiency ($E^{rec} < 0.4$ GeV)	2.5%
$\nu_\mu, \bar{\nu}_\mu$ CCQE efficiency ($E^{rec} = 0.4 \sim 1.1$ GeV)	3.9%
$\nu_\mu, \bar{\nu}_\mu$ CCQE efficiency ($E^{rec} > 1.1$ GeV)	9.5%
$\nu_\mu, \bar{\nu}_\mu$ CCnonQE efficiency	20%
$\nu_e, \bar{\nu}_e$ CC efficiency	100%
NC efficiency	111%
Energy scale	2.3%

Table 6.10 shows the breakdown of systematic errors for the detection efficiencies. A dominant error source in the detection efficiencies is the ring counting error. The ring counting error was evaluated by using atmospheric neutrino events (enriched events for ν_μ CCQE, ν_μ

CC nonQE, and NC interactions) with special event selections. The error size of the ring counting was assigned as the difference of the number of events between the atmospheric neutrino measurement and the MC prediction. For ν_μ CCQE event, a correlation of the ring counting errors among E_ν^{rec} bins is also evaluated. The covariance matrix of ν_μ CCQE ring count errors are defined in Eq. 6.2. The large ring counting errors for CC nonQE and NC originate from the large deviation between data and MC. The Particle ID (μ/e separation) error for NC events has not been studied well and assigned 100%. In principle, there are no leptons associated to the neutrino flavor from the NC interaction, hence it is difficult to evaluate the Particle ID error for NC events.

Table 6.10: Breakdown of the systematic errors for the SK detector efficiency. E^{rec} represents the reconstructed neutrino energy.

Error source	ν_μ CCQE	ν_μ CCnonQE	NC
Ring counting	1.7% ($E_\nu^{rec} < 0.4$ GeV)	19.9%	48.2%
	3.5% ($E_\nu^{rec} = 0.4 \sim 1.1$ GeV)		
	9.3% ($E_\nu^{rec} > 1.1$ GeV)		
Flasher cut	1%		
Fiducial volume	1%		
Decay electron	1%		
Particle ID	$\ll 1\%$		100%
Momentum cut	$\ll 1\%$		
Outer Detector VETO	$\ll 1\%$		

$$\begin{pmatrix}
 E_\nu^{rec} < 0.4 \text{ GeV} & E_\nu^{rec} = 0.4 \sim 1.1 \text{ GeV} & E_\nu^{rec} > 1.1 \text{ GeV} \\
 \left(\begin{array}{ccc}
 \sigma_1^2 & 0.59\sigma_1\sigma_2 & 0.33\sigma_1\sigma_3 \\
 & \sigma_2^2 & 0.61\sigma_2\sigma_3 \\
 & & \sigma_3^2
 \end{array} \right) & &
 \end{pmatrix} \quad (6.2)$$

$$\sigma_1 = 1.7\%, \sigma_2 = 3.5\%, \sigma_3 = 9.3\%$$

Since the contribution of the ν_e CC events is small in the SK ν_μ candidates events, the systematic error of the ν_e CC efficiency is negligible. The estimation of this error is postponed (assigned as 100%).

The error of the energy scale was assigned as 2.3%. This size is a quadratic sum of the uncertainty of the absolute scale (2.19%) and the stability (0.4%). The uncertainty of the absolute energy scale is evaluated by comparing data and MC, and the stability is checked by using cosmic-ray data. The stability was confirmed to be stable within 2.3% during Run 1+2+3.

6.3.4 Results of the measurement

Figure 6.17 shows the distributions of the PID parameter, the reconstructed muon momentum, and the number of decay electron. The MC prediction shown in this section are based on the following conditions unless otherwise stated: the MC prediction is normalized by POT and tuned based on the results of ND280 data fit (described at Sec. 7), and the two flavor oscillation ($\nu_\mu \rightarrow \nu_\tau$) is assumed with $(\sin^2 2\theta_{23}, \Delta m_{32}^2) = (1.0, 2.4 \times 10^{-3} \text{ eV}^2)$. The measurements are consistent with the MC prediction in all distributions.

Figure 6.18 shows the distributions of the reconstructed muon momentum and angle, and reconstructed neutrino energy. The distribution of the reconstructed energy is used as an input of

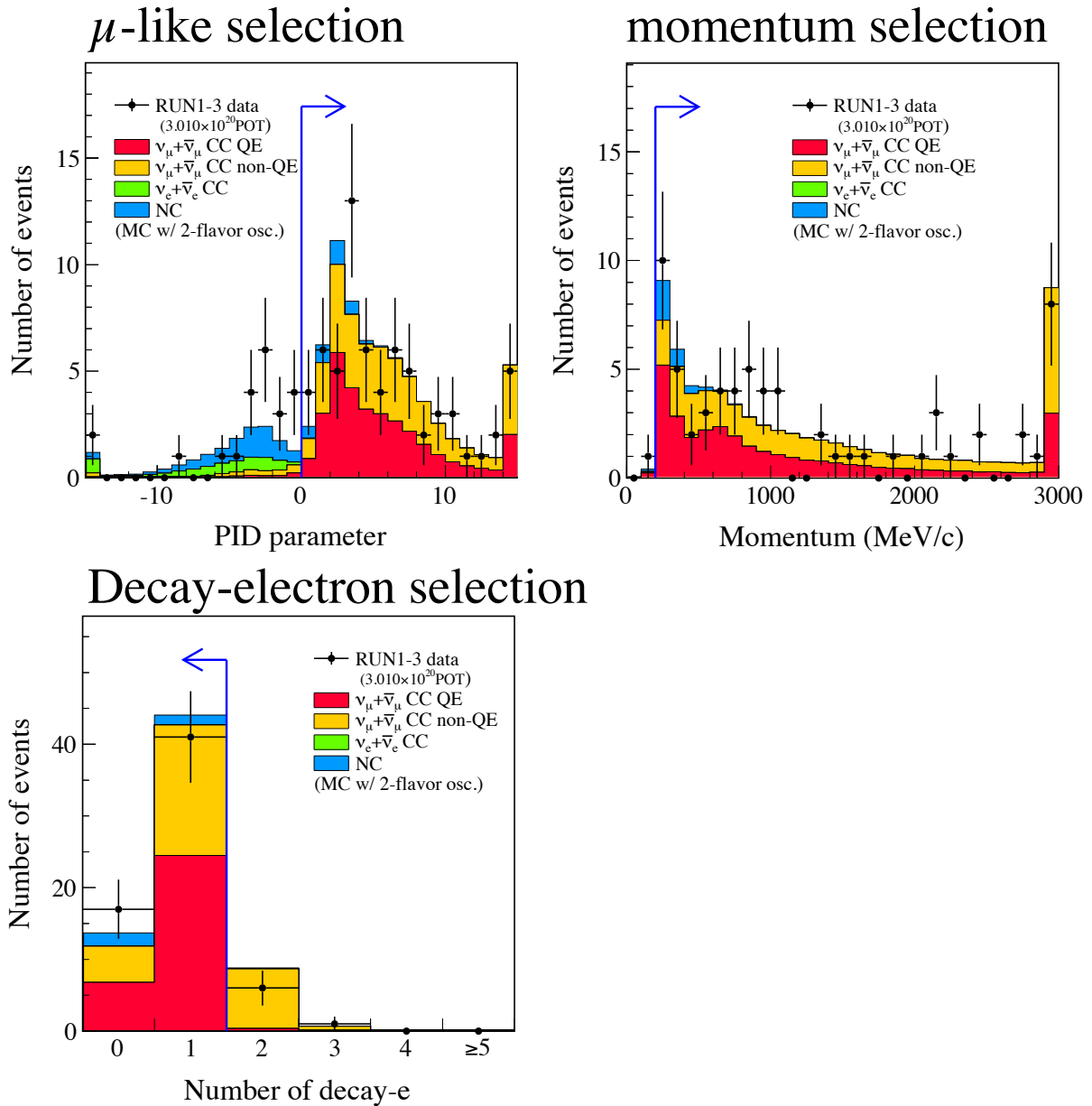


Figure 6.17: Distributions of the PID parameter (upper left), reconstructed muon momentum (upper right), and the number of decay electron (bottom) for Run1+2+3 data and the MC prediction. These variables are associated with ν_μ event selections. Blue arrows in plots indicate the selection criteria.

the oscillation analysis. The measurement is consistent with the MC prediction in all distributions. The two dimensional reconstructed vertex distribution is shown in Fig. 6.19. The vertex distribution of ν_μ candidate events is uniform and in the SK FV.

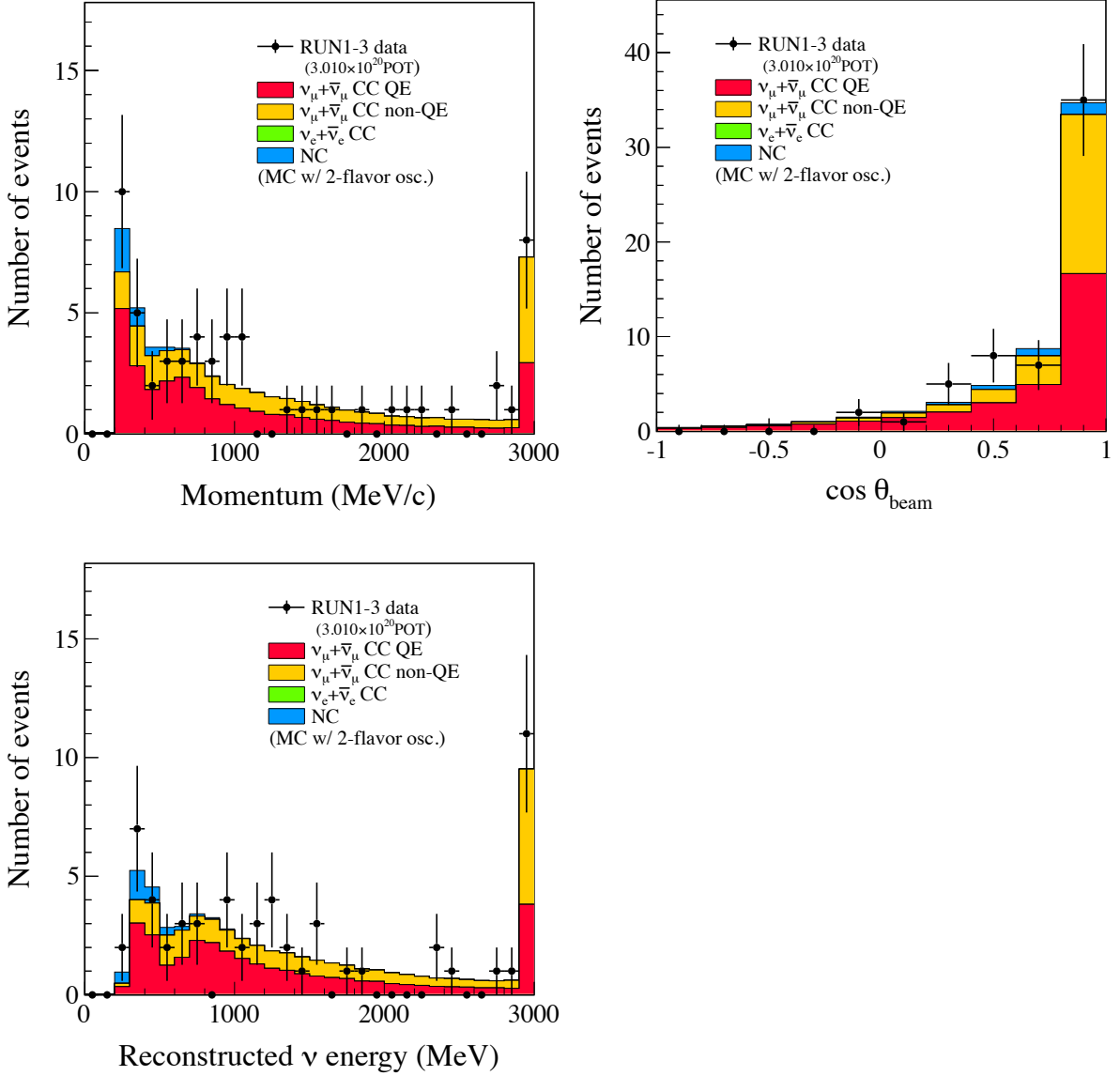


Figure 6.18: Distributions of the reconstructed muon momentum (upper left) and angle (upper right), and neutrino energy (bottom) in the ν_μ CCQE candidate events for Run 1+2+3 data with the MC prediction.

Table 6.11 and 6.12 summarize the number of events passing each selection step for Run1+2+3 data and the MC expectation. The MC expectation with oscillation is consistent with the observation.

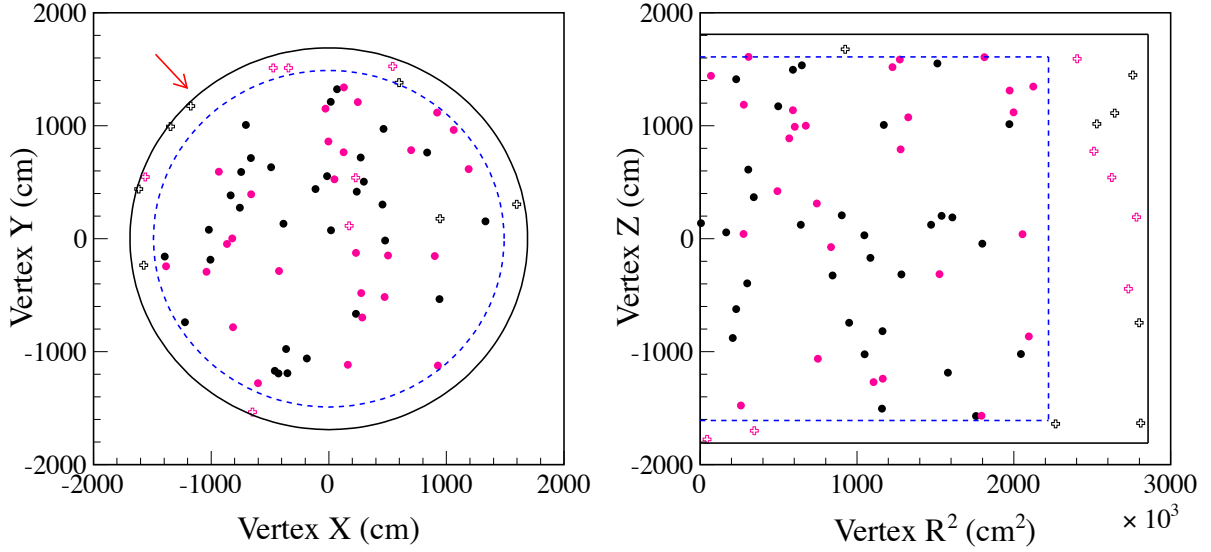


Figure 6.19: The vertex distribution of ν_μ candidate events. The left figure shows the vertex distribution projected onto the X - Y plane (at top view) and the red arrow indicates the neutrino beam direction. The right figure shows the vertical position (Z) vs. vertex R^2 from the central vertical axis of the SK tank. A dashed blue lines indicate the fiducial volume boundary. Black markers are events observed during Run 1+2 and pink markers are events from Run 3. Hollow crosses represent events passing all selection cuts other than the fiducial volume cut.

Table 6.11: Summary of events passing each selection step for Run 1+2+3 data and the MC expectation. "Interaction in FV" means that the true neutrino interaction point is within FV in MC. p_μ represents the muon reconstructed momentum. $N_{decay-e}$ represents the number of decay electrons.

Run1+2+3 Selection step	Data	MC expectation				
		MC Total	$\nu_\mu + \bar{\nu}_\mu$ CCQE	$\nu_\mu + \bar{\nu}_\mu$ CC nonQE	$\nu_e + \bar{\nu}_e$ CC	NC All
Interaction in FV (TrueFV)	–	296.67	45.22	110.25	8.31	132.89
FCFV	174	166.61	34.37	83.83	7.93	40.48
Single-ring	88	83.56	32.47	34.52	5.03	11.55
μ -like cut	66	67.74	31.83	32.42	0.04	3.45
$p_\mu > 200$ MeV/c	65	67.33	31.60	32.35	0.04	3.34
$N_{decay-e} \leq 1$	58	57.78	31.25	23.29	0.03	3.21
Efficiency for TrueFV [%]	–	19.5	69.1	21.1	0.4	2.4
Efficiency for FCFV [%]	–	34.7	90.9	27.8	0.4	7.9

Table 6.12: Summary of events passing each selection step for Run 1+2+3 data and the MC expectation (non-oscillation). The neutrino oscillation is not considered in the MC expectation. "Interaction in FV" means that the true neutrino interaction point is within FV in MC. p_μ represents the muon reconstructed momentum. $N_{decay-e}$ represents the number of decay electrons.

Run1+2+3 Selection step	Data	MC expectation (no oscillation)				
		MC Total	$\nu_\mu + \bar{\nu}_\mu$ CCQE	$\nu_\mu + \bar{\nu}_\mu$ CC nonQE	$\nu_e + \bar{\nu}_e$ CC	NC All
Interaction in FV (TrueFV)	–	503.28	171.16	190.92	8.31	132.89
FCFV	174	30.45	155.77	146.27	7.93	40.48
Single-ring	88	242.47	151.24	74.65	5.03	11.55
μ -like cut	66	219.20	149.11	66.61	0.04	3.45
$p_\mu > 200$ MeV/c	65	217.86	148.52	65.96	0.04	3.34
$N_{decay-e} \leq 1$	58	196.22	147.88	45.10	0.03	3.21
Efficiency for TrueFV [%]	–	19.5	69.1	21.1	0.4	2.4
Efficiency for FCFV [%]	–	34.7	90.9	27.8	0.4	7.9

Chapter 7

Extrapolation of ND280 measurements to SK prediction

7.1 Overview of the extrapolation of ND280 measurements

The flux normalizations and neutrino interaction parameters used in the ND280 prediction are refined by comparing the ND280 prediction with the measurements. The SK flux is refined based on the refined ND280 flux through the flux correlation. The refined interaction parameters are reflected to the interaction cross-section for the SK prediction. The flux normalizations and neutrino interaction parameters used in the SK prediction are tuned by the ND280 measurements.

In practice, the p - θ distributions of CCQE-like and CC nonQE-like events of the ND280 measurements are fitted with the prediction by varying the flux normalizations and neutrino interaction parameters within their uncertainties (called the ND280 fit). The ND280 detector systematic errors are taken into account. The flux normalizations and interaction parameters are refined by the ND280 fit. The correlation between flux normalizations and interaction parameters is also evaluated. The results of the ND280 fit are reflected to the SK prediction.

7.2 Fit of the ND280 p - θ distribution

7.2.1 ND280 samples used in the fit

The ND280 CCQE and CC nonQE events are used in the ND280 fit (described in Sec. 6.2). The CCQE-like events are sensitive to the flux at the energy around the oscillation maximum, while the CC nonQE-like events are sensitive to the flux in the higher energy. By increasing the purity of CCQE or CC nonQE interactions, the associated interaction parameters are refined well.

7.2.2 Parameters used in the fit

The Table 7.1 summarizes parameters used in the ND280 fit. The flux normalization parameters are the weights to change the normalizations predicted by the flux simulation. The condition that the value of the flux normalization parameter is one means the nominal normalization. The neutrino interaction parameters describe the neutrino interaction models. In the ND280 fit, these parameters are varied within their uncertainties. In addition, the ND280 detection systematic uncertainties are taken into account in the ND280 fit.

The only ND280 ν_μ flux normalizations are refined well by the ND280 fit. Other flavor's are tuned weakly because the contributions from other flavors are negligible (each less than 1% in the ND280 inclusive CC ν_μ samples). The SK ν_μ and ν_e flux normalizations are extrapolated based on the refined ND280 ν_μ flux normalizations.

Table 7.1: List of parameters varied in the ND280 fit.

Category	Parameter
Flux	ND280 ν_μ $\bar{\nu}_\mu$ ν_e $\bar{\nu}_e$ normalization as a function of neutrino energy (described in Sec. 4)
ν interaction	absolute cross-section normalizations for each interaction category M_A^{QE} , M_A^{RES} , $p_F(^{12}C)$, $E_B(^{12}C)$, Spectral function (^{12}C), CC other shape, W shape, Pion-less delta decay, FSI (described in Sec. 5)

Neutrino interaction parameters used in the ND280 fit are categorized into the following groups:

1. Parameters that are refined by the ND280 fit well and affect the SK prediction. The fit results of these parameters are reflected to the SK prediction. The following parameters are categorized here: the absolute cross-section normalizations for CCQE and CC1 π , M_A^{QE} , and M_A^{RES} .
2. Parameters that only affect the ND280 prediction and not SK. Therefore, the fit results of these parameters are not reflected to the SK prediction. Fermi gas (p_F , E_B) and spectral function parameters depend on the target nuclei and are different in ND280 (^{12}C) and SK (^{16}O).
3. Parameters that are weakly refined by the ND280 fit well and affect the SK prediction. These parameters are refined by external data. The fit results of these parameters are not reflected to the SK prediction.

In short, the cross-section normalization for CCQE and CC1 π interactions, M_A^{QE} , and M_A^{RES} are refined by the ND280 fit and extrapolated to the SK prediction. Other neutrino interaction parameters are refined by external data (not refined by the ND280 fit).

7.2.3 Results of the fit

Figure 7.1 and 7.2 shows the distributions of the reconstructed muon momentum and angle. The bottom of each plot shows the residuals, defined as (data-MC)/(statistical error of data) for the events in each bin. Table 7.2 summarizes the number of CCQE-like and CC nonQE-like events. The prediction after the ND280 fit reproduces the data better than before the ND280 fit.

Figure 7.3 shows the ND280 ν_μ flux normalization parameters before and after the ND280 fit. Table 7.3 summarizes the neutrino interaction parameters before and after the ND280 fit (here, only interaction parameters reflected to the SK prediction). The ND280 flux normalizations and neutrino interaction parameters are refined well by the ND280 fit.

7.3 Extrapolation to SK

The flux normalizations and neutrino interaction parameters used in the SK prediction are refined by the ND280 fit. The refined parameters improve the uncertainties of the event rate and energy spectrum at SK. Detail of this improvement is described at Sec. 8.1.2.

The SK ν_μ and $\bar{\nu}_\mu$ flux normalization parameters are defined according to the neutrino energy binning shown in Table 7.4. Figure 7.4 shows the SK ν_μ and $\bar{\nu}_\mu$ flux normalization parameters

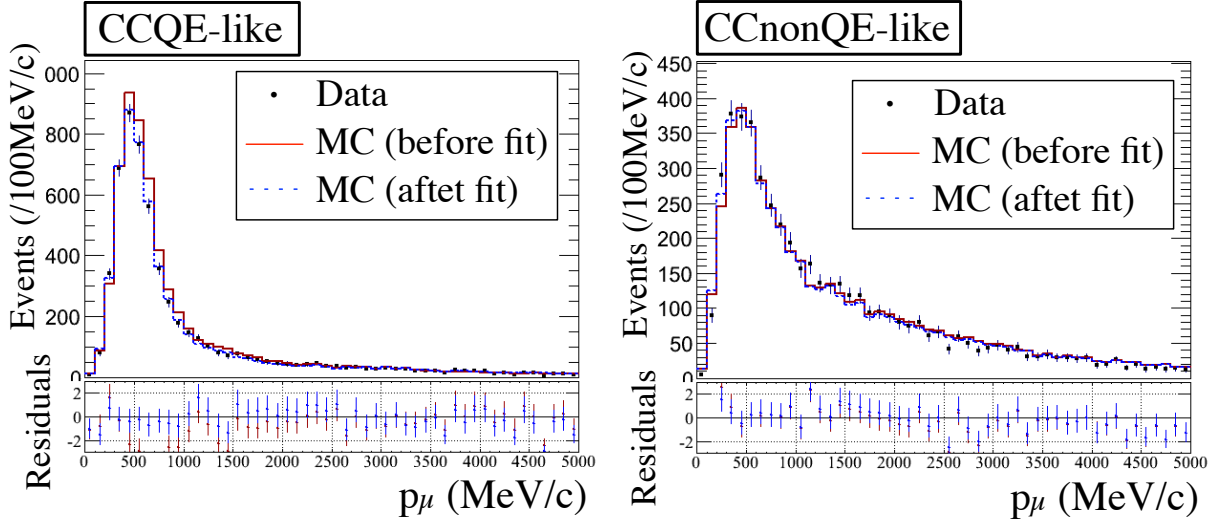


Figure 7.1: Distribution of the reconstructed muon momentum before and after the ND280 fit for CCQE-like events (left), and CC nonQE-like events (right). The error bars of data the statistical error.

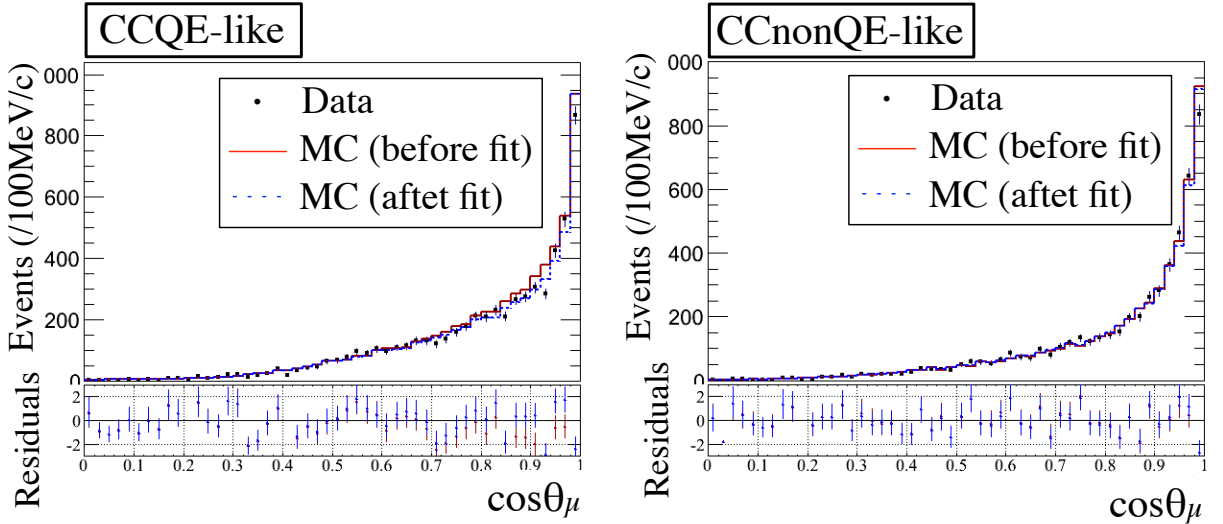


Figure 7.2: Distribution of the reconstructed muon angle before and after the ND280 fit for CCQE-like events (left), and CC nonQE-like events (right). The error bars of data the statistical error.

Table 7.2: Summary of ND280 CCQE-like and CC nonQE-like events before and after the ND280 fit. This residual is based on the total number events in each sub-sample.

	CCQE-like		CC nonQE-like	
	Events	Residual	Events	Residual
Data	5841	–	5214	–
MC(Before fit)	6243.8	-5.27	5255.4	-0.57
MC(After fit)	5854.4	-0.18	5202.7	0.16

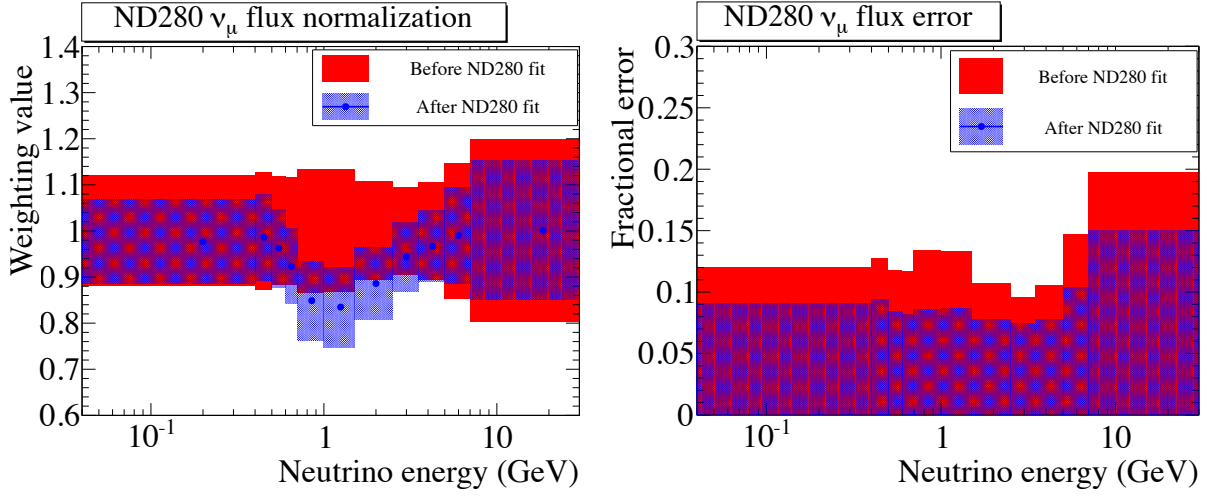


Figure 7.3: ND280 ν_μ flux normalization parameters as a function of energy before and after the ND280 fit. Left: the ND280 ν_μ flux normalization parameter before and after the ND280 fit. The envelope on the plot represents the systematic error size. Right: the fractional error size of the ND280 ν_μ flux normalization.

Table 7.3: Summary of neutrino flux and interaction parameters extrapolated to SK. E_ν represents the neutrino energy (GeV).

#	Parameter	Before ND280 fit		After ND280 fit	
		Central value	Error	Central value	Error
0~10	SK ν_μ Flux	1	0.09~0.19	0.90~1.01	0.07~0.14
11~15	SK $\bar{\nu}_\mu$ Flux	1	0.11~0.13	0.95~0.98	0.09~0.11
16	M_A^{QE}	1.21 GeV/ c^2	0.45	1.27 GeV/ c^2	0.19
17	M_A^{RES}	1.41 GeV/ c^2	0.22	1.22 GeV	0.13
18	CCQE norm. ($E_\nu < 1.5$)	1.0	0.11	0.95	0.09
19	CCQE norm. ($E_\nu = 1.5 \sim 3.5$)	1.0	0.30	0.71	0.21
20	CCQE norm. ($E_\nu > 3.5$)	1.0	0.30	1.35	0.22
21	CC1 π norm. ($E_\nu < 2.5$)	1.15	0.32	1.37	0.20
22	CC1 π norm. ($E_\nu > 2.5$)	1.0	0.40	1.02	0.28

before and after the ND280 fit. The ν_e and $\bar{\nu}_e$ flux normalizations are not varied in the oscillation analysis because the contributions of these uncertainties are negligible in the SK ν_μ candidates. Table 7.3 also summarizes the common neutrino interaction parameters used in the ND280 and SK prediction. All of flux and neutrino interaction errors are reduced significantly by the ND280 measurements.

Table 7.4: Energy binning for the SK ν_μ and $\bar{\nu}_\mu$ flux normalization parameters

Flavor	True neutrino energy binning [GeV]	# of bins
ν_μ	0–0.4, 0.4–0.5, 0.5–0.6, 0.6–0.7, 0.7–1.0, 1.0–1.5,	11
	1.5–2.5, 2.5–3.5, 3.5–5.0, 5.0–7.0, 7.0–30	
$\bar{\nu}_\mu$	0–0.7, 0.7–1.0, 1.0–1.5, 1.5–2.5, 2.5–30	5

Figure 7.5 shows the correlation matrix between the flux normalization parameters and interaction parameters extrapolated to the SK prediction before and after the ND280 fit. There is a significant anti-correlation between them. The reason is that the observed neutrino events are always affected from the both the flux normalizations and neutrino interaction cross-section. In other words, when flux normalizations reduce, the neutrino interaction cross-sections always increase so that the number of neutrino events does not change. It is important that this anti-correlation can reduce the uncertainties on the SK prediction more than the quadratic sum of the flux and neutrino interaction uncertainties (i.e. the uncorrelated case).

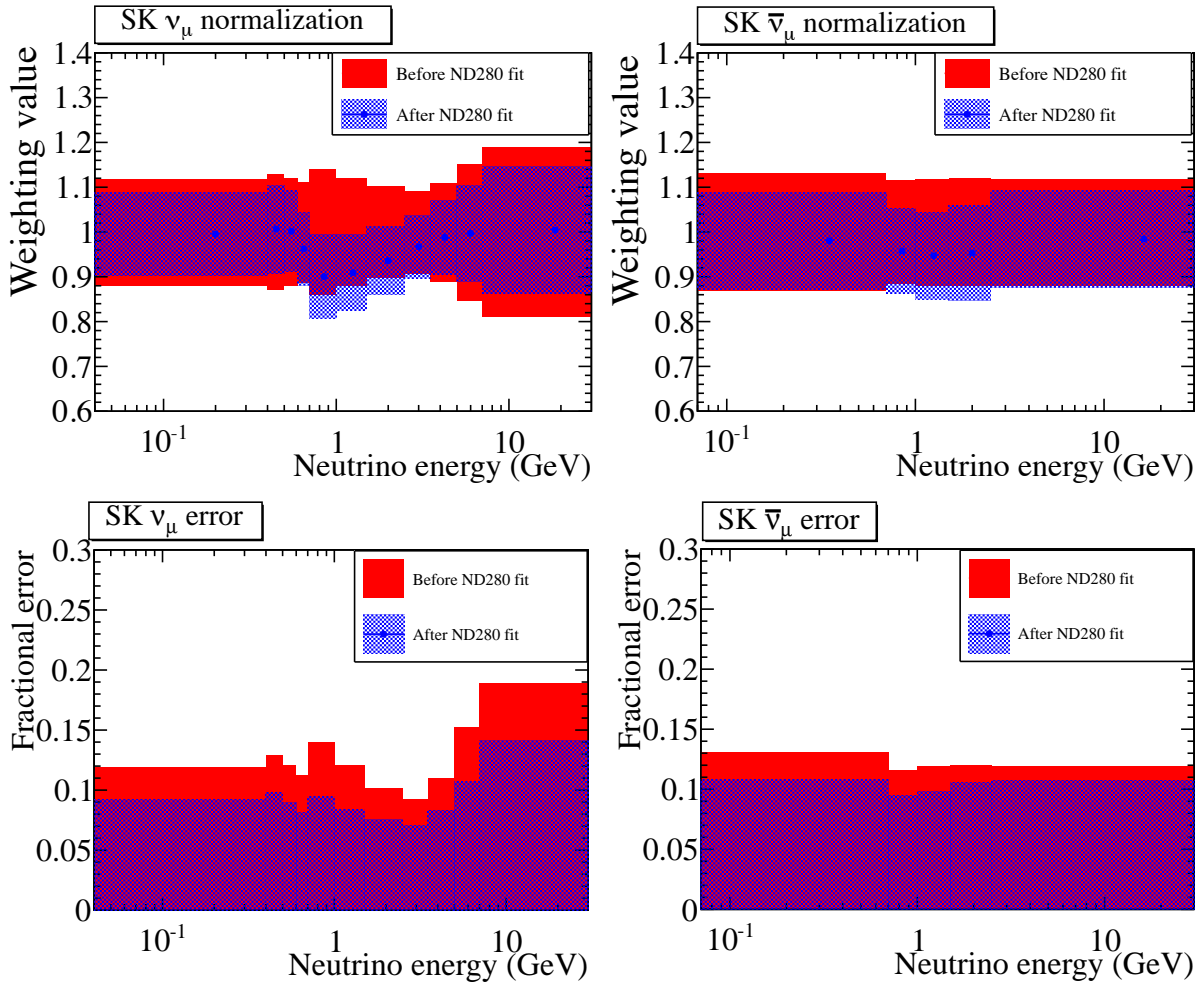


Figure 7.4: Top: SK ν_μ (top left) and $\bar{\nu}_\mu$ (top right) flux normalization parameters as a function of neutrino energy before and after ND280 fit. The envelope on each plot show the flux systematic error. Bottom: the fractional flux error for SK ν_μ (bottom left) and $\bar{\nu}_\mu$ (bottom right) flux.

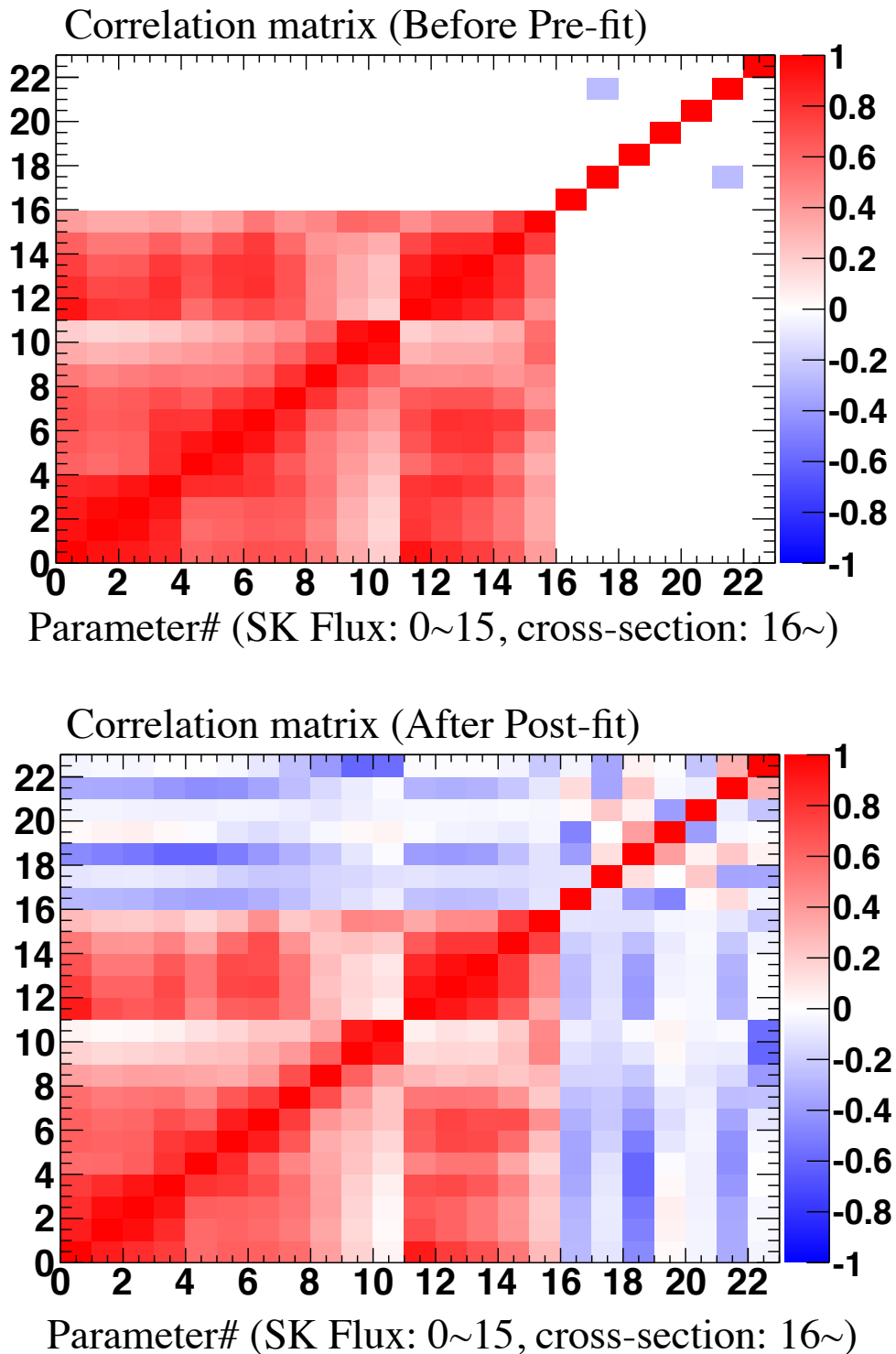


Figure 7.5: Correlation matrix of SK flux and cross-section parameters which are constrained by ND280 fit. These horizontal and vertical axes represent the parameter number in Table 7.3. The correlation matrixes before (top) and after (bottom) ND280 fit are shown.

Chapter 8

Analysis of muon neutrino disappearance

8.1 Analysis method

The goal of this analysis of muon neutrino disappearance is to determine the best oscillation parameters ($\sin^2 2\theta_{23}$, Δm_{32}^2) with high precision based on the 3.01×10^{20} POT (Run 1+2+3) data set. An extended unbinned maximum likelihood method is used in the analysis. The likelihood is constructed with the rate and energy spectrum of the SK ν_μ events including the systematic uncertainties of the SK prediction.

8.1.1 Definition of the likelihood

The likelihood is defined as:

$$\mathcal{L}(N_{obs}, \mathbf{E}_{obs}^{rec}, \mathbf{o}, \mathbf{f}) = \mathcal{L}_{norm}(N_{obs}; \mathbf{o}, \mathbf{f}) \times \mathcal{L}_{shape}(\mathbf{E}_{obs}^{rec}, \mathbf{o}, \mathbf{f}) \times \mathcal{L}_{syst}(\mathbf{f}) \quad (8.1)$$

where:

$\mathcal{L}_{norm}, \mathcal{L}_{shape}, \mathcal{L}_{syst}$: the likelihood for the event rate, neutrino energy spectrum and systematic uncertainties.

$N_{obs}, \mathbf{E}_{obs}^{rec}$: the rate and reconstructed energy (E^{rec}) spectrum of ν_μ events observed at SK. E^{rec} is calculated according to Eq. 6.1.

\mathbf{o} : the neutrino oscillation parameters ($\sin^2 2\theta_{23}, \Delta m_{32}^2$) to be measured.

\mathbf{f} : parameters representing systematic uncertainties for the prediction (called "systematic parameters"). These parameters act as weighting factors to change the nominal SK prediction. Following systematic uncertainties are taken into account: the neutrino flux, neutrino interaction, the SK detection efficiencies and energy scale, and final-state and secondary interactions (called FSI-SI, described in Sec. 5.2).

\mathcal{L}_{norm} is the event rate likelihood for the Poisson probability to observed N_{obs} candidate events:

$$\mathcal{L}_{norm}(N_{obs}; \mathbf{o}, \mathbf{f}) = \frac{e^{-N_{exp}(\mathbf{o}, \mathbf{f})} (N_{exp}(\mathbf{o}, \mathbf{f}))^{N_{obs}}}{N_{obs}!}, \quad (8.2)$$

where $N_{exp}(\mathbf{o}, \mathbf{f})$ is the expected event rate.

\mathcal{L}_{shape} is the unbinned likelihood for the neutrino energy spectrum. This is defined as the product of probabilities that each event is observed with the reconstructed energy $E_{obs,i}^{rec}$:

$$\mathcal{L}_{shape}(\mathbf{E}_{obs}^{rec}; \mathbf{o}, \mathbf{f}) = \prod_{i=1}^{N_{obs}} \rho(E_{obs,i}^{rec}; \mathbf{E}_{exp}^{rec}, \mathbf{o}, \mathbf{f}), \quad (8.3)$$

where $E_{obs,i}^{rec}$ represents the reconstructed energy of the i th observed event and ρ is the probability density function (PDF) of the reconstructed neutrino energy. The PDF ρ is calculated for given oscillation parameters and systematic parameters.

$\mathcal{L}_{syst}(\mathbf{f})$ is the probability density function of the systematic parameters. This acts as the penalty term by the systematic parameters. A multivariate normal distribution is used:

$$\mathcal{L}_{syst}(\mathbf{f}) = \frac{1}{(2\pi)^{k/2} \sqrt{|V|}} \exp\left(-\frac{1}{2} \Delta \mathbf{f}^T V^{-1} \Delta \mathbf{f}\right), \quad (8.4)$$

where k is the number of systematic parameters, V is the covariance matrix of systematic parameters, and $\Delta \mathbf{f}$ are the deviations of systematic parameters from their nominal values.

To measure the $\sin^2 2\theta_{23}$ and Δm_{32}^2 , the likelihood in Eq. 8.1 is maximized by varying oscillation parameters \mathbf{o} and systematic parameters \mathbf{f} simultaneously (called as the oscillation fit). In practice, the negative log likelihood $-2 \log \mathcal{L}(\mathbf{o}, \mathbf{f})$ is defined as χ^2 and minimized by the minimum search algorithm (MINUIT library [94]). The $\sin^2 2\theta_{23}$ and Δm_{32}^2 are bound in the following region:

$$\begin{aligned} 0 < \sin^2 2\theta_{23} < 1 \\ 1.0 \times 10^{-3} < \Delta m_{32}^2 (\text{eV}^2) < 6.0 \times 10^{-3} \end{aligned}$$

The $\sin^2 2\theta_{23} < 0$ or $\sin^2 2\theta_{23} > 1$ is un-physical. The boundary for Δm_{32}^2 is determined based on the clearly excluded region based on the current knowledge.

8.1.2 Prediction of the event rate and energy spectrum of SK ν_μ events

The expected event rate in each E^{rec} bin is calculated for given oscillation and systematic parameters. The expected event rate in the E_i^{rec} bin is defined as:

$$\begin{aligned} N_{exp}(E_i^{rec}, \mathbf{o}) &= \sum_F^5 \int_{E_i^{rec}}^{E_{i+1}^{rec}} dE^{rec} \int dE_\nu \Phi_{SK}^F(E_\nu) \cdot P_{osc}^F(E_\nu, \mathbf{o}) \\ &\times \sum_I^6 \sigma_{SK}^{F,I}(E_\nu) \cdot \epsilon_{SK}^{F,I}(E^{rec}) \cdot R_{SK}^{F,I}(E_\nu \rightarrow E^{rec}), \end{aligned} \quad (8.5)$$

where

F: Neutrino flavor category. There are five categories, ν_μ , $\bar{\nu}_\mu$, ν_e , $\bar{\nu}_e$ and $\nu_{e,app}$, where $\nu_{e,app}$ is ν_e oscillated from ν_μ .

I: Neutrino interaction category. There are six categories: CCQE, CC1 π , CC coherent, CC others, NC1 π C and NC others (see Sec 5).

E_ν, E^{rec} : True and reconstructed neutrino energy of the event. The energy binning for E_ν and E^{rec} used in this analysis is described in Table 8.1 or 8.2. The energy binning is defined so that the shape of energy spectrum around the oscillation maximum is kept fine and the number of bins is reduced to keep the analysis program simple.

Φ_{SK}^F : Predicted F flux at SK.

P_{osc}^F : Oscillation probability for the F flux, which is applied only on the CC interaction. Following oscillation probabilities are considered:

- $\nu_\mu \rightarrow \nu_\mu$ survival probability for $F = \nu_\mu$.
- $\bar{\nu}_\mu \rightarrow \bar{\nu}_\mu$ survival probability for $F = \bar{\nu}_\mu$.
- $\nu_e \rightarrow \nu_e$ survival probability for $F = \nu_e$.
- $\bar{\nu}_e \rightarrow \bar{\nu}_e$ survival probability for $F = \bar{\nu}_e$.
- $\nu_\mu \rightarrow \nu_e$ appearance probability for $F = \nu_{e,app}$.

The oscillation probabilities are calculated by the "Prob3++" library [95] which calculates the oscillation probability in the three-flavor-neutrino oscillation model including the matter effect. The oscillation parameters except for $\sin^2 2\theta_{23}$ and Δm_{32}^2 are fixed to the current best knowledge, as shown in Table 8.3. The matter effect is not considered because this effect is negligible for ν_μ disappearance.

$\sigma_{SK}^{F,I}$: Neutrino-nucleus interaction cross-section for the target material of SK (^{16}O).

$\epsilon_{SK}^{F,I}$: SK detection efficiency

$R_{SK}^{F,I}(E_\nu \rightarrow E^{rec})$: SK detector response function representing the probability to observe the event with E_ν as one with E^{rec} .

Table 8.1: Binning of the true neutrino energy (E_ν) used in the oscillation analysis. Bins at the energy around the oscillation maximum (0.3~1.0 GeV) are kept fine. Total number of bins is 85.

E_ν [GeV]	0.0~0.3	0.3~1.0	1.0~3.0	3.0~3.5	3.5~4.0	4.0~5.0	5.0~7.0	7.0~10.0	10.0~30.0
Bin width [GeV]	0.05	0.025	0.05	0.10	0.50	1.0	2.0	3.0	20.0
# of bins	7	28	40	5	1	1	1	1	1

Table 8.2: Binning of the reconstructed neutrino energy (E^{rec}) used in the oscillation analysis. Total number of bins is 74.

E^{rec} [GeV]	0.0~3.0	3.0~4.0	4.5~6.0	7.0~10.0	10.0~30.0
Bin width [GeV]	0.05	0.25	0.50	1.0	20.0
# of bins	61	4	4	4	1

The total expected event rate, $N_{exp}^{tot}(\mathbf{o})$, is calculated by integrating $N_{exp}(E_i^{rec}, \mathbf{o})$ over all reconstructed neutrino energy bins:

$$N_{exp}^{tot}(\mathbf{o}) = \sum_i^{74} N_{exp}(E_i^{rec}, \mathbf{o}). \quad (8.6)$$

Table 8.3: Summary of oscillation parameter values except for $\sin^2 2\theta_{23}$ and Δm_{32}^2 used in the probability calculation by Prob3++. These parameters are fixed in the oscillation fit.

Parameter	Value
Δm_{21}^2	$7.5 \times 10^{-5} \text{eV}^2$
$\sin^2 2\theta_{12}$	0.8757
$\sin^2 2\theta_{13}$	0.098
δ_{CP}	0
Mass hierarchy	Normal
Baseline length	295 km
Earth density	0 (Matter Effect off)

The PDF of the reconstructed energy spectrum, $\rho(E^{rec})$ is derived from the normalized $N_{exp}(E_i^{rec})$ (N_{exp}^{tot} is normalized to one). Since $N_{exp}(E_i^{rec})$ is separated with a finite bin width, the probabilities between neighboring bins are interpolated with the linear function to construct the unbinned likelihood. The PDF is calculated as:

$$\rho(E^{rec}) = \frac{x \cdot N_{exp}(E_{i+1}^{rec}) \cdot w_{i+1} + (1-x) \cdot N_{exp}(E_i^{rec}) \cdot w_i}{N_{exp}^{tot}}, \quad (8.7)$$

where

$$x = \frac{E^{rec} - E_i^{rec}}{E_{i+1}^{rec} - E_i^{rec}}, \quad w_i = \frac{0.05 \text{ GeV}}{E_{i+1}^{rec} - E_i^{rec}}, \quad (E_{i+1}^{rec} > E^{rec} > E_i^{rec}). \quad (8.8)$$

Figure 8.1 shows the normalized $N_{exp}(E_i^{rec})$ and the PDF according to Eq. 8.7.

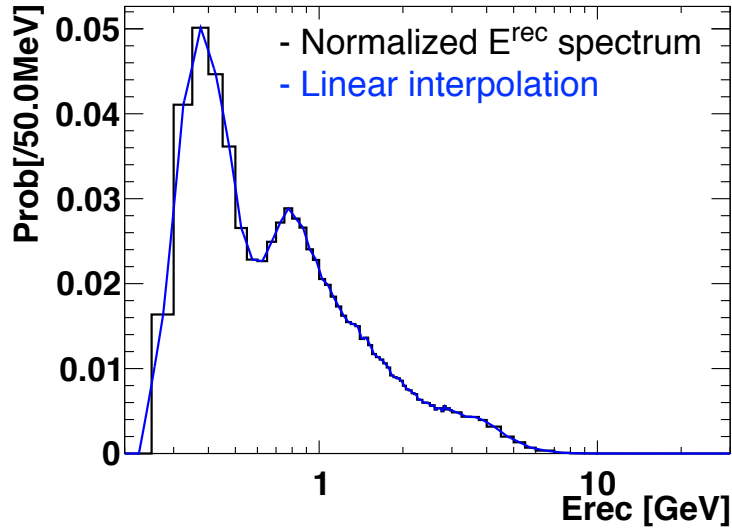


Figure 8.1: The PDF of reconstructed energy spectrum with oscillation. Black histogram shows the normalized E^{rec} spectrum. Blue line shows the linear function interpolated between neighboring bin centers.

The SK prediction is the one refined based on the results of ND280 fit (described at Sec. 7.3). The predicted E_ν and E^{rec} spectra are shown in Fig. 8.2 and 8.3 and the expected number of SK ν_μ events is summarized in Table 8.4 for a given oscillation case $(\sin^2 2\theta_{23}, \Delta m_{32}^2) = (1.0, 2.4 \times 10^{-3})$ at 3.01×10^{20} POT. Figure 8.4 shows expected number of SK ν_μ events for each oscillation parameter points $(\sin^2 2\theta_{23}, \Delta m_{32}^2)$.

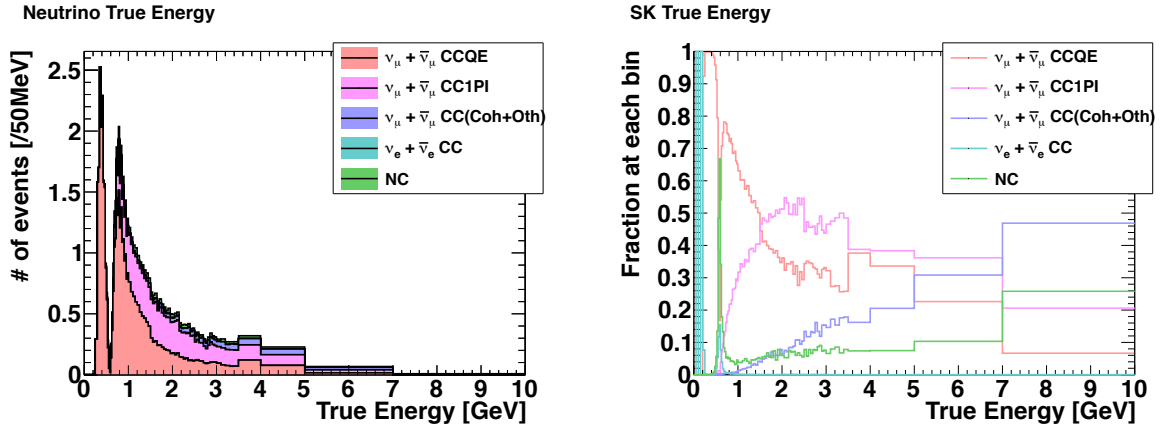


Figure 8.2: Predicted true-energy spectrum of ν_μ candidate events (left plot) and the fraction of each event category at each energy (right plot).

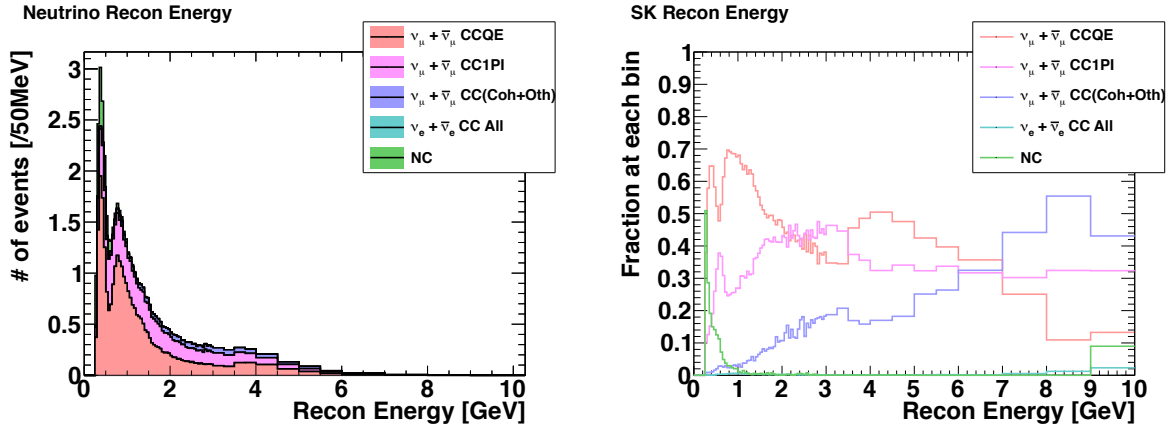


Figure 8.3: Predicted reconstructed energy spectrum of ν_μ candidate events (left plot) and the fraction of each event category at each energy (right plot).

Table 8.4: Predicted number of SK ν_μ events with neutrino oscillations ($\sin^2 2\theta_{23}, \Delta m_{32}^2 = 1.0, 2.4 \times 10^{-3}$) at 3.01×10^{20} POT.

Category	Before ND280 fit		After ND280 fit		After-fit/Before-fit Ratio
	Number	Fraction[%]	Number	Fraction[%]	
$\nu_\mu + \bar{\nu}_\mu$ CCQE	35.4	54.9	32.1	55.1	0.90
$\nu_\mu + \bar{\nu}_\mu$ CC1 π	20.3	31.4	18.2	31.1	0.90
$\nu_\mu + \bar{\nu}_\mu$ CCCoh	0.53	0.8	0.51	0.9	0.96
$\nu_\mu + \bar{\nu}_\mu$ CCOth	4.2	6.4	4.0	6.8	0.95
$\nu_e + \bar{\nu}_e$ CC	0.15	0.2	0.14	0.2	0.93
All NC1 π C	2.2	3.4	1.8	3.0	0.80
All NCOth	1.8	2.8	1.6	2.8	0.89
Total	64.5		58.3		0.90

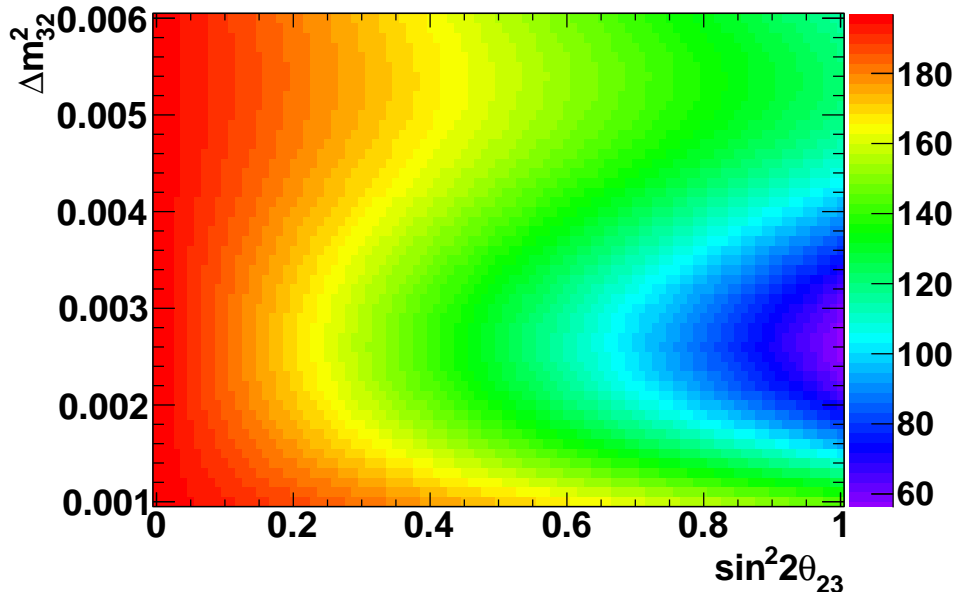


Figure 8.4: Expected total number of ν_μ candidate events for each oscillation parameter points at 3.01×10^{20} POT

8.2 Systematic parameters

The systematic uncertainties on the predicted number of ν_μ and reconstructed energy spectrum are built into the $N_{exp}(E_i^{rec})$ calculation (Eq. 8.5) via systematic parameters, \mathbf{f} . The correlation among systematic parameters are included by the covariance matrix in the likelihood. The contents of \mathbf{f} are:

$$\mathbf{f} = (\mathbf{f}^{flux}, \mathbf{f}^{xsec}, \mathbf{f}^{SK}, f^{e-scale})^T, \quad (8.9)$$

where:

\mathbf{f}^{flux} : Beam flux systematic parameters.

\mathbf{f}^{xsec} : Neutrino interaction cross-section parameters.

\mathbf{f}^{SK} : Systematic parameters representing combined SK detection efficiency error and the uncertainties of final state interaction (FSI) and the secondary interaction (SI) in SK

$f^{e-scale}$: SK energy scale systematic parameter.

In this analysis, 43 systematic parameters are used and summarized in Table. 8.5. Figure 8.5 shows the correlation matrix and fractional error size of all systematic parameters.

8.2.1 Beam flux systematics parameters

As mentioned, since the contribution from the uncertainties of ν_e and $\bar{\nu}_e$ flux were found to be negligible ($\sim 0.02\%$), only uncertainties of ν_μ and $\bar{\nu}_\mu$ are considered. The flux systematic parameters \mathbf{f}^{flux} change the flux normalization as a function of neutrino energy as:

$$\Phi_{SK}^F(E_\nu) \rightarrow f^{flux}(F, E_\nu^j) \cdot \Phi_{SK}^F(E_\nu) \quad (E_\nu^j < E_\nu < E_\nu^{j+1}), \quad (8.10)$$

where the binning of E_ν is defined in Table 8.6.

Table 8.5: Summary of systematic parameters used in the oscillation analysis. No.0~15 systematic parameters are categorized into the beam flux systematics parameters. No.16~33 systematic parameters are categorized into the neutrino interaction cross-section systematics parameters. Other systematic parameters are categorized into SK detection efficiency and FSI-SI systematics parameters. The SK detection and FSI-SI parameters (indicated by *) are combined into the common parameters having a size of quadratic sum of uncertainties. E_ν (E^{rec}) represents the true (reconstructed) energy in GeV unit.

No.	Parameter	Before ND280 fit		After ND280 fit	
		Value	Error(1σ)[%]	Value	Error(1σ)[%]
0~15	Beam flux	1	9.3~18.9	0.90~1.01	7.0~14.2
16	M_A^{QE} [GeV]	1.21	37.2	1.27	16.0
17	M_A^{RES} [GeV]	1.41	15.6	1.22	10.5
18	CCQE norm ($E_\nu < 1.5$)	1	11	0.95	8.6
19	CCQE norm ($E_\nu = 1.5 \sim 3.5$)	1	30	0.71	20.9
20	CCQE norm ($E_\nu > 3.5$)	1	30	1.35	22.5
21	CC1 π norm ($E_\nu < 2.5$)	1.15	31.7	1.37	20.4
22	CC1 π norm ($E_\nu > 2.5$)	1	40	1.02	28.2
23	CC other shape [GeV]	0	40	(same as before fit)	
24	Spectral function	0(Off)	100(On)	(same as before fit)	
25	E_b [MeV]	27	33.3	(same as before fit)	
26	p_F [MeV]	225	13.3	(same as before fit)	
27	CCcoh norm	1	100	(same as before fit)	
28	NC1 π C norm	1	30	(same as before fit)	
29	NC0th norm	1	30	(same as before fit)	
30	$\sigma_{\nu_e}/\sigma_{\nu_\mu}$	1	3	(same as before fit)	
31	W-shape [MeV]	87.7	51.7	(same as before fit)	
32	Pi-less delta decay	0	20	(same as before fit)	
33	$\sigma_{\bar{\nu}}/\sigma_\nu$	1	40	(same as before fit)	
34*	SK eff. for $\nu_\mu, \bar{\nu}_\mu$ CCQE ($E^{rec} < 0.4$)	1	2.5	(same as before fit)	
35*	SK eff. for $\nu_\mu, \bar{\nu}_\mu$ CCQE ($E^{rec} = 0.4 \sim 1.1$)	1	3.9	(same as before fit)	
36*	SK eff. for $\nu_\mu, \bar{\nu}_\mu$ CCQE ($E^{rec} > 1.1$)	1	9.5	(same as before fit)	
37*	SK eff. for $\nu_\mu, \bar{\nu}_\mu$ CCnonQE	1	20	(same as before fit)	
38*	SK eff. for ν_e CC	1	100	(same as before fit)	
39*	SK eff. for All NC	1	111	(same as before fit)	
40	SK energy scale	1	2.3	(same as before fit)	
34*	FSI-SI for $\nu_\mu, \bar{\nu}_\mu$ CCQE ($E^{rec} < 0.4$)	1	0.004	(same as before fit)	
35*	FSI-SI for $\nu_\mu, \bar{\nu}_\mu$ CCQE ($E^{rec} = 0.4 \sim 1.1$)	1	0.07	(same as before fit)	
36*	FSI-SI for $\nu_\mu, \bar{\nu}_\mu$ CCQE ($E^{rec} > 1.1$)	1	0.3	(same as before fit)	
37*	FSI-SI for $\nu_\mu, \bar{\nu}_\mu$ CCnonQE	1	8.7	(same as before fit)	
38*	FSI-SI for ν_e CC	1	1.1	(same as before fit)	
39*	FSI-SI for All NC	1	7.7	(same as before fit)	

Table 8.6: Binning of the flux systematic parameters

Flavor	Neutrino energy binning [GeV]	# of bins
ν_μ	0–0.4, 0.4–0.5, 0.5–0.6, 0.6–0.7, 0.7–1.0, 1.0–1.5, 1.5–2.5, 2.5–3.5, 3.5–5.0, 5.0–7.0, 7.0–30	11
$\bar{\nu}_\mu$	0–0.7, 0.7–1.0, 1.0–1.5, 1.5–2.5, 2.5–30	5

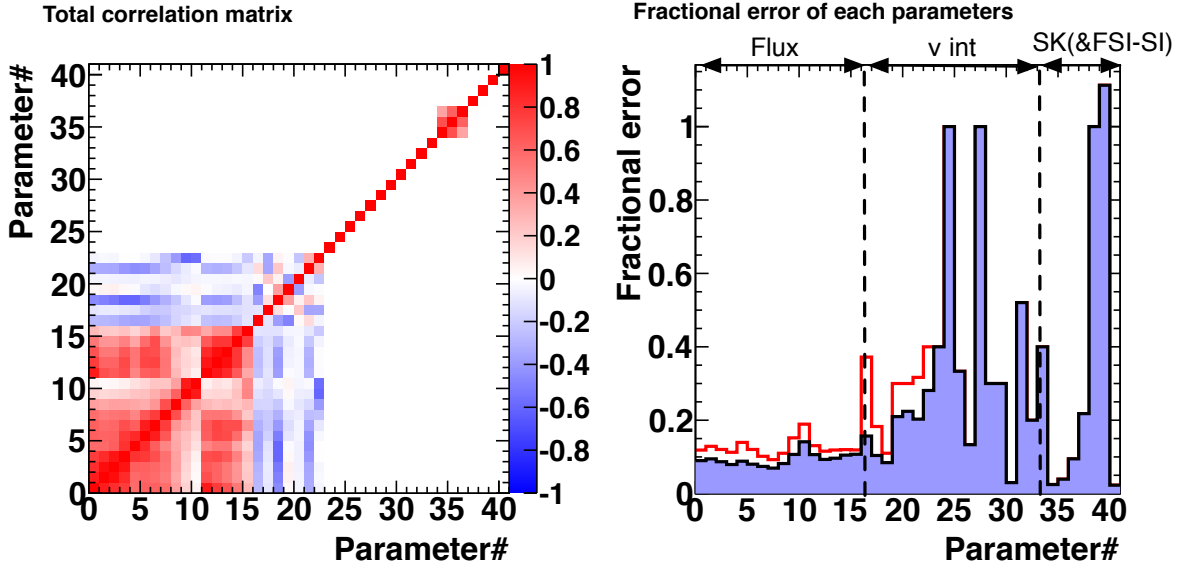


Figure 8.5: The correlation matrix (left) and diagonal fractional errors (right) of systematic parameters used in the oscillation analysis with the ND280 data constraint. The red histogram in the right figure represents the fractional errors before the ND280 fit.

8.2.2 Neutrino interaction systematics parameters

As described in Sec. 5.2, the neutrino interaction parameters f^{xsec} are classified into following categories: model parameters represented with the response function (f_{res}^{xsec}), absolute cross-section parameters (f_{norm}^{xsec}), and the cross-section difference parameter ($f_{\sigma_{\bar{\nu}}/\sigma_{\nu}}^{xsec}$ or $f_{\sigma_{\nu_e}/\sigma_{\nu_{\mu}}}^{xsec}$). The cross-section difference is applied to only CC events. The neutrino interaction systematic parameters change the cross-section value as:

$$\sigma_{SK}^{F,I}(E_{\nu}) \rightarrow \sigma_{SK}^{F,I}(E_{\nu}) \times f_{norm}^{xsec}(I, E_{\nu}) \cdot R(F, I, E_{\nu}, E^{rec}, f_{res}^{xsec}) \cdot \begin{cases} 1 & F = \nu_{\mu}, \\ f_{\sigma_{\bar{\nu}}/\sigma_{\nu}}^{xsec} & F = \bar{\nu}_{\mu}, \\ f_{\sigma_{\nu_e}/\sigma_{\nu_{\mu}}}^{xsec} & F = \nu_e, \\ f_{\sigma_{\bar{\nu}}/\sigma_{\nu}}^{xsec} \cdot f_{\sigma_{\nu_e}/\sigma_{\nu_{\mu}}}^{xsec} & F = \bar{\nu}_e, \end{cases} \quad (8.11)$$

where R is the response functions described at Sec. 5.3.

8.2.3 SK detection efficiency and FSI-SI systematics parameters

The systematic parameters for the SK efficiency, FSI and SI uncertainties are combined. Their error sizes are evaluated as the quadratic sum of all error sources. These systematic parameters change the SK detection efficiency as:

$$\epsilon_{SK}^{F,I}(E^{rec}) \rightarrow f^{SK}(F, I, E^{rec}) \cdot \epsilon_{SK}^{F,I}(E^{rec}) \quad (8.12)$$

8.2.4 SK energy scale systematic parameter

The uncertainty from the SK energy scale is given as the parameter to change the E^{rec} in the SK detector response function, which is represented as $f_{e-scale}^{SK}$. The SK energy scale systematic parameter changes the reconstructed energy for the response function as:

$$R^{F,I}(E_{\nu} \rightarrow E^{rec}) \rightarrow R^{F,I}(E_{\nu} \rightarrow E^{rec} \cdot (1 + f_{e-scale}^{SK})). \quad (8.13)$$

8.2.5 Effect of systematic uncertainties

To demonstrate the effect of each systematic uncertainty, N_{exp}^{tot} is calculated by changing each systematic parameter by $\pm 1 \sigma$ (σ is the error size) shown in Table 8.5. To check the individual effect, the systematic parameters of SK detection efficiency and FSI-SI are handled separately. Table 8.7 summarizes the effect of each systematic parameter. For the systematic uncertainties of beam flux (16 parameters), the correlation between them is considered.

As previously described, there is a significant anti-correlation between flux normalizations and some of neutrino interaction parameters which are refined by the ND280 measurements. To estimate the effect of the systematic uncertainties including their correlation, many toy-experiments (20000) of the systematic parameters are generated according to the multivariate normal distribution and the covariance matrix. For each toy-experiment, $N_{exp}(E^{rec})$ and N_{exp}^{tot} is calculated. The central values of systematic parameters in multivariate normal distribution is set to the values after the ND280 measurement. Figure 8.6 shows the N_{exp}^{tot} and $N_{exp}(E^{rec})$ distribution for the 20000 toy-experiments. The uncertainties of N_{exp}^{tot} and $N_{exp}(E^{rec})$ are reduced significantly by the ND280 measurement.

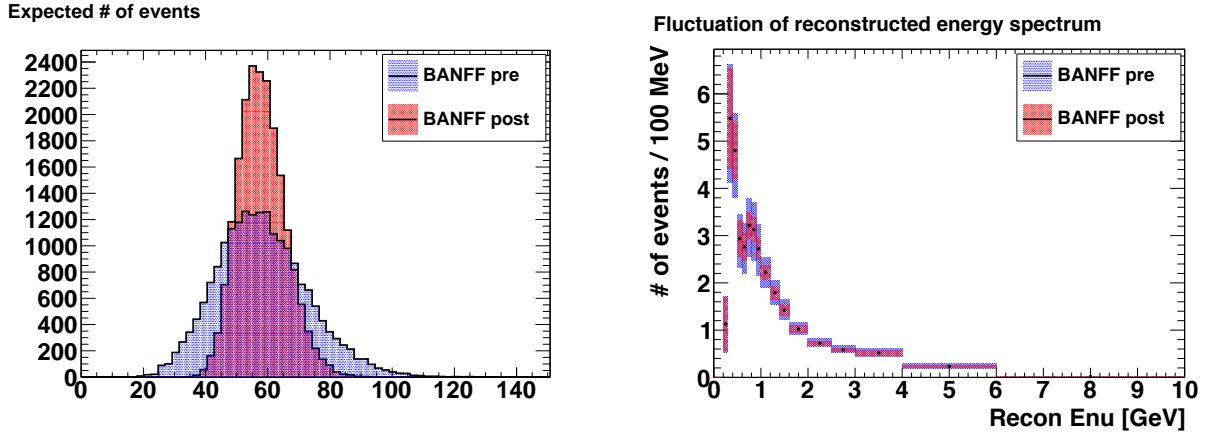


Figure 8.6: Fluctuation of the N_{exp}^{tot} and $N_{exp}(E^{rec})$ at $(\sin^2 2\theta_{23}, \Delta m_{32}^2) = (1.0, 2.4 \times 10^{-3})$. Left: the distribution of the N_{exp}^{tot} based on 20000 toy-experiments by systematic parameter variations. Right: the $N_{exp}(E^{rec})$ distribution with errors which correspond to r.m.s. from 20000 toy-experiments.

Table 8.8 summarizes the contribution of following systematic error sets to the uncertainty on the N_{exp}^{tot} .

- Flux and ν interaction (ND280 meas.): the neutrino flux and neutrino interaction parameters which are refined by the ND280 measurement.
- Other ν interaction: neutrino interaction parameters which are not extrapolated to the SK prediction.
- SK detector: the SK detector systematic parameters
- FSI-SI: the FSI-SI systematic parameters

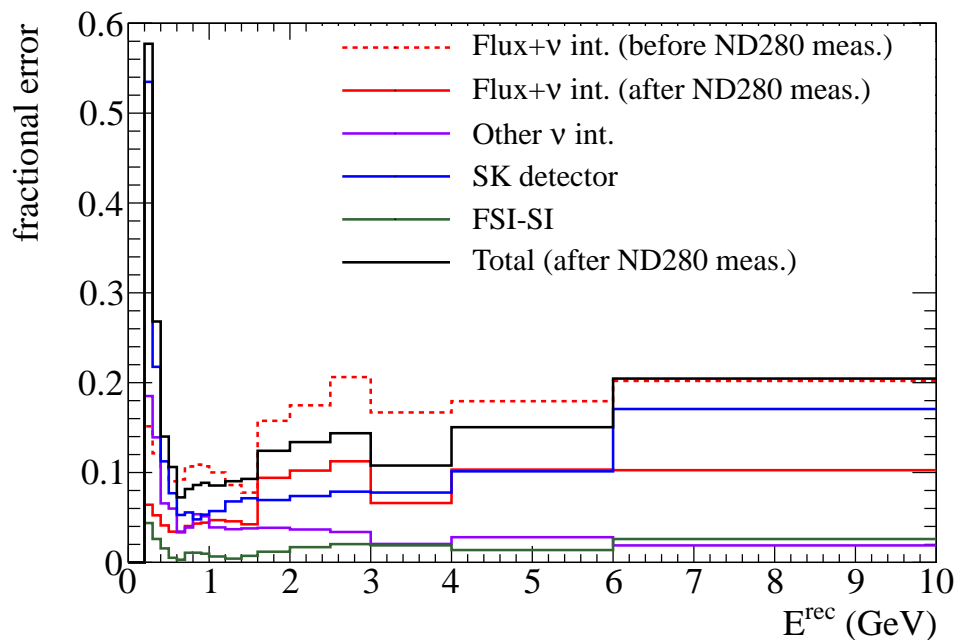
Fig. 8.7 shows the fractional uncertainties of the $N_{exp}(E^{rec})$ for each systematic error set. The dominant error sources at the energy around the oscillation maximum are the SK detection efficiencies (especially for CC nonQE and NC event). The next ones are neutrino interaction errors not refined by the ND280 measurement. The systematic uncertainties of the flux normalizations and interaction parameters refined by the ND280 measurement are small. The effects of FSI-SI errors are smallest.

Table 8.7: Summary of the fractional change (in %) of the number of ν_μ candidate events under a change to each systematic parameter by $\pm 1\sigma$ (σ represents the error size) of before and after ND280 fit shown in Table. 8.5. E_ν and E^{rec} are in the unit of GeV.

Systematic uncertainty	$(\sin^2 2\theta_{23}, \Delta m_{32}^2) = (1.0, 2.4 \times 10^{-3})$	
	Before ND280 meas.	After ND280 meas.
Beam flux	± 10.5	± 7.1
M_A^{QE}	14.0/-16.9	+6.3/-7.0
M_A^{RES}	7.6/-7.4	+4.4/-4.3
CCQE norm ($E_\nu < 1.5$)	± 4.5	± 3.5
CCQE norm ($E_\nu = 1.5 \sim 3.5$)	± 4.3	± 3.0
CCQE norm ($E_\nu > 3.5$)	± 1.4	± 1.0
CC1 π norm ($E_\nu < 3.5$)	± 4.4	± 2.9
CC1 π norm ($E_\nu > 3.5$)	± 4.8	± 3.4
CC other shape	± 0.8	(same as before fit)
E_b	+0.2/-0.06	(same as before fit)
p_F	+0.1/-0.02	(same as before fit)
Spectral function	± 0.7	(same as before fit)
CCcoh norm	± 0.9	(same as before fit)
NC1 π C norm	± 0.9	(same as before fit)
NC0th norm	± 0.8	(same as before fit)
$\sigma_{\nu_e}/\sigma_{\nu_\mu}$	± 0.01	(same as before fit)
W-shape	± 0.4	(same as before fit)
Pi-less delta decay	± 6.2	(same as before fit)
$\sigma_{\bar{\nu}}/\sigma_\nu$	± 2.4	(same as before fit)
SK eff. for $\nu_\mu, \bar{\nu}_\mu$ CCQE ($E^{rec} < 0.4$)	± 0.16	(same as before fit)
SK eff. for $\nu_\mu, \bar{\nu}_\mu$ CCQE ($E^{rec} = 0.4 \sim 1.1$)	± 0.95	(same as before fit)
SK eff. for $\nu_\mu, \bar{\nu}_\mu$ CCQE ($E^{rec} > 1.1$)	± 2.3	(same as before fit)
SK eff. for $\nu_\mu, \bar{\nu}_\mu$ CC nonQE	± 7.8	(same as before fit)
SK eff. for $\nu_e, \bar{\nu}_e$ CC	± 0.25	(same as before fit)
SK eff. for All NC	± 6.4	(same as before fit)
SK energy scale	(not changed)	(same as before fit)
FSI-SI for $\nu_\mu, \bar{\nu}_\mu$ CCQE ($E^{rec} < 0.4$)	± 0.00	(same as before fit)
FSI-SI for $\nu_\mu, \bar{\nu}_\mu$ CCQE ($E^{rec} = 0.4 \sim 1.1$)	± 0.02	(same as before fit)
FSI-SI for $\nu_\mu, \bar{\nu}_\mu$ CCQE ($E^{rec} > 1.1$)	± 0.07	(same as before fit)
FSI-SI for $\nu_\mu, \bar{\nu}_\mu$ CC nonQE	± 3.4	(same as before fit)
FSI-SI for $\nu_e, \bar{\nu}_e$ CC	± 0.00	(same as before fit)
FSI-SI for All NC	± 0.45	(same as before fit)

Table 8.8: Uncertainty (r.m.s./mean in %) on the N_{exp}^{tot} from each systematic error source set.

Errors	$(\sin^2 2\theta_{23}, \Delta m_{32}^2) = (1.0, 2.4 \times 10^{-3})$	
	Before ND280 meas.	After ND280 meas.
Flux and ν interaction (ND280 meas.)	21.7	4.2
Other ν interaction	6.2	6.2
SK detector	10.5	10.5
FSI-SI	3.5	3.5
Total	25.3	13.5


 Figure 8.7: Fractional error on the $\rho(E^{rec})$ with several systematic error sets. The fractional error is r.m.s./mean of 20000 toy-experiments at each E^{rec} bin.

8.3 Sensitivity

The sensitivity to determine $\sin^2 2\theta_{23}$ and Δm_{32}^2 at the 3.01×10^{20} POT is evaluated as follows:

1. Systematic parameters are generated randomly based on the multivariate normal distribution having the total covariance matrix.
2. The N_{exp}^{tot} and PDF are calculated based on the generated systematic parameters,
3. The observed number of events in this toy-experiment is determined as a random number following Poisson distribution having mean value of N_{exp}^{tot} .
4. For each of N_{obs}^{tot} events, the reconstructed energy is assigned according to the PDF given in the step 2.

The 1000 toy-experiments are generated for $(\sin^2 2\theta_{23}, \Delta m_{32}^2) = (1.0, 2.4^{-3})$. The sensitivity contour is drawn by applying the constant $\Delta\chi^2$ limit on the average $\Delta\chi^2$ of 1000 toy-experiments. The constant $\Delta\chi^2$ limit is calculated by the following steps:

1. The χ^2 for each point of $(\sin^2 2\theta_{23}, \Delta m_{32}^2)$ is calculated. The systematic parameters are allowed to change to obtain minimum χ^2 at that point.
2. The χ^2 differences ($\Delta\chi^2$) between the minimum χ^2 at each point and the minimum χ^2 in whole $(\sin^2 2\theta_{23}, \Delta m_{32}^2)$ points are calculated. The best $(\sin^2 2\theta_{23}, \Delta m_{32}^2)$ correspond to the point with the minimum χ^2 in the whole points.

The 68% (90%) sensitivity contour is defined the region where $\Delta\chi^2$ is less than 2.30 (4.61). To estimate the contribution of various systematic error sets, the sensitivity contours are estimated for each systematic error set (as shown in Table 8.8). In practice, one systematic parameter set is varied and others are fixed (e.g. the contribution of "ND280 meas" is estimated with systematic parameters of "Flux and ν interaction" varied and others fixed). The contribution of purely statistical errors ("No syst") is estimated with all systematic parameters fixed. Figure 8.8 shows the sensitivity contour for $(\sin^2 2\theta_{23}, \Delta m_{32}^2)$ with 90% confidence level (C.L.) and the $\Delta\chi^2$ distribution for $\sin^2 2\theta_{23}$ and Δm_{32}^2 . Table. 8.9 summarizes the 90% confidence interval (C.I.). The statistical uncertainty is a dominant error source to limit the sensitivity with the current POT. Among systematic parameters, the effect of SK detector efficiency & FSI-SI systematic parameters are dominant. The contribution of systematic uncertainties in the ND280 fit is reduced by the ND280 measurements.

Table 8.9: Summary of 90% C.I. sensitivities at 3.01×10^{20} POT. The C.I. for $\sin^2 2\theta_{23}$ (Δm_{32}^2) is evaluated at $\Delta m_{32}^2 = 2.4 \times 10^{-3}$ ($\sin^2 2\theta_{23} = 1.0$).

Source	$\sin^2 2\theta_{23}$ ($\delta(\sin^2 2\theta_{23})$)	Δm_{32}^2 ($\delta(\Delta m_{32}^2)$) [eV ²]
No syst	0.93~1.0 (0.070)	$2.09 \times 10^{-3} \sim 2.74 \times 10^{-3}$ (7.5×10^{-4})
ND280 fit(before fit)	0.861~1.0 (0.139)	$1.93 \times 10^{-3} \sim 2.76 \times 10^{-3}$ (8.3×10^{-4})
ND280 fit(after fit)	0.929~1.0 (0.071)	$2.08 \times 10^{-3} \sim 2.74 \times 10^{-3}$ (7.6×10^{-4})
Other ν int.	0.927~1.0 (0.073)	$2.08 \times 10^{-3} \sim 2.76 \times 10^{-3}$ (7.8×10^{-4})
SK&FSI-SI	0.925~1.0 (0.075)	$2.08 \times 10^{-3} \sim 2.74 \times 10^{-3}$ (7.6×10^{-4})
All syst (after fit)	0.922~1.0 (0.078)	$2.06 \times 10^{-3} \sim 2.77 \times 10^{-3}$ (7.9×10^{-4})

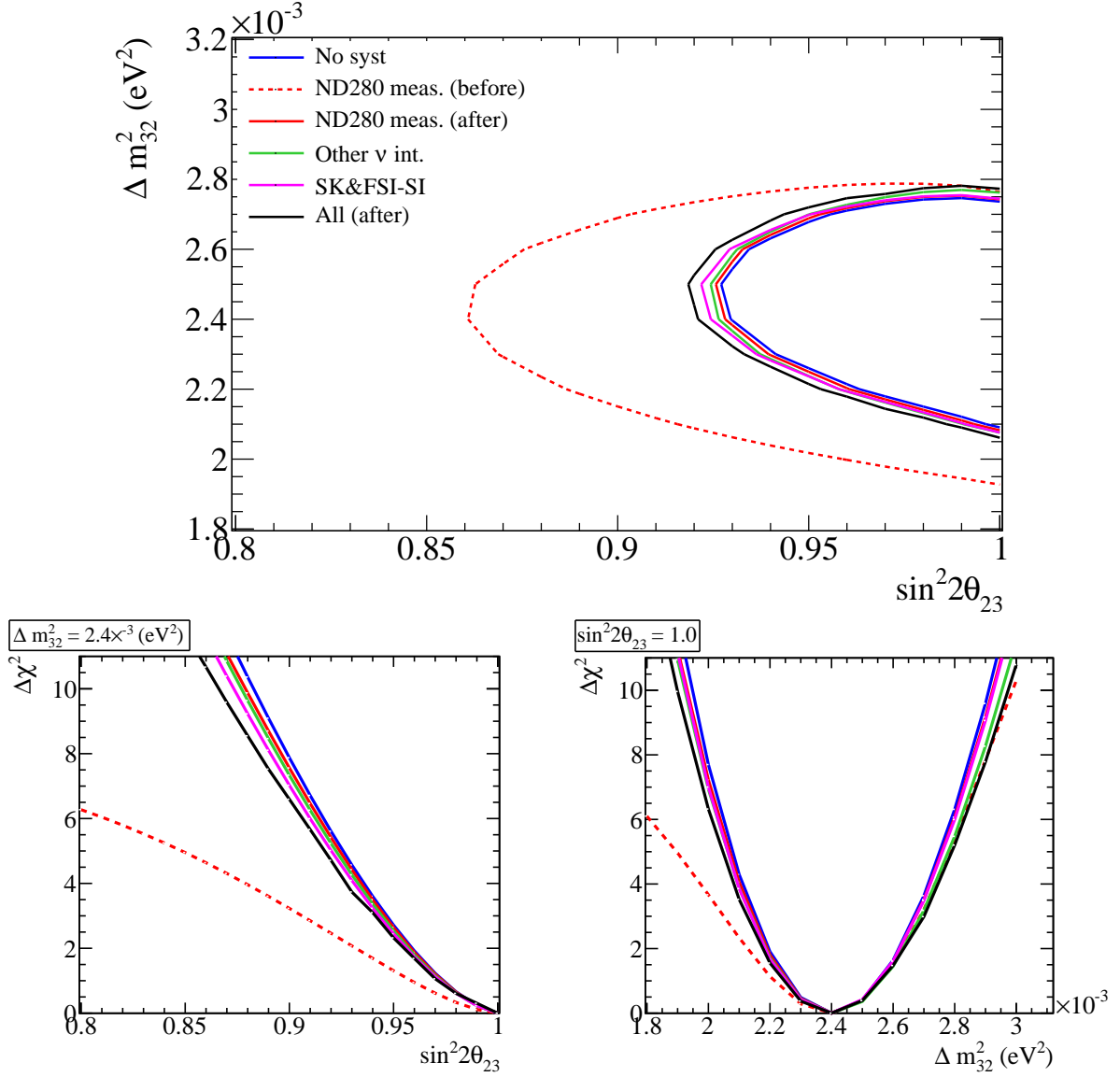


Figure 8.8: Expected allowed contour (upper) and the $\Delta\chi^2$ slices for $(\sin^2 \theta_{23}, \Delta m_{32}^2) = (1.0, 2.4 \times 10^{-3})$ at 3.01×10^{20} POT (lower two plots). The allowed contour shows the line with 90% C.L. based on the constant $\Delta\chi^2$ limit. The each color represents the each contribution as shown in the upper plot.

8.4 Results with Run 1+2+3 data

8.4.1 Fit result

As described in Sec. 6.3.4, the number of the selected events during Run 1+2+3 is 58. The reconstructed energy spectrum is shown in Fig. 6.18. From these data, the best fit oscillation parameters are obtained as:

$$(\sin^2 2\theta_{23}, \Delta m_{32}^2) = (1.00, 2.45 \times 10^{-3} \text{eV}^2).$$

These values are consistent with the current knowledge as shown in Sec 1.1.4. The expected number of events is 57.97 and the expected energy distribution is shown in Fig 8.9 for the best fit value of $(\sin^2 2\theta_{23}, \Delta m_{32}^2)$. Data is consistent with the prediction at the best fit point. For supplement, the systematic parameters at the best fit point are checked. The pull is calculated for each systematic parameter as follows:

$$\text{pull}^i = \frac{f_{post}^i - f_{prior}^i}{\sigma_{post}^i}, \quad (8.14)$$

where i is the systematic parameter number, f_{prior}^i and f_{post}^i is the value of the systematic parameter before and after the oscillation fit, and σ_{post}^i is the error estimated in the fit. The pull for each systematic parameter is shown in Fig. 8.10. All pulls are close to zero. This is because the systematic errors affect the prediction weakly since the statistical error is dominant at current statistics. Anyway, variations of systematic parameters are reasonable.

The goodness-of-fit are evaluated to confirm the validity of the best fit point. For this purpose, the simple binned χ^2 for the goodness-of-fit (χ_{gof}^2) is defined as:

$$\chi_{gof}^2 = 2 \sum_i \left[n_i^{obs} \times \ln \left(\frac{n_i^{obs}}{n_i^{exp}} \right) + n_i^{exp} - n_i^{obs} \right] + \mathbf{f}^T V^{-1} \mathbf{f}, \quad (8.15)$$

where n_i^{obs} (n_i^{exp}) is the observed (expected) number of events in the i th reconstructed energy bin. The energy binning for χ_{gof}^2 is (0.0~0.4, 0.4~0.7, 0.7~1.0, 1.0~2.0, 2.0~30.0) (GeV). This was determined so that each bin has about 10 events. The χ_{gof}^2 obtained with the data is 1.771 at the best fit point. To evaluate the goodness-of-fit, the possible χ_{gof}^2 distribution is estimated from the toy-experiments generated with the best fit oscillation parameters. The oscillation fit is performed for each toy-experiment, and the χ_{gof}^2 is calculated. The distribution of χ_{gof}^2 of 1000 toy-experiments is shown in Fig 8.11. The χ_{gof}^2 of real data (1.771) is compared with the χ_{gof}^2 distribution. The 85% of toy-experiments have larger χ_{gof}^2 s than that of real data. The χ_{gof}^2 of real data sits well within the expected χ_{gof}^2 distribution shown in Fig. 8.11. This confirms that the result of the data fit reasonably reproduces the data.

For further investigation of the data fit, the data fit is performed with the following likelihood combinations:

- $\mathcal{L}_{norm} \cdot \mathcal{L}_{shape}$ (all systematic parameters are fixed): to remove the contribution of systematic parameters to check the bias by them.
- $\mathcal{L}_{norm} \cdot \mathcal{L}_{syst}$ or $\mathcal{L}_{shape} \cdot \mathcal{L}_{syst}$: to separate into the normalization-only and shape constraint-only constraint.

The fit results are shown in Table 8.10. The fitted energy distributions are shown in Fig. 8.12. The fit results between all likelihoods are consistent within the allowed region. The systematic parameters show no significant bias.

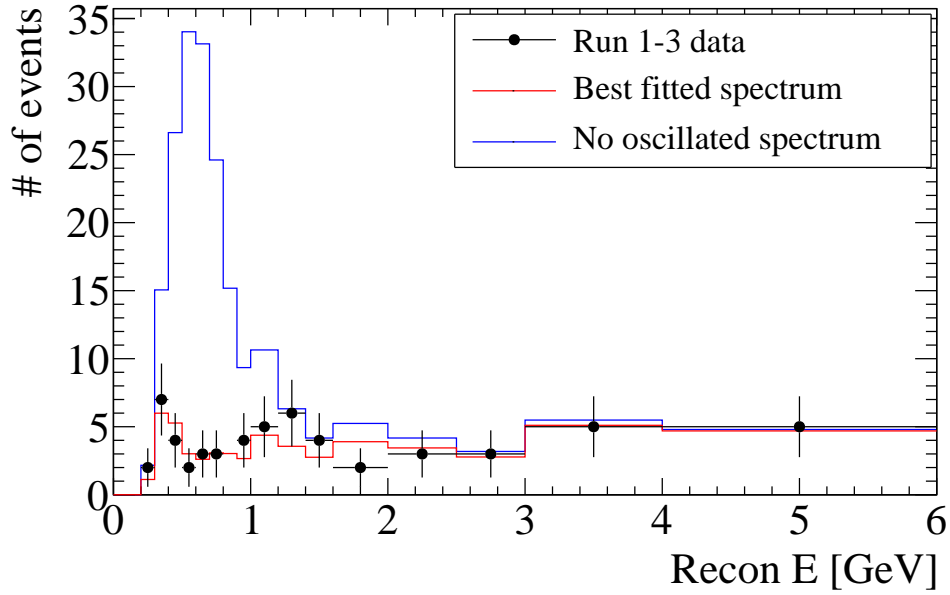


Figure 8.9: The E_{ν}^{rec} distribution. The points shows the data. The lines shows the prediction with the best fit oscillation parameters (red) and that for no-oscillation case (blue). The error bars on data represent the statistical error.

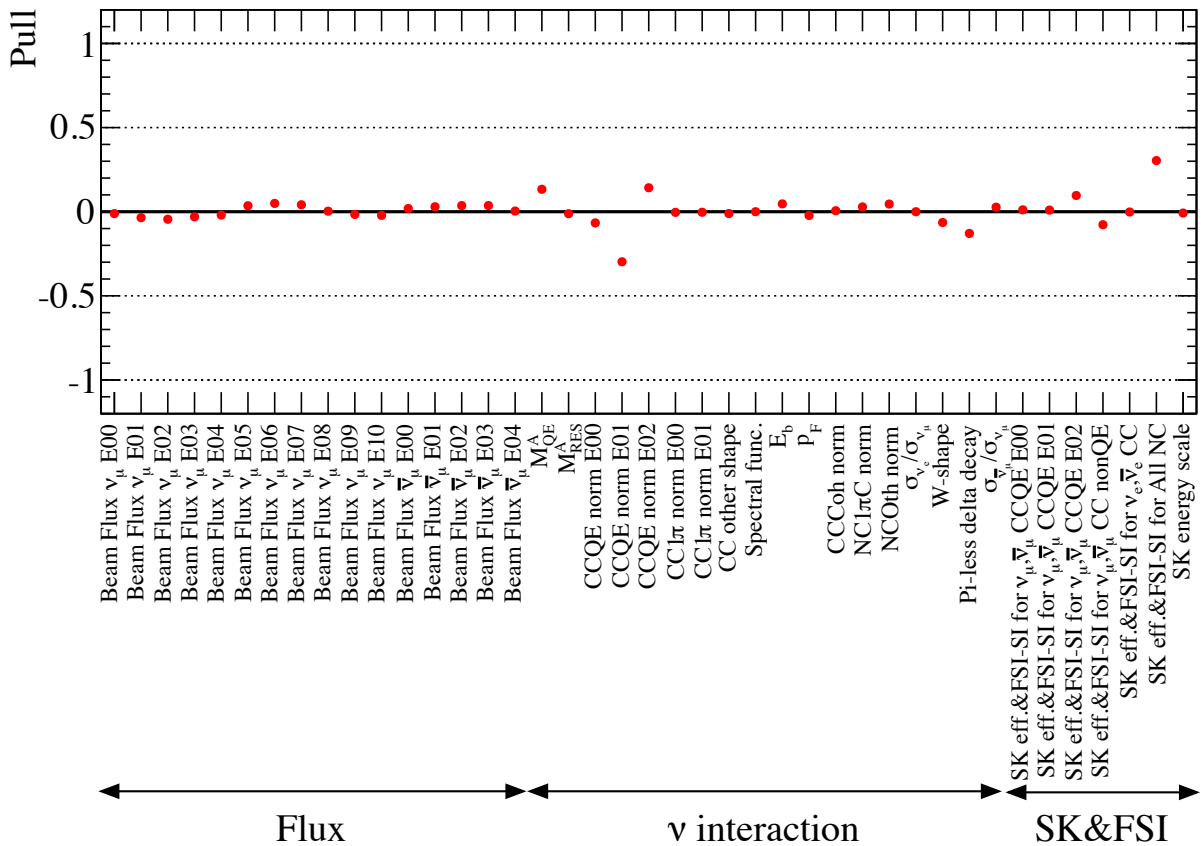


Figure 8.10: Pulls of systematic parameters at the best fit point. The horizontal axis represents the labels of systematic parameters shown in Table 8.5.

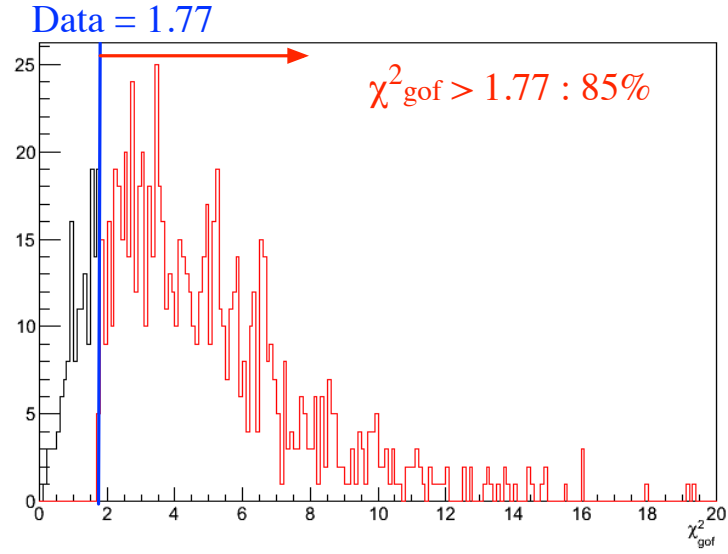
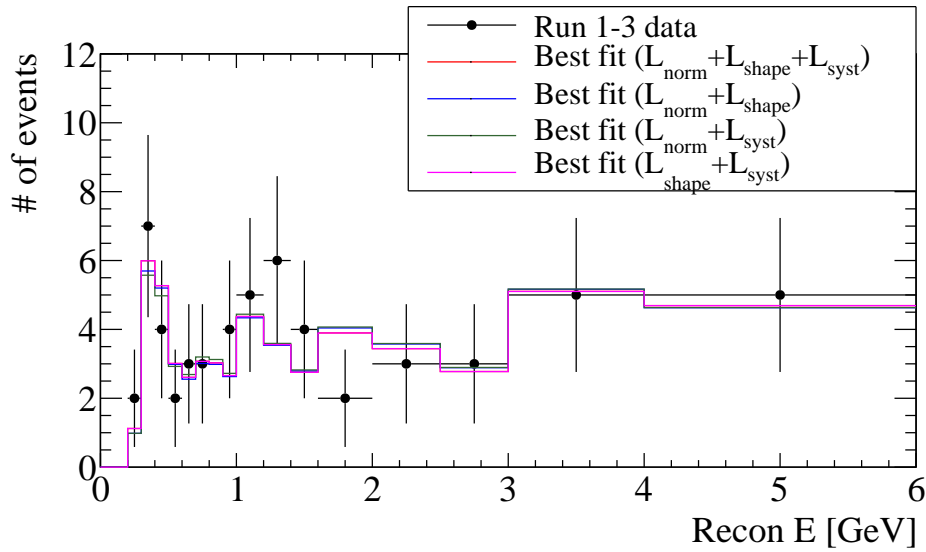

 Figure 8.11: χ^2_{gof} distribution for 1000 toy-experiments.

Table 8.10: Fit results for several likelihoods

Likelihood	Fitted N_{SK}^{exp}	$\sin^2 2\theta_{23}$	Δm_{32}^2 (eV ²)
$\mathcal{L}_{norm} \cdot \mathcal{L}_{shape} \cdot \mathcal{L}_{syst}$	57.97	1.00	2.45×10^{-3}
$\mathcal{L}_{norm} \cdot \mathcal{L}_{shape}$	57.61	1.00	2.46×10^{-3}
$\mathcal{L}_{norm} \cdot \mathcal{L}_{syst}$	58.00	1.00	2.42×10^{-3}
$\mathcal{L}_{norm} \cdot \mathcal{L}_{syst}$	57.94	1.00	2.44×10^{-3}


 Figure 8.12: The E_{ν}^{rec} distribution. The points shows the data. The lines shows the prediction with the best fit oscillation parameters for the each likelihood combination. The error bars on data represent the statistical error.

8.4.2 Allowed region

For the estimation of the allowed region around a physical boundary, strictly, the constant $\Delta\chi^2$ limit is not correct because this method is fully based on the Gaussian approximation. To obtain the correct allowed region, the Feldman & Cousins (F&C) method [96] is used. The F&C method determines the critical value of χ^2 (called $\Delta\chi_{crit}^2$) to evaluate the confidence level individually for each point of $(\sin^2 2\theta_{23}, \Delta m_{32}^2)$, while the constant χ^2 limit uses the same critical value for all points. In the F&C method, the allowed region is estimated as follows: a lot of (10000) toy experiments are generated for each point. For the each point, the $\Delta\chi_{crit}^2$ for $\alpha\%$ C.L. is determined such that the α of the toy experiments have $\Delta\chi_{toy}^2 < \Delta\chi_{crit}^2$. The $\Delta\chi_{toy}^2$ is for each toy experiment is calculated as:

$$\Delta\chi_{toy}^2 = \chi_{toy,true}^2 - \chi_{toy,best}^2 \quad (8.16)$$

where $\chi_{toy,true}^2$ is the χ_{toy}^2 calculated by using the true oscillation parameters at that point (the systematic parameters are varied to minimize the χ_{toy}^2), and $\chi_{toy,best}^2$ is the χ_{toy}^2 minimized by the oscillation fit. The allowed region for the best fit of data is defined such that the regions with $\Delta\chi_{data}^2 < \Delta\chi_{crit}^2$ are contained within the contour. The $\Delta\chi_{data}^2$ is calculated for real data by using the same way as the $\Delta\chi_{toy}^2$. Figure 8.13 and 8.14 shows the $\Delta\chi_{crit}^2$ distributions for 68% and 90% C.L. respectively. Figure 8.15 shows the $\Delta\chi_{data}^2$ distribution. By comparing these distribution, the allowed region of the obtained $(\sin^2 2\theta_{23}, \Delta m_{32}^2)$ is evaluated as Fig. 8.16. The error sizes of $\sin^2 2\theta_{23}$ and Δm_{32}^2 are evaluated as the 68% confidence interval:

$$(\sin^2 2\theta_{23}, \Delta m_{32}^2) = (1.00_{-0.04}^{+0}, 2.45 \pm 0.19 \times 10^{-3} \text{eV}^2).$$

The 90% confidence interval is:

$$\begin{aligned} 0.932 < \sin^2 2\theta_{23} \leq 1.0 & \quad (\text{at } \Delta m_{32}^2 = 2.45 \times 10^{-3} [\text{eV}^2]), \\ 2.15 \times 10^{-3} < \Delta m_{32}^2 [\text{eV}^2] < 2.75 \times 10^{-3} & \quad (\text{at } \sin^2 2\theta_{23} = 1.0). \end{aligned}$$

Figure 8.17 shows the comparison of the allowed region with the F&C method and that with the constant $\Delta\chi^2$ limit. There is a slight difference between them.

Figure 8.18 shows the allowed regions with the other likelihoods combinations: $\mathcal{L}_{norm} \cdot \mathcal{L}_{shape}$ (with all systematic parameters fixed), $\mathcal{L}_{norm} \cdot \mathcal{L}_{syst}$, $\mathcal{L}_{shape} \cdot \mathcal{L}_{syst}$. These allowed region are estimated by the constant $\Delta\chi^2$ limit. The allowed region without the shape constraint is much wider than the regions with the shape constraint. This is because the the best value is determined basically as a line ($N_{SK}^{exp} = N_{SK}^{obs}$) in the $(\sin^2 2\theta_{23}, \Delta m_{32}^2)$ plane without the shape constraint and has multiple values allowed. The contributions of statistical and systematic uncertainties to the error size of $\sin^2 2\theta_{23}$ ($\delta(\sin^2 2\theta_{23})$) are evaluated as:

- Statistics uncertainty $\delta_{stat}(\sin^2 2\theta_{23}) \sim 0.06$ ($0.94 < \sin^2 2\theta_{23} \leq 1.0$).
- Statistics and systematic uncertainty $\delta_{stat+syst}(\sin^2 2\theta_{23}) \sim 0.065$ ($0.935 < \sin^2 2\theta_{23} \leq 1.0$).
- Systematic uncertainty $\delta_{syst}(\sin^2 2\theta_{23}) = \sqrt{\delta_{stat+syst}^2(\sin^2 2\theta_{23}) - \delta_{stat}^2(\sin^2 2\theta_{23})} \sim 0.025$.

Here we use the 90% confidence interval at $\Delta m_{32}^2 = 2.45 \times 10^{-3}$ (eV^2) with the constant $\Delta\chi^2$ limit. The statistical uncertainty has a dominant contribution for the allowed region at the current statistics.

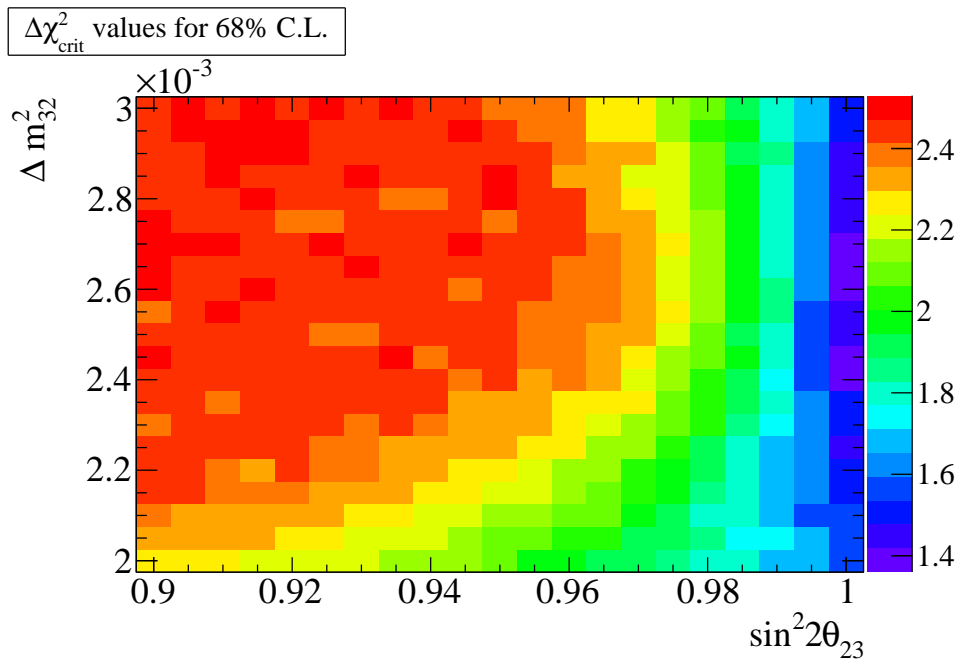


Figure 8.13: $\Delta\chi_{crit}^2$ values for 68% CL.

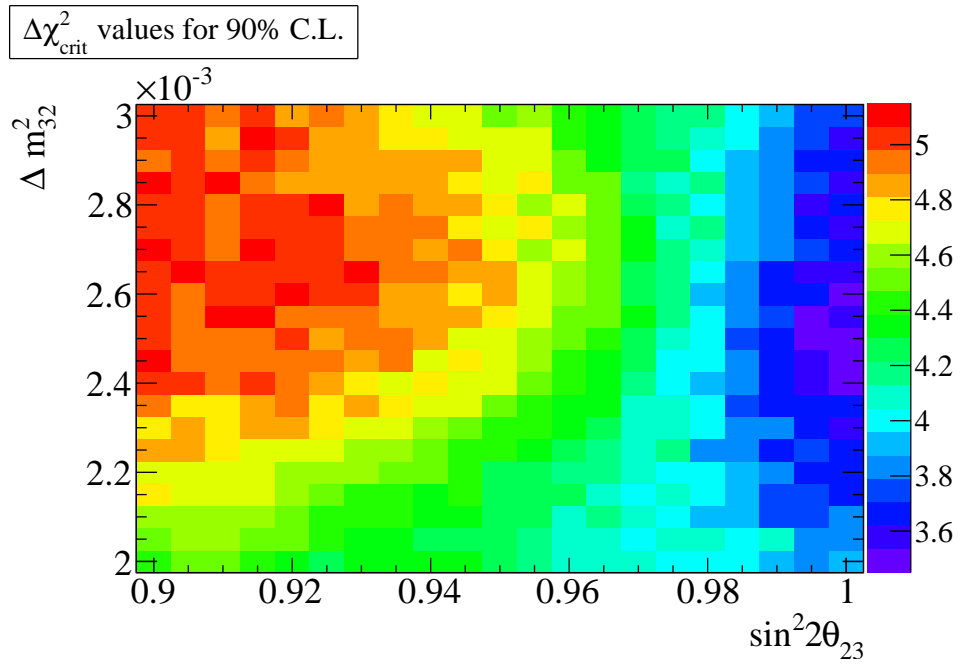


Figure 8.14: $\Delta\chi_{crit}^2$ values for 90% CL.

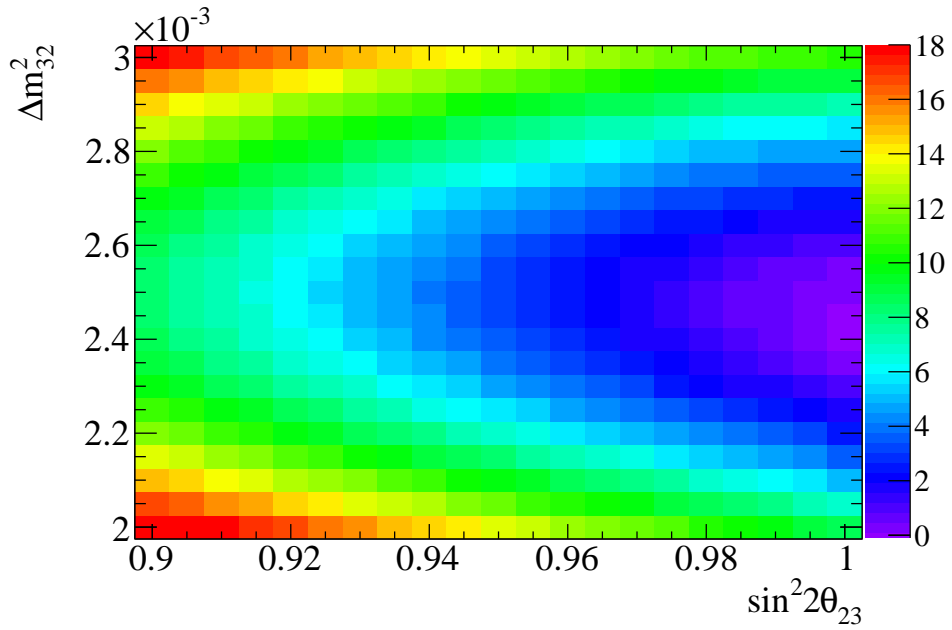


Figure 8.15: $\Delta\chi^2$ distribution for data.

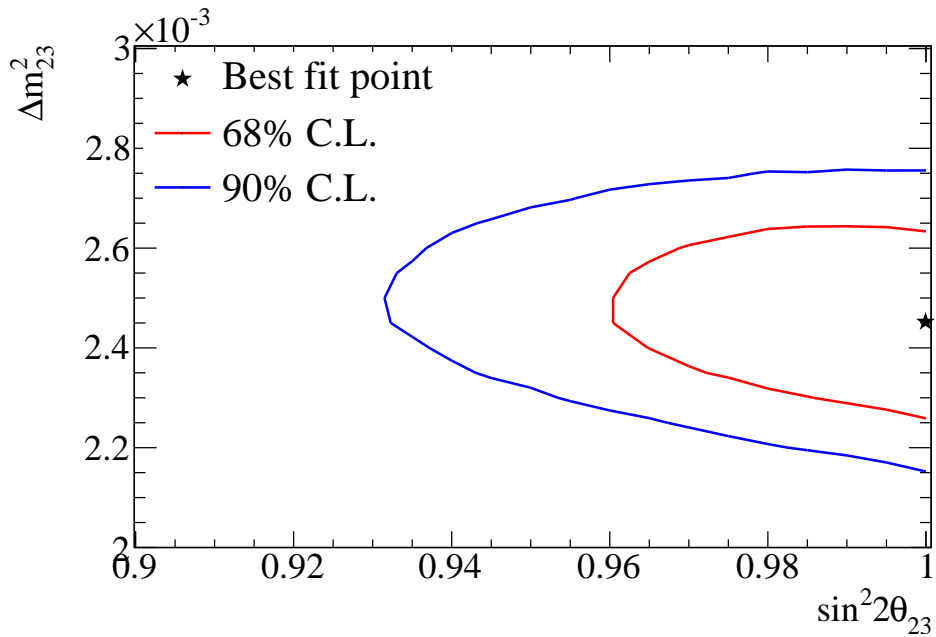


Figure 8.16: Allowed region of $(\sin^2 2\theta_{23}, \Delta m_{32}^2)$ for data. The contour is estimated with the F&C method

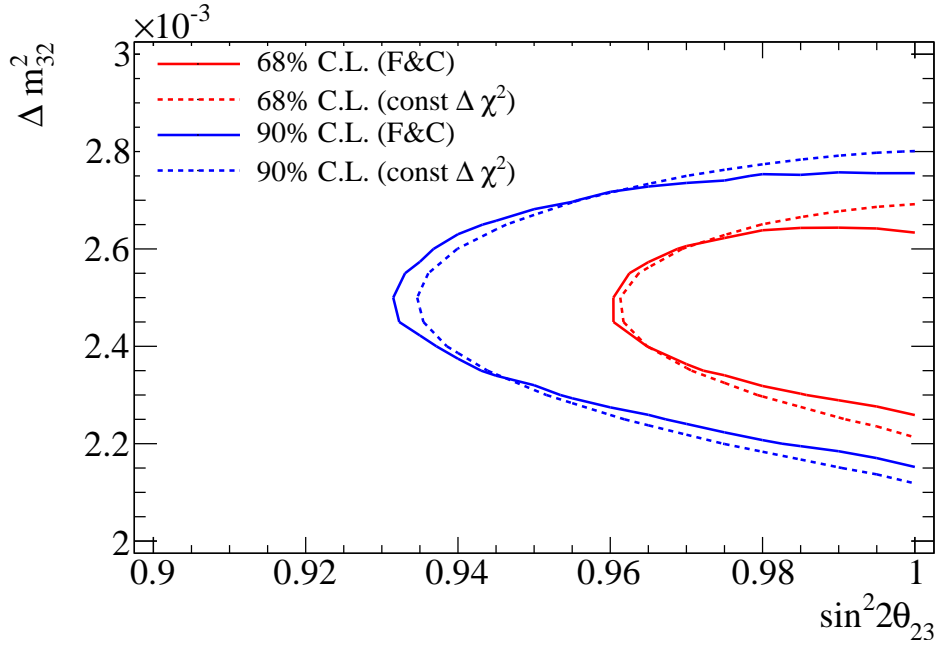


Figure 8.17: Comparison of the allowed regions of $(\sin^2 2\theta_{23}, \Delta m_{32}^2)$ for data with the F&C method and with the constant $\Delta\chi^2$ limit

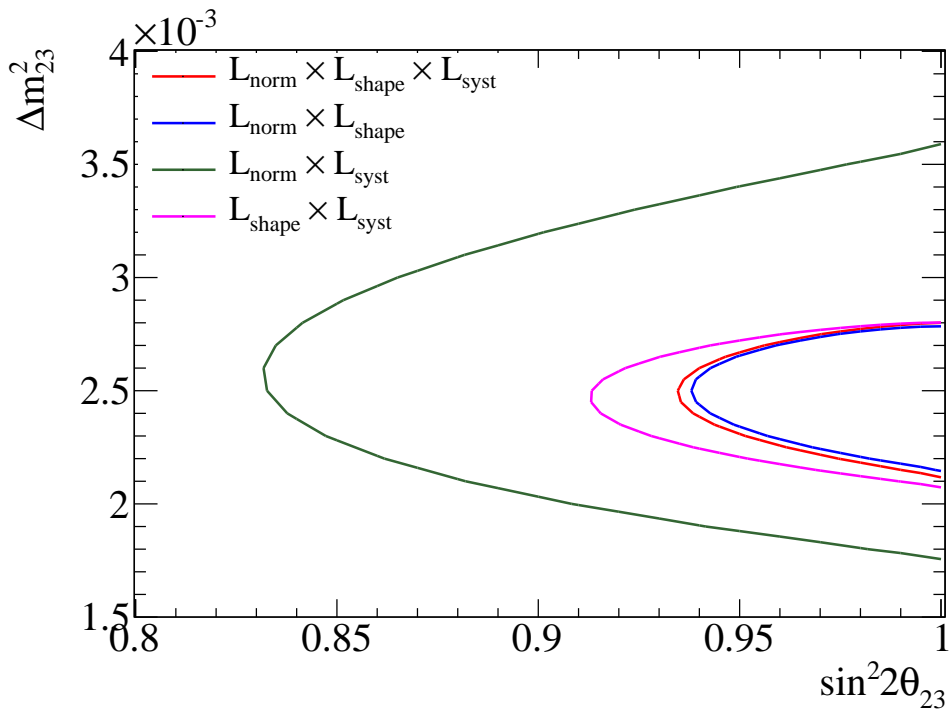


Figure 8.18: The 90% confidence level allowed region of $(\sin^2 2\theta_{23}, \Delta m_{32}^2)$ for several likelihoods combinations. These regions are estimated with the constant $\Delta\chi^2$ limit.

8.4.3 Comparison with other experimental results

Figure 8.19 shows the T2K results with results by other experiments: the MINOS long baseline experiment and the SK atmospheric neutrino measurement. The MINOS result was derived from a combined analysis of the ν_μ and $\bar{\nu}_\mu$ beam data and atmospheric neutrino data [97]. All SK results are based on the SK atmospheric measurements. The SK zenith angle analysis was performed by using the two or three flavor oscillation model (non-zero θ_{13} was taken into account in the three flavor oscillation model). The SK results were referred from the report at the international conference, *Neutrino2012* (reported by Y. itow [98]). Though the current T2K statistics is just 4% of the T2K final POT, the T2K's precision has reached to the current best precision in the world. The T2K Run 1–3 result is also consistent with the other experimental results.

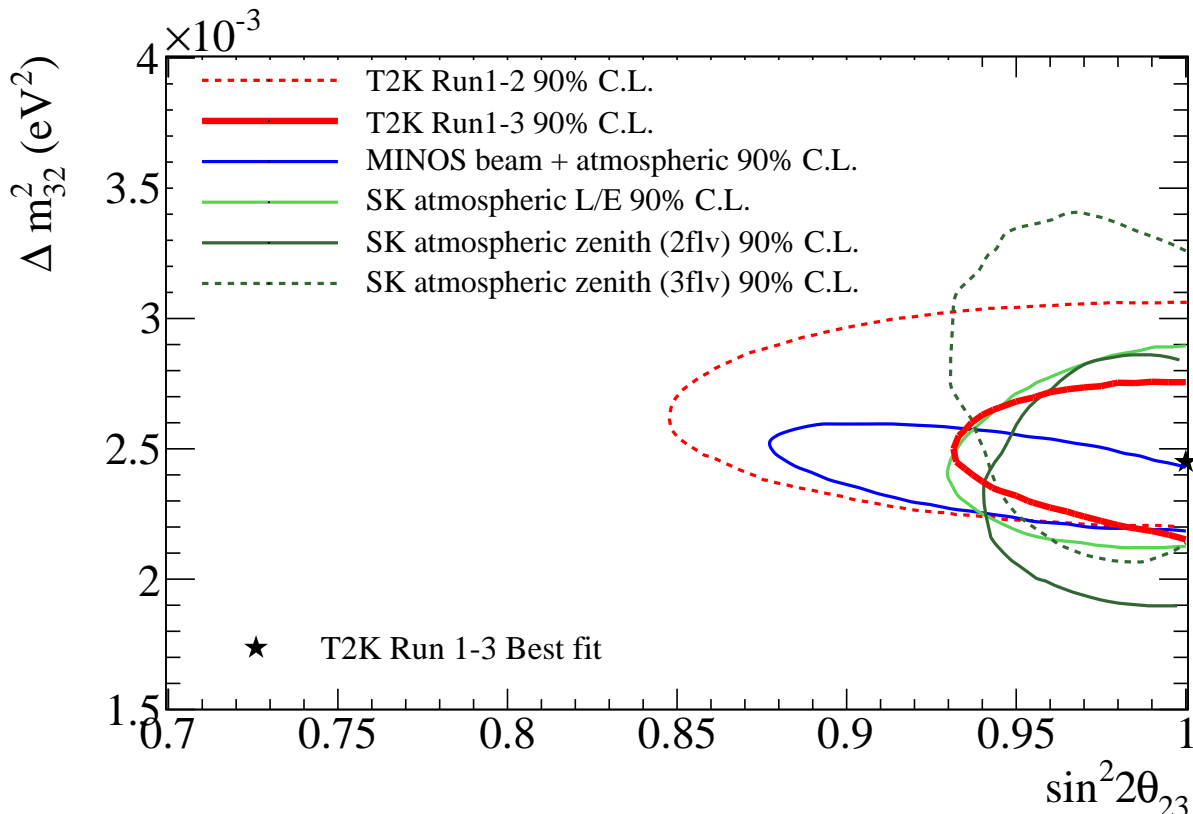


Figure 8.19: The 90% confidence regions allowed by T2K and other neutrino experiments. The results of MINOS [97] and Super-Kamiokande [98] are shown. The published T2K result [32] is based on Run 1-2 data. The SK zenith angle analysis was performed by using the two or three flavor oscillation model (shown as 2flv or 3flv).

8.4.4 Summary and prospect

We performed the oscillation analysis via the ν_μ disappearance based on 3.01×10^{20} POT data (just 4% of T2K exposure POT). The observed event rate and energy spectrum at SK are compared with the predictions including the oscillation effect. We have obtained the oscillation parameters with the errors (68% confidence interval):

$$(\sin^2 2\theta_{23}, \Delta m_{32}^2) = (1.00_{-0.04}^{+0}, 2.45 \pm 0.19 \times 10^{-3} \text{eV}^2).$$

This result is consistent with values measured by other experiments. The 90% confidence intervals are:

$$\begin{aligned} 0.932 < \sin^2 2\theta_{23} \leq 1 & \quad (\text{at } \Delta m_{32}^2 = 2.45 \times 10^{-3} [\text{eV}^2]), \\ 2.15 \times 10^{-3} < \Delta m_{32}^2 [\text{eV}^2] < 2.75 \times 10^{-3} & \quad (\text{at } \sin^2 2\theta_{23} = 1.0). \end{aligned}$$

We achieve the most precise measurement for the oscillation parameters in neutrino experiments based on the stable beam operation and well-tuned flux prediction. This precision is still inadequate to approach the unsolved problems of neutrino physics described in Sec. 1.1.5 (also worse than the precision of the global fit result as shown in Table 1.2). For example, for the observation of the CP asymmetry via ν_e appearance, the leading term in $P(\nu_\mu \rightarrow \nu_e)$ as Eq. 1.13 has a large ($\sim 20\%$) uncertainty so that it is difficult to distinguish the contribution of the CP violation term. The θ_{23} is still consistent with the maximal mixing ($\sin^2 2\theta_{23} > 0.96$), and the $\sin^2 \theta_{23}$ can be > 0.5 and < 0.5 within its error. We need the more precise measurement of the oscillation parameters.

Since the uncertainty of the flux and neutrino interaction are reduced by the careful tuning based on the external data and by the measurement at ND280, the sensitivity is limited by the statistical uncertainty. The sensitivity with more statistics is estimated by using the toy-experiment. The generated toy-experiments correspond to: 1.8×10^{21} POT (23% of T2K exposure POT, expected statistics until 2015), and 7.8×10^{21} POT (T2K final statistics). Figure 8.20 shows the expected future sensitivity of T2K based on 4000 toy-experiments with the constant $\Delta\chi^2$ limit. The sensitivity is estimated both with statistical uncertainty only and with the current systematic uncertainties. Table 8.11 summarizes the 90% confidence interval for $\sin^2 2\theta_{23}$ at $\Delta m_{23}^2 = 2.45 \times 10^{-3} \text{ eV}^2$. The sensitivity of T2K is expected to achieve the target sensitivity, $\delta(\sin^2 2\theta_{23}) \sim 0.01$ at 7.8×10^{21} POT without systematic uncertainties.

Table 8.11: The 90% confidence intervals for $\sin^2 2\theta_{23}$ and the contribution of statistical and systematic uncertainties with more statistics in future (at $\Delta m_{23}^2 = 2.45 \times 10^{-3} \text{ eV}^2$). These interval are evaluated with the constant $\Delta\chi^2$ limit.

POT	90% (stat+syst)	$\delta_{stat}(\sin^2 2\theta_{23})$	$\delta_{syst}(\sin^2 2\theta_{23})$
1.8×10^{21}	0.972~1.0	0.022	0.017
7.8×10^{21}	0.987~1.0	0.008	0.010

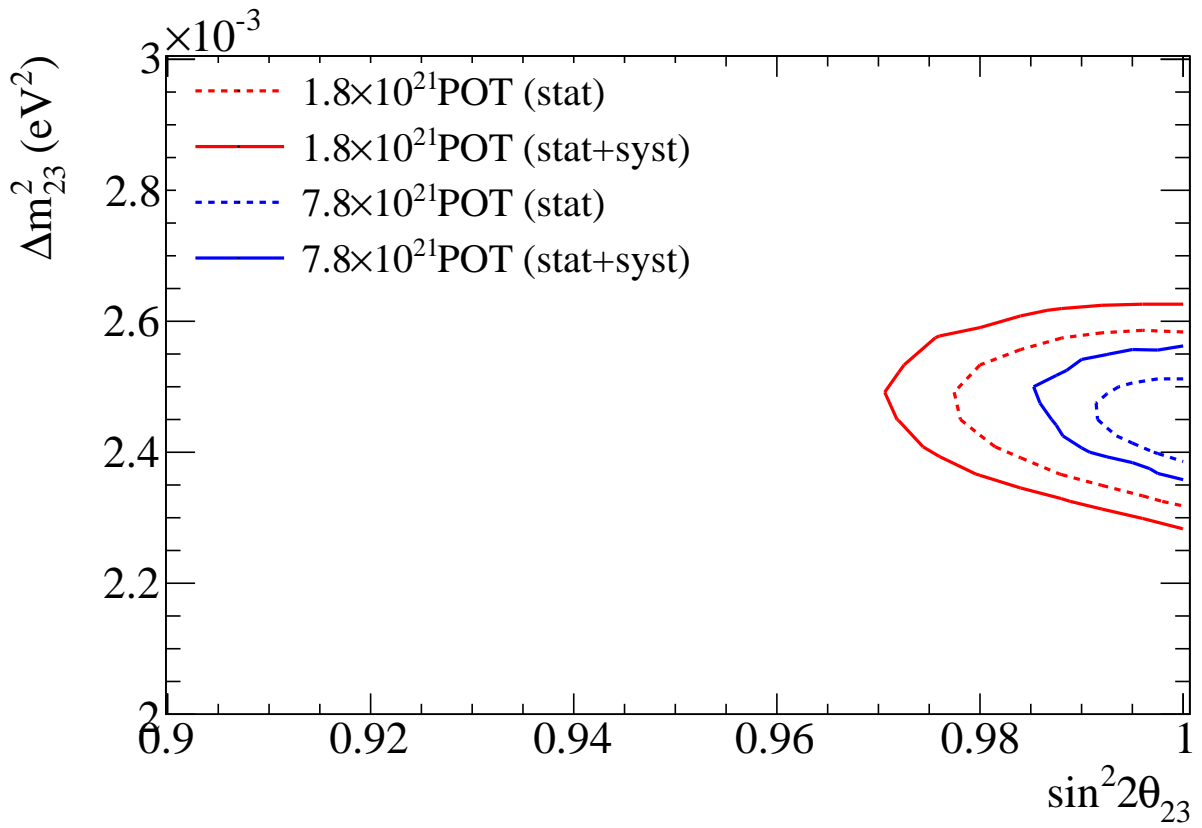


Figure 8.20: The sensitivity of T2K with more statistics in future. The allowed contour shows the line with 90% C.L. estimated with the constant $\Delta\chi^2$ limit.

Chapter 9

Conclusion

The T2K long baseline neutrino oscillation experiment has been performed to study physics of neutrino oscillations. The original T2K's purpose is to measure the oscillation parameters, $\sin^2 2\theta_{23}$ and Δm_{32}^2 via the ν_μ disappearance and measure the non-zero θ_{13} via the ν_e appearance. In T2K, a muon neutrino beam is produced with the proton beam in J-PARC, and is observed at the near neutrino detector (ND280) and Super-Kamiokande detector (SK). The J-PARC high power proton beam and the gigantic SK enable T2K to conduct the long baseline experiment with the highest neutrino production ever. An off-axis method has been adopted to adjust the peak energy of the neutrino flux at SK to the oscillation maximum. The oscillation parameters are determined by comparing the event rate and energy spectrum of ν_μ measured at SK with the prediction including the oscillation effect. The SK prediction are constructed by the neutrino flux prediction, the neutrino-nucleus interaction models and the detector response. The experiment was started in January 2010, and we analyzed the data of 3.01×10^{20} POT until June 2012 in this thesis. This data corresponds to 4% fraction of T2K design full statistics.

The stable beam operation is one of the most important issues both for the quick accumulation of data and the protection of the beam equipment from the high intensity proton beam. For this purpose, we monitor and control the beam properties: the proton beam parameters (intensity, position, and profile), neutrino beam direction and the horn currents. Especially, since the neutrino energy spectrum at SK depends on the off-axis angle in the off-axis method, the neutrino beam direction has to be tuned within 1 mrad. The neutrino beam direction is monitored by MUMON and INGRID. MUMON measures the beam direction indirectly by measuring those of the muon beam spill-by-spill, while INGRID measures the beam direction directly. The stable beam operation was achieved during data taking and the efficiency of the beam data taking was 99.7%. The intensity of the neutrino beam was stable within 2% from the nominal rate which is the nominal intensity of the neutrino beam divided by the POT. The neutrino beam direction was confirmed to be stable within 0.4 mrad. The neutrino beam with good quality was efficiently delivered to the ND280 and SK.

The main subject of this thesis is the improvement of the neutrino flux prediction, which is one of the most important part of the sensitivity to the oscillation parameters. The neutrino flux is predicted by the neutrino flux simulation. The precision of the flux simulation is affected by the uncertainties of the hadron production models and uncertainties of the beam properties. The hadron production models, which are dominant error sources in the flux simulation, were tuned based on the external hadron production data (CERN NA61/SHINE, and so on). The CERN NA61/SHINE was performed to provide the hadron production data for T2K. The beam properties were measured precisely by beam monitors in T2K. The fluxes at ND280 and SK were predicted as a function of neutrino energy precisely (e.g. the systematic uncertainty of the SK flux was estimated as 12% at the energy around the oscillation maximum).

The predicted SK flux and neutrino-nucleus interaction models is further refined by the

ND280 measurements. The predicted ND280 flux and interaction models were refined by comparing the event rate and energy spectrum of neutrinos measured at ND280 with the prediction. The predicted SK flux was refined based on the refined ND280 flux by using the correlation between fluxes at SK and ND280 (e.g. the systematic uncertainty of the SK flux was reduced to 8% at the energy around the oscillation maximum).

Fifty eight ν_μ events were observed at SK during the data taking, while the expectation is 57.97 at the best fit point. From the measurements and precise predictions, we obtained the $\sin^2 2\theta_{23}$ and Δm_{32}^2 :

$$(\sin^2 2\theta_{23}, \Delta m_{32}^2) = (1.00_{-0.04}^{+0}, 2.45 \pm 0.19 \times 10^{-3} \text{eV}^2).$$

and the 90% confidence interval of:

$$\begin{aligned} 0.932 < \sin^2 2\theta_{23} \leq 1.0 & \quad (\text{at } \Delta m_{32}^2 = 2.45 \times 10^{-3} [\text{eV}^2]), \\ 2.15 \times 10^{-3} < \Delta m_{32}^2 [\text{eV}^2] < 2.75 \times 10^{-3} & \quad (\text{at } \sin^2 2\theta_{23} = 1.0). \end{aligned}$$

We have provided the best precision of the measurement of $\sin^2 2\theta_{23}$ and Δm_{23}^2 with just 4% of T2K exposure statistics in the neutrino experiments. We have achieved this precision thanks to the stable beam operation and the well-tuned flux prediction. This precision is still inadequate to approach the unsolved problems of neutrino physics (e.g. for the observation of the CP asymmetry via the ν_e appearance, the leading term in $P(\nu_\mu \rightarrow \nu_e)$ has a large ($\sim 20\%$) uncertainty). We can further improve our precision with more data.

List of Tables

1.1	Sensitivity of several neutrino oscillation experiments	4
1.2	The best-fit values of the three-neutrino oscillation parameters, obtained from a global fit of the current neutrino oscillation data [26], including the T2K [12] and MINOS [13] (but not the Daya Bay and RENO) results. The PDG (Particle Data Group) average of the results of the three reactor experiments [14–16] is given in the last line. The 1σ accuracy is defined as the $1/6$ of the $\pm 3\sigma$ interval.	5
1.3	Summary of the fractional change of the amplitude for the leading and CP violation terms in the ν_e appearance probability	6
2.2	Summary of the horn and target alignment uncertainties. x , y , and z represent the horizontal, vertical position and the parallel position to the proton beam axis. The θ_H and θ_V represent the rotation in the horizontal and vertical plane.	24
2.3	Number of spills and POT after each good quality data selection	29
2.4	Summary of the data taking, horn current setting, good beam spills and accumulated POT for oscillation analysis	30
2.5	Summary of measured proton beam parameters in the horizontal direction at the baffle for each run period : center position (X) and angle (Θ_X), Gaussian width (σ), emittance (ϵ), and Twiss (α) parameter.	31
2.6	Summary of measured proton beam parameters in the vertical direction at the baffle for each run period : center position (Y) and angle (Θ_Y), Gaussian width (σ), emittance (ϵ), and Twiss (α).	31
2.7	Systematic errors and correlations for the position and angle of the beam center at the baffle front surface. The $X(Y)$ and $\Theta_X(\Theta_Y)$ stand for horizontal (vertical) position and angle of the beam center, respectively.	32
4.1	The fraction of the neutrino flux by the final hadron in the interaction history.	41
4.2	Differential hadron production data used for the T2K neutrino flux predictions.	41
4.3	Inelastic and production cross-section data used for the T2K neutrino flux predictions.	41
4.4	The fraction of the total SK flux by flavor in bins of the neutrino energy. The fractions in parentheses are relative to the total flux over all neutrino energies.	50
4.5	Summary of the fractional errors in the kaon production data. The error in the overall normalization is σ_N . The error for a given data bin is $\sigma_{\Delta p \Delta \theta}$. The error in the normalization for a given angular bin is $\sigma_{\Delta \theta}$	54
4.6	Summary of the off-axis angle error (σ_{OA}) in each period	61
5.1	Summary of nominal values and errors of neutrino interaction parameters. The nominal values and errors are constrained by external data. E_ν represents the neutrino energy (GeV).	73

6.1	Summary of data taking of INGRID	77
6.2	Summary of INGRID detector systematic errors	82
6.3	Summary of the predicted and measured INGRID beam center and event rate for Run 1. The systematic error is only from the uncertainty of the detection efficiency and does not include uncertainties of the flux and neutrino interaction cross-section.	83
6.4	Neutrino beam direction measured by INGRID	84
6.5	Summary of data taking at ND280	85
6.6	Summary of all ND280 detector systematic errors.	87
6.7	Summary of the ND280 measurement in Run1+2+3. Here, the error represents the only statistic error.	87
6.8	Summary of data taking at SK	91
6.9	Summary of the SK detector systematic errors	93
6.10	Breakdown of the systematic errors for the SK detector efficiency	94
6.11	Summary of events passing each selection step for Run 1+2+3 data and the MC expectation.	97
6.12	Summary of events passing each selection step for Run 1+2+3 data and the MC expectation (non-oscillation).	98
7.1	List of parameters varied in the ND280 fit.	100
7.2	Summary of ND280 CCQE-like and CC nonQE-like events before and after the ND280 fit	101
7.3	Summary of neutrino flux and interaction parameters extrapolated to SK	102
7.4	Energy binning for the SK ν_μ and $\bar{\nu}_\mu$ flux normalization parameters	103
8.1	Binning of the true neutrino energy (E_ν) used in the oscillation analysis	108
8.2	Binning of the reconstructed neutrino energy (E^{rec}) used in the oscillation analysis	108
8.3	Summary of oscillation parameter values except for $\sin^2 2\theta_{23}$ and Δm_{32}^2 used in Prob3++.	109
8.4	Predicted number of SK ν_μ events with neutrino oscillations ($\sin^2 2\theta_{23}, \Delta m_{32}^2 = 1.0, 2.4 \times 10^{-3}$) at 3.01×10^{20} POT.	110
8.5	Summary of systematic parameters used in the oscillation analysis	112
8.6	Binning of the flux systematic parameters	112
8.7	Summary of the fractional change (in %) of the number of ν_μ candidate events under a change to each systematic parameter by $\pm 1\sigma$	115
8.8	Uncertainty (r.m.s./mean in %) on the N_{exp}^{tot} from each systematic error source set.	116
8.9	Summary of 90% C.I. sensitivity at 3.01×10^{20} POT.	117
8.10	Fit results for several likelihoods	121
8.11	The 90% confidence intervals for $\sin^2 2\theta_{23}$ and the contribution of statistical and systematic uncertainties with more statistics in future (at $\Delta m_{23}^2 = 2.45 \times 10^{-3}$ eV ²). These interval are evaluated with the constant $\Delta\chi^2$ limit.	127

List of Figures

1.1	Two neutrino oscillation scenario.	2
1.2	Oscillation probability for ν_μ disappearance (two flavor oscillation)	4
1.3	ν_e appearance probability in the three flavor model	7
1.4	Two possible hierarchy cases for the neutrino masses	8
1.5	Bird's eye view of T2K layout	9
1.6	Expected neutrino energy spectrum	10
2.1	Schematic view of T2K components	12
2.2	The relation between neutrino energy (E_ν) and pion momentum (p_π) in the pion two body decay.	13
2.3	Muon neutrino survival probability at 295 km and neutrino fluxes for different off-axis angles.	14
2.4	Schematic view of the beam spill	15
2.7	Side view of the secondary beamline	18
2.8	Cross section view of horns	18
2.9	Muon beam monitor	19
2.10	Overview of SK event timing	20
2.11	Overview of GPS system	21
2.12	Overview of timing calculation	21
2.13	History of the time difference between GPS 1 and GPS 2	22
2.14	Distribution of the time difference	23
2.15	T2K near neutrino detectors	25
2.16	Schematic view of INGRID	26
2.17	Schematic view of INGRID module	27
2.18	Schematic view of ND280	28
2.19	Schematic view of SK	28
2.20	Cross section view of the SK water tank.	29
2.21	History of total accumulated protons and protons per pulse for the good quality beam data. The solid line shows the accumulated POT. The dot points show the number of protons per pulse.	30
2.22	History of the measured horn current during all data taking period. Top: Horn 1, Middle: Horn 2, Bottom: Horn 3. The current is stable within 5kA from mean values of each data taking period.	33
2.23	History of the measured muon profile center at MUMON in all run periods. A top and bottom figure shows the profile center in the horizontal(X) and the vertical(Y), respectively. A dashed line corresponds to 1 mrad at MUMON.	34
3.1	Overview of the ν_μ disappearance analysis flow.	36
4.1	Overview of the neutrino flux simulation	38

4.2	Flow chart of how we predict the neutrino fluxes at T2K detectors.	38
4.3	A two-dimensional projected view of the geometrical set-up in the FLUKA simulation of the baffle and the target.	39
4.4	Labels of hadrons produced in each hadronic interaction.	41
4.5	The phase space of π^\pm and K^+ contributing to the predicted neutrino flux at SK, and the regions covered by NA61/SHINE measurements.	42
4.6	The differential production weights from NA61/SHINE data for π^\pm	45
4.7	The differential production weights for GCALOR (Al) from A-scaled NA61/SHINE data for π^\pm	45
4.8	Diagram of a particle with momentum p_1 interacting a material A to produce a particle with momentum p_2	47
4.9	Ratio of the hadron interaction weighted flux over the not weighted flux for ν_μ (upper left), $\bar{\nu}_\mu$ (upper right), ν_e (lower left), $\bar{\nu}_e$ (lower right). These ratio is calculated based on the 250kA horn current simulation.	47
4.10	The flux predictions for the SK far detector broken down by the neutrino parent particle type. The ν_μ (upper left), $\bar{\nu}_\mu$ (upper right), ν_e (bottom left), and $\bar{\nu}_e$ (bottom right) fluxes are shown. The error bars, which is too small to be seen in most of the region, are MC statistical error.	48
4.11	The flux predictions for the ND280 near detector broken down by the neutrino parent particle type. The ν_μ (upper left), $\bar{\nu}_\mu$ (upper right), ν_e (bottom left), and $\bar{\nu}_e$ (bottom right) fluxes are shown. The error bars, which is too small to be seen in most of the region, are MC statistical error.	49
4.12	The fractional error on the NA61/SHINE measurements in each of the p - θ bins. The gap at π^+ momentum of 1.0-1.2 GeV/c is a region with no NA61/SHINE data points.	52
4.13	NA61 kaon errors	52
4.14	Fractional flux uncertainties from pion production uncertainties as a function of neutrino energy, for each flavor and at the near and far detectors. The breakdowns of the flux uncertainties are defined as follows: "NA61 Error" represents the uncertainty on the NA61/SHINE data. "Tertiary Tuning Error" represents the uncertainties on the Feynman momentum scaling. "Outside NA61 Error" represents the uncertainty from phase space not covered by the NA61/SHINE data.	53
4.15	Fractional flux uncertainties from kaon production uncertainties as a function of neutrino energy, for each flavor and at ND280 and SK. The breakdowns of the kaon flux uncertainties are defined as follows: "NA61 Error" represents the uncertainty on the NA61/SHINE data, "Other Data Error" represents the uncertainty on the Eichten <i>et al.</i> and Allaby <i>et al.</i> data. "Tertiary Tuning Error" represents the uncertainties on the Feynman momentum scaling. "No Data Error" represents the uncertainty from phase space not covered by any data. "Out-of-target Error" represents the uncertainty on the kaon production outside the target.	55
4.16	Production cross-section measurements for protons on graphite targets for momenta 20–60 GeV/c. The data from Denisov <i>et al.</i> are shown with and without the quasi-elastic subtraction since the measured quantity is ambiguous.	56
4.17	Fractional SK flux uncertainties from hadron production uncertainties.	57
4.18	Fractional ND280 flux uncertainties from hadron production uncertainties.	57
4.19	Overview of the generated pion tracking for nominal case (top right), different position (bottom right) and angle (bottom left) of inject proton beam.	58

4.20	The fractional change of SK ν_μ flux when the beam center position (Y) and center angle (θ_Y) are changed by 1σ (σ means the error size) from the measured values in Run 1, i.e. set to 1.42 mm and 0.29 mrad, respectively.	58
4.21	Beam profile in the position-angle phase space: left plot shows actual beam profile for the neutrino flux simulation (at Run1 case), right plot shows wide beam used to simulate the sample for re-weighting	59
4.22	Fractional ND280/SK ν_μ flux uncertainties from proton beam errors for Run1 measurements	60
4.23	Fractional change of the ν_μ flux at ND280 (left) and SK (right) for the $\pm 1\sigma_{OA}$ off-axis angle shift for the Run 1 measurement ($\sigma_{OA}=0.465$).	61
4.24	Fractional flux uncertainties for all sources of uncertainties.	63
4.25	The far/near ratio for the ν_μ flux prediction (top) and the uncertainty on the ratio (bottom).	64
4.26	Conceptual scheme of the flux extrapolation.	65
4.27	Fractional covariance matrix of the neutrino flux for each flavor, energy and detector	66
4.28	Fractional covariance matrix of the neutrino flux for ND280 ν_μ v.s. SK ν_μ or SK ν_e	67
4.29	Correlations of the neutrino flux for each flavor, energy and detector	67
4.30	Correlation of the neutrino flux for ND280 ν_μ v.s. SK ν_μ or SK ν_e	68
5.1	Neutrino-nucleus cross-sections as a function of neutrino energy in NEUT	70
5.2	The M_A^{QE} response function for one energy bin of ν_μ CQQE event. The " σ " represents a error size of M_A^{QE}	75
5.3	The change of the reconstructed energy distribution of SK ν_μ candidate events under the change of M_A^{QE} by $\pm 1\sigma$. The " σ " represents a error size of M_A^{QE} . The oscillation effect is included. Left plot shows the the energy distribution at each case and right plot shows the fractional deviation from the center.	75
6.1	A typical neutrino event at INGRID	77
6.2	The overview of the simulation for the INGRID neutrino event.	78
6.3	PE distribution of beam related sand muon. Left plot shows the distribution of the MC samples and right plot shows one in data.	80
6.4	Photo of the cross-section of the scintillator bar (left) and the cross-section in the MC simulation (right) after changed.	80
6.5	Tracking inefficiency as a function of the reconstructed track angle with respect to the beam direction. The cosmic-ray data is used.	81
6.6	Left: The wall of the ND280 hall reproduced in the GEANT4 simulation (downstream view). The INGRID 14 modules (green and purple boxes) and the wall of the ND280 hall (gray wall) are shown. Right: Black shows the vertex of the neutrino interaction in the background MC simulation (top view)	81
6.7	Efficiency and CC purity of INGRID selection	82
6.8	The horizontal neutrino beam profile reconstructed by INGRID for Run 1. The profile is fitted with a Gaussian function (lines in this plot). The statistical errors are smaller than the marks. Systematic errors are not shown.	83
6.9	Neutrino events per 10^{14} POT measured by INGRID	84
6.10	Neutrino beam profile center	84
6.11	A typical neutrino event at ND280	85
6.12	Energy loss distribution as a function of the reconstructed momentum for negative particles measured by TPCs	86
6.13	Reconstructed muon momentum distribution in Run1+2+3	88
6.14	Reconstructed muon angle distribution in Run1+2+3	89

6.15	Two dimensional distribution of the reconstructed muon momentum and angle in Run1+2+3	90
6.16	Example of a single-ring μ -like event detected at SK	92
6.17	Distributions of the PID parameter, reconstructed muon momentum, and the number of decay electron	95
6.18	Distributions of the reconstructed momentum and angle, and neutrino energy in the ν_μ CCQE candidate events for Run 1+2+3 data.	96
6.19	Two dimensional reconstructed vertex distribution of ν_μ candidate events.	97
7.1	Results of the ND280 fit	101
7.2	Results of the ND280 fit	101
7.3	ND280 ν_μ flux normalization.	102
7.4	SK flux normalization parameters before and after the ND280 fit	104
7.5	Correlation matrix of SK flux and cross-section parameters	105
8.1	The PDF of reconstructed energy spectrum with oscillation. Black histogram shows the normalized E^{rec} spectrum. Blue line shows the linear function interpolated between neighboring bin centers.	109
8.2	Predicted true-energy spectrum of ν_μ candidate events	110
8.3	Predicted reconstructed energy spectrum of ν_μ candidate events	110
8.4	Expected total number of ν_μ candidate events for each oscillation parameter points at 3.01×10^{20} POT	111
8.5	The correlation matrix (left) and diagonal fractional errors (right) of systematic parameters used in the oscillation analysis with the ND280 data constraint. The red histogram in the right figure represents the fractional errors before the ND280 fit.	113
8.6	Fluctuation of the N_{exp}^{tot} and $N_{exp}(E^{rec})$ at $(\sin^2 2\theta_{23}, \Delta m_{32}^2) = (1.0, 2.4 \times 10^{-3})$. Left: the distribution of the N_{exp}^{tot} based on 20000 toy-experiments by systematic parameter variations. Right: the $N_{exp}(E^{rec})$ distribution with errors which correspond to r.m.s. from 20000 toy-experiments.	114
8.7	Fractional error on the $\rho(E^{rec})$ with several systematic error sets. The fractional error is r.m.s/mean of 20000 toy-experiments at each E^{rec} bin.	116
8.8	Expected allowed contour (upper) and the $\Delta\chi^2$ slices for $(\sin^2 \theta_{23}, \Delta m_{32}^2) = (1.0, 2.4 \times 10^{-3})$ at 3.01×10^{20} POT (lower two plots). The allowed contour shows the line with 90% C.L. based on the constant $\Delta\chi^2$ limit. The each color represents the each contribution as shown in the upper plot.	118
8.9	The E_ν^{rec} distribution of the data, the best data fit, and the no oscillation	120
8.10	Pulls of systematic parameters at the best fit for data.	120
8.11	χ_{gof}^2 distribution for 1000 toy-experiments	121
8.12	The E_ν^{rec} distribution of the data, the best data fit with several likelihoods	121
8.13	$\Delta\chi_{crit}^2$ distribution for 68% CL.	123
8.14	$\Delta\chi_{crit}^2$ distribution for 90% CL.	123
8.15	$\Delta\chi_{crit}^2$ distribution for data	124
8.16	Allowed region of $(\sin^2 2\theta_{23}, \Delta m_{32}^2)$ for data with the F&C method	124
8.17	Comparison of allowed region of $(\sin^2 2\theta_{23}, \Delta m_{32}^2)$ for data with the F&C method and with the constant $\Delta\chi^2$ limit	125
8.18	The 90% confidence level allowed region of $(\sin^2 2\theta_{23}, \Delta m_{32}^2)$ for several likelihoods-combinations.	125
8.19	The 90% confidence regions allowed by T2K and other neutrino experiments	126
8.20	Sensitivity of T2K with more statistics in future	128

Bibliography

- [1] C. Kraus et al., *Eur.Phys.J. C*40 (2005) 447, hep-ex/0412056.
- [2] K. Assamagan et al., *Phys. Rev. D* 53 (1996) 6065.
- [3] ALEPH Collaboration, R. Barate et al., *Eur.Phys.J. C*2 (1998) 395.
- [4] Super-Kamiokande Collaboration, Y. Fukuda et al., *Phys.Rev.Lett.* 81 (1998) 1562, hep-ex/9807003.
- [5] Super-Kamiokande Collaboration, J. Hosaka et al., *Phys.Rev. D*73 (2006) 112001, hep-ex/0508053.
- [6] K2K Collaboration, M. Ahn et al., *Phys.Rev. D*74 (2006) 072003, hep-ex/0606032.
- [7] MINOS Collaboration, D. Michael et al., *Phys.Rev.Lett.* 97 (2006) 191801, hep-ex/0607088.
- [8] Super-Kamiokande Collaboration, K. Abe et al., *Phys.Rev. D*83 (2011) 052010, 1010.0118.
- [9] SNO Collaboration, B. Aharmim et al., (2011), 1109.0763.
- [10] The Borexino Collaboration, G. Bellini et al., *Phys.Rev.Lett.* 107 (2011) 141302, 1104.1816.
- [11] KamLAND Collaboration, S. Abe et al., *Phys.Rev.Lett.* 100 (2008) 221803, 0801.4589.
- [12] T2K Collaboration, K. Abe et al., *Phys. Rev. Lett.* 107 (2011) 041801.
- [13] MINOS Collaboration, P. Adamson et al., *Phys.Rev.Lett.* 107 (2011) 181802, 1108.0015.
- [14] DOUBLE-CHOOZ Collaboration, Y. Abe et al., *Phys.Rev.Lett.* 108 (2012) 131801, 1112.6353.
- [15] DAYA-BAY Collaboration, F. An et al., *Phys.Rev.Lett.* 108 (2012) 171803, 1203.1669.
- [16] RENO collaboration, J. Ahn et al., *Phys.Rev.Lett.* 108 (2012) 191802, 1204.0626.
- [17] Z. Maki, M. Nakagawa and S. Sakata, *Prog.Theor.Phys.* 28 (1962) 870.
- [18] B. Pontecorvo, *Sov.Phys.JETP* 26 (1968) 984.
- [19] Y. Katayama et al., *Progress of Theoretical Physics* 28 (1962) 675.
- [20] N. Cabibbo, *Phys.Rev.Lett.* 10 (1963) 531.
- [21] M. Kobayashi and T. Maskawa, *Prog.Theor.Phys.* 49 (1973) 652.
- [22] L. Wolfenstein, (1978).
- [23] J. Davis, Raymond, D.S. Harmer and K.C. Hoffman, *Phys.Rev.Lett.* 20 (1968) 1205.

-
- [24] Super-Kamiokande Collaboration, Y. Fukuda et al., *Phys.Rev.Lett.* 81 (1998) 1158, hep-ex/9805021.
- [25] CHOOZ Collaboration, M. Apollonio et al., *Eur.Phys.J. C* 27 (2003) 331, hep-ex/0301017.
- [26] G. Fogli et al., *Phys.Rev. D* 84 (2011) 053007, 1106.6028.
- [27] Particle Data Group, J. Beringer et al., *Phys.Rev. D* 86 (2012) 010001.
- [28] B. Richter, (2000), hep-ph/0008222.
- [29] K. Abe et al., (2011), 1109.3262.
- [30] T. Collaboration, (2003), http://neutrino.kek.jp/jhfnu/loi/loi_JHFcor.pdf, Letter of Intent: Neutrino Oscillation Experiment at JHF.
- [31] T2K Collaboration, K. Abe et al., *Nucl.Instrum.Meth. A* 659 (2011) 106, 1106.1238.
- [32] T2K Collaboration, K. Abe et al., *Phys. Rev. D* 85 (2012) 031103.
- [33] NA61/SHINE Collaboration, N. Abgrall et al., *Phys. Rev. C* 84 (2011) 034604.
- [34] NA61/SHINE Collaboration, N. Abgrall et al., *Phys. Rev. C* 85 (2012) 035210.
- [35] S. van der Meer, CERN-61-07 (1961).
- [36] R. Palmer, CERN-65-32 (1965) 141.
- [37] D. Beavis et al., Physics Design Report, BNL 52459 (1995).
- [38] S. Bhadra et al., accepted by *Nucl.Instrum.Meth.* (2012), 1201.1922.
- [39] A. Ichikawa, *Nucl. Instrum. Meth. A* 690 (2012) 27.
- [40] K. Matsuoka et al., *Nucl. Instrum. Meth. A* 624 (2010) 591.
- [41] T. Higuchi et al., eConf C0303241 (2003) TUGT004, hep-ex/0305088.
- [42] H. Berns and R. Wilkes, FADC board for T2K beam monitors, http://neutrino.phys.washington.edu/~berns/T2K/ADCCARD/adc2_status.html, <http://neutrino.phys.washington.edu/~berns/T2K/ADCCARD/docs/UWFADC-technote.pdf>, 2008.
- [43] S. Ritt, P. Amaudruz and K. Olchanski, MIDAS (Maximum Integration Data Acquisition System), <http://midas.psi.ch>, 2001.
- [44] H. Berns and R. Wilkes, *IEEE Trans.Nucl.Sci.* 47 (2000) 340, hep-ex/9909021.
- [45] T2K Collaboration, K. Abe et al., *Nucl. Instrum. Meth. A* 694 (2012) 211.
- [46] M. Otani et al., *Nucl.Instrum.Meth. A* 623 (2010) 368.
- [47] T2K ND280 TPC Collaboration, N. Abgrall et al., *Nucl. Instrum. Meth. A* 637 (2011) 25.
- [48] T2K ND280 FGD Collaboration, P.A. Amaudruz et al., *Nucl. Instrum. Meth. A* 696 (2012) 1.
- [49] Super-Kamiokande Collaboration, Y. Fukuda et al., *Nucl.Instrum.Meth. A* 501 (2003) 418.

- [50] T2K Collaboration, Y. Itow et al., (2001) 239, hep-ex/0106019.
- [51] Y. Hayato, Nucl. Phys. (Proc. Suppl.) B112 (2002) 171.
- [52] A. Ferrari et al., CERN-2005-010, SLAC-R-773, INFN-TC-05-11 .
- [53] R. Brun, F. Carminati and S. Giani, CERN-W5013 (1994).
- [54] C. Zeitnitz and T.A. Gabriel, In Proc. of International Conference on Calorimetry in High Energy Physics (1993).
- [55] J.B. et al. (Particle Data Group), Phys. Rev. D 86 (2012) 010001.
- [56] T. Eichten et al., Nucl. Phys. B 44 (1972).
- [57] J.V. Allaby et al., CERN preprint 70-12 (1970).
- [58] I. Chemakin et al., Phys. Rev. C 77 (2008) 015209.
- [59] R.J. Abrams et al., Phys. Rev. D 1 (1970) 1917.
- [60] J.V. Allaby et al., Yad. Fiz. 12 (1970) 538.
- [61] B.W. Allardyce et al., Nucl. Phys. A 209 (1973) 1.
- [62] G. Bellettini et al., Nucl. Phys 79 (1966) 609 .
- [63] B.M. Bobchenko et al., Sov. J. Nucl. Phys. 30 (1979) 805.
- [64] A.S. Carroll et al., Phys. Lett. B 80 (1979) 319.
- [65] J.W. Cronin et al., Phys. Rev. 107 (1957) 1121.
- [66] F.F. Chen et al., Phys. Rev. 99 (1955) 857.
- [67] S.P. Denisov et al., Nucl. Phys. B 61 (1973) 62.
- [68] M.J. Longo and B.J. Moyer, Phys. Rev. 125 (1962) 701.
- [69] A.V. Vlasov et al., Sov. J. Nucl. Phys. 27 (1978) 222.
- [70] R. Feynman, Phys. Rev. Lett. 23 (1969) 1415.
- [71] M. Bonesini et al., Eur. Phys. J. C 20 (2001).
- [72] D.S. Barton et al., Phys. Rev. D 27 (1983).
- [73] P. Skubic et al., Phys. Rev. D 18 (1978).
- [74] R.P. Feynman, Photon-Hadron Interactions (Benjamin, New York, 1972).
- [75] J.D. Bjorken and E.A. Paschos, Phys. Rev. 185 (1969) 1975.
- [76] F.E. Taylor et al., Phys. Rev. D 14 (1976) 1217.
- [77] R. Smith and E. Moniz, Nucl. Phys. 43 (1972) 605.
- [78] D. Rein and L. Sehgal, Ann. Phys. 133 (1981) 79.
- [79] D. Rein, Z. Phys. C 35 (1987) 43.

- [80] D. Rein and L. Sehgal, Nucl. Phys. B223 (1983) 29 .
- [81] D. Rein and L. Sehgal, Phys.Lett. B657 (2007) 207 .
- [82] S. Adler, Phys.Rev. 135 (1964) B963.
- [83] S. Adler, Ann. Phys. 50 (1968) 89.
- [84] M. Gluck et al., Eur.Phys.J. C5 (1998) 461.
- [85] A. Bodek and U. Yang, AIP Conf. Proc. 670 (2003) 110.
- [86] M. Nakahata et al., Journal of the Physical Society of Japan 55 (1986) 3786.
- [87] T. Sjostrand, Computer Physics Communications 82 (1994) 74 .
- [88] E. Moniz et al., Phys.Rev.Lett. 26 (1971) 445.
- [89] A.M. Ankowski and J.T. Sobczyk, Phys.Rev. C77 (2008) 044311, 0711.2031.
- [90] C. Juszczak, J.A. Nowak and J.T. Sobczyk, (2003), nucl-th/0311051.
- [91] MINOS Collaboration, P. Adamson et al., Phys.Rev. D81 (2010) 072002, 0910.2201.
- [92] S.K. Singh, M.J. Vicente-Vacas and E. Oset, Phys.Lett. B416 (1998) 23.
- [93] MiniBooNE Collaboration, A.A. Aguilar-Arevalo et al., Phys. Rev. D 83 (2011) 052007.
- [94] <http://wwasdoc.web.cern.ch/wwasdoc/minuit/minmain.html> .
- [95] <http://www.phy.duke.edu/~raw22/public/Prob3++> .
- [96] G.J. Feldman and R.D. Cousins, Phys.Rev. D57 (1998) 3873, physics/9711021.
- [97] MINOS Collaboration, P. Adamson et al., Phys.Rev. D86 (2012) 052007, 1208.2915.
- [98] Y. Itow, Atmospheric neutrinos ~ Results from running experiments ~, <http://neu2012.kek.jp>, 2012.